Title
Probing the Interactions between Functionalized Silica and Aqueous Uranyl Species

Author
Uribe, Eva Cristina

Publication Date
2016

Peer reviewed|Thesis/dissertation

Probing the Interactions between Functionalized Silica and Aqueous Uranyl Species

by

Eva Cristina Uribe

A dissertation submitted in partial satisfaction of the

requirements for the degree of

Doctor of Philosophy

in

Chemistry

in the

Graduate Division

of the

University of California, Berkeley

Committee in charge:

Professor Darleane C. Hoffman, Chair
Professor John Arnold
Professor Michael Nacht

Summer 2016

Probing the Interactions between Functionalized Silica and Aqueous Uranyl Species

Abstract

Probing the Interactions between Functionalized Silica
and Aqueous Uranyl Species

by

Eva Cristina Uribe

Doctor of Philosophy in Chemistry

University of California, Berkeley

Professor Darleane C. Hoffman, Chair

Efficient extraction and separation of actinides, lanthanides, and fission products from acidic or high ionic strength media is desirable for applications in nuclear waste reprocessing, environmental remediation, and laboratory scale processing of accelerator targets or forensics samples. The adaptation of traditional solvent extraction agents for use in solid phases would potentially reduce or eliminate the generation of mixed hazardous, radioactive waste streams. This dissertation presents the synthesis and evaluation of organically functionalized silica for the extraction of U(VI) from aqueous solutions. Diethylphosphonate and acetamide diethylphosphonate were grafted to an ordered mesoporous silica substrate, Santa Barbara Amorphous (SBA)-15. The phosphonate functional groups were chosen based on their demonstrated utility in solid and liquid phase extraction studies. SBA-15 has shown great potential as a framework for organic modification due to its high surface area, tunable pore size and particle morphology, resilience in acidic media, and hydrothermal robustness.

The work presented here is motivated by the need to obtain a better fundamental understanding of 1) the functionalization process, 2) the structure of the organometallic complexes formed at the functionalized silica surface, and 3) the limitations of metal extraction. Most previous studies on heavy metal extraction using organically modified silica have relied on measurement of macroscopic properties. In contrast, this work uses a combination of batch contact and nuclear magnetic resonance spectroscopic techniques to more thoroughly characterize the functional layer, and to probe the interaction between uranyl and the surface. In doing so, a greater understanding of the limitations of these types of materials has been achieved.

The fundamental interaction of U(VI) with diethylphosphatoethyl triethoxysilane (DPTS) functionalized SBA-15 mesoporous silica is studied by macroscopic batch experiments and solid-state nuclear magnetic resonance (NMR) spectroscopy. DPTS-functionalized silica has been shown to extract U(VI) from nitric acid solutions at or above pH 3. Extraction is dependent on pH and ionic strength. Single-pulse ^{31}P NMR on U(VI) contacted samples revealed that U(VI) only interacts with a fraction of the ligands present on the surface. At

pH 4 the U(VI) extraction capacity of the material is limited to 27-37% of the theoretical capacity, based on ligand loading. Single pulse ^{31}P NMR spectroscopy on U(VI)-contacted samples was combined with batch studies to measure a ligand-to-metal ratio of approximately 2:1 at pH 3 and 4. Batch studies and cross-polarization NMR measurements reveal that U(VI) binds to deprotonated phosphonate and/or silanol sites. ^{31}P$-^{31}$P DQ-DRENAR (Double-Quantum-based Dipolar Re-coupling effects Nuclear Alignment Reduction) NMR studies were used to compare the average dipolar coupling between phosphorus spins for both U(VI)-complexed and non-complexed ligand environments. These measurements reveal that U(VI) extraction is not limited by inadequate surface distribution of ligands, but rather by low stability of the surface phosphonate complex.

Acetamide diethylphosphonate (AcPhos)-functionalized silica has been shown to have a high affinity for U(VI) in pH 2-3 nitric acid solutions. Previous work has focused on actinide and lanthanide extraction under various conditions, but has shown poor reproducibility in the functionalization process. For this work, four AcPhos-functionalized SBA-15 materials were synthesized and evaluated based on their U(VI) sorption capacity and their resilience to contact with pH 3 nitric acid solutions. Materials synthesized with a pyridine base catalyst were shown to form a greater fraction of polymeric structures at the silica surface, which correlated with higher structural integrity upon contact with acidic solutions. The single-pulse ^{31}P and ^{1}H NMR spectra of these materials show evidence of the formation of phosphonic acid groups, as well as hydrogen-bonding interactions between ligands or with the silica surface. Additionally, these materials were found to have a significantly higher U(VI) sorption capacity and K_{eq} than the materials synthesized without pyridine, most likely due to the ion-exchange properties of the phosphonic acid groups. The ^{31}P$-^{31}$P DQ-DRENAR NMR technique was again employed to compare the average strength of dipolar coupling interactions between phosphorus atoms for the four different materials. Because the strength of dipolar coupling interactions depends on the number and proximity of neighboring spins, this technique provides information about the average density of ligands on the surface. The conventional functionalization procedure yielded materials with the lowest average surface ligand density, while those using extended reaction times and the pyridine base catalyst yielded materials with higher surface ligand densities.

para Mamá y Papá

Cheryl Wampler y Francisco Uribe

И для Миши

И для наших будущих серебряных зайчат

Contents

Contents **ii**

List of Figures **iv**

List of Tables **vii**

1 Introduction **1**
1.1 Introduction 1
1.2 Adaptation of Spent Fuel Reprocessing Ligands to the Solid Phase 2
1.3 Previous Work on Phosphate and Phosphonate Complexing Agents 4
1.4 Project Scope and Motivation 6
1.5 F-element Chemistry 7

2 Material Synthesis **17**
2.1 The Properties and Synthesis of Silica 17
2.2 Synthesis of Santa Barbara Amorphous (SBA)-15 Mesoporous Silica 27
2.3 Adsorption of Heavy Metals on Silica Surfaces 30
2.4 Functionalization of the Silica Surface 33

3 Fundamentals of Nuclear Magnetic Resonance (NMR) Spectroscopy **39**
3.1 Basic Principals of Solid-State NMR 39
3.2 Cross-Polarization 51
3.3 Dipolar Recoupling Sequences 62

4 Interactions between U(VI) and Diethylphosphonate Functionalized Silica **69**
4.1 Introduction 69
4.2 Synthesis and Functionalization of Mesoporous Silica Microspheres 70
4.3 Material Characterization 71
4.4 Batch Contact Results in Nitrate Media 75
4.5 Batch Contact Results with U(VI), Pu(VI), and Eu(III) 76
4.6 ^{31}P NMR Characterization of U(VI) Samples 82
4.7 ^{31}P$-^{31}$P Dipolar Coupling Measurements 87
4.8 Discussion 89

4.9 Conclusions and Future Work 94

5 Monolayer Formation and Sorption of U(VI) on Acetamide Diethylphosphonate Functionalized Silica 95
5.1 Introduction 95
5.2 Material Synthesis and Functionalization 97
5.3 Characterization by N_2 Adsorption 98
5.4 ^{13}C and ^{29}Si NMR Spectroscopy 102
5.5 Single-Pulse ^{31}P NMR Spectroscopy 108
5.6 Comparison of Ligand Distribution 111
5.7 Batch Contact Experiments with U(VI) 112
5.8 ^{31}P NMR Spectroscopy of U(VI) Samples 118
5.9 Discussion 119
5.10 Conclusions and Future Work 127

6 Experimental Methods 129
6.1 Synthesis of SBA-15 Microspheres 129
6.2 Synthesis of SBA-15 Rods 129
6.3 Functionalization Procedures 130
6.4 Measurement and Detection of Radioisotopes 132
6.5 Radioisotope Stock Preparation 134
6.6 Batch Contact Procedures: Diethylphosphonate-functionalized silica 135
6.7 Batch Contact Procedures: Acetamide diethylphosphonate-functionalized silica 136
6.8 NMR Spectroscopy and Instrumentation 137
6.9 Fitting of Other Data 140

Bibliography 141

List of Figures

1.1 The tributyl phosphate ligand used in the PUREX process 4
1.2 The carbamoyl methylphosphine oxide ligands used in solvent extraction 4
1.3 The f-block of the periodic table 7
1.4 Radioactive decay of ^{152}Eu 9
1.5 Formation of ^{232}U impurity in ^{233}U stocks 12
1.6 Radioactive decay chains of ^{233}U and ^{232}U 12
1.8 Structure of uranyl nitrate complexes 14
1.9 Uranyl hydroxide speciation diagram 15

2.1 IUPAC classification for adsorption isotherm and hysteresis loop shape 19
2.2 Structure and self-assembly of the triblock copolymer P123 used for synthesis of SBA-15 21
2.3 Diagram of three types of surface silanols on silica gel 25
2.4 The (111) face of β-cristobalite. 26
2.5 SEM images of large pore spherical SBA-15 particles 27
2.6 Nitrogen adsorption isotherm data for spherical SBA-15 particles 28
2.7 Nitrogen adsorption isotherm showing type H_2 hysteresis 29
2.8 Overview of the chemical processes underlying self-assembled monolayers on silica 34
2.9 Idealized ^{29}Si NMR spectrum and assignment of Q and T peaks 37

3.1 Diagram depicting Zeeman splitting in a finite applied magnetic field 41
3.2 Summary of the single-pulse FT-NMR experiment 42
3.3 Anisotropic dipolar coupling interactions 45
3.4 Diagram depicting magic-angle spinning of solid-state NMR samples 48
3.5 Pulse sequence for the cross-polarization experiment 52
3.6 The Hartmann-Hahn match condition for cross-polarization 54
3.7 Typical CP nutation curve for variable ^{1}H channel pulse widths 55
3.8 Typical CP nutation curve for variable X channel power levels 56
3.9 Classical cross-polarization kinetics model 57
3.10 Simulated CP variable contact time curve data for the $I - S$ kinetics model . . 58
3.11 I-I*-S cross polarization kinetics model 59
3.12 Simulated CP variable contact time curve data for the I-I^*-S kinetics model . . 60

3.13 REDOR pulse sequence for measuring heteronuclear dipolar coupling 63
3.14 Energy states of a two-spin system depicting quantum coherences 65
3.15 POST-C7 pulse sequence for exciting double quantum coherences 66
3.16 Pulse sequence for DQ-DRENAR technique for homonuclear dipolar recoupling 67

4.1 Nitrogen adsorption isotherm data for non-functionalized SBA-15 microspheres . 71
4.2 Nitrogen adsorption isotherm data for DPTS-SBA 72
4.3 $^{13}C\{^1H\}$ CP/MAS NMR spectra for pristine and acid-washed DPTS-SBA . . . 73
4.4 $^{31}P\{^1H\}$ CP/MAS NMR for pristine and acid-washed DPTS-SBA 74
4.5 $^{29}Si\{^1H\}$ CP/MAS NMR spectra for pristine and acid-washed DPTS-SBA . . . 75
4.6 Single pulse ^{31}P spectrum of pristine and acid-washed DPTS-SBA with triphenylphosphine 76
4.7 Percent sorption of U(VI) on DPTS-SBA from various nitrate media 77
4.8 Percent sorption of U(VI) by SBA and DPTS-SBA from 3 M $NaClO_4$ at pH 1-4 78
4.9 Percent loss of U(VI) from $HClO_4$ media 79
4.10 Percent sorption of Pu(VI) by SBA and DPTS-SBA from 3 M $NaClO_4$ 80
4.11 Percent sorption of Eu(III) by SBA and DPTS-SBA from 0.1 M $NaNO_3$ at pH 2-6. 80
4.12 Linearized Langmuir U(VI) sorption isotherm fit for DPTS-SBA and SBA . . . 81
4.13 Linearized Freundlich U(VI) sorption isotherm fit for DPTS-SBA and SBA . . . 82
4.14 Single-pulse ^{31}P MAS spectra of U(VI)-DPTS-SBA samples at various pH levels 84
4.15 $^{31}P\{^1H\}$ CP variable contact time curves for various DPTS-SBA samples 85
4.16 DQ-DRENAR data for U(VI)-DPTS-SBA-pH 4.0 and the control sample 88
4.17 $^{29}Si\{^1H\}$ CP/MAS NMR spectra for U(VI)-DPTS-SBA-pH 4.0 and the control . 91
4.18 Proposed structure for uranyl nitrate complex extracted by DPTS-SBA 91
4.19 Surface modification models based on rigid phosphonate ligands grafted to the 111-surface of β-cristobalite 93

5.1 Inspiration for the AcPhos ligand: carbamoyl methylphosphine oxide 96
5.2 Schematic showing the synthesis of the AcPhos ligand in previous work 96
5.3 The acetamide diethylphosphonate (AcPhos) ligand 97
5.4 Nitrogen adsorption isotherm data for non-functionalized SBA-15 rods 99
5.5 Nitrogen adsorption isotherm data for AcPhos-SBA (1) and AcPhos-SBA (2) . . 100
5.6 Nitrogen adsorption isotherm data for AcPhos-SBA (3) and AcPhos-SBA (4) . . 101
5.7 $^{13}C\{^1H\}$ CP/MAS spectra for pristine and acid-washed AcPhos-SBA (1) and(2) 103
5.8 $^{13}C\{^1H\}$ CP/MAS spectra for pristine and acid-washed AcPhos-SBA (3) and(4) 104
5.9 $^{29}Si\{^1H\}$ CP/MAS spectra for pristine and acid-washed AcPhos-SBA (1) and (2) 106
5.10 $^{29}Si\{^1H\}$ CP/MAS spectra for pristine and acid-washed AcPhos-SBA (3) and (4) 107
5.11 ^{31}P SP/MAS spectra for pristine and acid-washed AcPhos-SBA (1) and (2) . . . 109
5.12 ^{31}P SP/MAS spectra for pristine and acid-washed AcPhos-SBA (3) and (4) . . . 110
5.13 DQ-DRENAR data for AcPhos-SBA (1), (2), (3), and (4) 113
5.14 DQ-DRENAR data for two different resonances of AcPhos-SBA (4) 114

5.15 Percent sorption of U(VI) by AcPhos-SBA materials as a function of nitric acid concentration 115
5.16 Comparison of U(VI) sorption on AcPhos-SBA materials in from low and high ionic strength solutions 116
5.17 Langmuir and Freundlich isotherm fits for U(VI) sorption isotherm data for the AcPhos-SBA materials 117
5.18 Single-pulse ^{31}P spectra for U(VI)-AcPhos-SBA samples 118
5.19 ^{1}H decoupled single-pulse ^{31}P NMR spectra for AcPhos-SBA (4) pristine, acid-washed, and U(VI)-contacted 120
5.20 Comparison of ^{29}Si{^{1}H} CP/MAS spectra of pristine AcPhos-SBA (1)-(4) . . . 121
5.21 Single-pulse ^{1}H NMR spectrum of acid-washed AcPhos-SBA (4) 123

6.1 Electrodeposition cell for preparing alpha plates 133
6.2 NMR rotor and rotor inserts used for samples containing depleted ^{238}U. 140

List of Tables

1.1 Prominent gamma ray emissions for ^{152}Eu 9
1.2 Radioactive decay properties of relevant uranium and plutonium isotopes 11
1.3 Thermodynamic constants governing the formation of uranyl hydroxide species . 16

2.1 Summary of nitrogen adsorption characterization of SBA-15 rods 30

3.1 Properties relevant for NMR of ^{1}H, ^{13}C, ^{29}Si, and ^{31}P nuclei 49

4.1 Nitrogen adsorption results for SBA and DPTS-SBA 71
4.2 U(VI) isotherm fit parameters for SBA and DPTS-SBA 81
4.3 Single-pulse ^{31}P NMR resonance fit parameters for U(VI)-DPTS-SBA 83
4.4 Correlation between ^{31}P NMR fit data and U(VI) extraction data 83
4.5 ^{31}P$\{^{1}$H$\}$ CP variable contact time curve fit parameters 87

5.1 Summary of the difference in synthetic procedures for the AcPhos-SBA materials 98
5.2 Summary of N_2 adsorption isotherm data for AcPhos-SBA materials 99
5.3 Comparison of peak ratios for AcPhos-SBA ^{29}Si$\{^{1}$H$\}$ CP/MAS spectra 105
5.4 Ligand quantification using tripheylphosphine and ^{31}P NMR 111
5.5 Dipolar coupling constants measured for AcPhos-SBA using DQ-DRENAR . . . 112
5.6 Langmuir and Freundlich fit parameters for U(VI) isotherms on AcPhos-SBA . . 116
5.7 Fit parameters used to deconvolute the ^{31}P spectra for the U(VI)-AcPhos-SBA samples 119

Acknowledgments

The work presented in this dissertation was made possible by the contributions of many others. Darleane C. Hoffman has provided extraordinary support, inspiration, and encouragement as my committee chair for the past two years. Many thanks to John Arnold for his advice and for his interest in continuing the educational legacy of Heino Nitsche. I thank Michael Nacht for taking me under his wing, and for his wisdom and untiring sense of humor. Michael, you have been the most consistent adviser that I have had over the past five years, and it has been an honor and a privilege to work with you.

I thank Heino Nitsche for inspiring me to become a radiochemist, for loving his students, and for never having any doubts about me. I thank Stan Prussin for offering me his support at a crucial time, and his family for their endurance and patience. Stan pushed me to understand my research on a more fundamental level, and he instilled in me the great and under-appreciated value of the precise use of language. The time I spent with Stan as my adviser was the most challenging and most valuable year of my life so far. For that experience, I am very grateful to him.

I also thank my other friends and colleagues in the Department of Nuclear Engineering, including Karl Van Bibber, Patricia Schuster, Laurence Lewis, David Weisz, Araina Hansen and Denia Djokic, for welcoming me into their fold and for their support during hard times.

I came to Berkeley in 2011 to join Heino Nitsche's research group. Heino always told us that to earn a Ph.D. you had to go through the Valley of Tears. For me, learning to conduct research was like walking through a dark cave. When Heino was with us, the cave was filled with twinkling stars and distracting, blinking lights. At the moment I was trying to decide which light to follow, they all went out. After some initial panic, I was very fortunate to find an emergency flashlight, Wayne Lukens. With a seemingly endless reservoir of knowledge and patience, Wayne helped me identify and work around unforeseen obstacles. He also read this entire dissertation and gave me very valuable comments and suggestions. Thank you, Wayne! I would never have found my way without the incredible Harris Mason, who was like the sun at the end of a dark tunnel. Harris contributed many great ideas, many afternoons in the NMR lab, and many gentle but insistent nudges to keep on moving forward. Harris, I cannot thank you enough.

Even on the darkest days, I was never a lone explorer. To my fellow Nitsche group mates, I want you to know that I consider this a victory for all of us, and I thank each of you for being wonderful friends along the way. I am a better scientist and a better person for knowing all of you. I extend my gratitude to all past and current Nitsche group members, especially Ken Gregorich, Jackie Gates, Greg Pang, Carolina Fineman-Sotomayor, Roxana Farjadi, Stephen Jones, Brendan Baartman, Adam Rice, Jon Bowers, Kestrel Brogan, Paul Ellison, Julie Champion, Daniel Olive, Michele Pixa, and honorary members Rex Lake and Lauren Borja. Many thanks especially to Nick Esker, Oliver Gothe, and Jeff Kwarsick, my friends at the 88" Cyclotron. I thank and acknowledge Anthony Bruchet, our very talented

post-doc, who conducted much of the initial material synthesis work that got this project off the ground. Thank you, Tashi Parsons-Moss, for being courageous enough to start the mesoporous project in the first place, and for helping me learn much of what I know about actinide chemistry and the fruits of perseverance. Thank you, Erin May, for being a kind friend and fantastic hostess of many Nitsche group festivities. Thank you, Deborah Wang, for your endless patience, for always listening to others, and for never giving up on the best in yourself or any of us. Thank you, Philip Mudder, for your steadiness and quirky sense of humor, and for always being there for me. And finally, a thousand thanks to Jen Shusterman, who also read most of this dissertation. Jen, you taught me so much about science, research, and the pursuit of being alive, and you motivated me to teach myself even more. Thank you for consistently reminding all of us that we were lucky to have seen the stars at all.

I would like to thank those who make up the backbone of the Department of Chemistry, especially Lynn Keithlin, Dante Valdez, and Carl and Roy from shipping and receiving. Many thanks to Doug Reed from Jeff Long's group for his assistance with the nitrogen adsorption measurements presented in this work. I also thank Lawrence Berkeley Lab's Radiation Protection Group, who helped make this work possible, especially Naomi Reeves, Paul Trapani, Israel Tadesse, Bill Rowley, Mike Dupray, Tho Nhan, Jeff Bramble, and John van Wart. Thanks also to Marty White for keeping us safe. You all were amazing to work with! Many thanks also to the LBL bus drivers who made each day more cheerful.

I have benefited greatly from being a graduate research fellow with the National Science Foundation (Grant No. DGE 1106400). I thank the NSF for their continued support of basic science research at the graduate level. Additionally, portions of this work were performed in collaboration with Lawrence Berkeley National Laboratory and Lawrence Livermore National Laboratory of the U.S. Department of Energy under Contract No. DE-AC02-05-CH11231 and DE-AC52-07NA27344, respectively. Special thanks to Annie Kerstine and the Glenn T. Seaborg Institute at Lawrence Livermore National Laboratory for hosting me as a student for the past several years.

Finally, I want to thank my family, especially my parents, Cheryl and Francisco, for their constant love and encouragement, and for teaching me to lift up my heart. Many thanks also to my three beloved siblings and their families: Sr. Mariana Benedicta, Francisco, Marcela, Marco, Sebastián, and Dominga. I also thank my marvelous Aunt Janine. To my partner and life-teammate, Misha, the most generous and optimistic person I know, and to your wonderful family (Olga, Misha, and Sonya), thank you for helping me seek joy and opportunity in adversity.

Chapter 1

Introduction

1.1 Introduction

Organically functionalized SBA-15 materials have potential towards a broad array of applications, including heavy metal sequestration [1], catalysis [2, 3], drug delivery [4–6], and chromatograhy[7–9]. A number of self-assembled monolayers on mesoporous supports (SAMMS) have been developed for extraction of heavy metals, including the sequestration of lanthanides and actinides [10–16]. The use of functionalized mesoporous silica in the nuclear industry has steadily increased in the past two decades [17]. Sequestration of uranium is of particular interest due to its prevalence in the nuclear fuel cycle and in the environment, including sea water [18].

Mesoporous silica provides a high-surface area framework for the grafting of organic ligands. In acidic solutions, the surface is reactive towards alkoxysilane moieties, which can be used to tune the functionality of the surface for a variety of applications. The advent of highly ordered, thick-walled mesoporous silica Santa Barbara Amorphous (SBA)-15, developed by Zhao et al.[19] provided synthetic avenues for the careful control of pore size and particle morphology [20, 21]. Due to their relatively thick walls, SBA-15 type mesoporous silicas were found to have improved hydrothermal stability compared to previously synthesized mesoporous MCM-41 silicas [22]. For the purposes of developing heavy metal extraction materials, the great advantage of mesoporous silica is its high surface area, often between 800-1000 m^2 g^{-1}. In principle, the high surface area allows for greater accessibility of the functional groups to species in solution, compared to polymer substrates coated with organic ligands.

The research presented in this dissertation focuses on the synthesis, characterization, and comparison of SBA-15 materials functionalized with two different organic ligands: diethylphosphonate (DPTS) and acetamide diethylphosphonate (AcPhos). The extraction of U(VI) from nitric acid media by these materials is investigated. The novel contribution of this work is that it combines batch sorption experiments with spectroscopic studies using solid-state nuclear magnetic resonance (NMR) spectroscopy. NMR is used not only to

characterize the functionalized material, but also to examine the structure of the extracted U(VI)-phosphonate-silica complexes.

1.2 Adaptation of Spent Fuel Reprocessing Ligands to the Solid Phase

The ligands studied for this work were chosen based on their utility in the reprocessing of spent nuclear fuel. The efficient partitioning of elements produced in the generation of nuclear power is desirable for a number of reasons. It was first believed that reprocessing nuclear waste to recover unfissioned uranium and any ^{239}Pu produced for reuse would extend the world's uranium resources. In recent decades, however the demands of the nuclear energy industry have not yet come close to exceeding the supply of naturally-occurring uranium ore. Furthermore, it has been argued that the economic costs of reprocessing exceed the cost of direct disposal and a geological repository [23–25]. The proliferation risk of advanced nuclear fuel cycle reprocessing for commercial nuclear energy production is also of concern. As of 2013, the global plutonium stockpile includes over 250 metric tons of separated plutonium from civilian reprocessing [25]. The United States ceased reprocessing of civilian nuclear fuel in 1972. Today, there are active civilian reprocessing programs in France, the United Kingdom, Russia, India, Japan, and China, many of which also possess additional military reserves. North Korea, Pakistan, and Israel separate plutonium for military use. Of the non-nuclear weapons states, Japan possesses the largest stockpile of separated plutonium. Japan is estimated to have over 47 metric tons of separated plutonium [26], including 11 tons stored in Japan and 36 tons at reprocessing facilities in France and the United Kingdom [25]. These materials now have an uncertain fate in the aftermath of the accident at the Fukushima-Daiichi power plants in 2011. Fortunately there have been renewed efforts to reduce the global stockpile of separated plutonium. At the 2016 Nuclear Security Summit in Washington, D. C., the United States and Japan announced the completion of a project to remove all separated plutonium fuel from the Fast Critical Assembly [27], approximately 293 kg in total [28]. The plutonium was subsequently transported to the United States for ultimate disposal in the Waste Isolation Pilot Plant near Carlsbad, New Mexico [29]. Nevertheless, there is concern that in principle Japan's excess plutonium reserves undermine its significant nonproliferation efforts by reducing the time needed to obtain a fission weapon. The plutonium production in nuclear weapons states not party to the Nonproliferation Treaty continues to grow. The International Panel on Fissile Material estimates that by 2025, the combined plutonium production capacity of Israel, Pakistan, and India will reach over 2.5 metric tons per year [26]. The panel also estimates that by the end of 2014, North Korea had 30 kg of weapons-grade plutonium, enough for approximately 10 weapons.

Reprocessing has also been promoted as part of a potential solution to the nuclear waste disposal dilemma. During nuclear fission, long-lived transuranic isotopes are generated. Especially of concern are ^{239}Pu ($t_{1/2} = 2.41\times10^4$ years) which decays to ^{235}U ($t_{1/2} = 7.04\times10^8$

years), as well as the so-called "minor actinides" ^{237}Np ($t_{1/2} = 2.14 \times 10^6$ years), ^{241}Am ($t_{1/2} = 432.6$), ^{243}Am $t_{1/2} = 7370$ years), which decays to ^{237}Np), and ^{247,248,250}Cm ($t_{1/2} = 1.56 \times 10^7, 3.48 \times 10^5, 8.3 \times 10^3$ years, respectively). These isotopes and their decay products will contribute to the high level radioactivity of spent nuclear fuel over the next hundred thousand years. In contrast, many of the fission products, including ^{137}Cs, ^{90}Sr, and many lanthanide isotopes have shorter half-lives, on the order of several years. Overall, the long-lived fission products and minor actinides, along with ^{239}Pu make up only 1.2% of spent fuel by weight [30]. Therefore, efficient separation of the long-lived fission products and actinides from the bulk of un-spent uranium fuel and short-lived fission products would greatly reduce the volume of radioactive waste that would need long-term storage. The *partitioning and transmutation* strategy goes a step further. The idea is that long-lived minor actinides would first be partitioned from the lanthanides, which have high neutron absorption cross sections and act as neutron poisons. This step itself presents difficulties on an industrial scale due to the similarity in chemistry between Am and Cm and the lanthanides, as discussed in the following section. Following partitioning from the lanthanides, minor actinides would be further neutron irradiated in a fast neutron reactor, which would result in their fissioning to shorter-lived decay products [30].

Regardless of the evolving economic or technical viability of spent nuclear fuel reprocessing, the research to improve the efficiency and selectivity of f-element sequestration and separation has produced a large variety of extraction agents selective for various f-elements or fission products. Most of these have been optimized for solvent extraction procedures. However, there are several advantages to adapting these extraction agents for use on solid-phase substrates. Translation of solvent extraction processes to solid-liquid processes in the aqueous phase only would reduce the amount of high-level radioactive mixed waste produced. The use of high-surface area, porous substrates, has the potential to increase sequestration efficiency by increasing the area of interaction between dissolved species and extraction agents. Additionally, aqueous-solid phase extractions could in some cases eliminate the formation of third phases, which have often plagued solvent extraction studies. Finally, the change in ligand distribution and posture that occurs upon constraining it to a solid surface may in principle be co-opted to improve those criteria essential for extraction. For example, the bistriazinyl pyridines (BTPs), which showed great potential for the separation of trivalent actinides from lanthanides, were shown to form 3:1 ligand:metal complexes that bound so strongly that back-extraction to the aqueous phase was very difficult [31]. However, grafting the ligands to a solid surface, might limit complex formation to 2:1 ligand:metal species, thereby improving back extraction.

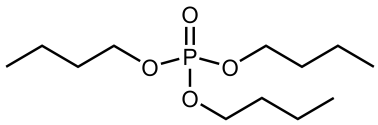

Figure 1.1: The tributyl phosphate (TBP) ligand used in the PUREX process.

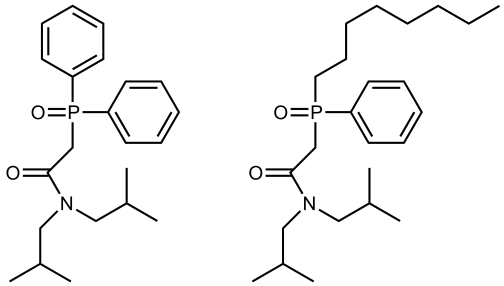

Figure 1.2: Two CMPO ligands used for solvent extraction of trivalent cations.

1.3 Previous Work on Phosphate and Phosphonate Complexing Agents

Many prominent extraction agents developed for spent fuel reprocessing contain phosphate, phosphonate, and phosphine oxide functional groups. The PUREX (**P**lutonium **U**ranium **R**edox **Ex**traction) process uses tributyl phosphate (TBP, Figure 1.1) dissolved in kerosene to extract U(VI) and Pu(IV) from concentrated nitric acid media. Pu(III) can then be back-extracted to the aqueous phase after chemical reduction, typically using Fe(II). More recent efforts have focused on expanding the PUREX process to include the extraction of Np by careful control of the Np(V)-Np(VI) redox chemistry [32]. One of the most commonly used solvent extraction agents used for selective extraction of transuranic elements is carbamoyl methylphosphine oxide or CMPO (Figure 1.2). CMPO was initially developed for use in the TRUEX (TRansUranium EXtraction) process [33–36]. Pre-arrangement of CMPO ligands, for instance by grafting them to calixarenes, crown ethers, or C_3-symmetric triphenoxymethane was shown to enhance affinity for the actinides and lanthanides [37–40]. Room temperature ionic liquids based on the CMPO functional group have been used for the extraction of actinides and lanthanides [41–43].

TBP and CMPO have also been used as synergists or co-extracting agents for the extraction of actinides from aqueous media in concert with other organic ligands. The term *synergist* is used to describe a pair of ligands that extract more of a desired species together than either does separately. Modolo and Geist describe the selective extraction of Am from Eu using synergistic mixtures of dithiophosphinic acid and TBP or tri-*n*-octyl phosphine oxide [44, 45]. This synergism was also observed by Wang et al. [46]. Molecular dynamic simulations revealed that TBP played an important role in solvating the metal-dithiophosphinic acid complex in the organic phase [47]. Mixtures of TBP and bistriazinyl

bipyridines were used to achieve group separation of the actinides (Am, Pu, U, and Np) from the lanthanides (La, Nd, Sm, Eu), though some fission products were also extracted [48]. CMPO and TBP act synergistically when combined together for solvent extraction processes. Horwitz and Kalina showed that combinations of CMPO and TBP demonstrated slightly increased extraction of Am(III) from concentrated (> 2 M) nitric acid solutions, and slightly decreased extraction from more dilute (< 2 M) solutions, compared to only CMPO [34].

CMPO has been incorporated into solid-phase extraction materials in many different ways. It has been coated onto polymeric resin supports, often in combination with other ligands such as tributyl phosphate [49, 50] or dicarbollide acid [51]. Yantasee et al.[52] made a carbamoylphosphonic acid-modified carbon paste electrode for the preconcentration and detection of uranium.

A variety of phosphinic and phosphoric acid-impregnated resins were tested for extraction of actinides from acidic media [53–55]. Wei et al. [54] developed a series of extraction chromatography resins by impregnating polymer resins with carbamoyl methylphosphine oxide (CMPO), diethylhexyl orthophosphoric acid (HDEHP), and dithiophosphinic acid (Cyanex 301) for the selective extraction of trivalent f-elements from fission products in high level waste. While the Cyanex-301 material was found to separate Am from bulk lanthanides, an absence of stability of the impregnated resin material was noted.

Horwitz et al. have reported a number of extraction chromatography resins designed for the selective extraction of actinides and rare earths [49, 56, 57]. These resins are made by sorbing the desired organic ligand onto inert polymer support beads. The TRU (TRansUranic) and RE (Rare Earth) resins combine the CMPO and TBP functionalities. They were shown to extract actinides from nitric and hydrochloric acid solutions at concentrations greater than 1 M [57]. Since actinides in the +4 and +6 oxidation states were retained even in dilute acid[49], these resins could be used to separate trivalent actinides and lanthanides from actinides with higher oxidation states. The UTEVA resin is coated with the ligand diamyl amylphosphonate, which forms similar complexes as TBP. Extraction of U(VI) was found to be highest at nitric acid concentrations above 1 M, whereas U(VI) could be stripped from the materials into dilute acid [57]. The advantage of the synthetic approach described by Horwitz et al.[56] is its simplicity. Resin beads are coated with ligands in methanol, and the methanol is then subsequently removed under vacuum. The approach taken for my work is quite different: ligands form a covalent bond to the silica surface via an alkoxysilane anchor. Functionalization proceeds through simultaneous cross-linking of the ligands to each other together with their condensation on the surface, creating what is called "a self-assembled monolayer." This method has the potential to make materials with increased stability that can be reused multiple times, compared to the coated resins. Part of the motivation for my work is to examine the stability of materials upon contact with nitric acid solutions.

Several studies examine the use of phosphonic acid-functionalized silica substrates for catalysis and chromatography [58–60]. Nesterenko et al. synthesized and characterized the ion-exchange properties of aminophosphonic acid-modified silica [61]. There have been

several investigations of U(VI) extraction using diethylphosphonate-modified mesoporous silica [62–69]. Additionally, Dudarko et al. used phosphonic acid tethered to mesoporous silica for the extraction of trace U(VI) from aqueous solution under mildly basic conditions [70].

The largest body of work on the extraction of lanthanides and actinides using self-assembled monolayers on silica substrates has been done by Fryxell et al.[10–16]. These studies were limited to testing the uptake of radionuclides via batch contact methods. A separate body of literature reports examination of the structural features of phosphonate- and phosphonic acid-functionalized silica using NMR spectroscopy, among other methods. Pan et al. and Bibent et al. have conducted in-depth NMR studies on the surface of diethylphosphonate- and phosphonic acid-modified silica and found evidence that the ligands engage in hydrogen bonding interactions [71, 72]. Very few have used solid-state NMR spectroscopy to examine the extracted metal-ligand-silica complex formed Shusterman et al. conducted the first study of the binding mechanism of metal sorption on functionalized silica via NMR spectroscopy on the metal nuclei [73]. NMR spectroscopy is an underutilized, but ideal tool for studying the complexation of metal ions to functionalized silica surfaces. The work presented here aims to make more complete use of NMR spectroscopy to answer fundamental questions about the function and limitation of these materials.

1.4 Project Scope and Motivation

This work was motivated by the need to understand the surface functionality and the extraction mechanism for organically functionalized silica surfaces on a molecular level. Experiments that probe the bulk, macroscopic properties of materials via batch contact experiments are useful for ascertaining certain kinetic and thermodynamic quantities, provided that extraction occurs as expected. However, a great deal about the material must be known before the ideal batch experiments can be designed. For example: what is the ligand loading on the surface? Is the material stable when exposed to the conditions of the batch contact experiment? These questions can be answered by characterizing the material using solid-state NMR spectroscopy. ^{13}C NMR spectroscopy is useful for verifying the structure of the carbon backbone of the ligand after functionalization and after exposure to acidic, aqueous media. ^{29}Si NMR spectroscopy can be used to examine the structure of the material at the organic-inorganic interface. In particular, ^{29}Si NMR spectroscopy gives information about the degree of cross-linking between ligands in the functionalized material. For phosphonate ligands, ^{31}P NMR spectroscopy can be used to observe the interaction between metal cations in solution and the phosphonate functional group.

This work was also motivated by the need to obtain a greater understanding of the functionalization process. The extraction of metal cations from aqueous solutions is affected by not only the extent of loading and the stability of the functional layer, but also by the relative proximity and posture of ligands. Solid-state NMR spectroscopy can also be used to measure the average density or distribution of ligands on the surface. These types of

58	59	60	61	62	63	64	65	66	67	68	69	70	71
Ce	**Pr**	**Nd**	**Pm**	**Sm**	**Eu**	**Gd**	**Tb**	**Dy**	**Ho**	**Er**	**Tm**	**Yb**	**Lu**
cerium	praesodymium	neodymium	promethium	samarium	europium	gadolinium	terbium	dysprosium	holmium	erbium	thulium	ytterbium	lutetium
90	91	92	93	94	95	96	97	98	99	100	101	102	103
Th	**Pa**	**U**	**Np**	**Pu**	**Am**	**Cm**	**Bk**	**Cf**	**Es**	**Fm**	**Md**	**No**	**Lr**
thorium	protactinium	uranium	neptunium	plutonium	americium	curium	berkelium	californium	einsteinium	fermium	mendelevium	nobelium	lawrencium

Figure 1.3: The f-block of the periodic table.

experiments also provide a way of evaluating different functionalization procedures. Silica gel materials are amorphous on a macroscopic level, but possess short-range, local order. This makes them inaccessible to diffraction methods that rely on long-range order to make structural determinations. For this reason, NMR spectroscopy is ideal for the study of functional layers on mesoporous materials.

The scope of the work presented in this dissertation is the synthesis and characterization of functionalized SBA-15 particles. NMR spectroscopy is used to examine 1) the stability of the monolayers of different materials, 2) how the functionalization procedure can be used to control the extent of cross-linking between ligands, 3) the reasons for heavy metal extraction limitations, and 4) what kinds of interactions occur between metal cations in solution and the ligand or between the metal and the silica framework under various conditions.

The remainder of this chapter reviews important aspects of f-element chemistry, with particular attention to the aqueous chemistry of uranyl species. Radioactive decay properties of relevant isotopes are also reviewed. In Chapter 2 the underlying principals and practical aspects of the synthesis of functionalized SBA-15 mesoporous silica is discussed. Chapter 3 reviews important fundamental concepts in nuclear magnetic resonance (NMR) spectroscopy, and describes the experiments used to probe the integrity of the functional layer and the interaction between U(VI) and silica-grafted phosphonate ligands. Chapter 4 presents results from the work probing the interaction between U(VI) and diethylphosphonate-functionalized SBA-15. Finally, Chapter 5 presents the synthesis and comparison of four different acetamide diethylphosphonate-functionalized SBA-15 materials. Details regarding experimental methods and instrumentation are given in Chapter 6.

1.5 F-element Chemistry

The majority of work presented in this dissertation investigates the sorption of aqueous uranium species on organically functionalized mesoporous silica surfaces. For a few select conditions, the uptake of U(VI) was compared to that of Pu(VI) or Eu(III). This section gives an overview of the radiochemistry of these f-elements, including their basic aqueous phase chemistry and their radioactive decay properties.

Chemistry of the Lanthanides

The lanthanides are typified by the stability of the +3 oxidation state in aqueous solution. They are considered hard Lewis acids that form stable complexes with hard Lewis bases. As will be discussed below, the $4f$ orbitals participate very little in complex formation, such that coordination geometries are limited more by steric effects than crystal field effects [74]. The lanthanides tend to form 8- or 9-coordinate complexes with small ligands. At approximately neutral pH, they form insoluble hydroxide species.

Because of their similarity in chemistry and confusion in naming early in their discovery, over 70 "new" rare earth elements were claimed to have been discovered throughout the 1800s [74]. In 1913, Henry Moseley showed that the proton number in a nucleus could be identified by the X-ray spectra emitted by an element upon excitation, leading to the concept of *atomic number* [75, 76]. Combined with Bohr's model of the atom, it was discovered that the rare earths being discovered were only the 15 elements between lanthanum and lutetium. Furthermore, it was discovered that this group of elements had valence electrons in the 4f subshell, which would give them markedly different chemistry than that of the transition metals and alkaline earth metals.

At the beginning of the lanthanide series, the $4f$ orbitals are slightly higher in energy than the $5d$ orbitals. As the number of protons in the nucleus increases across the series, the $4f$ orbitals are stabilized and begin to fill before the $5d$ orbitals. The $4f$ orbitals are more contracted than the $5s^2$ and $5p^6$ orbitals in the +3 oxidation state, which makes the $4f$ electrons "core-like" and unavailable for interactions with ligands. At the same time, the $4f$ orbitals do not shield the nucleus very well. This results in a contraction of the ionic radius as the proton number increases across the series. While this contraction is not unique (as it is also observed for the actinides and transition metals) it is most obvious in the lanthanide series because of the uniform oxidation state and lack of additional electron shielding as the proton number increases.

The chemistry of the lanthanides is similar across the series. While the most stable oxidation state for europium in aqueous solution is +3, it can also access the +2 oxidation state more easily than most of the other lanthanides. The ground state electron configuration of atomic europium has a half-filled $4f$ subshell: $[Xe]4f^7 6s^2$. The stability of the half-filled $4f$ subshell makes the +2 oxidation state slightly more favorable for Eu than for other lanthanides. Nonetheless, europium is often used as a model lanthanide. One reason for this is because europium sits midway through the lanthanide series, and so has an intermediate ionic radius. As extraction and separation of the lanthanides is often based on the subtle differences in their ionic radii, europium makes an ideal test case for the intermediate size. Another reason is that the radioactive isotope ^{152}Eu is both readily available and readily observable. Unlike radioactive isotopes available for other lanthanides, ^{152}Eu has a sufficiently long half-life (13.537 years) to allow for experimental study without decay corrections, as well as several intense gamma ray emissions. These properties make ^{152}Eu an ideal radiotracer.

^{152}Eu decays by both beta decay and electron capture (Figure 1.4). Table 1.1 shows the prominent gamma emission for ^{152}Eu and their percent intensities. Due to isotopic impurities

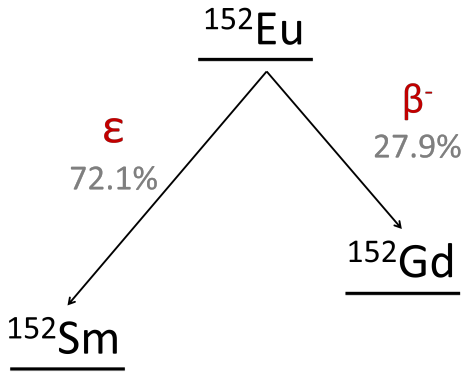

Figure 1.4: Radioactive decay of ^{152}Eu.

Table 1.1: Prominent gamma ray emissions for ^{152}Eu

γ Energy (keV)	% Intensity
121.8	28.6
344.3	26.5
778.9	12.9
964.1	14.6
1085.9	10.2
1112.0	13.6
1408.0	21.0

(^{154}Eu) that also emit gamma rays near 121 keV, the 344 keV gamma line is typically chosen for quantification of Eu in solution.

Chemistry of the Actinides

The actinides demonstrate greater variability in stable oxidation states compared to the lanthanides. For the early actinide atoms (Ac, Th, Pa, U, and Np), the $5f$ orbitals and $6d$ orbitals are nearly degenerate, and their ground state electron configurations contain partially filled $5f$ and $6d$ subshells. Atomic uranium has an electron configuration of $[Rn]5f^36d^17s^2$. As proton number increases across the series, the f-orbitals are stabilized and start to fill first. For example, plutonium has a ground state of $[Rn]5f^67s^2$ and Am of $[Rn]5f^77s^2$. The stability of the half-filled $5f$ subshell means that curium's ground state electron configuration is also mixed: $[Rn]5f^76d^17s^2$. However, for the later actinides (Bk-No), the f-orbitals are lower in energy than the $6d$ and are therefore filled first.

The $5f$ orbitals are less "core-like" than the $4f$ orbitals are for the lanthanides. For the early actinides (Ac-Np), the near degeneracy of the $5f$, $6d$, and $7s$ orbitals means that a greater range of oxidation states are accessible, and a wider variety of compounds are formed,

including the formation of covalent oxides AnO_2^+ and AnO_2^{2+}, the actinyls. In this sense, the early actinides resemble the transition metals. This is at least in part due to relativistic effects. For hydrogen and other low-Z elements, the angular velocity of electrons is low enough that relativistic effects do not influence their chemistry. By the actinides, however, the orbital angular velocity of atomic electrons increases significantly, and approaches the speed of light. This causes an increase in the mass of the electron. For the actinides, the effects of relativity have an observable influence on their chemistry. The s and p orbitals contract and are stabilized relative to theoretical atoms where relativistic effects are set to zero. In comparison the f and d orbitals are expanded and destabilized. Thus, the $5f$ orbitals play a more active role in bonding than the $4f$ orbitals do for the lanthanides [74]. The similarity in chemistry of the early actinides to that of the transition metals, the stability of multiple oxidation states, and the existence of very high stable oxidation states for some elements, resulted in their initial placement in the d-block. However, their chemistry was ultimately found not to match that of their d-block homologues. Moreover, the chemistry of the later actinides, americium and curium, was found to resemble that of the lanthanides. Not until 1944 when Glenn T. Seaborg formulated his "actinide concept" did the actinides take their present place in the f-block below the lanthanides [77].

The Radioactive Decay Properties of Uranium and Plutonium Isotopes

Naturally occurring uranium consists of 0.72% ^{235}U and 99.27% ^{238}U. A very small amount of ^{234}U occurs naturally from the decay chain of ^{238}U. Isotopic separations yield *enriched* uranium, which has greater than 0.72% ^{235}U and *depleted* uranium, which has less than 0.72% ^{235}U. The isotope ^{233}U is not naturally occurring. It is obtained through neutron capture on ^{232}Th (100% abundant in nature), followed by subsequent beta decay:

$$^{232}\mathrm{Th} + n \longrightarrow {}^{233}\mathrm{Th} \xrightarrow{\beta^-} {}^{233}\mathrm{Pa} \xrightarrow[27\ \mathrm{days}]{\beta^-} {}^{233}\mathrm{U}$$

^{233}U is fissile, like ^{235}U and ^{239}Pu. They have sufficiently high thermal neutron induced fission cross sections such that under certain conditions, a fission chain reaction can occur, in which more neutrons per fission are emitted than are captured. This makes them suitable for use in fission weapons or in nuclear power reactors. The abundance of the ^{232}Th isotope in monazite sands in coastal India has made the concept of the thorium fuel cycle very popular there in recent decades, though it has not yet been achieved on a commercial scale.

^{239}Pu is also not naturally occurring and is made via neutron capture on ^{238}U and subsequent beta decay:

$$^{238}\mathrm{U} + n \longrightarrow {}^{239}\mathrm{U} \xrightarrow{\beta^-} {}^{239}\mathrm{Np} \xrightarrow[2.4\ \mathrm{days}]{\beta^-} {}^{239}\mathrm{Pu}$$

Table 1.2: Radioactive decay properties of relevant uranium and plutonium isotopes

Isotope	Natural Abundance	Half-life (y)	Specific Activity (Ci/g)	α Energy (MeV)	% Intensity
^{232}U	N/A	68.9	22.3	5.263	31.6
				5.32	68.2
^{233}U	N/A	$1.592 \cdot 10^5$	$9.637 \cdot 10^{-3}$	4.784	13.2
				4.824	84.4
^{234}U	0.0054%	$2.455 \cdot 10^5$	$6.223 \cdot 10^{-3}$	4.722	28.4
				4.775	71.4
^{235}U	0.72%	$7.04 \cdot 10^8$	$2.161 \cdot 10^{-6}$	4.366	17.0
				4.398	55.0
^{238}U	99.27%	$4.46 \cdot 10^9$	$3.362 \cdot 10^{-7}$	4.151	21.9
				4.198	79.0
^{239}Pu	N/A	$2.411 \cdot 10^4$	$6.207 \cdot 10^{-2}$	5.105	11.5
				5.144	15.1
				5.156	73.3

Table 1.2 summarizes the relevant uranium and plutonium isotopes and their radioactive decay properties. For batch contact experiments in this work, the α-activity of ^{233}U was used to measure the total uranium concentration in solution. For preparation of solid-state NMR samples, the total α-activity was minimized by using only depleted uranium. This was done to minimize the impact of contamination if a rotor crash occurred while spinning at 10 kHz.

The isotope ^{233}U is usually made in a nuclear power reactor, which has a high flux of thermal neutrons. During neutron irradiation of ^{232}Th in a reactor, side reactions occur involving neutron capture by ^{233}U and ^{233}Pa (Figure 1.5). This results in the production of ^{232}U, which cannot be removed from the ^{233}U produced except through isotopic separation. The presence of ^{232}U is problematic from an experimental and materials perspective because it is relatively short-lived compared to ^{233}U and has many short-lived daughter products. Many of these are also α emitters, and some emit very energetic gamma rays. The decay chains of ^{233}U and ^{232}U are shown in Figure 1.6. Therefore, ^{232}U has the effect of introducing significant α impurities to a ^{233}U stock. For this reason, it must be purified from the ^{232}U daughters on a regular basis - every few months to a year, depending on the desired radiopurity. Figure 1.7a shows an alpha spectrum of a ^{233}U stock left for approximately 11 years without separation from its daughters, while Figure 1.7b shows a spectrum of the same stock immediately following purification. The procedure used for purification of ^{233}U stocks and for conducting alpha spectroscopy to quantify impurities is described in detail in Chapter 6.

The Chemistry of Uranium

The most stable oxidation states of uranium in aqueous solution are +4 and +6. In the +4 oxidation state, the bare ion U^{4+} exists. For higher oxidation states, the uranyl compound

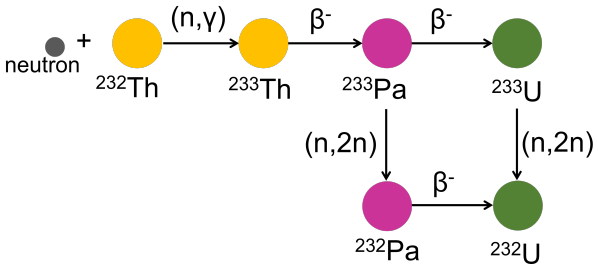

Figure 1.5: Formation of ^{232}U stock impurity by neutron capture on ^{233}Pa and ^{233}U.

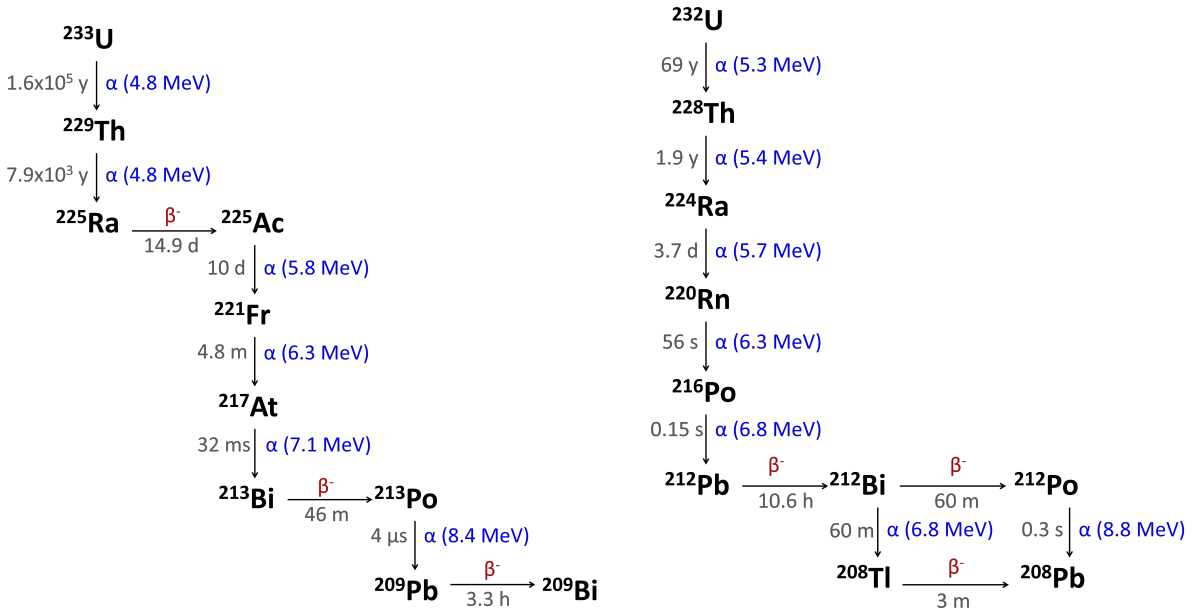

Figure 1.6: Radioactive decay chains of a) ^{233}U and b) ^{232}U.

is formed: UO_2^+ for U(V) and UO_2^{2+} for U(VI). In aqueous solution open to air, U(IV) readily oxidizes to U(VI). Pentavalent U(V) will disproportionate to U(IV) and U(VI):

$$2\,UO_2^+\,(aq) + 4\,H^+\,(aq) \longrightarrow UO_2^{2+} + U_4^+\,(aq) + 2\,H_2O\,(l)$$

Uranyl adopts a linear geometry with a U-O distance of approximately 1.8 Å [78]. This relatively short bond length corresponds to strong bonds, each consisting of one σ and two π bonds, such that the uranyl bond can be thought of as a triple bond [79]. The UO_2^{2+} complex is linear, unlike other MO_2 complexes observed in the transition metals, or isoelectric ThO_2, which is bent. The formal charge of uranium in $UO_2(H_2O)_5^{2+}$ (gas phase) is +2.43, and the oxygens' formal charge is -0.43 [80]. The basicity of the uranyl oxygens can be controlled by

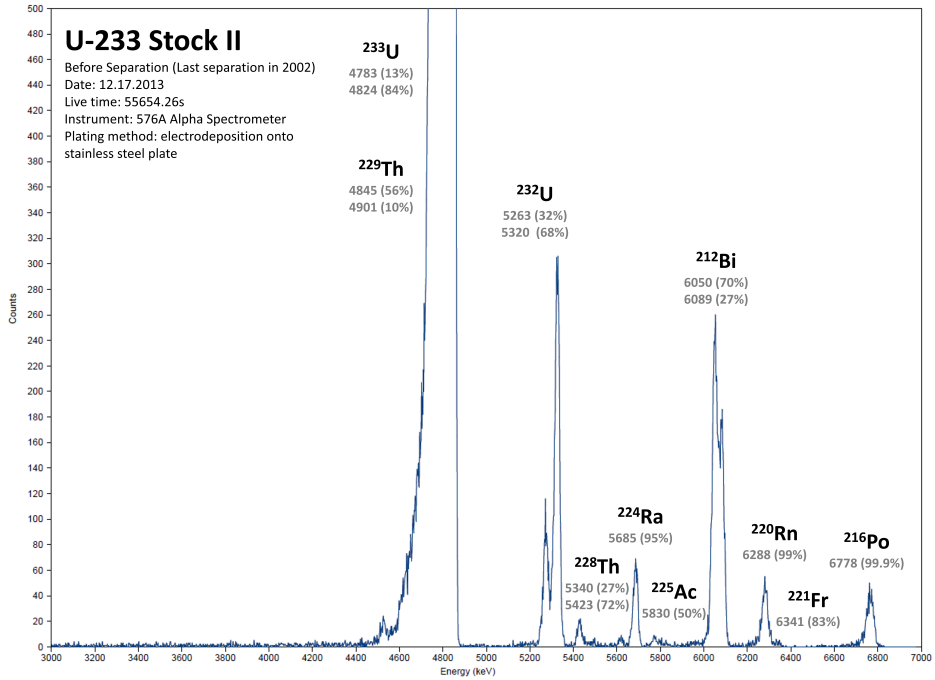

(a) Alpha spectrum of a ^{233}U stock approximately 11 years after the last separation from its decay daughters. The alpha plate was made by electrodeposition of a stock aliquot onto a stainless steel plate.

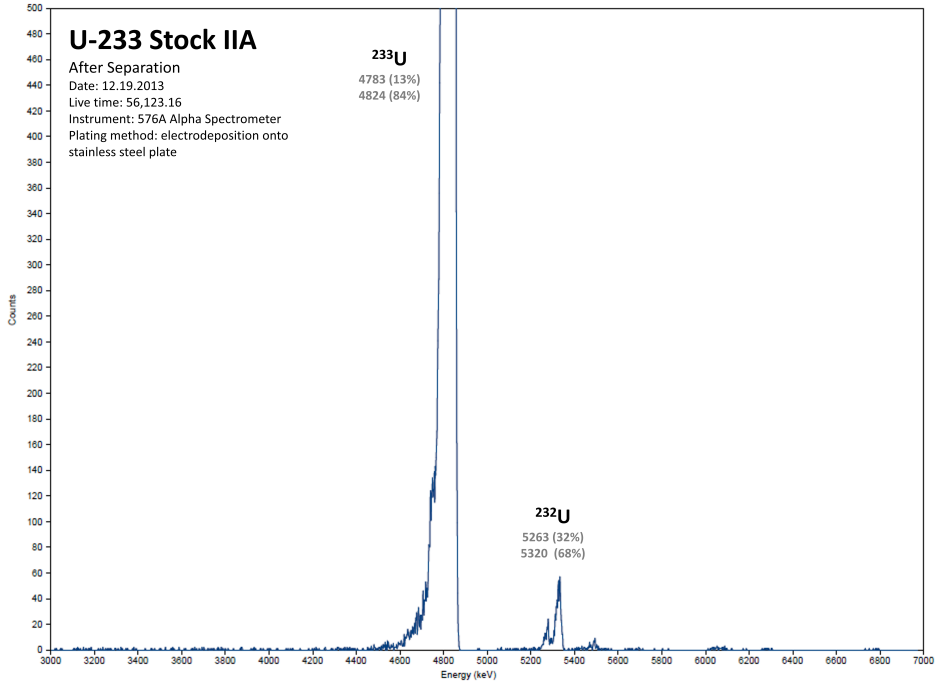

(b) Alpha spectrum of a ^{233}U stock immediately after purification from its daughters. The alpha plate was made by electrodeposition of a stock aliquot onto a stainless steel plate.

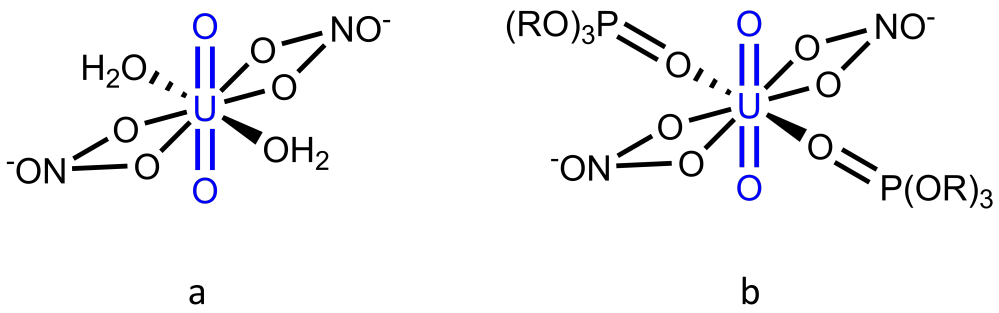

Figure 1.8: Complexes formed between uranyl and nitrate and water ligands (left) and between uranyl, nitrate, and phosphate (right).

changing the ligands complexed to uranyl, such that the uranyl cation can complex other cations through the axial oxygens [79].

In the aqueous chemistry of uranyl, the linear UO_2 component is inert, but the equatorial positions are labile. Uranyl interacts with ligands in the equatorial positions via σ bonds and *d-p* and *f-p* π bonding interactions [74]. Depending on their size, typically 4-6 ligands can occupy the equatorial positions. Coplanarity in the equatorial positions can be maintained even for six small ligands, though for bulkier ligands puckering of the plane may occur. The U(VI) aquo ion has five H_2O molecules in the equatorial positions at a distance of 2.421 Å from the uranyl ion [81–83]. Crystal structures show that the NO_3^- anion complexes uranyl in a bidentate manner, with three nitrates occupying six equatorial positions [84]. In aqueous solution, the highly soluble, 8-coordinate uranyl nitrate $UO_2(NO_3)_2 \cdot (H_2O)_2$ is formed (Figure 1.8a). This hydrated uranyl nitrate complexes readily with phosphates, phosphonates, or phosphine oxide ligands (Figure 1.8b) [74]. Variation of the steric bulk of the R groups in Figure 1.8 alters its hydrophobicity. Tributyl phosphate (TBP) dissolved in kerosene is used for the selective extraction of uranyl and plutonyl nitrate complexes from acidic media in the PUREX method for reprocessing of spent nuclear fuel. The hexagonal bipyriamidal geometry also results from complexation with CO_3^{2-} [85].

The uranyl ion is a hard Lewis acid that interacts with ligands primarily through electrostatic interactions. The strength of electron donor-acceptor interactions follows the trend [79]:

$$F^- \gg Cl^- > Br^- \approx I^-$$

$$O \gg S > Se$$

$$N \gg P \approx As$$

One of the most important aspects of the chemistry of uranyl is its ability to form insoluble complexes with oxyhydroxides, silicates, and phosphates. Gorman-Lewis, Burns,

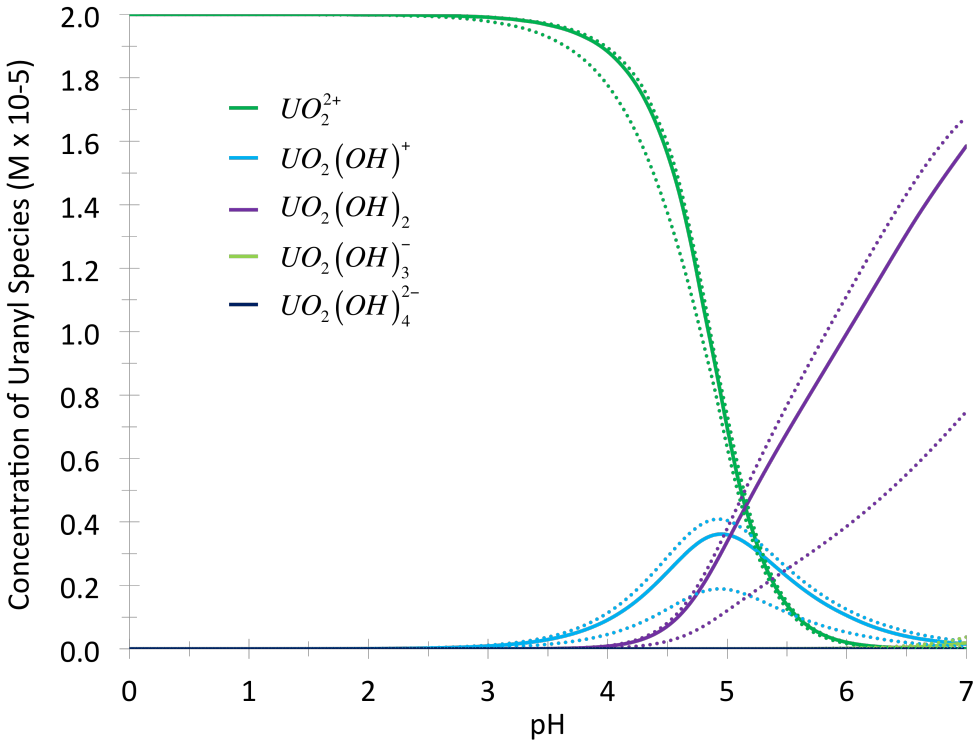

Figure 1.9: Uranyl hydroxide speciation diagram calculated using the speciation software Ljunskile 2.0. All thermodynamic data is from reference [87]. This simulation was done with $[UO_2{}^{2+}] = 20\ \mu M$ with no CO_2 from pH 0 to 7.

and Fein[86] give a thorough review on the thermodynamic constants governing the solubility of these uranyl mineral phases. When conducting batch contact experiments above pH 3, it is imperative to conduct control experiments to distinguish sorption to solid phases from spontaneous precipitation from solution.

Uranyl hydrolyzes in water. The extent of hydrolysis depends on the solution pH, the temperature, and the ionic strength. At zero ionic strength and a temperature of 25 °C the speciation of uranyl hydrolysis products is distributed according to Figure 1.9, which was calculated using the thermodynamic constants given in Table 1.3. The experiments conducted in this work were conducted at pH 6 or below, where speciation is dominated by $UO_2{}^{2+}$, with one or two nitrate ions complexed in equatorial positions, depending on the nitrate concentration.

$UO_2(OH)_2$ has limited solubility. In the absence of any ligands that stabilize soluble uranyl species, the minimum solubility for uranyl hydroxide occurs around pH 7, where the total concentration of uranium in solution is less than 10^{-6} M [88]. At higher pH values, the formation of carbonate complexes dominates aqueous chemistry, especially in high ionic strength solutions like sea water [89]. For calcium rich waters, the complex $Ca_2UO_2(CO_3)_3$ has been found to significantly influence speciation [90]. Silicate species also influence uranyl solubility and speciation. The solubility of $(UO_2)_2SiO_4 \cdot H_2O$ decreases with increasing pH,

Table 1.3: Thermodynamic constants governing the formation of uranyl hydroxide species from reference [87].

Reaction	$log\beta$
$UO_2^{2+} + H_2O \rightleftharpoons UO_2OH^+ + H^+$	-5.2 ± 0.3
$UO_2^{2+} + 2\,H_2O \rightleftharpoons UO_2(OH)_2 + 2\,H^+$	-10.3
$UO_2^{2+} + 3\,H_2O \rightleftharpoons UO_2(OH)_3^- + 3\,H^+$	-19.2 ± 0.4
$UO_2^{2+} + 4\,H_2O \rightleftharpoons UO_2(OH)_4^{2-} + 4\,H^+$	-33.0 ± 2

and reaches a minimum around pH 6-7 [91]. This could mediate the precipitation of uranyl silicate species onto silica surfaces at pH levels and uranium concentrations where it would otherwise be soluble.

Chapter 2

Material Synthesis

2.1 The Properties and Synthesis of Silica

Silica: background and history

Silica (SiO_2 or $SiO_2 \cdot xH_2O$) is ubiquitous in natural and synthetic forms. In nature, it can be found in minerals including quartz and cristobalite. It is the main constituent of most sands. Mineral forms of silica exist as mostly dense, ordered, crystalline phases, with surface areas restricted to their geometric surface areas. The exceptions are the naturally occurring zeolites.

Various forms of synthetic silica have been produced industrially. Amorphous, porous silica possesses higher surface area and surface reactivity than crystalline phases. From a commercial materials perspective, the ability to precisely control the pore structure, pore volume, external particle morphology, and therefore the surface area, is highly desirable. Some of the first porous silicates synthesized for commercial applications were zeolites, a family of crystalline aluminosilicate materials with narrow pore distributions and pore diameters on the order of 0.4 - 1.3 nm. Zeolites were synthesized using small organic templates and have been used as molecular sieves to separate gas molecules based on their size and shape [92]. In the 1970's, Mobil Oil Corporation researchers synthesized ordered, porous silicas, MCM-41 and MCM-48, using a cationic liquid crystal structure directing agent combined with anionic silicate in basic solutions [93]. The resulting structures contained highly tunable pore diameters in the range of 15-300 Å, larger than had been achieved with template-synthesized zeolites up until that point [94]. Their surfactant-based templating method launched a new field of highly controlled pore design on the mesoscale.

Characterization by Nitrogen Adsorption

The classification of materials based on their pore size and properties is not always consistent. For this work, materials are named according to the classification established by the International Union of Pure and Applied Chemistry (IUPAC) [95]:

Megaporous	>7500 nm
Macroporous	50-7500 nm
Mesoporous	2-50 nm
Microporous	<2nm

Materials with pore diameters between 0.7 and 2 nm are called *supermicroporous*, between 0.4 and 0.7 *ultramicroporous*, and less than 0.4 nm *submicroporous*. Although the *mesoporous* materials used for this work have pore diameters on the order of nanometers, they are generally not referred to as *nanoporous*.

Silica materials can be described and compared by their specific surface area, average pore size and pore size distribution, and macroscopic particle size and morphology. A great deal of information about the surface area and pore structure can be determined by measuring the absorption of nitrogen gas as a function of nitrogen pressure.

In a typical nitrogen adsorption isotherm experiment, a sample is sealed in a tube, which is then evacuated to remove water or other compounds that may be adsorbed to the silica surface under ambient conditions. The sample is then weighed and transferred to an evacuated gas adsorption apparatus, where it is exposed to low pressure nitrogen gas while suspended in a cold bath at 77 K. The sample is allowed to equilibrate, the pressure recorded, and the process repeated, gradually increasing the pressure of nitrogen gas each time. When a saturation pressure is reached, the process is reversed to measure desorption as a function of gas pressure.

Materials with different pore properties have distinct nitrogen adsorption isotherm shapes. Figure 2.1a shows a variety of isotherm shapes and their IUPAC classification. Microporous materials demonstrate a Langmuir (type I) isotherm. Upon exposure to nitrogen gas, the micropores fill quickly, resulting in a sharp rise followed by a plateau as the micropores fill up. Nonporous or macroporous materials demonstrate type II, III, and VI isotherms. Mesoporous materials, typified by type IV and V isotherms, have a desorption branch that deviates from the adsorption branch, resulting in a hysteresis loop. The hysteresis loop is due to capillary condensation, which causes a difference in energy between the adsorbing and desorbing of gas molecules at surface sites for pores of a certain size, though the underlying physical principals are still debated [96]. Capillary condensation is followed by a plateau after the pores are completely filled [97]. Analysis of the linear part of the adsorption isotherm via the Brunauer-Emmett-Teller (BET) method yields the surface area of the material [98]. The average pore size and pore size distribution can be calculated using the Barret-Joyner-Halenda (BJH) analysis method [99].

Additional information about pore ordering and morphology can be gleaned from the shape of the hysteresis loop. Mesoporous hysteresis loops usually occur above $P/P_0 = 0.4$, where P is the equilibrium pressure in the sample chamber and P_0 is the bulk saturation pressure of the sample. Figure 2.1b shows the four different hysteresis loop types observed for mesoporous materials. Hysteresis loop shape has been classified empirically. An H_1 hysteresis loop is observed for ordered, cylindrical-like pore channels, while H_2 loops are observed for disordered pore structures, poorly defined pore shape and distribution, and

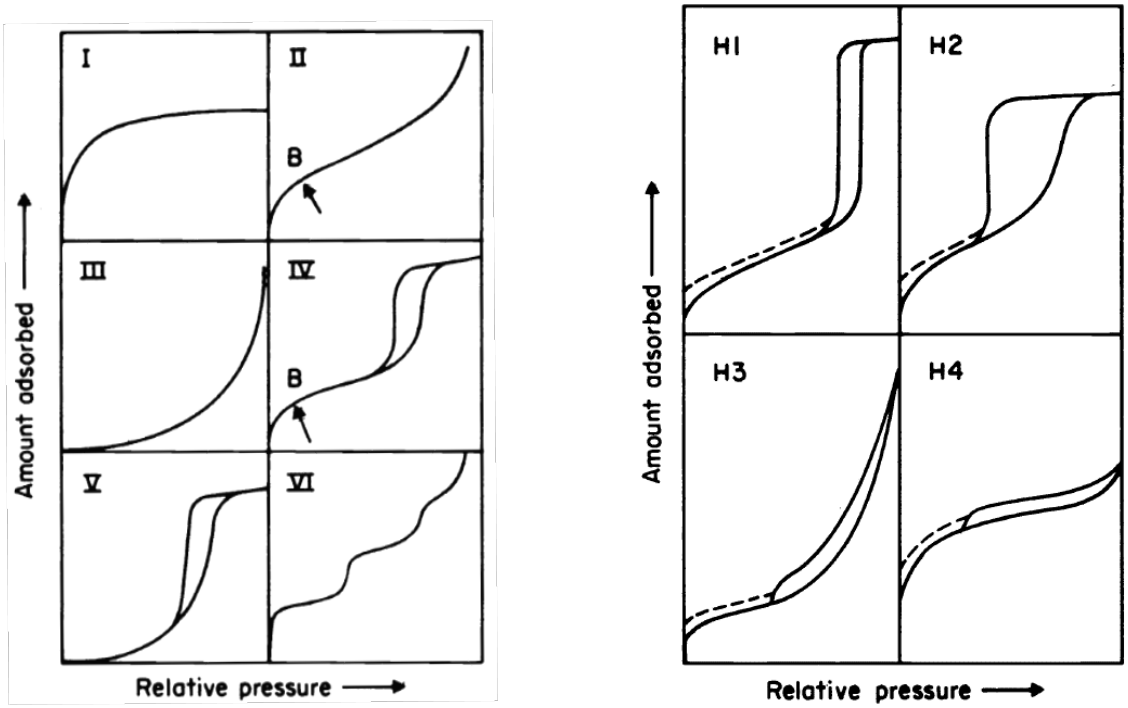

Figure 2.1: IUPAC classification of adsorption isotherm (a) and hysteresis loop (b) shape. Images are from reference [100], ©1985 IUPAC

narrow opening or "bottle-neck" obstacles. Type H_3 and H_4 hysteresis loops are observed for materials with slit-shaped pores [92].

Hysteresis loops at low partial pressures (dashed lines in Figure 2.1b) may indicate that the material swells upon contact with the adsorbent, that total volume of the adsorbent fluctuates, or that adsorbent molecules are stuck in smaller pores [92]. However, this phenomenon has also been observed for organic layers grafted onto inorganic adsorbents [101]. Boutin et al. studied nitrogen adsorption on alkylsilane-grafted MCM-41 materials. They built a model around the concept that, as the relative nitrogen pressure increases, the number of sorption sites increases because gas molecules are able to penetrate the organic layer and sorb to the substrate surface.Thus, the number of sorption sites is dependent on the relative pressure of nitrogen during adsorption, but not during desorption. Using this model, they were able to estimate the local density of organic chains at the material surface.

The Sol-gel Process

The most prevalent methods of silica synthesis involve the sol-gel process, in which dissolved metal oxide or alkoxide monomers hydrolyze, condense, and agglomerate into larger colloidal particulates, called a gel. Of particular interest for this work is the sol-gel synthesis of silica using tetraethylorthosilicate (TEOS), which was first observed by Ebelman and Graham in

the mid-1800s [102]. In the presence of acid, TEOS monomers hydrolyze via nucleophilic attack of water on the silicon atom. Condensation reactions then begin to occur between partially hydrolyzed alkoxysilanes or sililic acid monomers. The relative rates of hydrolysis and condensation control the structure of the sol. The solution pH and the presence or absence of dissolved salts influence the relative rates of particle growth and agglomeration [97]. The oligomers grow to form a more extended polymer throughout the solution, which thickens to become a gel that can resist elastic stress. As the gel is further aged and dried, the extended silica structure shrinks as surface groups condense and the aqueous solution exerts capillary forces on the pore walls as it evaporates. Finally, the silica is heated to dehydrate the surface.

Surfactant Templated Mesoporous Silica

Ordered mesoporous silica is synthesized using ionic or nonionic surfactants as structure directing agents for the sol-gel process. Two different mechanisms of template-directed ordered mesostructure formation have been proposed in the literature. In the *liquid crystal* route, surfactant structure directing agents self-assemble into an ordered supramolecular phase independently, and silicate monomers condense and polymerize around the template in a separate stage. In the *cooperative self-assembly* mechanism, it is cooperation between the organic template and the inorganic silicate monomers that drives the formation of the ordered supramolecular phase. For SBA-15, the material used for the work presented in this manuscript, ordered mesostructure is believed to be derived from cooperative assembly. Excellent reviews of the extensive work investigating these mechanisms are provided by Wan and Zhao [94, 103]. They are briefly summarized here in the context of SBA-15.

Santa Barbara Amorphous 15

SBA-15 is synthesized via a hydrothermal process, i.e. in acidic, aqueous media under applied heat. SBA-15 is made using a nonionic surfactant structure directing agent known as P123, which is a triblock copolymer of the form polyethylene oxide-polypropylene oxide-polyethylene oxide, or PEO-PPO-PEO (Figure 2.2). The two types of blocks have different hydrophobicity; PEO more readily protonates under acidic conditions and becomes hydrophilic, while PPO is hydrophobic. This structure promotes the formation of micelles (Figure 2.2).

Synthesis of SBA-15 is a five step process: template preparation, reaction with silicate, hydrothermal treatment, separation and drying, and template removal. The template is prepared by dissolution of the surfactant in an acidic solution. P123 readily dissolves in acid after gentle mixing for approximately one hour. The solution is heated. For nonionic surfactants, the temperature must be above the critical micelle temperature and below the "cloud point", or the temperature at which the surfactant precipitates and the solution becomes cloudy. For P123, the temperature range 35-40 °C is ideal [94].

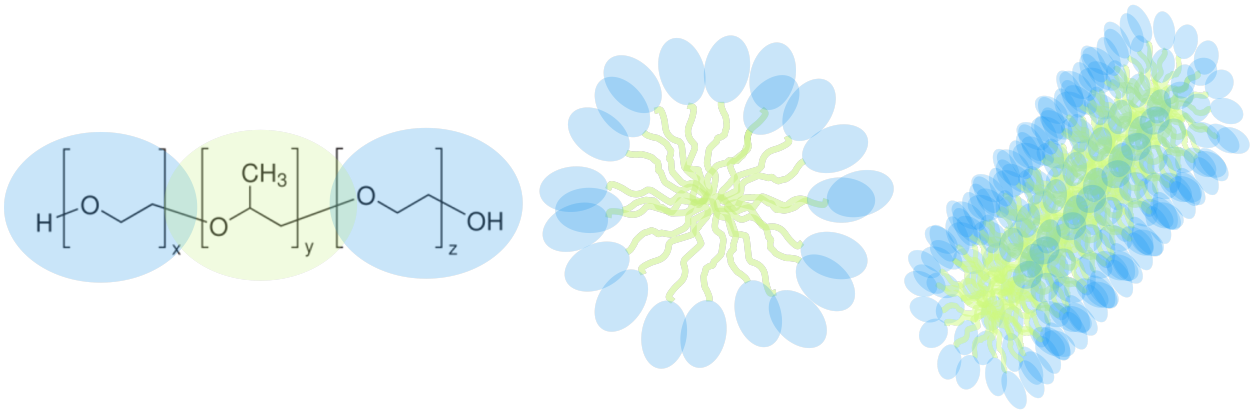

Figure 2.2: Triblock copolymer PEO-PPO-PEO in P123 surfactant structure directing agent (left) which spontaneously self-assembles into micelles (center) and larger supramolecular assemblies (right) in acidic solutions.

Following preparation of the template, tetraethylorthosilicate (TEOS) is added, hydrolyzes to sililic acid under the acidic conditions, and begins to polymerize. Cooperative self-assembly occurs. Hydrolyzed silicate oligomers interact with the P123 micelles and promote further aggregation of micelles, which in turn promotes further condensation of silicates [104, 105]. Structure at this stage is affected by the solution conditions. Decreasing the pH results in an increase in the hydrophilic nature of the PEO groups relative to the PPO groups, which increases the rate of condensation of the silicate monomers. This in turn promotes the formation of two dimensional hexagonal structure with column-like micelles, as opposed to the three dimensional cubic structure that result from a lower acid concentration. Additional salts or organic constituents, such as trimethylbenzene (TMB), also alter the micellar structure and condensation rates.

In situ time-resolved small angle X-ray scattering and small angle neutron scattering experiments have shown the precise mechanism of cooperative self-assembly for SBA-15 [106]. Prior to and roughly five minutes following the addition of TEOS, the solution phase demonstrates no ordered phase formation. At this stage, the micelles are spherical. Between 5 and 20 minutes after the addition of TEOS, non-interacting, rod-like micelles are observed, which grow longer as reaction time increases. Micelles begin to aggregate and form hexagonal arrays after 20-25 minutes, and a white precipitate is observed. Precipitation is accompanied by the observation of the (10), (11), and (20) diffraction peaks in the small-angle X-ray diffraction data, which are characteristic of two dimensional hexagonal mesostructures.

Hydrothermal treatment occurs at a higher temperature, typically 80-150°C for 1 day to 1 week [94]. This process promotes further condensation of the silicate phase, and has been shown to improve pore regularity by allowing reordering of the mesostructure. Following hydrothermal treatment, the solid phase is filtered and dried.

There are many methods for template removal, including calcination, organic extraction, ultraviolet irradiation, or microwave digestion. Calcination has the advantage of complete

removal of the template. During synthesis, the PEO chains extrude into the silica gel. Rapid heating during calcination can cause local overheating in the silica walls as the PEO branches combust, leading to loss of ordered pore structure. To prevent this, it has become standard practice to carry out the first hour of calcination under inert nitrogen atmosphere, or to calcine in air using a slow heating rate of 1-2°C min^{-1} to 550°C, which is the temperature required for total template removal [94]. The main disadvantage of calcination template removal is partial loss of the reactive hydroxyl groups from the silica surface.

Features of SBA-15

The main advantage of SBA-15 is that it retains the high degree of pore order and surface area of other micro- or mesoporous silicas, but has larger pores and thicker walls. SBA-15 materials typically have specific surface areas of 800-1000 m^2g^{-1}. SBA-15 contains a two dimensional mesostructure with hexagonal symmetry. The pores are cylindrical and arranged in the $p6mm$ symmetry group [94]. Pore diameters are generally in the 6.5-10 nm range, with a narrow pore size distribution (>95% of pores are between 2.5 and 10 nm). SBA-15 typically has a wall thickness between 3.1 and 6.4 nm, which contributes to its higher thermal stability compared to MCM-41 [22]. Due to inclusion of PEO chains in the silica walls during the sol-gel process, the large mesopores are connected by a disordered array of micropores [107]. Microporosity can be decreased by hydrothermal treatment or by addition of a cosolvent such as ethanol [94].

Control of Pore and Particle Size and Morphology

The pore size of SBA-15 depends on the size of the hydrophobic group of the block copolymer. Longer chains result in larger pores. For P123, larger pores can be made by increasing the size of the PPO block relative to the PEO blocks. Pore size can also be increased by hydrothermal treatment. During heating, the PEO blocks become more hydrophobic and retract away from the pore walls. Longer hydrothermal treatment at higher temperatures results in larger pores, thicker walls, and lower microporous volumes, as PEO chains withdraw from the walls. Pore size can also be increased by addition of an organic swelling agent, which will dissolve in the hydrophobic region of the micelles and cause expansion of the hydrophobic cavity. This process can also cause disordering of the pores, however. For this project, it was necessary to obtain large pore diameters (5-10 nm) such that surface modification with a variety of functional groups was possible, and the diffusion of aqueous solution through the pores of the functionalized material was not inhibited.

A large variety of particle morphologies has been developed for templated amorphous silica materials, including spheres, fibers, doughnuts, ropes, thin films, and monoliths [20, 108]. Factors controlling particle morphology include micellar shape, interaction between the silicate oligomers and the micelle during cooperative self-assembly, and other solution constituents [94]. Much research has been conducted to prepare SBA-15 with spherical particle morphology due to its utility in liquid chromatography [7, 8, 109–111]. For chromatographic

applications, particles must be spherical and mono-disperse, i.e. of uniform size and shape, to ensure proper packing of the column. If particles vary in size and shape, cavities or channels may form, which prevent the mobile phase from reaching dynamic equilibrium with the stationary phase.

Surfactant organization can be described by the effective surfactant packing parameter,

$$g = \frac{V}{a_0 l} \tag{2.1}$$

where V is the total volume of the hydrophobic chains and organic cosolvent molecules between the chains, l is the kinetic surfactant tail length, and a_0 is the effective hydrophilic head group area at the micelle surface [94, 112]. The packing parameter g comprises three factors that govern micelle packing: the preference of hydrophobic groups to minimize contact with water and maximize contact with each other, Coulombic interaction between charged or polar head groups, and solvation energies [112]. Micellar packing is affected by the presence of inorganic silicate species polymerizing at the surface of the micelles, but Equation 2.1 can still be used as a first-order approximation [112]. Controlling the relative size and hydrophilicity or hydrophobicity of the surfactant blocks influences the morphology of the micelles, which thereby influences the shape and ordering of their aggregates. Spherical aggregates can be obtained when the micellar surface curvature is high, or when g is low [112]. This occurs when the area of the hydrophilic head group is large. The size of the head group can be increased by adding a charged cosurfactant or by changing the pH to increase the polarity of the head groups. Slowing the reaction also increases micelle curvature. Thus, spherical particles tend to be synthesized using TEOS as opposed to tetramethylorthosilicate (TMOS), which is more reactive.

Zhao et al. report the synthesis of uniform SBA-15 spheres with particle diameters of approximately 1 μm using the cosurfactant cetryltrimethylammonium bromide (CTAB) [20]. CTAB is a cationic surfactant that increases the bonding interactions at the organic-inorganic interface. A neutral surfactant, S^0 interacts with positively charged silicate groups, I^+ via a hydrogen-bonded ion pair, $S^0H^+X^-I^+$, where X^- is a counterion, typically chloride. In the presence of CTAB, the surfactant becomes positively charged and interacts indirectly with the silicate salt via the anionic counterion: $S^+X^-I^+$ [110]. Ma et al. synthesized large-pore (9.8 nm diameter) silica microspheres using CTAB as a cosurfactant and ethanol as a cosolvent [8]. Katiyar et al. studied the effects of cosurfactant, cosolovents, swelling agents, aging temperature, and synthesis time on the formation of large pore SBA-15 spherical particles for the adsorption of large biomolecules [110]. They found that CTAB was necessary for the formation of uniformly-sized, spherical particles. With increased aging temperature in the range of 80-120°C, particles became more uniform in size, and pore diameter increased due to the increased volume of the hydrophobic blocks of the surfactant. Addition of the swelling agent trimethylbenzene (TMB) resulted in an increase in pore size. Increasing the mass ratio of TMB:P123 from zero to 0.5 doubled the average pore size from 6.44 to 12.74 nm without significantly increasing the pore size distribution.

Ethanol is a product of TEOS hydrolysis. Addition of ethanol as a cosolvent was intended to slow the condensation reaction to increase micelle curvature. Too much ethanol, however, degraded the spherical particle morphology and increased the pore size distribution. While addition of cosurfactants, swelling agents, and cosolvents can allow more precise control of pore and particle size and morphology, each adds complexity to the system, which makes syntheses harder to reproduce.

The Silica Surface

Silica produced by the sol-gel method is amorphous. Whereas a crystalline material like quartz has well-defined short-range and long-range order, silica glass has no long-range order and limited short-range order. Amorphous silica gel has been shown to be between these two substances on the order-disorder spectrum. ^{29}Si NMR studies suggest that silica gel has modestly well-defined short-range order, approximating that of small intersecting regions of β-cristobalite, but poor long-range disorder, such that no diffraction pattern is observed [113]. Because of the amorphous surface structure, it is difficult to generate an accurate model to describe the surface properties of the silica. Additionally, depending on the precise synthetic route and post-synthetic heat treatment, the quantity and geometric spacing of surface hydroxyl groups is unknown. As these two attributes are important for the consideration of surface modification, they are briefly discussed below.

Surface Hydroxyl Content

The bulk substance of silica gel is a network of SiO_4 tetrahedra. The surface is made up of bridged Si−O−Si *siloxane* groups or terminal silanols of which there are three types: isolated, vicinal, and geminal (Figure 2.3) [97]. There are also silanol groups internal to the bulk silica, which are considered to be inaccessible to water. The maximum number of surface silanol groups for amorphous silica has been calculated to be 4.6 OH nm^2 [114]. In this manuscript, *silanol* and *hydroxyl* are often used interchangeably when referring to −OH groups on the surface of silica.

At ambient temperatures and pressure, water from air is readily adsorbed by the silica surface via hydrogen bonding interactions. Calcination at 550°C both dehydrates and dehydroxylates the surface. Zhuravlev has conducted extensive studies on the surface hydroxyl content of amorphous silica, including the establishment of a physico-chemical model for the de- and re-hydroxylation of various amorphous silica materials under different temperatures [114]. These studies show that for calcination up to 1100°C, complete rehydroxylation of the surface can be obtained in water at room temperature. For silica calcined above 400°C, rehydroxylation has a high energy barrier, and full rehydroxylation can take years. For these materials, elevated temperature reduced rehydroxylation time to several hours. For calcination between 400 °C to 900 °C, the total hydroxyl content decreases from 2.35 to 0.40 OH nm^{-2}. Internal hydroxyl groups were shown to disappear in this temperature range. Isolated surface hydroxyl groups decrease from 2.05 to 0.40 OH nm^{-2}, while geminal hydroxyl groups

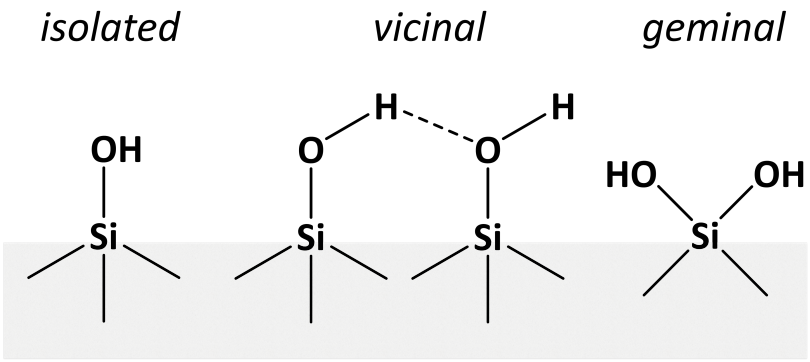

Figure 2.3: Diagram of three types of surface silanols: isolated, vicinal, and geminal. Vicinal silanols are close enough to participate in hydrogen-bonding interactions. Isolated silanols are too far apart to hydrogen bond to neighboring silanols. Geminal silanols are attached to the same silicon atom, and are too close to hydrogen bond to one another. Reprinted from reference [97], Copyright (1995), with permission from Elsevier.

decrease from 0.3 to 0.0 nm^{-2}. Based on Zhuravlev's data, it is estimated that amorphous silica calcined at 550°C would have approximately 1.5 to 2.0 OH nm^{-2} on the surface.

Ide et al combined NMR and IR spectroscopy to determine the silanol content for a variety of mesoporous silica surfaces [115]. For SBA-15 calcined at 550°C, they measured a total silanol content of 3.5 mmol OH g^{-1} (equivalent to 3.2 OH nm^{-2}), comprised of isolated silanols (88%) and geminal silanols (12%). They further quantified the fraction of silanol sites that were accessible to grafting by trimethylsilyl, and found it to be 1.7 OH nm^{-2}, or 53% of the total surface silanols. The difference can be explained by the presence of silanol groups inside the micropores inherent to the SBA-15 pore structure, which cannot be accessed by larger organic groups [115].

Surface Hydroxyl Spacing

Chuang and Maciel [113] describe the features of silica gel using a generalized β-cristobalite model, which assumes that the surface is made up of small regions (on the order of tens of atoms) that closely resemble the (100) and (111) crystal faces of β-cristobalite. These intersecting regions preclude long-range ordering and makes silica gel technically *amorphous*. Their model is built on spectroscopic data that suggests that isolated silanols occur in areas resembling the (111) crystal face of β-cristobalite, while geminal silanols occur in areas akin to the (100) crystal face of β-cristobalite. Since 88% of the surface silanols in SBA-15 are isolated [115], the surface may be approximated as small (111) faces of β-cristobalite irregularly interspersed with (100) faces of β-cristobalite.

Figure 2.4 gives a birds' eye view of the (111) crystal face of β-cristobalite, where the blue circles represent Si atoms with surface hydroxyl groups pointing upwards out of the page, and the unfilled circles represent silicon atoms with oxygen bonds pointing downwards into the page. Each Si atom is in a tetrahedral arrangement. The Si−O−Si bond angle is

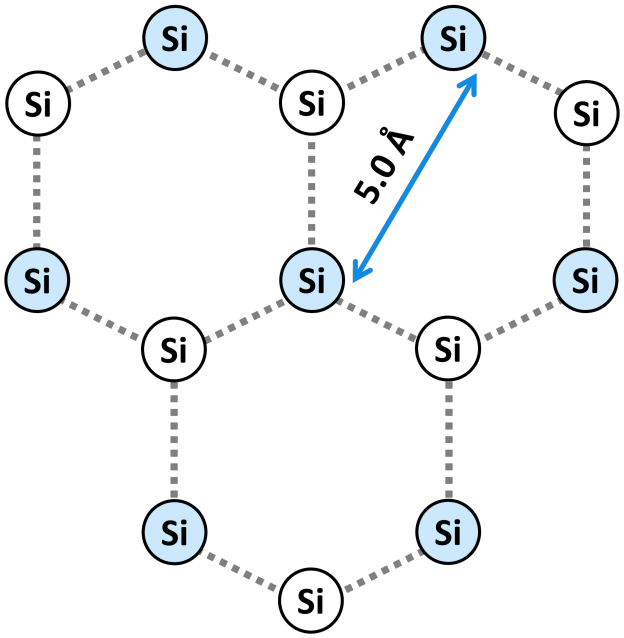

Figure 2.4: The (111) face of β-cristobalite.

147° with an Si−O bond length of 0.16 nm [113, 116]. These parameters can be used to calculate the approximate distance between adjacent isolated silanols on the (111) face of β-cristobalite, which is 5 Å[113]. for a fully hydroxylated surface. The approximate distance between two adjacent silicon atoms is 3 Å, determined geometrically. Given the area of a hexagon,

$$A = \frac{3\sqrt{3}}{2}a^2$$

where a is the length of a side, the area of one hexagon in Figure 2.4 is 0.23 nm^2. Each hexagon in Figure 2.4 contains one third of three silanols, or one silanol. Therefore, according to this model, the number of silanols per square nanometer is 4.35 OH nm^2, which is consistent with the Kiselev-Zhuravlev constant of 4.6 OH nm^2 assuming that some fraction of those silanols is geminal.

Summary

Although the silica surface is amorphous, there is a clear understanding about the surface silanol content and spacing, which determines the material's reactivity. SBA-15 calcined at 550 °C would likely have between 1.5 and 3.2 OH nm^2. This number is expected to increase during the functionalization process, during which the surface is exposed to water at elevated temperatures. Though amorphous, silica possesses short-range order similar to that of β-cristobalite, in which silanols are spaced approximately 5 Å apart on average.

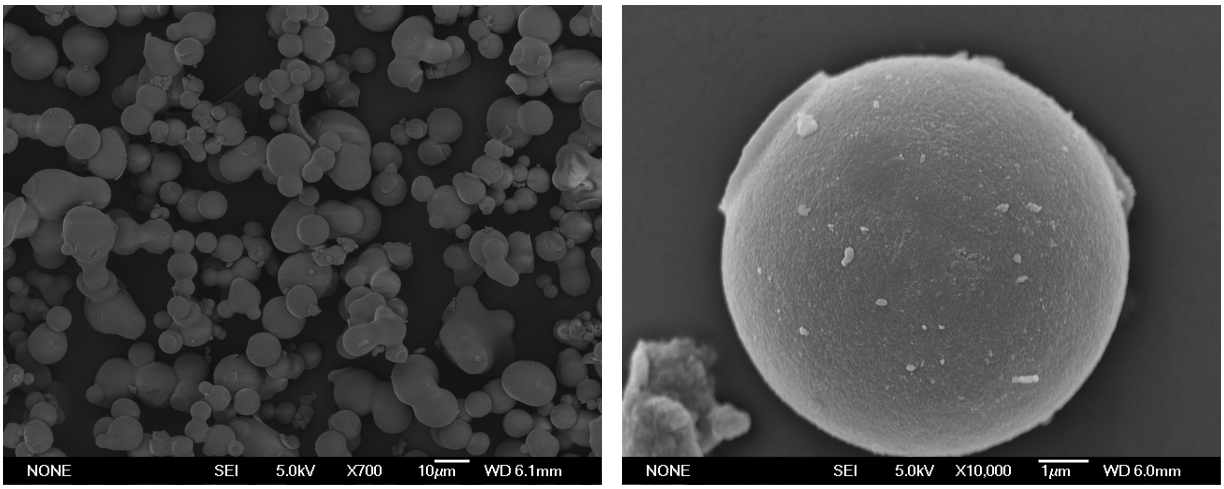

Figure 2.5: SEM images of large pore spherical SBA-15 particles. Particles were sputtered with 5 nm gold.

2.2 Synthesis of Santa Barbara Amorphous (SBA)-15 Mesoporous Silica

This section includes a description of the synthesis and characterization by nitrogen adsorption of the materials made for the work presented in Chapters 4 and 5.

Synthesis of SBA-15 Microspheres

For this work, initial attempts were made to synthesize large-pore spherical SBA-15 particles in anticipation of conducting proof-of-principle column chromatography tests. A former postdoctoral scholar, Anthony Bruchet, adapted procedures by Katiyar et al.[110] and Giaquinto[9] to synthesize particles that were approximately 5-10 μm in diameter, had an average pore size of 8 nm, a large pore volume of 1.254 cm^3g^{-1}, and a surface area of 878 m^2g^{-1} (Figure 2.5 and 2.6).

The procedure developed by Bruchet is summarized as follows. In the *pre-mixing* stage, CTAB and TMB are first combined, and water slowly added. The P123 structure directing agent and HCl are combined separately. Each solution is alternately sonicated for 15 minutes, followed by 5 minutes on a rotoshake or vortex mixer, repeated three times. In the *mixing* stage, the solutions are combined in a polytetrafluoroethylene (PTFE) bottle in a water bath at 38°C under slow stirring (250 rpm). Ethanol is added dropwise under more vigorous stirring (500 rpm). The bottle is closed with a tight-fitting screw top and stirred at 38°C for three hours at 500 rpm. In the *reaction* stage, TEOS is added dropwise, the PTFE bottled sealed tightly, and left stirring at 38°C for 45 minutes. The particles then undergo an *aging* step in a thermostatic bath at 80°C under static conditions for five hours. Following this, the particles undergo *hydrothermal treatment* by placing them in an oven at 120°C for approximately 15 hours (no stirring). After cooling completely, the particles are recovered

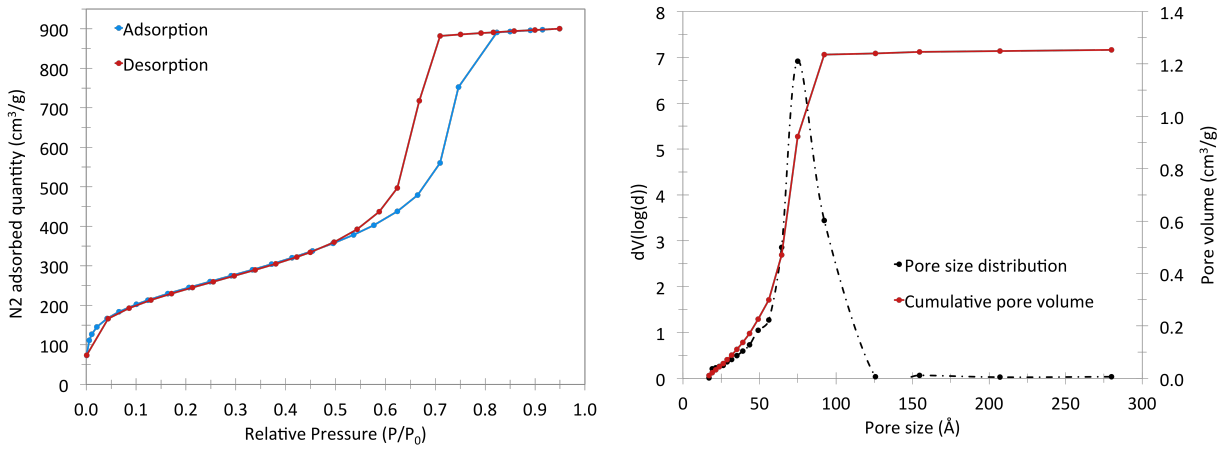

Figure 2.6: Nitrogen adsorption isotherm and pore size distribution for large-pore, spherical SBA-15 using procedure adapted from Katiyar et al. and Giaquinto.

by vacuum filtration and rinsed with water. They are dried overnight, and then calcined in ambient atmosphere by heating to 550°C at a rate of 1°C min^{-1}, held at 550°C for 6 hours, and then cooled. Particles are stored in an evacuated desiccator to avoid rehydration of the surface.

Several variations of this procedure were tested, including varying the pre-mixing procedure for the CTAB/TMB/H_2O and P123/HCl solutions, varying the aging time, reducing or eliminating hydrothermal treatment, increasing the mixing time before addition of TEOS, varying the concentration of HCl, and increasing the concentration of TMB. Generally, Bruchet found that obtaining homogeneous solutions during the pre-mixing and mixing stages prior to the addition of TEOS was crucial for obtaining homogeneous particle sizes and shapes, as well as ordered pore structures. Increasing the concentration of HCl or raising the temperature of reaction resulted in an increased rate of hydrolysis for TEOS, which resulted in smaller particles and better pore ordering. Increasing the TMB/P123 ratio from 0.2 to 0.3 caused an increasing in pore size from approximately 5 nm to 8 nm.

A majority of the batches synthesized by Bruchet demonstrated large pore volumes, high surface areas, and H_1 hysteresis loops typical for hexagonally ordered, cylindrical pore structures similar to those shown in Figure 2.6. These batches were used to synthesize the materials used in Chapter 4. However, approximately 40% of the batches synthesized demonstrated low specific surface area, low pore volume, small pore diameters, and type H_2 hysteresis loops in their nitrogen adsorption isotherms, indicating low or amorphous pore ordering on the mesoscale. There was no discernible pattern concerning which syntheses resulted in high versus low pore ordering, and it was concluded that the synthetic procedure was not highly reproducible.

When I attempted to repeat the synthesis, the resulting materials all demonstrated type H_2 hysteresis, low mesopore ordering, and low pore volume and diameter (on average 0.5 cm^3g^{-1} and 4.3 nm, respectively). Figure 2.7 shows a typical nitrogen adsorption isotherm

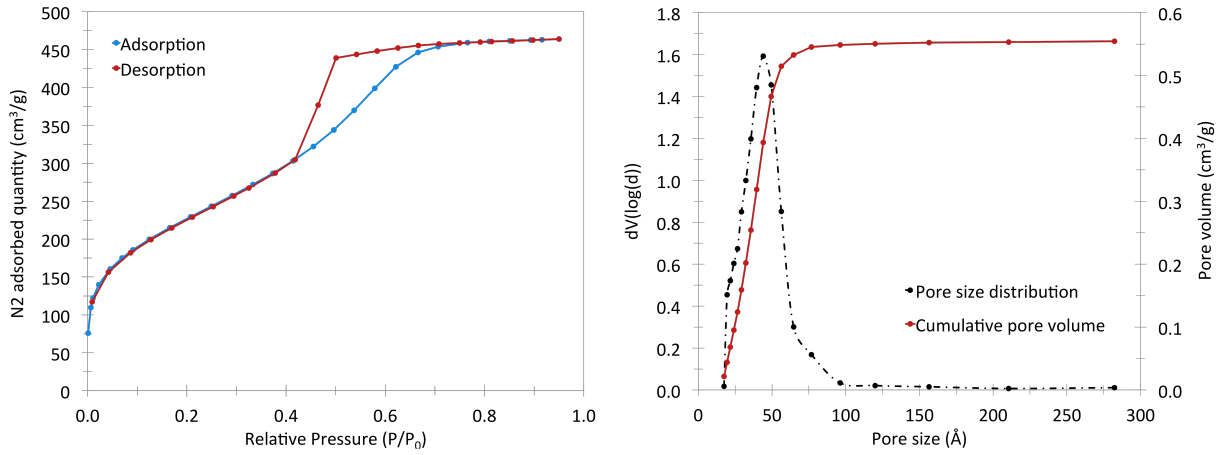

Figure 2.7: A typical nitrogen adsorption isotherm for attempted SBA-15 microspheres demonstrating type H_2 hysteresis.

for these materials. Ten separate attempts were made to improve the synthesis. It was observed that the CTAB/TMB/H_2O solution was cloudy in the early attempts, so efforts were made to improve homogeneity of the solutions prior to addition of TEOS. These included increasing the pre-mixing and mixing times prior to addition of TEOS, changing the order of adding reagents, changing the types and combinations of pre-mixing (rotoshaking, sonication, manual stirring and shaking), increasing the mixing temperature, purchasing and using all new reagents, and using recrystallized CTAB. None of these approaches improved the mesopore ordering, pore volume, and pore diameter. This procedure for synthesizing spherical SBA-15 particles was abandoned for a more reproducible synthetic procedure for SBA-15 silica rods. As the work presented in this dissertation was not concerned with conducting chromatographic separations and therefore did not depend on the particle morphology, this substitution was considered acceptable.

Synthesis of SBA-15 Silica Rods

The procedure for synthesizing SBA-15 silica rods was adapted from Sayari, Han, and Yang [117]. This simplified procedure involves the dissolution of P123 in HCl by gentle rocking for an hour, followed by stirring at 35°C overnight. TEOS is added under vigorous stirring. After 5 minutes, stirring is stopped, and the sealed mixture is heated at 35°C for 20 hours. In place of an aging step and hydrothermal treatment is one hydrothermal treatment at 100°C. The particles are collected by vacuum filtration, rinsed thoroughly with H_2O, air-dried, and calcined to 550°C in air following the same procedure used for the spherical particles. Sayari, Han, and Yang controlled pore diameter by varying the hydrothermal treatment temperature. Increasing the hydrothermal treatment temperature from 35 to 130°C caused an increase in the pore diameter from 5.8 to 12.5 nm [117]. At a hydrothermal treatment temperature of

Table 2.1: Summary of nitrogen adsorption characterization of SBA-15 rods

Batch Number	BET Surface Area (m^2 g^{-1})	BJH Pore Diameter (nm)	BJH Pore Volume (cm^3 g^{-1})	Hysteresis Loop Type
1	787	7.51	0.949	H_1
2	810	9.16	0.829	H_1
3	838	7.48	0.817	H_1
4	844	7.44	0.840	H_1
5	846	7.50	0.809	H_1
6	831	7.47	0.818	H_1
Average	826	7.76	0.844	H_1
Standard Deviation	3	0.7	0.05	

130°C, particles demonstrated lower specific surface area, although pore ordering was still high. For this reason, a temperature of 100°C was chosen.

Six consecutive batches of SBA-15 rods demonstrated type H_1 hysteresis loops in their nitrogen adsorption isotherms, with hysteresis beginning at a relative pressure of 0.625, indicating cylindrical pores ordered in a two dimensional hexagonal array. They also demonstrated high surface area, large average pore diameter, and large pore volume. Table 2.1 summarizes the nitrogen adsorption characterization for these materials.

As the data in Table 2.1 shows, this synthetic procedure proved to be much more reproducible than the one for SBA-15 microspheres. Thus, the SBA-15 rods were chosen for subsequent work. In particular, batches 5 and 6 in Table 2.1 were used to synthesize the materials for the experiments presented in Chapter 5.

2.3 Adsorption of Heavy Metals on Silica Surfaces

Adsorption of heavy metal on non-functionalized silica is largely due to Coulombic attraction between the anionic silica surface and positively charged cations. The surface charge of silica suspended in aqueous solution depends on the pH of the solution. The pH at which the surface demonstrates zero net charge is defined as the *point-of-zero charge* (PZC). If additional ions besides H^+ and OH^- are adsorbed onto the surface, the pH at which the surface has net neutral charge is defined as the *isoelectric point* (IEP). If no additional ions are adsorbed, PZC and IEP are equal. The PZC for SBA-15 silica has been measured to be between pH 4 and 5 [118, 119]. Kokunešoski et al. [119] measured a $pH_{PZC} = 5.2 \pm 0.2$ and a $pH_{IEP} = 2.3 \pm 0.1$ for SBA-15. They found that PZC and IEP did not vary significantly for two different synthetic procedures tested. Washing the SBA-15 with dilute nitric acid solutions resulted in a higher $pH_{IEP} = 3.0 \pm 0.2$, and no significant change was observed for the PZC.

These studies are consistent with Kosmulski's generalization that above pH 3, the silica surface is negatively charged, and metal cation adsorption is favorable. Below pH 3, the

silica surface is positively charged, and cations do not readily adsorb [120]. This property makes SBA-15 an appealing choice of scaffold for the grafting of organofunctional groups that complex heavy metal ions in low pH conditions. Below pH 3, the silica surface is effectively inert, and the chemistry is reduced to that of the ligand's functional groups. However, any studies investigating the interaction of aqueous metal cations with functionalized silica surfaces conducted above pH 3 must not ignore the potential contribution of the silica surface to adsorption.

Compared to other naturally occurring metal oxides, such as hematite and alumina, silica is a relatively weak adsorbent of cations from aqueous solution, despite being negatively charged at neutral pH. In nature, heavy metals more readily sorb to iron or manganese oxides than silica, even when silica is more abundant [120]. One reason for this difference is the higher solubility of silica, even in acidic solutions. Dissolved silicate species compete with bound surface sites for heavy metal complexation [120]. Therefore, it is also important to address the stability of the functionalized layer for grafted materials under experimental conditions used to measure adsorption of heavy metals. In general, significant sorption of a given heavy metal cation onto the silica surface is observed at a pH value slightly below that at which formation and precipitation of the metal hydroxide occurs. A correlation has been observed between the hydrolysis constant of metal cations and their stability constants with amorphous silica [120]. Furthermore, chemistry at the silica surface may stimulate hydrolysis and subsequent adsorption of heavy metal cations at a pH lower than predicted by their thermodynamic constants in the absence of silica [121].

Adsorption of heavy metal cations to silica can be described by the law of mass action and likely occurs through a combination of several ion-exchange reactions that involve the release of a proton from the surface [120, 122]:

$$\equiv\mathrm{SiOH} + \mathrm{M}^{2+} \rightleftharpoons \equiv\mathrm{SiOM}^{+} + \mathrm{H}^{+}$$

$$2\,\equiv\mathrm{SiOH} + \mathrm{M}^{2+} \rightleftharpoons (\equiv\mathrm{SiO})_2\mathrm{M} + 2\,\mathrm{H}^{+}$$

$$\equiv\mathrm{SiOH} + \mathrm{M}^{2+} + \mathrm{H_2O} \rightleftharpoons \mathrm{SiOMOH} + 2\,\mathrm{H}^{+}$$

Calculation of thermodynamic constants for the above reactions is complicated by determination of the electrostatic potentials governing surface adsorption[120]. For example, the processes involving adsorption and desorption of H^+ and other ions are associated with an electrostatic work function. Various models have been developed to account for these. Such models take into account the number of surface sites needed to complex a single cation (generally one or two sites), the number of protons released per adsorption of a single cation, the presence of anions coadsorbed with a single cation, and the distance of adsorption from the surface. They also consider inner- versus outer-sphere complexation [120]. In general, sorption of heavy metals on silica is found to be highly sensitive to pH, relatively insensitive to changes in ionic strength (except in the case where a complex is formed and the charge of the cation changes), and positively correlated with increasing temperature [120]. The

sorption of non-hydrolyzed ions on silica gel occurs quickly; equilibrium is typically reached within five minutes. For hydrolyzed ions, it takes much longer to reach equilibrium [122].

Interaction of U(VI) with Silica

The adsorption of uranyl onto amorphous silica solids has been thoroughly studied by macroscopic [121–125] and spectroscopic [78, 126–129] means. Silica gel has been used for the separation of plutonium and fission products from mineral acid solutions of uranyl for decades [123]. Early studies by Ahrland, Grenthe, and Norén [122] report U(VI) isotherms for various silica gel materials in perchloric acid solutions. They found U(VI) sorption decreases with increasing acid concentration. Milonjic, Čokeša, and Stevanović [121] investigated the dynamic adsorption of U(VI) and a mixture of U(VI) and Zr(IV) on silica gel columns as a function of temperature, pH, and column flow rate. Sorption capacity was found to increase with decreasing acid concentration; marginal increase was found with increasing temperature. Pathak and Choppin [124] conducted an extensive investigation of the kinetics and thermodynamics of uranyl sorption on silica gel as a function of time, temperature, and ionic strength. They found an increase in U(VI) sorption with increased ionic strength. They also showed that for the uranyl concentration range $5 \times 10^{-5} - 1 \times 10^{-3}$ M, the presence of carbonate anion did not significantly affect sorption of U(VI) in the pH range 2-6. Sorption of uranyl was found to have endothermic enthalpy. Wang et al. [125] measured sorption of U(VI) on SBA-15 silica as a function of pH in the range 3-11. Analysis of U(VI) sorption isotherms yielded a maximum sorption capacity of 203 mg U g^{-1} silica at pH 6.

Uranyl sorption on silica has also been studied spectroscopically. Time-resolved laser-induced fluorescence spectroscopy revealed the presence of two surface complexes with distinct fluorescence lifetimes, $\equiv SiO_2UO_2^{\circ}$ and $\equiv SiO_2UO_2OH^{-}$ in the pH range 4-8.8. The former species was shown to be dominant in the lower pH range, while the later was dominant as pH was increased. A third complex, $\equiv SiO_2UO_2OHCO_3^{3-}$ was postulated for solutions between pH 8.0-8.8 [130]. Several studies used extended X-ray absorption fine structure to investigate adsorption or incorporation of U(VI) on silica gel. The first EXAFS studies compared sorption of uranyl on silica and montmorillonite clay in the pH range 3-5. They found that uranyl sorbed as a mononuclear aquo-complex with 5-6 water or hydroxide ligands in the equatorial plane. For silica, the uranyl complex did not change significantly between pH 3 and 5. Based on the similarity of the spectra to that of uranyl hydrous oxide precipitate, it was postulated that uranyl forms polynuclear species, either with metal impurities on the silica surface or with neighboring uranyl ions, as it sorbs [126]. In contrast, later studies conducted in similar U(VI) concentrations and pHs found no evidence of polynuclear complex formation, and instead concluded that uranyl sorbs to silica as an inner-sphere, mononuclear, bidentate complex [78, 127, 128]. Sylwester, Hudson, and Allen [128] found evidence of polynuclear complex formation at pH 6.5 for similar uranyl solution concentrations.

2.4 Functionalization of the Silica Surface

Silica gel can be modified by extending the sol-gel process to alkoxy- or chlorosilanes bearing organic functional groups [131]. This can be achieved either through co-condensation of the organofunctional silanes with TEOS during substrate synthesis or by post-synthetic grafting [132]. In contrast to the co-condensation method, post-synthetic grafting has the advantage of limiting functional groups to the surface of the substrate, which makes them more accessible for reactions at the surface. Grafting also avoids changing the chemistry governing mesopore formation and ordering. Finally, this method allows some control over the spacing of functional groups and their proximity to each other.

Alkoxy- or chlorosilanes react with silanol groups at the silica surface. Chlorosilanes are reactive enough that they can react directly with silanols. Alkoxysilanes demonstrate reduced reactivity towards silanols and require hydrolysis of the alkoxy group prior to condensation with a silanol. Hydrolysis of alkoxysilanes can be either acid- or base-catalyzed.

The reactivity of alkoxysilanes correlates with their steric bulk. The rate of hydrolysis follows the order $Si-OCH_3 > Si-OC_2H_5 > Si-OC_4H_9$. Methoxysilanes hydrolyze 6-10 times faster in the presence of water than ethoxysilanes. Alkoxysilanes can be stable for weeks or months in very pure water at neutral pH with low concentrations of other ionic constituents, if they lack internal reactivity [133]. Acidic or basic conditions increase the rate of hydrolysis of alkoxysilanes.

Overview of the Functionalization Method

Ideally, the functionalization of silica involves the formation of a self-assembled monolayer (SAM) at the silica surface [134, 135]. Alkoxysilanes are contacted with a hydrated silica surface suspended in anhydrous organic solvent. Use of water or wet solvents results in premature hydrolysis and polymerization of alkoxysilanes, whereas anhydrous solvents restrict hydrolysis and condensation reactions to the surface of the silica. Once in contact with the hydrated surface, alkoxysilanes hydrolyze, hydrogen bond to surface silanols, and undergo condensation reactions to the surface. Simultaneously, condensation reactions between hydrolyzed silanes can occur, resulting in polymeric structures. This procedure is summarized in Figure 2.8.

The extent and type of coverage achieved on the silica surface depends on the relative rates of alkoxysilane hydrolysis and condensation. The most challenging aspect of achieving a self-assembled monolayer is balancing the rates of hydrolysis, condensation of siloxanes to one another, and condensation of siloxane monomers and oligomers to surface silanols. In principle, these rates are affected by the concentration of the alkoxysilanes, the concentration of water in solution and adsorbed to the silica surface, and the concentration of other constituents, for example, acids or bases that may affect the rate of alkoxysilane hydrolysis and condensation. In practice, study of self-assembled monolayers on silica surfaces has been restricted to varying how much water is added, when it is added, and by which method.

Silica dehydrated under vacuum, then rehydrated with two monolayers of water.

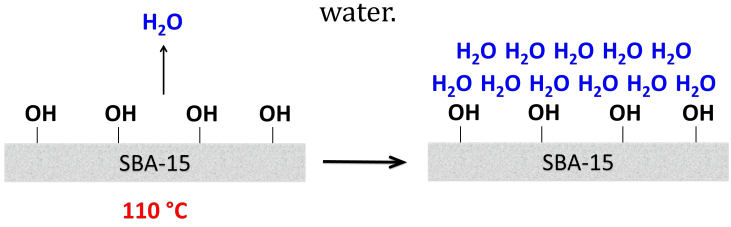

Functionalized alkoxysilane added, which hydrolyzes upon contact with water adsorbed to the surface.

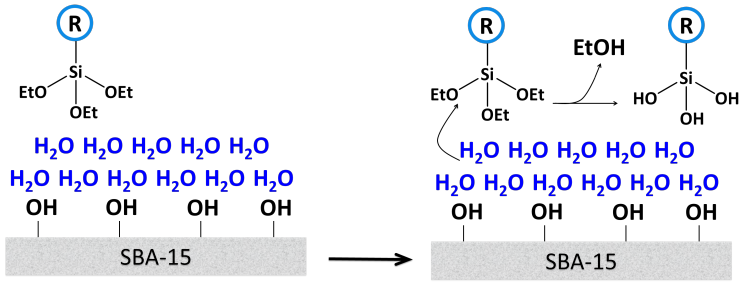

Silanes undergo condensation reactions to cross-link with each other and the silica surface.

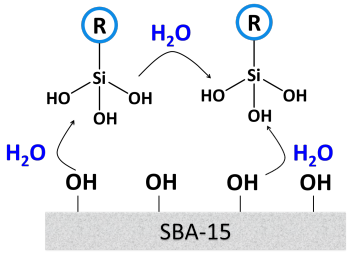

Various types of functional layers may form, depending on the relative rates of hydrolysis and condensation.

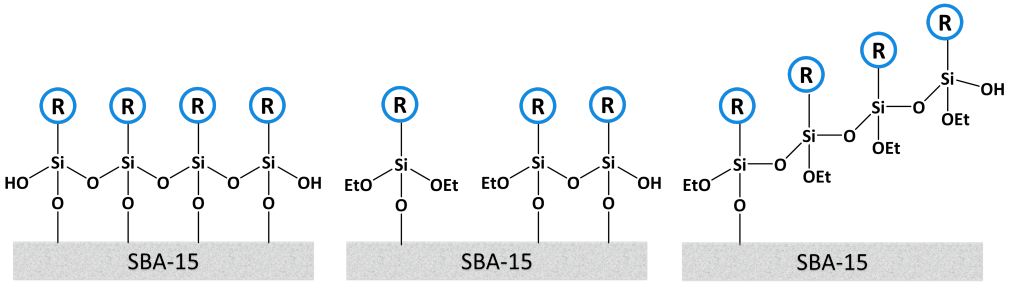

Figure 2.8: Diagram summarizing the chemical processes underlying functionalization of self-assembled monolayers at the silica surface

Monomeric functionalization, in which no cross-linking between silane groups occurs, can be achieved by the reaction of monochlorosilanes or monoalkoxysilanes with dehydrated silica in anhydrous solvents [136]. For monoalkoxysilanes, a catalyst (e.g. pyridine) must be used to mediate the reaction, as the direct reactivity with silanols is very low. The use of di- and tri-functional organosilanes introduces the possibility of polymer formation. Polymerized monolayers have demonstrated increased stability in acidic solutions, presumably due to the formation of a hydrophobic layer that excludes water at the surface [137, 138]. Sander and Wise [131] describe two distinct methods of polymerization methods. In the *solution polymerization* method, alkoxysilane is first mixed with silica, followed by the addition of water. Polymerization occurs in solution, and alkoxysilane polymers deposit onto the silica surface. In the *surface polymerization* method, water is first adsorbed to the silica surface, followed by the addition of alkoxysilane. Alkoxysilane polymerization and condensation to the surface occurs simultaneously.

The literature reports various methods for controlled hydration of the silica surface. Too much water may result in excess polymerization of alkoxysilanes, whereas too little may cause incomplete monolayer formation. Wirth and Fatunmbi [137, 138] report an apparatus designed to flow hydrated nitrogen or purified air over silica, which results in deposition of one monolayer of water on the surface at 50% hydration. Others have simply suspended the silica in anhydrous solvent and added water stoichiometrically, based on the specific surface area of the silica, so that there are twice the number of water molecules as the number of silanols on a fully hydroxylated surface [11, 131]. This approach has been adopted for the material synthesized in this dissertation. It has been observed in this work and others' that silica suspended in anhydrous toluene disperses and forms a homogeneous slurry. Upon addition of water, the silica aggregates as the hydrophilic surface interacts with water. After a few hours, the water diffuses through the pores, and the slurry becomes homogeneous again.

The Effect of Functional Group Chemistry on Surface Reactions

Acid-base chemistry of the organic functional group will affect the rate of hydrolysis and condensation of alkoxysilanes. A good example of this is aminopropyltrialkoxysilanes, which possess an internal basic group, the amine. The amine group has been shown to interact with surface silanols via hydrogen bonding, where it is situated to catalyze direct condensation of the alkoxysilane with the silica surface. This can occur without the presence of water. Aminopropylsiloxanes have been shown to be more reactive towards the silica surface than other groups that lack acidic or basic functional groups [97].

Characterization of the Functional Layer

Comprehensive characterization of self-assembled monolayers on silica substrates can only be achieved by combining several techniques, each of which provides partial information [134]. X-ray photoelectron spectroscopy (XPS) is a valuable elemental analysis technique

that identifies elements based on the energy required to eject core or valence electrons using photons of known energy. Secondary ion mass spectrometry (SIMS) ionizes surface species by bombardment with ions, and analyzes resulting "secondary" ions that detach from the surface using mass spectrometry. Similarly, thermogravimetric analysis coupled with mass spectrometry (TGA-MS) identifies and quantifies species emitted from the surface as a substrate is heated. Optical techniques like ellipsometry provide information about the thickness of the layer. Fourier transform infrared spectroscopy (FT-IR) and Fourier transform nuclear magnetic resonance spectroscopy (NMR), particularly on ^{1}H and ^{13}C nuclei, are used to verify the presence of desired organofunctional groups.

Solid-state ^{29}Si NMR spectroscopy is a powerful tool for analyzing the attributes of self-assembled monolayers on silica supports. Internal bridged siloxanes, isolated silanols, and geminal silanols demonstrate resonances at distinct chemical shifts in the ^{29}Si NMR spectrum. The species SiO_4, $SiO_3(OH)$, and $SiO_2(OH)_2$ have been named Q^4, Q^3 and Q^2, respectively. The ^{29}Si resonances for these species occur at -109, -100, and -90 ppm (in reference to tetramethylsilane), respectively [139, 140]. Silanes covalently bonded to the silica surface also demonstrate distinct ^{29}Si resonances depending on their chemical environment. The species $RSiO_3$, $RSiO_2(OX)$, and $RSiO(OX)_2$, where R is the organofunctional group and X is a non-hydrolyzed alkyl group or H, are named T^3, T^2, and T^1, respectively. Their resonances occur at -70, -59, and -49 ppm (in reference to tetramethylsilane), respectively [10, 141]. These resonances are most often assigned to isolated functional siloxanes (T^1), terminal functional siloxanes only bound to one neighboring functional siloxane or functional siloxane dimers (T^2), or cross-linked functional siloxanes bound to two neighboring functional siloxanes (T^3) [10]. However, in principle they may also be assigned to functional siloxanes that have one, two, or three siloxane bridges to the silica surface. Figure 2.9a shows an idealized ^{29}Si NMR spectrum of surface-polymerized silica gel, and Figure 2.9b shows a diagram of the Q and T resonances.

To some extent, the surface silane and silanol species may be identified, and in some cases quantified, using ^{29}Si NMR spectroscopy. Fatunmbi, Bruch, and Wirth [142] have studied the surface coverage obtained for monolayers achieved with different functionalization methods using quantitative ^{29}Si and ^{13}C NMR spectroscopy. They found that carefully conducted surface polymerization approached the theoretical maximum density of surface silanes, 8 μmol m^{-2}. Quantitative analysis of ^{29}Si and ^{13}C NMR spectra is hindered by the low isotopic abundance and low sensitivity of ^{29}Si and ^{13}C. Therefore, observation of these nuclei often requires the use of spectral enhancement tools, such as cross-polarization, which results in signal amplitudes that are no longer proportional to the spin populations they represent. Challenges associated with obtaining quantitative information from spectra obtained using cross-polarization, and their potential solutions, will be discussed further in Chapter 3.

In addition to studying the chemical environments of the silicon atoms at the interface between inorganic silica and organic monolayers, solid-state NMR is useful for studying the interaction between neighboring ligands. A number of NMR techniques probe the strength of dipolar coupling between nuclei, which provides structural information about the functional layer that is difficult to obtain by other means. These techniques are most accessible to ^{1}H

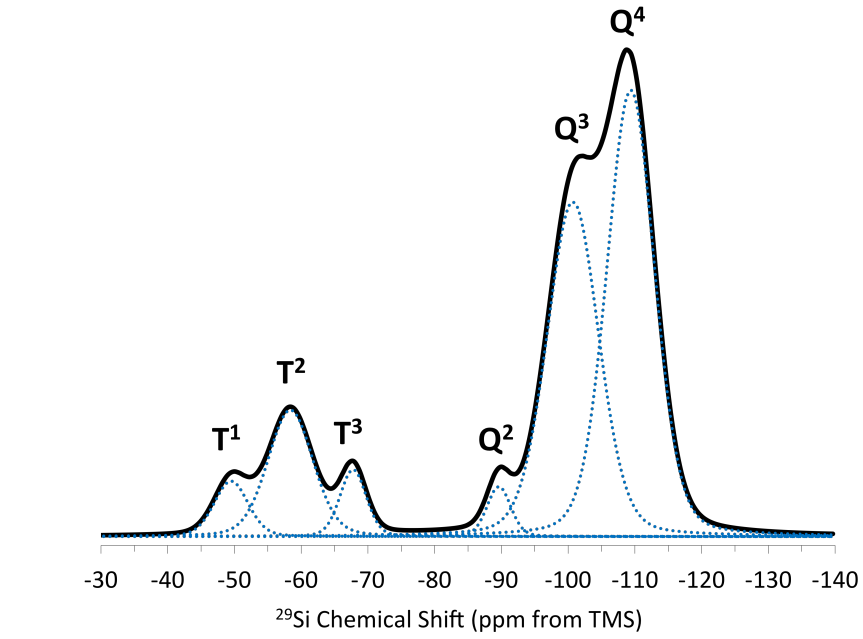

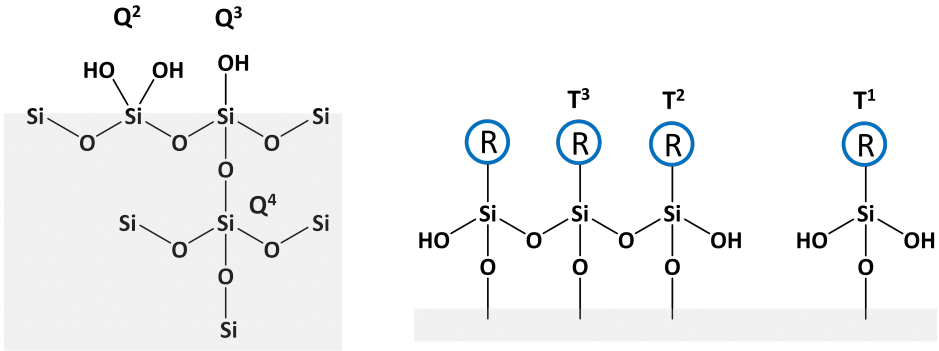

Figure 2.9: Example of an idealized ^{29}Si NMR spectrum for functionalized silica showing the presence of both Q and T peaks (top). Diagram depicting chemical environments corresponding to the Q and T resonances (bottom).

and ^{31}P nuclei, which are both observable by NMR and are naturally abundant. The use of NMR to study dipolar coupling in phosphonate-functionalized silica will be described in Chapter 3.

Chapter 3

Fundamentals of Nuclear Magnetic Resonance Spectroscopy

Nuclear magnetic resonance (NMR) spectroscopy is a powerful tool used to identify and characterize structural features in organic and inorganic materials and metal complexes. A comprehensive description of the fundamental principals of NMR spectroscopy is given by Levitt [143]. Duer [144] extends the fundamental discussion to NMR spectroscopy of solid-state materials. Mackenzie and Smith [145] provide a thorough account of the application of NMR to solid-state inorganic materials. This chapter provides a conceptual description of NMR spectroscopy and establishes a basis for understanding the experiments reported in chapters 4 and 5.

3.1 Basic Principals of Solid-State NMR

Nuclear Spin

Elementary particles possess an intrinsic property known as *spin*. Spin has the effect of producing quantized angular momentum states for a particle. The spin angular momentum is directly proportional to its magnetic moment:

$$\hat{\mu} = \gamma \hat{S}$$

where γ is the gyromagnetic ratio, a constant unique to each nucleus, which is either positive or negative. Positive values of γ indicate that the spin angular momentum and magnetic moment vectors are parallel; negative values indicate they are anti-parallel. Particles that have integer spin, like photons, are called *bosons*. *Fermions*, including electrons, neutrons, and protons, have half-integer spin. NMR spectroscopy measures the interaction of an external magnetic field with nuclear spins.

A particle with spin S has a total angular momentum of $[S(S+1)]^{1/2}\hbar$. A spin S has $2S+1$ sublevels, M_S, which take on values of $-S, -S+1 ... +S$. M_S can be roughly conceptualized

as the "orientation" of the spin. In the absence of any external electric or magnetic fields, the energy of these sublevels is degenerate. The presence of an electric or magnetic field effectively orients these states, making some higher or lower in energy depending on their orientation with respect to the field, an effect known as *Zeeman splitting*.

Nuclei are made up of protons and neutrons, known collectively as nucleons. Each nucleon has spin 1/2. When protons and neutrons are combined into a nucleus, their spins are added together by the rules of vector addition:

$$S_{total} = |S_1 - S_2|, |S_1 - S_2| + 1 \ldots or |S_1 + S_2|$$

Nuclei with an even number of nucleons have integer spin, while those with an odd number of nucleons have half-integer spin. For nuclei with an even number of protons *and* an even number of neutrons, the ground state nuclear spin is zero. These nuclei cannot be observed by NMR. Nuclei with an odd number of protons *and* and odd number of neutrons have non-zero integer spin.

All of the nuclei observed in this work have spin $S = 1/2$, with sublevels $M_S = +1/2$ and $M_S = -1/2$. When placed in a magnetic field, B_0, the energy levels between these two states are split (Figure 3.1). The difference in energy levels between the two states is

$$\Delta E = \gamma \hbar B_0$$

Spins with magnetic moments aligned with the magnetic field are in the lower energy state, while those aligned anti-parallel to the B_0 field are in the higher energy state. Spins preferentially occupy the lower energy state. The actual difference in population between the two energy states is very small, and is determined by the Boltzmann distribution. In the high temperature approximation, the difference in population between the higher and lower energy states n can be approximated by:

$$n \cong N \frac{\Delta E}{2kT}$$

where N is the total number of spins.

Transitions between energy states can occur by the absorption or emission of a photon at the correct radiofrequency. The most basic Fourier transform NMR experiment involves equilibrating spins in an external magnetic field, perturbing them from their equilibrated state by application of a radiofrequency electromagnetic pulse, and measuring the emission of radiofrequency as the spins relax back to their equilibrium condition. Because the precise radiofrequency involved in these processes depends on the local electromagnetic environment of the spins, NMR spectroscopy yields chemical information.

The Single Pulse Experiment

Consider a sample of spin 1/2 nuclei placed in an external magnetic field, B_0, which by definition lies along the z-axis of the laboratory frame of reference. Spins placed in this magnetic

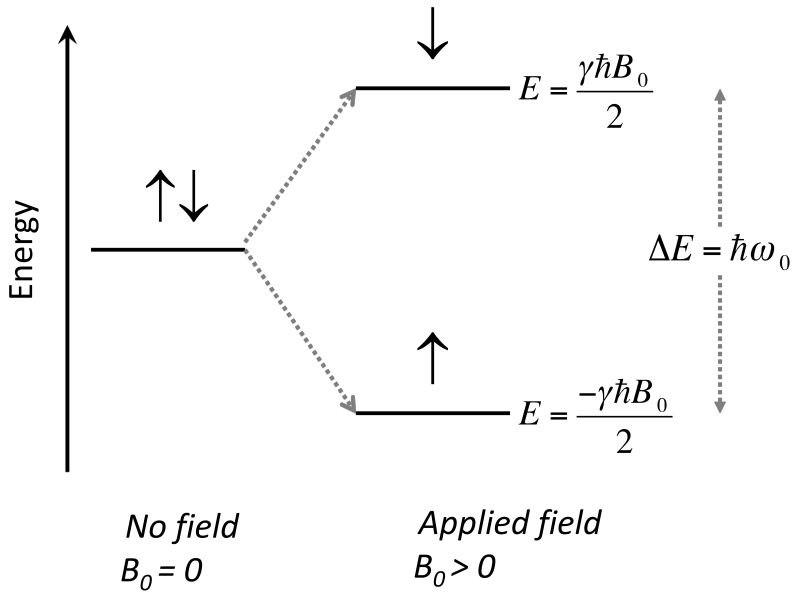

Figure 3.1: Diagram depicting Zeeman splitting in a finite applied magnetic field, B_0.

field experience a torque that causes them to precess around the z-axis at a frequency specific for each nucleus, known as the Larmor frequency:

$$\omega_0 = -\gamma B_0$$

Since the difference in the Zeeman energy states is equal to $\Delta E = \gamma\hbar B_0 = \hbar\omega_0$, irradiation at the Larmor frequency can cause *spin flips* to occur between the Zeeman states.

A large number of randomly-placed spins precessing about the z-axis possess every possible projection onto the xy plane, which cancels out any net magnetization in the xy plane. The presence of the B_0 field along the $+z$ axis has the effect of generating a slightly higher population of spins oriented parallel to the magnetic field, which is the lower energy state. Thus, over time, a net magnetization builds up in the $+z$ direction. Although the orientation of individual spins is dynamic, it is this net magnetization that is manipulated and observed in the NMR experiment.

Now consider a plane-polarized radiofrequency pulse applied to this sample in the $+x$ direction at the Larmor frequency. Often it is helpful to visualize spin precession in a "rotating frame" of reference, that is, a frame where the xy plane is spinning about the z-axis at the Larmor frequency, such that the magnetic moment of the spin appears to be stationary. In the rotating frame, the radiofrequency pulse simply appears as a static pulse on the net magnetic moment M, which causes it to precess about the x-axis at a typical *nutation* frequency. In a single-pulse experiment, the pulse duration is adjusted so that the net magnetization is translated to the xy plane. This is known as a $\pi/2$ pulse. This precession proceeds until the radiofrequency pulse ceases, at which point the spins relax back to their equilibrium states in the magnetic field. In the laboratory frame, relaxation of the

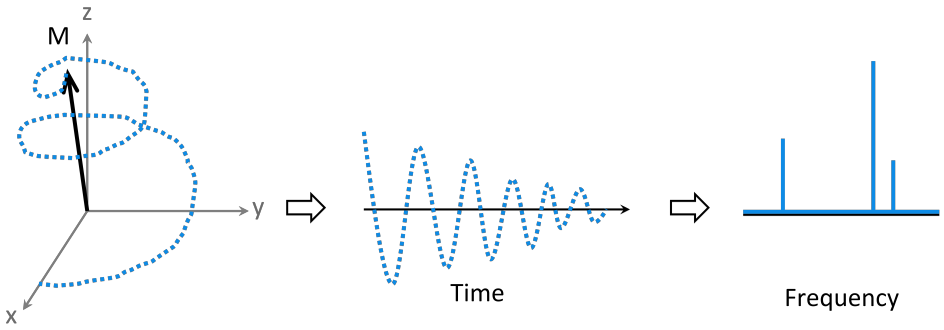

Figure 3.2: Summary of the single-pulse Fourier Transform NMR experiment.

spins results in the exponential decay of the spins' net magnetization from the xy plane back to the $+z$-axis. A coil measuring the emission of radiofrequency as a function of time in the xy plane registers an exponentially decaying sinusoidal signal, known as the *free induction decay* (*FID*). This FID can then be Fourier transformed to extract the radiofrequencies emitted by the spins as they relax (Figure 3.2). Typically, many FID scans are collected and averaged together to improve the signal-to-noise of the spectrum prior to Fourier transform. After Fourier transforming the FID, the observed radiofrequencies are often reported in reference to a standard material:

$$\delta = \left(\frac{\omega_0 - \omega_{0,ref}}{\omega_{0,ref}} \right) \times 10^6 \tag{3.1}$$

where ω_0 is the Larmor frequency for the spins of interest in the sample, $\omega_{0,ref}$ is the Larmor frequency for the standard, and δ is in parts per million (ppm). For ^{1}H, ^{13}C, and ^{29}Si, tetramethyl silane (TMS) is used as a standard. For ^{31}P, 85% H_3PO_4 is used. This convention is used so that the *chemical shift* of functional groups from the reference compound can be compared across different magnetic field strengths.

Spin Relaxation

The process responsible for the transfer of energy from excited spins as they decay to their ground states is termed *relaxation*. There are two separate relaxation processes that occur, each with their own time constant. The first is *longitudinal* relaxation, which is also known as *spin-lattice* relaxation. Longitudinal relaxation is the relaxation of the net magnetization back to the z-axis of the laboratory frame after a perturbation. After a $\pi/2$ pulse, the net spin magnetization lies entirely in the xy plane. The z-component of the net spin magnetization vector will evolve according to Equation 3.2:

$$M_z(t) = M_z^0\left(1 - e^{-t/T_1}\right) \tag{3.2}$$

assuming that $M_z = 0$ at time $t = 0$, where M_z^0 is the net magnetization along the z-axis at equilibrium and T_1 is the longitudinal relaxation time constant. Longitudinal relaxation is mediated by interactions between the observed spins and the extended *lattice* environment surrounding them. As neighboring atoms, unpaired electrons, and spins vibrate and rotate in the vicinity of a given spin, they generate transient, fluctuating electromagnetic fields in the transverse (xy) plane. Occasionally, these fields oscillate at or near the Larmor frequency of the spin, which can induce energy transfer from the excited spin to the lattice and result in relaxation to a lower energy level. Homonuclear dipolar coupling and molecular motion are excellent longitudinal relaxation agents. Therefore, the time constant T_1 depends on the proximity of spins, the rigidity of the material, and the temperature. In liquids, T_1 tends to be very short; molecules tumble rapidly and the excited spins sample a larger number of transient fields more quickly. For solid-state samples, T_1 can be very long, on the order of tens of seconds to minutes. This can make collection times very long because magnetization along the z-axis must be fully reestablished before repeating the pulse sequence for each scan.

The second type of relaxation is *transverse* relaxation, which constitutes relaxation of the net spin magnetization vector in the xy plane caused by the dephasing of the individual spins in the xy plane. Transverse relaxation is also known as spin-spin relaxation because in solids, the dominant magnetic fields mediating de-phasing of the spins in the xy plane after a $\pi/2$ pulse are the static magnetic dipole fields from neighboring spins. Thus, spin-spin dipolar coupling causes the transverse relaxation in solids to be very fast. After a $\pi/2$ pulse, the net magnetization in along the laboratory frame's x- and y-axes evolves according to:

$$\begin{aligned} M_x(t) &= -M_x^0 sin(\omega_0 t) exp[-t/T_2] \\ M_y(t) &= -M_y^0 cos(\omega_0 t) exp[-t/T_2] \end{aligned} \tag{3.3}$$

where M_x^0 and M_y^0 are the x and y net spin magnetization vectors immediately after the $\pi/2$ pulse and T_2 is the time constant for transverse relaxation. The spectral resolution in the Fourier transform of the FID is related to T_2 by:

$$FWHM = \frac{1}{\pi T_2}$$

where the FWHM is expressed in Hz.

To summarize, T_1, the time constant for longitudinal relaxation, determines the length of the NMR experiment. T_2, the time constant for transverse relaxation, determines the resolution of the spectrum. In non-viscous solutions, the time constants governing longitudinal and transverse relaxation are quite similar. For solids, transverse relaxation occurs much more quickly than longitudinal relaxation, which contributes to the poorer spectral resolution obtained for solid samples.

Common Spin Interactions

The actual Larmor frequency observed for a given nuclear spin depends on the magnetic field present at its specific location, B_{local}, which differs slightly from B_0. Often variations correlate with structural details, such as the number and proximity of nearby spins or the local electron density. Three major contributions that result in a difference between B_0 and B_{local} are: 1) chemical shielding by electrons, 2) dipolar coupling with nearby spins, and 3) quadrupolar coupling for nuclei with electric quadrupole moments.

Quadrupolar nuclei have spin greater than 1/2, and therefore they have more than two Zeeman states when placed in a magnetic field. Since no quadrupolar nuclei were studied for this work, this discussion is limited to chemical shielding and dipolar coupling interactions.

Chemical Shielding

The electrons surrounding nuclear spins interact with the applied B_0 field. These interactions mean that the local magnetic field experienced by each spin depends on the local electronic environment. The presence of electrons can either decrease or increase the magnitude of B_0, known as *diamagnetic* and *paramagnetic* shielding, respectively. This change in local magnetic field results in a shift of the Larmor frequency for a spin in a given chemical environment, known as a chemical shift.

Diamagnetic shielding arises from the diamagnetism induced in electrons by B_0, which induces a small magnetic field in the $-z$ direction, effectively reducing the magnitude of B_0. In contrast, paramagnetic shielding arises from distortion of the ground electronic state by mixing the ground and excited electronic states [144]. Some of these electronic excited states are paramagnetic, and thus produce a local magnetic field that increases B_0.

The magnetic field at a given spin is the sum of the applied B_0 field and the magnetic fields produced by diamagnetic and paramagnetic shielding:

$$B_{local} = B_0 + B_{dia} + B_{para}$$

The direction of a chemical shift is often correlated with the local electron density of an atom. Chemical interactions that reduce local electron density, such as bonding to a more electronegative atom or complexation with a cation, typically reduce diamagnetic shielding, which increases B_{local} and produces a chemical shift towards more positive frequencies. The opposite is often thought to be true for bonding interactions that increase the local electron density around an atom.

However, this qualitative correlation of chemical shift with electron density does not accurately reflect chemical shift trends for atoms with significant paramagnetic shielding, including ^{31}P. For these atoms, the relationship between chemical shift and bonding structure is more difficult to conceptualize [146].

In solution, the rapid isotropic tumbling of molecules results in a single average chemical shielding value for each nucleus. However, in solid-state samples, the molecules are rigid with respect to one another. The chemical shielding environment experienced by a given

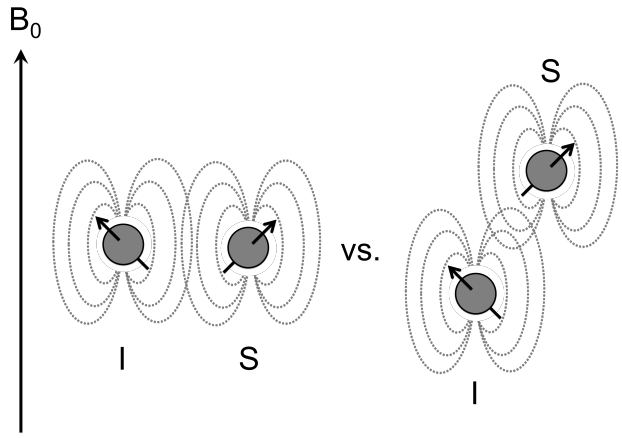

Figure 3.3: Anisotropy of the dipolar coupling interaction between two spins I and S in the B_0 field.

spin depends on its orientation with respect to electrons causing the shielding in the B_0 field. This is known as *chemical shift anisotropy* and is a significant source of line-broadening in solid-state samples. The effects of chemical shift anisotropy are similar to those introduced by the anisotropy of the dipolar coupling interaction, described below and depicted in Figure 3.3.

Dipolar Coupling

Spins possess magnetic moments. Each magnetic moment generates a local magnetic field, which is felt by neighboring spins. When two spins in close proximity are influenced by each others' magnetic moments, they are said to be *coupled*. The strength of this interaction increases with decreasing distance between the two spins. In fact, it is proportional to $1/r^3$, where r is the internuclear distance between the two spins. Therefore, measuring the strength of dipolar coupling can be an effective way to determine internuclear distances.

The strength of dipolar coupling between two spins also depends on their orientation with respect to each other in the B_0 field. This is because the B_0 orients the magnetic moments, meaning that some relative orientations demonstrate stronger or weaker coupling (Figure 3.3).

For non-viscous liquids, rapid molecular motion averages the dipolar coupling interaction to a single value. Because this rapid molecular tumbling is restricted in solids, the orientation dependence of dipolar coupling is a significant source of line-broadening and loss of spectral resolution in solid-state NMR.

For homonuclear spins, the first-order average Hamiltonian describing the dipole-dipole coupling interaction of two spins I and S is:

$$\hat{H}_{dd}^{homonuclear} = \frac{-b}{2}\big(\cos^2\theta - 1\big)\big(3\hat{I}\cdot\hat{S}\big) \tag{3.4}$$

where $\hat{I}$ and $\hat{S}$ are the spin vectors of the I and S spins, respectively ($\hat{I}_z$ and $\hat{S}_z$ are their z components), and θ is the angle between the spin interaction vector and the B_0 field. The dipolar coupling constant b is defined as:

$$b = \hbar\left(\frac{\mu_0}{4\pi}\right)\frac{1}{r^3}\gamma_I\gamma_S \tag{3.5}$$

where μ_0 is the vacuum permeability constant, γ is in Hz T^{-1}, and b is in Hz. For heteronuclear decoupling, there is an energy mismatch in the xy plane due to the unequal precession frequencies of heteronuclear spins. Therefore, the component describing spin-coupling interactions are reduced to only those along the z-axis:

$$\hat{H}_{dd}^{heteronuclear} = -d\big(\cos^2\theta - 1\big)\hat{I}_z\hat{S}_z \tag{3.6}$$

Implications of Spin Interactions for Solid-State NMR

For solid samples, the molecular orientation of spins is fixed. Chemical shielding and dipole-dipole coupling are oriented in the B_0 field, which makes the energy of their interactions orientation dependent, or *anisotropic*. This causes significant line broadening for powder samples that lack long-range order, since every possible orientation is present, each experiencing a slightly different B_{local} and precessing at a slightly different Larmor frequency. For liquid samples, rapid, isotropic tumbling of molecules averages these interactions to yield a single value of B_{local}. The advantage of solid-state NMR is that, through the application of specific pulse sequences designed to manipulate the relaxation of spins, one can "recouple" select spin interactions to gain additional structural information.

Fitting Spectra using Pseudo-Voigt Profiles

Fourier transform NMR measures the free induction decay of a magnetic moment induced in the sample by a radiofrequency pulse. The decay is exponential, and yields a Lorentzian line shape in the frequency domain. In solid-state NMR, because of chemical shift anisotropy, dipolar coupling, and other magnetic effects are not averaged out over the time frame of the experiment, we observe a Gaussian distribution of Lorentzian line shapes. The Voigt profile is the most appropriate for describing these line shapes, and the pseudo-Voigt profile achieves nearly the same fit while being computationally simpler. Therefore, peaks in the frequency domain of a solid-state NMR spectrum are typically fit with a pseudo-Voigt function, $V_p(x)$, to obtain parameters including the peak location, width, and integrated area:

$$V_p(x) = \eta \cdot G(x) + (1-\eta)\cdot L(x) \tag{3.7}$$

$$G(x) = exp\Bigg[-ln(2)\cdot\left(\frac{x-x_0}{\omega}\right)^2\Bigg] \tag{3.8}$$

$$L(x) = \frac{1}{1 + \left(\frac{x - x_0}{\omega}\right)^2} \tag{3.9}$$

where x_0 is the peak centroid and $2\omega = FWHM$. The term η can take any value between zero and 1, and describes the *shape* of the peak. A value of $\eta = 1$ gives a Gaussian distribution, and a value of $\eta = 0$ gives a Lorentzian distribution.

Magic Angle Spinning

In liquid samples, molecules tumble about one another isotropically and rapidly. If this motion is fast enough, the molecular orientation dependence of chemical shielding and dipolar coupling interactions averages to zero over the course of an experiment. This yields relatively narrow peaks in the frequency domain. For solid-state samples, spins are stationary and occupy every possible orientation in the magnetic field with respect to each other and the shielding electrons. The effects of chemical shielding and dipolar coupling anisotropy are therefore readily observed, manifesting as significant broadening of peaks that often obscure spectral details. The same effect of isotropic tumbling of spins in the solution phase can be produced by spinning solid samples at a specific angle with respect to the B_0 field. Figure 3.4 depicts magic-angle spinning (MAS). The orientation dependence of spin interactions, including chemical shielding and dipole-dipole coupling, include a $3\cos^2\theta - 1$ factor, where θ is the angle between the z-axis of the spin interaction tensor and the z-axis of the laboratory frame.

Spinning the sample at an angle θ_{rotor} with respect to the B_0 field results in averaging the spin interaction orientation over time:

$$\left\langle 3\cos^2\theta - 1 \right\rangle = \frac{1}{2}\left(3\cos^2\theta_{rotor} - 1\right)\left(3\cos^2\beta - 1\right) \tag{3.10}$$

where β is the angle between the z-axis of the spin interaction tensor and the spinning axis, as shown in Figure 3.4. The angle β is fixed for each spin, and for a large number of spins, every possible value of β occurs. The angle θ_{rotor} can be controlled. The term $\left\langle 3\cos^2\theta - 1 \right\rangle$ is equal to zero when θ_{rotor} is 54.74 °, which is known as the *magic* angle. If the sample is spun rapidly at the magic angle, the anisotropic effects of chemical shielding and dipolar coupling are greatly reduced, and spectral resolution is improved.

For this work, samples were typically spun at 10 kHz unless otherwise noted. To eliminate the spin orientation dependence of chemical shielding and dipolar coupling, samples must be spun at a rate faster than the anisotropy of the spin interaction. If the spinning rate slower than the anisotropy of the spin interaction, *spinning side bands* are observed. In the frequency domain, spinning side bands are peaks that appear symmetrically about the isotropic chemical shift, and they are separated by the spinning rate. They can be distinguished from the main isotropic chemical shift resonance because their location depends on the spinning rate. If the spinning rate is changed, the position of the spinning side bands

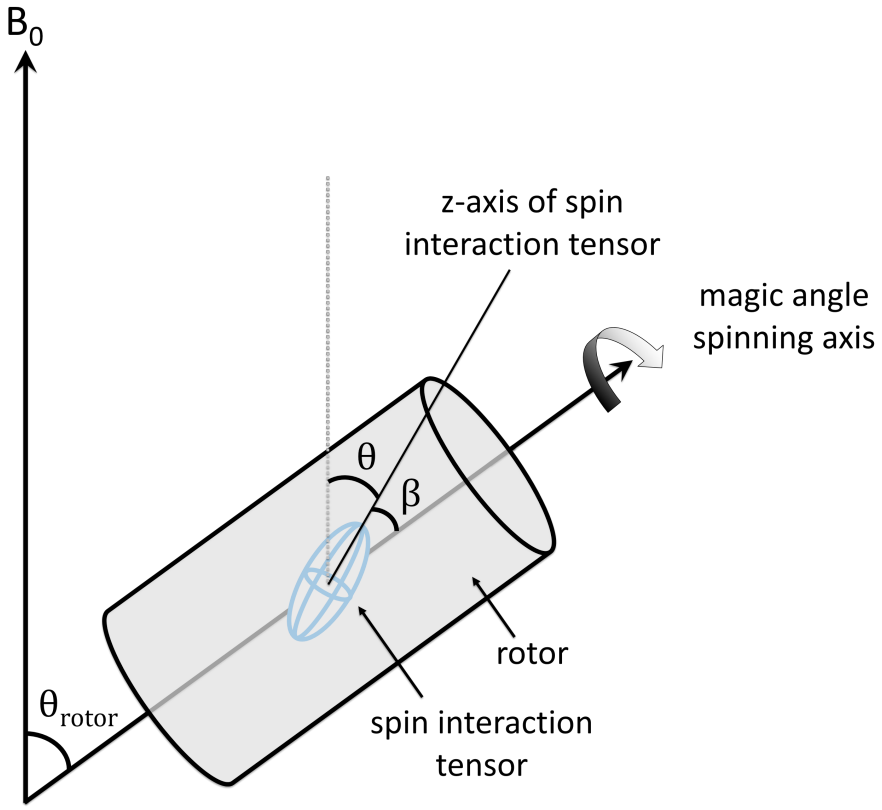

Figure 3.4: Diagram depicting magic angle spinning. θ is the angle between the z-axis of the spin interaction tensor and the z-axis of the laboratory frame, which is parallel to the applied magnetic field, B_0. β is the angle between the z-axis of the spin interaction tensor and the spinning axis. Θ_{rotor} describes the angle between the z-axis of the laboratory frame and the spinning axis, which is set to 54.74 ° for magic-angle spinning. Image adapted with permission from reference [144].

changes, while that of the isotropic chemical shift remains the same. State of the art "very fast MAS" probes have achieved spinning rates of 111 kHz.

^{1}H Dipolar Decoupling

Due to the natural abundance of ^{1}H, most nuclei with spin experience strong spin-spin dipolar coupling to neighboring protons. The dipolar coupling interaction between two spins is anisotropic, which causes significant line broadening in solid-state materials. The H-X dipolar coupling interaction, where X is a ^{13}C, ^{29}Si, or ^{31}P nucleus, is strong enough that magic-angle spinning is often not sufficient to remove dipolar coupling that may obscure important spectral details.

One solution is to collect X spectra while irradiating ^{1}H with continuous wave radiofrequency at its Larmor frequency. If I_z and S_z represent the net magnetization of protons and the X spin population in the direction of the B_0 field, respectively, then their dipolar

coupling interaction is proportional to

$$I_z S_z$$

Irradiation with plane-polarized radiofrequency at the ^{1}H Larmor frequency will cause precession of I through the xy plane until it is oriented along the $-I_z$ axis, and then back around to the $+I_z$ axis. If continuous, cycled rotation from $+I_z$ to $-I_z$ is fast enough, the dipolar coupling interaction $I_z S_z$ averages to zero. The result is greatly improved spectral resolution.

NMR of the ^{1}H, ^{13}C, ^{29}Si, and ^{31}P Nuclei

Table 3.1 shows the properties relevant for NMR studies on ^{1}H, ^{13}C, ^{29}Si, and ^{31}P nuclei. All of these nuclei are spin 1/2. The relative receptivity is given in reference to the ^{29}Si nucleus, and is equal to $\gamma^3 C(I(I+1))$, where γ is the gyromagnetic ratio and C is the natural abundance [145].

Table 3.1: Properties relevant for NMR of ^{1}H, ^{13}C, ^{29}Si, and ^{31}P nuclei

Nucleus	Natural Abundance	$\gamma/(2\pi)$ (MHz/T)	Relative Receptivity	Standard
^{1}H	99.985%	42.576	2.71×10^3	TMS
^{13}C	1.108%	10.705	4.77×10^{-1}	TMS
^{29}Si	4.70%	-8.465	1	TMS
^{31}P	100%	17.235	1.8×10^2	H_3PO_4

^{1}H NMR

^{1}H has high isotopic abundance and a high γ value, making it the most receptive nucleus for NMR study. Due to the high abundance of ^{1}H nuclei, their solid-state NMR spectra often demonstrate strong homonuclear dipolar coupling. This results in significant peak broadening. In inorganic materials, including silica, the spatial density of ^{1}H nuclei may be low enough to reduce dipolar coupling via magic-angle spinning. However, the density of ^{1}H nuclei can be increased by the presence of hydroxyl groups, the adsorption of water to the silica surface, as well as the adsorption or grafting of organic molecules. Proton NMR spectroscopy for these types of materials requires more sophisticated techniques to improve resolution. Bronnimann et al. [147] used magic-angle spinning combined with multiple-pulse line narrowing techniques to study the adsorption of water to silica gel. Water physisorbed to silica gel results in a resonance centered at 3.5 ppm relative to TMS. Isolated hydroxyl groups give a relatively sharp peak at 1.7 ppm relative to TMS. In contrast, hydroxyl groups participating in hydrogen bonding on the surface give rise to a very broad resonance centered at 3.0 ppm relative to TMS, reflective of a highly varied hydrogen bonding environment [147].

Direct observation of ^{1}H nuclei for surface-modified silica is thus complicated by the inevitable adsorption of water and complex hydrogen bonding environment of hydroxyl groups

at the surface. However, due to their high relative receptivity, ^{1}H nuclei are useful as sources of polarization transfer and for studying heteronuclear dipolar coupling with other nuclei of interest.

^{13}C NMR

^{13}C has a low natural abundance and a low γ, resulting in a very low relative receptivity. Additionally, surface-functionalized silica materials often have a low mass percentage of organic material. Therefore, collection of ^{13}C spectra is often plagued by low signal-to-noise ratio. Fortunately, the signal of ^{13}C spectra can be significantly increased using cross-polarization from ^{1}H nuclei. Cross-polarization with ^{1}H nuclei also has the advantage of reducing the T_1 relaxation time from minutes to seconds or less. Nonetheless, collection of a ^{13}C NMR spectrum for approximately 50-100 mg of functionalized silica typically requires the averaging of tens of thousands or even hundreds of thousands of scans, which can take several days. Furthermore, due to the very low natural abundance of the ^{13}C nucleus, NMR experiments measuring the dipolar coupling between ^{13}C and other low abundance nuclei are not possible unless the sample is prepared with carbon enriched in the ^{13}C isotope.

^{29}Si NMR

Similar to ^{13}C nuclei, ^{29}Si nuclei have low natural abundance and low γ, which limits signal-to-noise ratio and can prolong collection times. However, silicon compounds are ubiquitous in naturally occurring minerals, and therefore many solid-state NMR methods were developed and perfected for this nucleus. The percent mass of silicon is high in organically-modified silica samples. Furthermore, by using cross-polarization from ^{1}H, collection times can be reduced to a day or two, depending on the mass of the sample. Like the other spin = 1/2 nuclei, the major sources of line broadening for ^{29}Si spectra are dipolar coupling interactions and chemical shift anisotropy, both of which can be greatly reduced using magic-angle spinning. ^{29}Si NMR is a powerful tool for investigating the silica surface. The chemical shift of cross-linked tetrahedral silicon dioxide compounds gives an indication of the degree of cross-linking, as discussed in Chapter 2. Spectral resonances from tetrahedral silicate structures are denoted Q^n, where n represents the number of other cross-linked silicate groups attached. For example, Q^0, the monosilicate, has a chemical shift of approximately -65 ppm with respect to TMS. As the number of cross links increases, the chemical shift decreases by roughly 10 ppm with each additional link to another silicate. Q^4 represents silicates fully cross-linked to four other silicate groups, and has a chemical shift of approximately -110 ppm with respect to TMS [139, 140, 145].

Additionally, information about the interaction of ^{29}Si and ^{1}H through cross-polarization and other spin relaxation studies has provided a wealth of information about the complex hydrogen bonding environment present on silica surfaces [140].

^{31}P NMR

With a high natural abundance and a high γ, ^{31}P has a high relative receptivity, which makes collection of high-quality spectra easier than for ^{13}C and ^{29}Si nuclei. The natural abundance of ^{31}P nuclei also facilitates the observation of homonuclear and heteronuclear dipolar coupling interactions, which can give valuable structural information.

Unlike the nuclei discussed above, chemical shifts for ^{31}P spectra do not necessarily correlate directly with the local electron density. This is because chemical shifts for phosphorus compounds tend to be dominated by paramagnetic contributions to the shielding tensor [145, 146]. Therefore, assignment of chemical shifts to specific structural features can be rather more complicated than for ^{1}H, ^{13}C, and ^{29}Si spectra.

3.2 Cross-Polarization

Purpose of Cross-Polarization

The technique of transferring polarization from an abundant spin population I to a less-abundant or "dilute" spin population X was originally developed to solve two of the problems in solid-state NMR spectroscopy that prevented the collection of spectra for nuclei such as ^{13}C and ^{29}Si. The first was the prohibitively low receptivity of nuclei with small gyromagnetic ratios and low natural abundance, leading to a very poor signal to noise ratio. The second was their very long T_1 relaxation times, leading to very long collection times. Polarization is usually transferred from ^{1}H to an X nucleus, where X is ^{13}C, ^{29}Si, or ^{31}P. The resulting FID for the X nuclei is observed.

In the original experiment by Hartmann and Hahn [148], reduced magnetization of the abundant ^{1}H spin population as a result of polarization transfer to the X spin population was observed. A decade later, Pines, Gibby, and Waugh [149] modified this experiment and observed the gain in magnetization for dilute X spins after polarization transfer from ^{1}H spins, combined with ^{1}H-X decoupling to achieve high-resolution spectra. They showed that compared to conventional observation of dilute spins, the cross-polarization (CP) technique yielded a gain in signal amplitude by a factor of $N_H\gamma_H^2/N_X\gamma_X^2$, on the order of 10^2 and 10^3 for X = ^{29}Si and ^{13}C, respectively. Cross-polarization can be used not only as a signal-enhancing tool, but also as a spectral editing tool. Because the mechanism of $^{1}H- > X$ polarization transfer involves ^{1}H-X dipolar coupling, CP spectra give information about the relative number and proximity of protons near to the X nucleus of interest, as will be discussed below.

Theory of Cross-polarization

Figure 3.5 shows the cross-polarization experiment. The sample is irradiated with a sequence of radiofrequency pulses via two channels, the ^{1}H and the X channels, each tuned to the Larmor frequency of their respective nuclei.

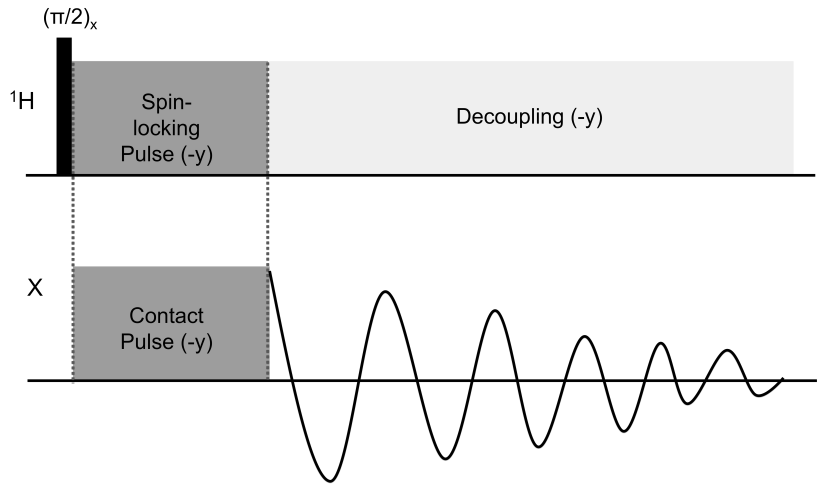

Figure 3.5: Cross-polarization pulse sequence for magnetization transfer from abundant ^{1}H nuclei to the observed X nuclei

It is helpful to view this technique in a doubly rotating frame. ^{1}H pulses are applied in a frame where the xy plane rotates about the laboratory z axis at the Larmor frequency of the ^{1}H spins, such that all ^{1}H pulses appear static. In the second rotating frame, the xy plane rotates about the laboratory z axis at the Larmor frequency of the X spins, such that all X pulses appear static. As usual, the sample is first allowed to equilibrate in the B_0 field, which generates a net magnetization along the $+z$ axis for both ^{1}H and X nuclei, $M_{0,H}$ and $M_{0,X}$, respectively. Curie's Law describes the equilibrium net magnetization as:

$$M_0 = \frac{N\gamma^2 B_0 \hbar^2 I(I+1)}{3kT_L} \tag{3.11}$$

where I is the spin (I = 1/2), N is the total number of spins, k is the Boltzmann constant, and T_L is the "thermodynamic lattice temperature" [145].

The first step is to irradiate ^{1}H nuclei with a $\pi/2$ pulse, which causes $M_{0,H}$ to precess into the xy plane. After the $\pi/2$ pulse, a "spin-locking" pulse is sent through the ^{1}H channel. The spin-locking pulse generates a magnetic field in the transverse plane, known as $B_{1,H}$. $B_{1,H}$ is parallel to the net ^{1}H magnetization ($M_{1,H}$) just after the $\pi/2$ pulse, and it rotates at the Larmor frequency. Under the influence of $B_{1,H}$, the ^{1}H spins do not dephase as quickly, and instead relax via spin-lattice relaxation in the $B_{1,H}$ field with the relaxation time constant $T_{1\rho}$. Since spins do not dephase rapidly, transverse magnetization lasts longer and is said to be *locked* in the xy plane.

The $B_{1,H}$ field acts on $M_{1,H}$ the same way that B_0 acts on $M_{0,H}$. The magnitude of B_0 is much larger than that of $B_{1,H}$. However, in the rotating frame, the effect of B_0 on $M_{1,H}$ is averaged to zero over time, and the only magnetic field influencing $M_{1,H}$ is that generated by the spin-locking pulse, $B_{1,H}$. Application of the $B_{1,H}$ field breaks the degeneracy of the spin states into two states, one with the magnetic moment aligned with $B_{1,H}$ and one with

the magnetic moment aligned against it. Simultaneously with the spin-locking pulse in the ^{1}H channel, a *contact pulse* is sent through the X channel. As discussed below, this contact pulse generates favorable conditions for polarization transfer from ^{1}H to X nuclei. During the contact pulse, a net transverse magnetization of X nuclei builds up in the xy plane. When the contact pulse and spin-locking pulse are stopped, the transverse magnetization of ^{1}H and X spins relax, and the free induction decay is observed for the X nuclei.

Cross-polarization can be conceptualized using a *spin thermodynamics* analogy [145]. The initial $\pi/2$ pulse in the ^{1}H channel results in the transfer of $M_{0,H}$ to the transverse plane, which is locked in place by application of B_1. Only the orientation of the net ^{1}H magnetization has changed; the magnitudes of $M_{0,H}$ and $M_{1,H}$ are the same:

$$M_{0,H} = \frac{N\gamma^2 B_0 \hbar^2 I(I+1)}{3kT_L} = \frac{N\gamma^2 B_{1,H} \hbar^2 I(I+1)}{3kT_{\rho H}} = M_{1,H} \tag{3.12}$$

where $T_{\rho H}$ is the thermodynamic lattice temperature of ^{1}H spins in the $B_{1,H}$ field. Solving Equation 3.12 for $T_{\rho H}$ yields:

$$T_{\rho H} = \left(\frac{B_{1,H}}{B_0}\right) T_L \tag{3.13}$$

Since $B_{1,H} << B_0$, $T_{\rho H}$ is much smaller than T_L, and the ^{1}H spins are said to be *cold*. Effectively, this means that a greater number of ^{1}H spins are in the lower Zeeman state, but under the influence of a much weaker magnetic field than just prior to the $\pi/2$ pulse. In contrast, the net transverse spin magnetization of the X nuclei at the start of the spin-locking pulse is zero, which means that $T_{\rho X}$, the spin lattice temperature of X spins in the $B_{1,H}$ field, is infinite, or very *hot*. Thermodynamics drives transfer of energy from *hot* to *cold* spin systems if the two are brought into thermodynamic contact. This can be done by applying a B_1, X field via a radiofrequency *contact* pulse through the X channel, such that

$$\gamma_H B_{1,H} = \gamma_S B_{1,S}$$

known as the Hartmann-Hahn match condition [148]. These conditions result in the Larmor frequencies of the ^{1}H and X spins being equal to each other in their B_1 fields, since ($\omega_1 = -\gamma B_1$). Therefore, the difference in energy between the Zeeman states is equal for both spin systems, meaning that the same radiofrequency mediates their spin-flip interactions. The laws of thermodynamics dictate that heat will be transferred between the two spin systems and that overall energy will be conserved. A spin flip from the lower to the higher $B_{1,H}$ Zeeman state for a ^{1}H spin is more likely to occur than the reverse because of the relative abundance of ^{1}H spins in the lower state. Energy is conserved, so each of these transitions is exactly compensated for by a transition of an X nucleus from the higher to the lower $B_{1,X}$ Zeeman state. This is demonstrated pictorially in Figure 3.6.

Over time, the X spins reach a new temperature [145]:

$$T_{\rho X} = T_{\rho H}\left(\frac{N_X}{N_H} - 1\right) \tag{3.14}$$

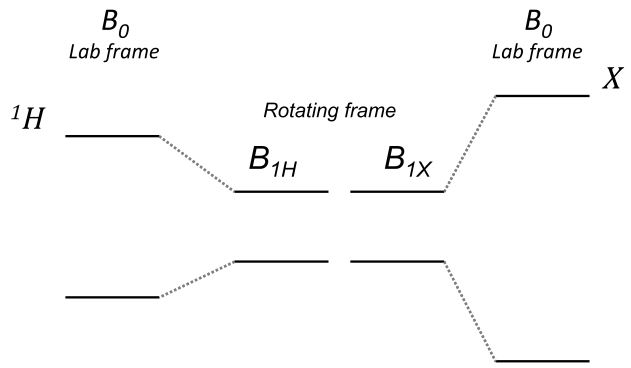

Figure 3.6: Conceptual drawing of the Hartman-Hahn match condition required for cross-polarization between ^{1}H and X spin populations. Image adapted with permission from reference [145].

Since $N_X \ll N_H$ in most cases, this means that $T_{\rho X}$ is a very small, negative number. The X spins have *cooled* slightly, meaning that they have acquired transverse magnetization (see Equation 3.12). Meanwhile, $T_{\rho H}$, does not significantly change. Thus, magnetization is transferred from the abundant spins to the less abundant spins during the contact pulse. When the contact and spin-locking pulses stop, magnetization evolves with the relaxation time constants of the abundant spins, ^{1}H, so that T_1 relaxation is significantly reduced for nuclei such as ^{29}Si and ^{13}C.

Setting Up a Cross-Polarization Experiment

The notation $X\{^1H\}$ is used to indicate the observation of X spins after polarization from ^{1}H nuclei. The cross-polarization (CP) experiment is typically set up on a standard reference compound, which also serves as a secondary chemical shift reference. For this work, glycine is used for ^{13}C{^{1}H} CP, kaolinite for ^{29}Si{^{1}H} CP, and hydroxyapatite for ^{31}P{^{1}H} CP.

There are two major steps for setting up the CP experiment. The first is to set the $\pi/2$ pulse width for the ^{1}H spins. The radiofrequency power level and pulse duration (or "width") must be set to the correct values to achieve a $\pi/2$ pulse. Generally the power level is set based on previous experimentation and according to the electronic limitations of the NMR probe and spectrometer. Then spectra are collected observing the free induction decay of X nuclei for an array of pulse widths. Figure 3.7 shows the shape of the nutation curve for ^{1}H magnetization for various pulse widths. Typically, the 2π value is determined, and from it the $\pi/2$ value calculated and set for the ^{1}H power level chosen. The power level of the spin-locking pulse is usually kept the same as that of the $\pi/2$ pulse.

The next step is to set the Hartmann-Hahn match condition for the contact pulse. Spectra are collected observing the free induction decay of X nuclei for an array of X-channel power levels for the contact pulse. The duration of this pulse is chosen to maximize the signal intensity of the standard to facilitate observation of signal in on a reasonable timescale, and must be kept constant for CP spectra that are to be compared. Under static conditions

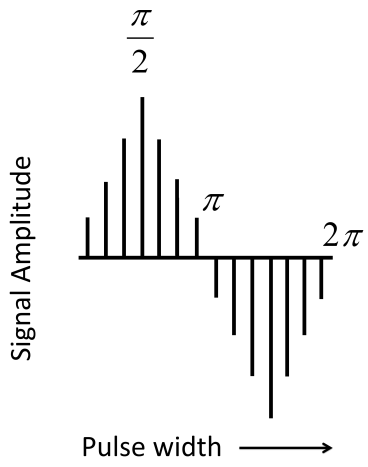

Figure 3.7: Typical nutation curve for variable ^1H channel $\pi/2$ pulse widths at an arbitrary power level during set-up for a cross-polarization experiment.

(no MAS) the nutation curve rises, reaches a maximum, and then falls (gray lines in Figure 3.8.) The Hartmann-Hahn match is achieved when the signal reaches its maximum value (red arrow in Figure 3.8). However, magic-angle spinning introduces a time dependency to the CP signal, which manifests as breaking the curves up into a series of spinning side bands (black lines in Figure 3.8). Therefore, the Hartmann-Hahn match condition is dependent on the rotational velocity of the rotor. For CP/MAS sequences, the Hartmann-Hahn match condition is set to the X-channel power level where the maximum signal intensity occurs (blue arrows in Figure 3.8).

The relative amplitude of different peaks in the frequency domain is dependent on the duration of the contact pulse. Depending on the proximity and number of ^{1}H nuclei to X nuclei in a given chemical environment, they will polarize faster or slower, and the ^{1}H nuclei will demonstrate shorter or longer $T_{1\rho}$ relaxation times. Thus, spectra collected using cross-polarization are not quantitative in the sense that the relative signal amplitudes are not proportional to the relative abundance of their corresponding species. However, analysis of the polarization transfer kinetics can yield a wealth of structural information.

Kinetics of Cross-polarization

An excellent review discussing the kinetic processes governing polarization transfer from abundant spins I to dilute spins S is provided by Kolodziejski and Klinowski [150]. There are two different models describing polarization transfer, the "classical" I-S CP kinetics model and the I-I^*-S CP kinetics model.

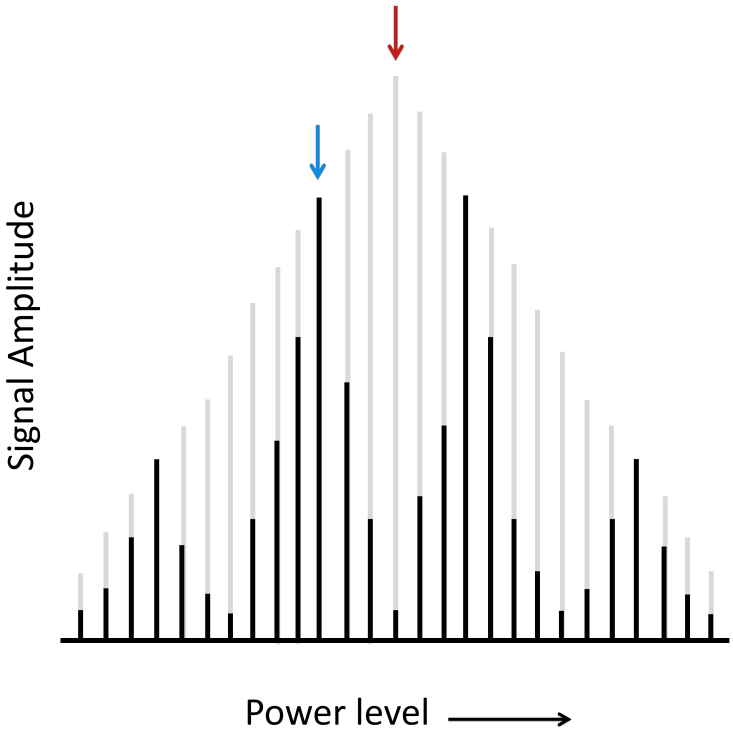

Figure 3.8: Typical nutation curve for variable X channel power levels at an arbitrary pulse width during set-up for a cross-polarization experiment. The grey lines show nutation under static conditions, where the Hartmann-Hahn match occurs at the signal maximum (red arrow). The black lines show the shape of the curve under MAS, which causes it to be broken up into a series of spinning side bands. MAS introduces time dependency to the CP signal, effectively making the Hartmann-Hahn match dependent on the rotor velocity. Under MAS, the Hartmann-Hahn match is set to the signal maximum at the lower power level (blue arrow).

The I-S Cross Polarization Kinetics Model

The I-S model follows the theoretical description of cross-polarization provided in the previous section. Figure 3.9 diagrams the physical processes underlying the I-S model. Polarization is transferred from an abundant population of spins I at a uniform spin temperature during the contact pulse. Polarization is transferred with a time constant T_{IS} typical for each system.

As discussed above, thermodynamics drives the equalization of spin temperatures for the two spin populations during the contact pulse. Simultaneously, spin-lattice relaxation occurs for the I and S spins in their rotating frames, with relaxation time constants $T_{1\rho}^{I}$ and $T_{1\rho}^{S}$, respectively. During the contact pulse, the change in spin temperature over time for the two spin populations can be described by the following differential equations:

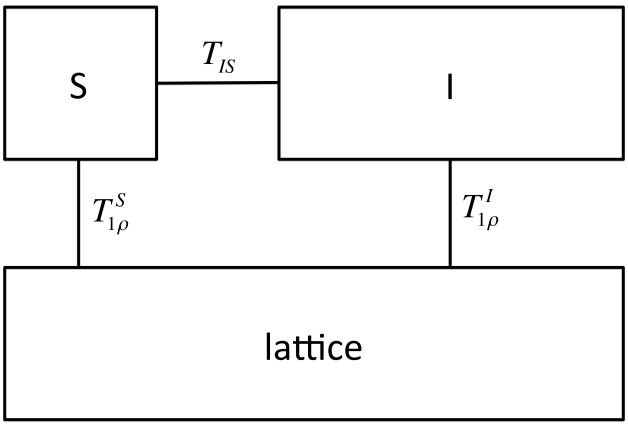

Figure 3.9: Diagram of the classical cross-polarization kinetics model, showing the S, I, and lattice spin populations and the time constants governing their interactions. Reprinted with permission from [150]. Copyright 2002 American Chemical Society.

$$\begin{aligned} \frac{d\beta_S}{dt} &= \frac{-(\beta_S - \beta_I)}{T_{IS}} - \frac{\beta_S}{T_{1\rho}^S} \\ \frac{d\beta_I}{dt} &= \frac{-\epsilon\alpha^2(\beta_I - \beta_S)}{T_{IS}} - \frac{\beta_I}{T_{1\rho}^I} \end{aligned} \tag{3.15}$$

where β_S and β_I are the inverse spin temperatures for the I and S spin populations, respectively, ϵ is the ratio of the spin populations N_S/N_I, and α is the ratio of the precession frequencies of the S and I spin magnetizations in the doubly rotating frame, or $\alpha = \gamma_S B_{1S}/\gamma_I B_{1I}$. The first term in each equation above describes the transfer of magnetization to S spins, and the second describes the spin-lattice relaxation of each spin system in the rotating frame. As can be seen from Equation 3.12, the inverse spin temperature is directly proportional to the net magnetization of each spin population. The general solution to Equations 3.15 can be shown to be:

$$I(t) = I_0(1 + T_{IS}/T_{1\rho}^S - T_{IS}/T_{1\rho}^I)^{-1}\{exp(-t/T_{1\rho}^I) - exp[-t(1/T_{IS} + 1/T_{1\rho}^S)]\} \tag{3.16}$$

where t is the duration of the contact pulse and $I(t)$ is the intensity of the S resonance in the frequency domain, if the following assumptions are made: 1) that at the start of the contact pulse (t=0), β_I is a non-zero value, β_I^0, while $\beta_S = 0$, and 2) that the abundant spins I are sufficiently more abundant than the dilute spins S that $\epsilon \approx 0$. For dilute spins, $T_{1\rho}^S$ is usually very long due to a lack of homonuclear dipolar coupling which stimulates relaxation in the B_{1S} field. If $T_{IS}/T_{1\rho}^S \approx 0$, then Equation 3.16 reduces to:

$$I(t) = I_0(1 - T_{IS}/T_{1\rho}^I)^{-1}[exp(-t/T_{1\rho}^I) - exp(-t/T_{IS})] \tag{3.17}$$

Figure 3.10 shows simulated CP kinetics curves for three different I-S spin systems. A sample with stronger I-S dipolar coupling will have a relatively lower T_{IS} value, leading to

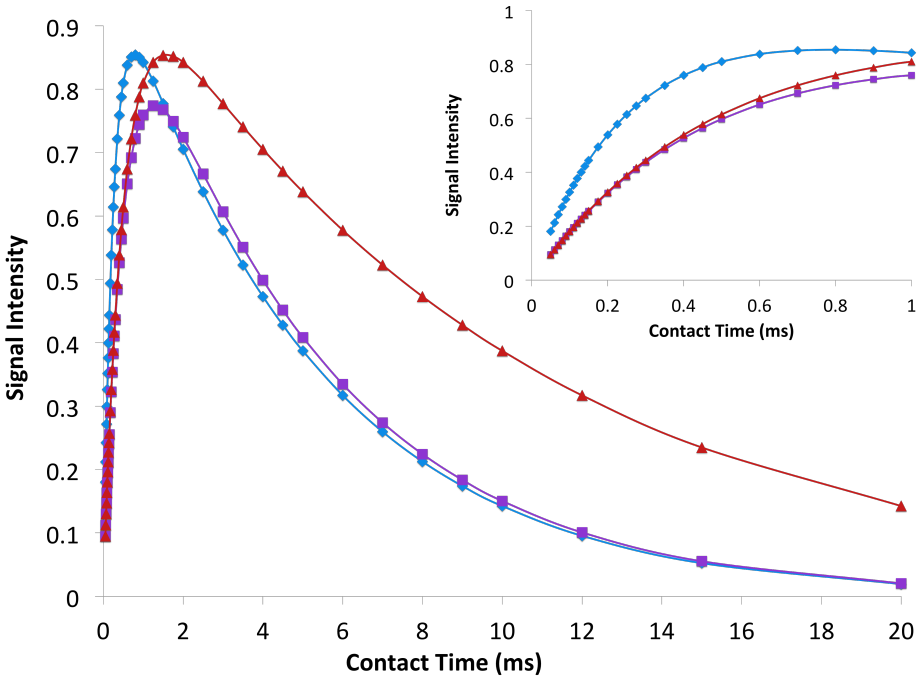

Figure 3.10: Simulated variable contact time curve data for three different $I - S$ spin systems fit with Equation 3.17. Cross-polarization kinetics time constants for the blue, purple, and red curves, respectively, are $T_{IS} = 0.25$, 0.5, and 0.5 ms, and $T_{1\rho}^{I} = 5$, 5, and 10 ms. The inset shows the same data at short contact times.

a sharper rise at low contact times, as shown in the blue curve in Figure 3.10. Higher T_{IS} values indicate longer polarization transfer times, most likely the result of lower I-S dipolar coupling. $T_{1\rho}^{I}$ also gives information about the local structure. A relatively high $T_{1\rho}^{I}$ value indicates slower relaxation of the abundant spins in their rotating frame (red curve in Figure 3.10. Slower relaxation may be caused by a lower degree of homonuclear dipolar coupling between I spins, or by restricted molecular motion.

The I-I^*-S Cross Polarization Kinetics Model

The non-classical I-I^*-S cross-polarization kinetics model was originally conceived to explain the observation of oscillations in the variable contact time curves for stationary single crystals. These oscillations were found to be dependent upon the orientation of the crystal in the B_0 field [151, 152]. Figure 3.11 diagrams the I-I^*-S CP kinetics model. In this model, there are clusters of I^*-S spins that are relatively isolated from the bulk of the I spin population.

Instead of assuming that the abundant I spins are at a uniform spin temperature, the I-I^*-S model effectively accounts for two populations of I spins that are at two different spin temperatures. I^* spins are in close proximity to S spins, and magnetization is transferred between them in an oscillatory fashion. I spins, which are farther away from S spins,

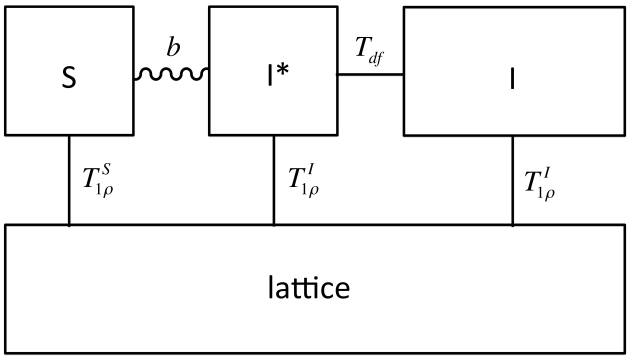

Figure 3.11: Diagram of the I-I^*-S cross-polarization kinetics model showing the lattice, S, I^*, and I spin populations and the time constants governing their interactions. Reprinted with permission from [150]. Copyright 2002 American Chemical Society.

contribute much less to the polarization of S spins. However, I spins are in contact with S spins indirectly through spin diffusion with I^* spins. Spin diffusion can be though of as the dipolar coupling-induced spin-flip interactions occurring through space between I^* and I spins at a rate of $R = 1/T_{df}$, where T_{df} is the spin diffusion time constant. At longer contact times, spin diffusion in the I-I^* system dampens these oscillations as the spin temperature of the I and I^* spins equalizes.

Assuming very slow relaxation for S spins in their rotating frame such that $T_{1\rho}^{S} = \infty$, as well as negligible spin diffusion between S spins and isotropic spin diffusion for I spins, the evolution of signal intensity for observed spins over time, I(t), is described by:

$$I(t) = I_0 exp\left(\frac{-t}{T_{1\rho}^{1}}\right)\left[1 - \frac{1}{2}exp\left(\frac{-t}{T_{df}}\right) - \frac{1}{2}exp\left(\frac{-3t}{2T_{df}}\right)\cos\left(\frac{bt}{2}\right)\right] \tag{3.18}$$

Figure 3.12 shows simulated variable contact time curve data for three different I-I^*-S spin systems. The frequency of oscillations is related to the average strength of dipolar coupling between S spins and their nearest I spin neighbors. Increasing the strength of dipolar coupling increases the oscillation frequency, which can be seen by comparing the blue and purple curves in Figure 3.12. The spin diffusion time constant describes how rapidly energy is transferred from I^* spins in close proximity to S spins to the bulk of I spins farther away. A higher diffusion rate, or a relatively lower time constant T_{df} causes a more rapid dampening of the oscillations, which can be seen by comparing the purple and red curves in Figure 3.12.

Utility of Cross-Polarization for Studying Solid Materials and Silica Surfaces

In addition to enhancing the signal-to-noise ratio for nuclei with low natural abundance and to shortening experimental time, the cross-polarization technique can be used as a valuable spectral editing tool, which can give information about the local proton environment in a

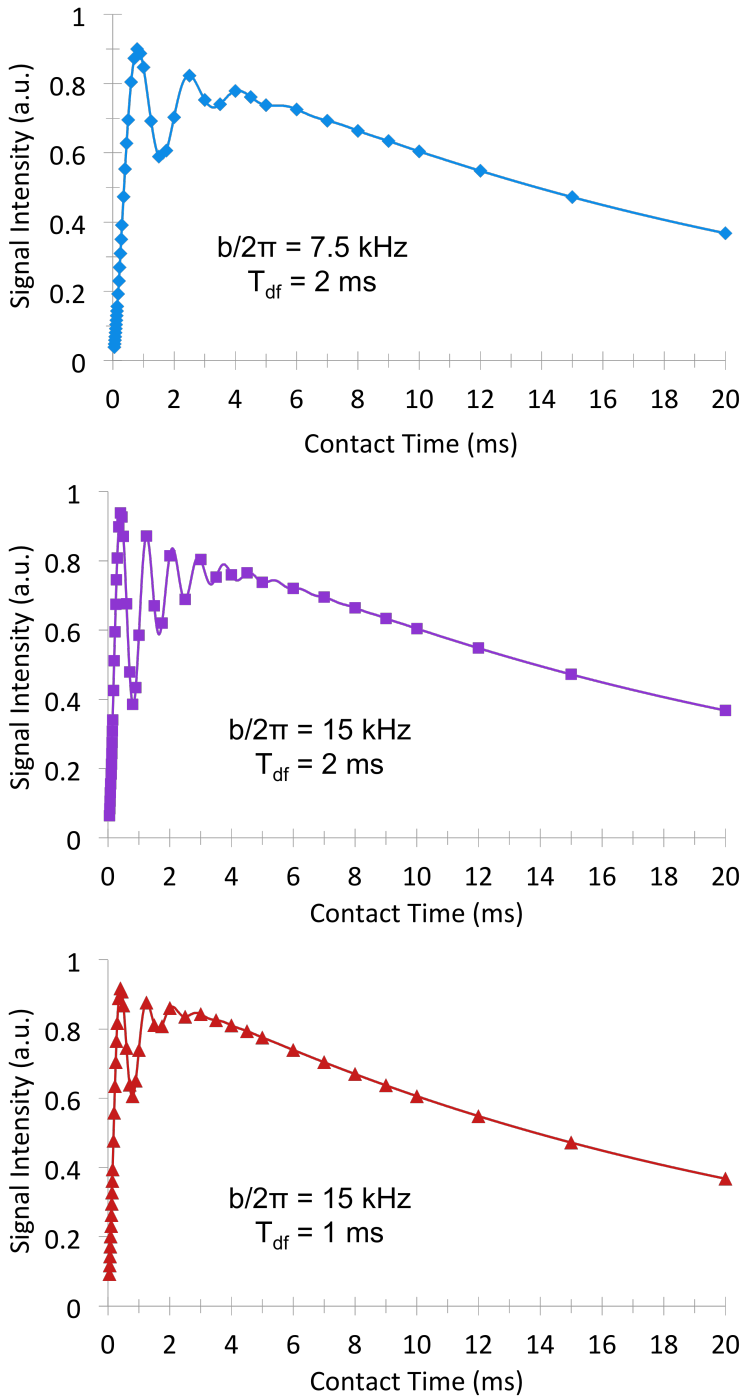

Figure 3.12: Simulated variable contact time curve data for three different I-I^*-S spin systems fit with Equation 3.18. For each curve, $I_0 = 1$ and $T_{1\rho}^I = 20$ ms. The dipolar coupling constant b and the abundant spin diffusion time constant T_{df} vary as shown in the figure.

sample. Cross-polarization relies on the dipolar coupling between the observed nucleus of interest and the nearest neighboring ^{1}H spins.

For silica samples, this means that cross-polarization is largely restricted to studying the surface of the silica, where ^{1}H spins are present in the form of hydroxyl groups, adsorbed water, and grafted organic groups. Maciel and Sindorf conducted numerous studies on the silica surface using ^{29}Si$\{^1$H$\}$ CP/MAS. These studies include investigations of non-modified silica materials [139, 140], of the processes underlying dehydration and rehydration of silica gel [153], and of silica gel modified with trimethylchlorosilane [141, 153–157]. They found that cross-polarization kinetics differ for the various species present on the silica surface. While Q^2, Q^3, and Q^4 ^{29}Si spin populations demonstrate similar $T^I_{1\rho}$ relaxation, their polarization transfer constants, T_{SiH} were found to be 2.3 ± 0.2, 2.9 ± 0.1, and 12.7 ± 1.7 ms, respectively [139]. This shows that polarization transfer is significantly delayed for Si(OSi)$_4$ atoms, which are isolated from the abundant ^{1}H spin population. Additionally, polarization transfer occurred more quickly for geminal silanols because of the greater number of nearby protons. Following this result, they developed a methodology for interpreting ^{29}Si$\{^1$H$\}$ CP/MAS spectra quantitatively in the regime where

$$T_{SiH} \ll \textit{contact time} \ll T^H_{1\rho}$$

By combining this method with quantification of silanol content via reaction with trimethylchlorosilane, they determined that geminal silanols react more extensively than isolated silanols, and are therefore more reactive [154].

Liu and Maciel [140] compared the ^{29}Si$\{^1$H$\}$ CP kinetics of fumed silica and silica gel. They observed two different components for silanols, which demonstrated different T_{SiH} constants. One component polarized very quickly ($T_{SiH} <$ ms, while the other polarized more slowly ($T_{SiH} \approx 10$ ms). Both components were observed for both geminal and isolated silanols. They concluded that the faster polarizing component has a stronger ^{1}H-^{29}Si dipolar coupling interaction. The stronger dipolar coupling is caused by more ^{1}H spins in close proximity to ^{29}Si atoms that are part of hydrogen-bonded silanols, and by restricted molecular motion, which results in less motional averaging that can dampen dipolar coupling. They also found that in contrast to fumed silica, which contains both hydrogen-bonded and non-hydrogen-bonded silanols, untreated silica gel contains only hydrogen-bonded surface species.

Mason et al. [158] used ^{29}Si$\{^1$H$\}$ CP/MAS to study the binding of paramagnetic cations Cu^{2+} and Ni^{2+} to amorphous silica. They found two components in the ^{29}Si NMR spectrum of silica that had very different CP kinetics. The first was concentrated in the Q^2 and Q^3 peaks and was characterized by a rapid polarization followed by rapid decay, characteristic of silica sites bound to protons, Si–OH. The second component was concentrated in the Q^3 and Q^4 peaks and demonstrated much slower polarization and relaxation. This component was assigned to deprotonated silanols and bridged siloxane groups with no attached hydroxyls, i.e. Si–(OSi)$_4$. The paramagnetic effect of Cu^{2+} and Ni^{2+} upon binding to the silica surface was to cause a decrease in signal amplitude in the ^{29}Si$\{^1$H$\}$ CP/MAS spectrum. It was

observed however, that this decrease was most apparent for the spectral component assigned to deprotonated silanols. Therefore, CP kinetics studies were able to corroborate the sorption model describing inner-sphere complexation of cations to negatively charged silanol sites, as opposed to metal hydroxide precipitation. A follow-up study by Mason et al. [159] investigated the sorption of low concentrations of Eu^{3+} to the silica surface using CP/MAS and a modified cross-polarization method designed to measure spin diffusion. They found that Eu^{3+} was evenly distributed on the silica surface. Furthermore, they showed that $^{29}Si\{^{1}H\}$ cross-polarization methods were useful for distinguishing monomeric sorption from precipitation at intermediate and high surface loadings for solubility-limited paramagnetic metal cations.

Kaflak et al. [160] studied $^{31}P\{^{1}H\}$ cross polarization kinetics in human bone. They found that the bone contained three different phosphate phases, each of which demonstrated distinct polarization kinetics. In addition to hydroxyapatite, which makes up the bulk of bone matter, they observed a proton-rich phase, which had a very short T_{SiH} accompanied by subtle I-I^*-S oscillations, and a proton-deficient phase, which demonstrated slow $T^I_{1\rho}$ relaxation. Klimavicius, Kareiva, and Balevicius [161] used high-density data point $^{31}P\{^{1}H\}$ cross-polarization kinetics measurements to characterize spin clusters in amorphous and nanostructured hydroxyapatite. They found that the non-classical I-I^*-S model described spin interactions in hydroxyapatite better than the classical CP kinetics model.

In summary, the cross-polarization technique is useful not only for the observation of low-sensitivity nuclei on a reasonable timescale, but also for probing the local proton environment around a given spin population. In this work, CP kinetics studies are used to support macroscopic batch contact techniques to study the mechanism of adsorption of heavy metal cations to mesoporous silica surfaces.

3.3 Dipolar Recoupling Sequences

Homonuclear and heteronuclear dipolar coupling causes significant line broadening for solid-state NMR samples, leading to prohibitively poor resolution. Magic-angle spinning and decoupling pulse sequences are used to minimize dipolar coupling, which has allowed for the observation of spectral details for solid samples. However, in some cases, it is useful to observe dipolar coupling between spins. The strength of the dipolar coupling interaction depends on $1/r^3$, where r is the internuclear distance between two coupled spins. Therefore, measurement of dipolar coupling can elucidate important structural information. This can be achieved by irradiating the sample with pulse sequences designed to reintroduce dipolar coupling.

The ability to recouple dipolar coupling interactions is an advantage of solid-state NMR spectroscopy. By probing the strength of dipolar coupling between spin systems, structural information can be determined for samples that have little or no long-range order. Diffraction techniques rely on the even spacing of planes in an ordered crystal lattice and are of little use for powdered, amorphous solids. Therefore, NMR is ideal for characterizing amorphous silica

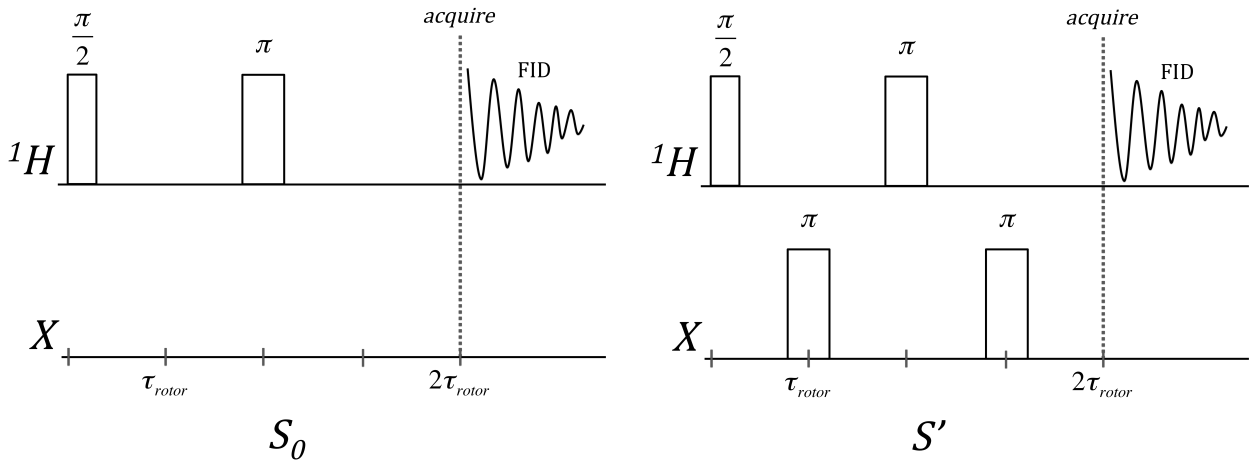

Figure 3.13: REDOR pulse sequence for measuring heteronuclear dipolar coupling. The left panel shows the S_0 reference experiment in which complete rephasing of the H spins occurs. The left panel shows the S experiment, in which rotor-synchronized π pulses on the X channel prevents complete rephasing of the H spins, resulting in a decrease in the amplitude of the echo observed in the H channel. Figure adapted from reference [162].

and modified silica surfaces, where short-range order of structural features drives reactivity. The following sections describe the relevant recoupling experiments used for the experimental work presented in Chapters 4 and 5.

Heteronuclear Recoupling: REDOR

Figure 3.13 shows the pulse sequences for the Rotational Echo Double Resonance (REDOR) technique. REDOR involves analysis of the difference in observed signal intensity between two experiments. The first experiment, S_0, is a standard *spin-echo* experiment on the observed nucleus, H in this case (Figure 3.13, left). During a spin-echo sequence, a $\pi/2$ pulse on H spins transfers net magnetization to the xy plane. The spins dephase in the xy plane with a characteristic T_2 relaxation time. Application of a π pulse after a given time τ results in the rephasing of the H spins, which results in observation of an "echo" signal at a time τ after the π pulse.

In the second experiment, S', the spin-echo sequence on the H channel occurs simultaneously with a series of π pulses on the X channel (Figure 3.13, right). The purpose of the π pulses is to prevent complete rephasing of the H spins, which results in a reduction in signal amplitude of the echo signal observed for the H spins. For the REDOR technique, the $\pi/2$ and π pulses are rotor-synchronized, such that an integer number of rotor cycles occurs between them. The dipolar coupling interaction between H and X spins averages to zero over the course of one rotor period. The rotor-synchronized π pulses on the X channel result in an inversion of the magnetic field due to X spins felt by the H spins, which partially reintroduces H-X dipolar coupling and inhibits complete rephasing of the H spins.

The REDOR sequence is repeated for various dephasing times $n\tau_{rotor}$, where n is an integer number. The difference in signal amplitude, $S_0 - S'$, depends on the strength of H-X dipolar coupling and the length of the dephasing time. Plots of $(S_0 - S')/S_0$ versus $n\tau_{rotor}$ are then fit with dipolar coupling models to extract internuclear distance information according to Equation 3.5.

Homonuclear Recoupling: DQ-DRENAR

One of the most common ways to measure homonuclear dipolar coupling involves the excitation of double quantum (DQ) coherences in a population of coupled spins. The probability of these excitations depends on the strength of dipolar coupling between spins. Although double quantum coherences cannot be observed directly, their effects on single-quantum transitions in the same spin system can be observed and related to the dipolar coupling strength between spins.

Double Quantum Coherence

In order to understand how the DQ-DRENAR approach works, it is first necessary to understand what it means to excite a double quantum coherence in a spin-coupled system. Levitt gives a thorough description of the quantum mechanics of isolated spin and spin pair ensembles (see chapters 9-10 of reference [163]), some of which is reviewed below.

The z-axis component of the angular momentum of a spin 1/2 has two eigenstates. These are the Zeeman states described earlier. In the lower energy state, the spin is aligned parallel to B_0. In the higher energy state, it is aligned anti-parallel to B_0. The 'bra-ket' notation commonly used in quantum mechanics labels these states $|\alpha\rangle$ and $|\beta\rangle$, respectively. In fact, spins are not restricted to just these two states. If a spin is aligned with the x-axis its z-component value is undefined; half of the time it will be measured as $+1/2$ and the other half as $-1/2$. The wavefunction describing this state is a superposition of the $|\alpha\rangle$ and $|\beta\rangle$ eigenstates:

$$|+x\rangle = \frac{1}{\sqrt{2}}\Big(|\alpha\rangle + |\beta\rangle \Big)$$

Almost every spin in a sample is in a superposed state, unless it happens to be exactly with or against B_0. Equation 3.19 shows the wavefunctions for spins aligned along the Cartesian axes. Similar states describe any orientation of the spin in the B_0 field.

$$\begin{array}{ll} |+z\rangle = |\alpha\rangle & |-z\rangle = |\beta\rangle \\ |+x\rangle = \frac{1}{\sqrt{2}}\big(|\alpha\rangle + |\beta\rangle \big) & |-x\rangle = \frac{1}{\sqrt{2}}\big(-i\,|\alpha\rangle + i\,|\beta\rangle \big) \\ |+y\rangle = \frac{1}{2}(1-i)\,|\alpha\rangle + (\frac{1}{2}(1+i)\,|\beta\rangle & |-y\rangle = \frac{1}{2}(1+i)\,|\alpha\rangle + \frac{1}{2}(1-i)\,|\beta\rangle \end{array} \tag{3.19}$$

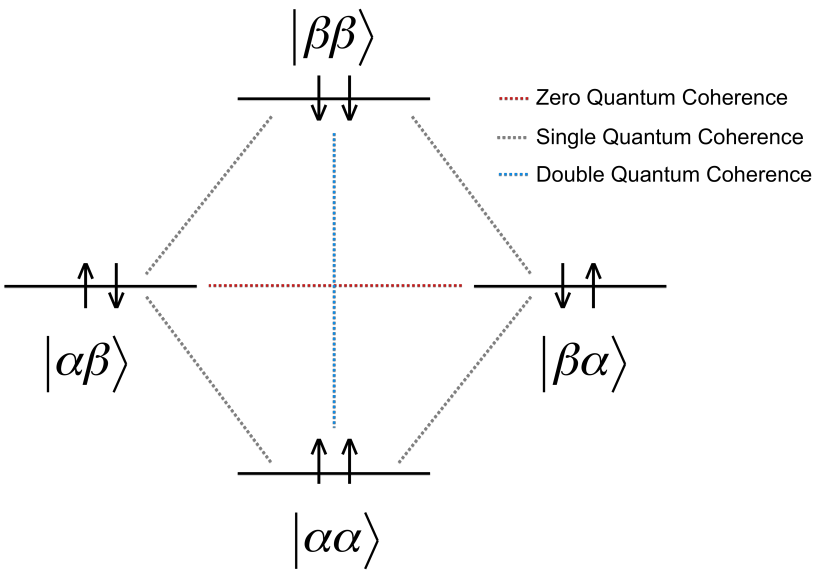

Figure 3.14: Energy states of a two-spin system, and the zero-, single-, and double-quantum coherences of these states.

An ensemble of non-coupled spins can be described by a density matrix, $\hat{\rho}$ [163]:

$$\hat{\rho} = \begin{pmatrix} \rho_{\alpha\alpha} & \rho_{\alpha\beta} \\ \rho_{\beta\alpha} & \rho_{\beta\beta} \end{pmatrix}$$

where $\rho_{\alpha\alpha}$ and $\rho_{\beta\beta}$ are the 'populations' of the $|\alpha\rangle$ and $|\beta\rangle$ eigenstates, respectively, and $\rho_{\alpha\beta}$ and $\rho_{\beta\alpha}$ are the *coherences* between the $|\alpha\rangle$ and $|\beta\rangle$ states. The coherences are superpositions of the eigenstates. It is the difference in population of states $|\alpha\rangle$ and $|\beta\rangle$ that gives rise to net magnetization along the B_0 axis. Coherences can be understood physically as net transverse magnetization, perpendicular to B_0.

An ensemble of coupled spin-1/2 pairs has a larger density matrix comprised of four populations and twelve coherences. This is because a coupled spin pair has four energy eigenstates, two of which are degenerate, as shown in Figure 3.14. These correspond to the coupled spins both aligned parallel to B_0 ($|\alpha\alpha\rangle$), one aligned with B_0 and the other against ($|\alpha\beta\rangle$ and $|\beta\alpha\rangle$), and both aligned anti-parallel to B_0 ($|\beta\beta\rangle$).

The dotted lines in Figure 3.14 represent coherent states. The order of a quantum coherence is defined as the difference between the z-component angular momentum quantum number of the connected eigenstates states. For non-coupled 1/2-spins, only single quantum coherence is observed because the total difference in angular momentum quantum number of the connected eigenstates is $\Delta M = \pm 1$. However, for pairs of coupled 1/2-spins, quantum coherences can be single ($\Delta M = \pm 1$, grey lines), double ($\Delta M = \pm 2$, blue line), or zero ($\Delta M = 0$, red line). The goal of double quantum NMR experiments is to excite coupled spin pairs to these double coherent states. Double and zero quantum coherences cannot be directly observed, so various methods are used to convert them to single coherent states that

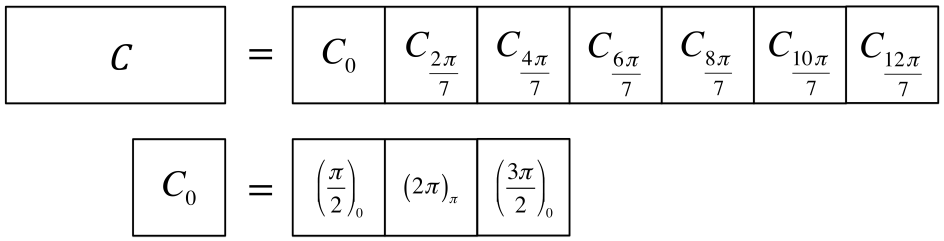

Figure 3.15: The POST-C7 pulse sequence used to excited double quantum coherences in dipolar coupled spins.

are observed as transverse magnetization in the NMR experiment (see chapter 4 of reference [144]).

The DQ-DRENAR Method

There are several pulse sequences designed to excited double quantum coherences, including the C_7 sequences [144]. Magic-angle spinning has the effect of reducing or eliminating dipolar coupling. Levitt et al. report the POST-C7 sequence (Figure 3.15). Application of the POST-C7 sequence results in the reintroduction of dipolar coupling to the spin Hamiltonian describing a two spin-1/2 coupled system. With the reintroduction of dipolar coupling, excitation of double quantum coherences may occur.

Typical double quantum coherence methods involve the conversion of double quantum coherences to single quantum coherences that are measured and analyzed. The DQ-DRENAR approach is simpler.

Unlike the cross-polarization and REDOR methods, the DQ-DRENAR experiment is a single-resonance method, meaning that only a single nucleus is irradiated with radiofrequency and observed. However, like REDOR, the DQ-DRENAR method involves analysis of the difference in signal amplitude for two different experiments.

Figure 3.16 shows the pulse sequence of the Double-Quantum-based Dipolar Recoupling effects Nuclear Alignment Reduction (DQ-DRENAR) method. In each experiment, two successive POST-C7 sequences are applied to the observed spin. The pulse sequences are rotor-synchronized such that each POST-C7 block occurs within two rotor periods. The free-induction decay of the observed spin is collected at a series of 'signal evolution times', NT_r, where N is the number of rotor cycles (always a multiple of four) and T_r is the rotor period, or approximately 0.143 ms for a spinning rate of 7 kHz.

In the S' experiment (Figure 3.16, lower panel), the POST-C7 blocks are applied in phase. This results in the reintroduction of dipolar coupling to the spin system, which in turn provides for the excitation of double quantum coherences. This excitation results in fewer single-quantum coherences, which manifests as a reduction in signal intensity. In a second control experiment, S_0 (Figure 3.16, top panel), the second POST-C7 block is applied out of phase by 90 ° from the first block, which prevents dipolar recoupling but subjects the spin system to the same spin relaxation environment as the S' experiment.

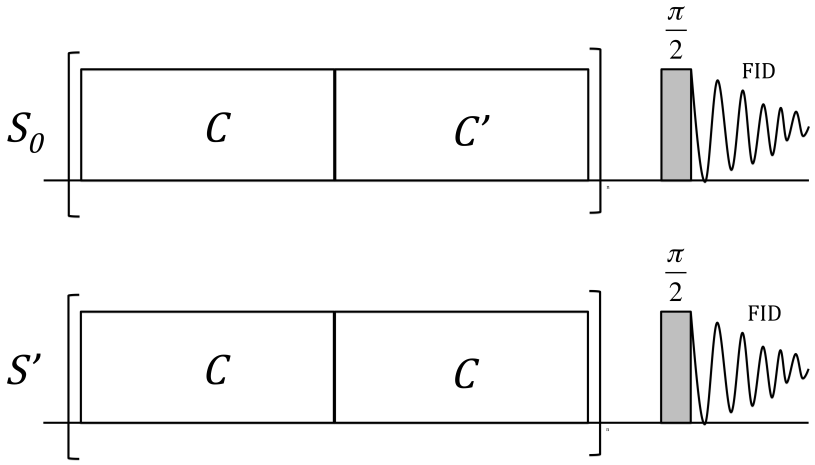

Figure 3.16: Pulse sequence for DQ-DRENAR technique to recouple homonuclear spins. The diagram shows the non-recoupled control experiment S_0 (top) and the recoupled DRENAR experiment S' (middle). The C blocks in each experiment are the POST-C7 blocks, shown in Figure 3.15.

The simplicity of the DQ-DRENAR approach is that rather than convert the double-quantum coherence excitation to observable single-quantum excitations, the decrease in signal amplitude of the single-quantum excitations is directly observed. A larger decrease corresponds to stronger coupling between spins. Ren and Eckert show that this approach is valid for a multiple spin system with a distribution of dipolar coupling constants [164, 165]. For short signal evolution times, such that $(S' - S_0)/S_0 < 0.5$, the relationship between the difference in signal amplitudes and the sum of the pairwise dipolar coupling constants can be well approximated by:

$$\frac{S_0 - S'}{S_0} = \frac{0.86\pi^2}{15} \cdot b_{jk}^2 \cdot (NT_r)^2 \tag{3.20}$$

where b_{jk}^2 is the dipolar coupling constant for two spins j and k. For a multi-spin system, b_{jk} is replaced by the sum of the squares of all spin-pair dipolar coupling constants:

$$\frac{S_0 - S'}{S_0} = \frac{0.86\pi^2}{15} \cdot \sum_{j<k} b_{jk}^2 \cdot (NT_r)^2 \tag{3.21}$$

Therefore, for short signal evolution times, $\Delta S/S_0$ can be plotted as a function of NT_r and fitted with a parabola to extract the sum of pairwise dipolar coupling constants. By combining Equations 3.5 and 3.21, $\sum_{j<k} b_{jk}^2$ can be used to calculate the average distance between coupled spins:

$$\sum_{j<k} b_{jk}^2 = h^2\gamma^4 \left(\frac{\mu_0}{4\pi}\right)^2 \sum_{j<k} \frac{1}{r_{jk}^6} \tag{3.22}$$

In summary, measurement of the $\sum_{j<k} b_{jk}^2$ value for an amorphous spin system allows one to calculate the distance between spins if the number of coupled spins is assumed, or the number of coupled spins if the average distance is assumed. As discussed in Chapter 2, amorphous silica gel materials have no long-range order, but possess local order similar to that of β-cristobalite, which has known spacing between silanol groups. Therefore, the DQ-DRENAR method provides a way to approximate and compare the density of the organic functional group layers grafted to silica surfaces.

Probing the strength of heteronuclear and homonuclear dipolar coupling using NMR spectroscopic methods has been shown to be a powerful tool for the structural analysis of functionalized silica surfaces. For example, Pan et al. [71] synthesized and characterized phosphonate-modified SBA-15 silica by the co-condensation of diethylphosphatoethyl triethoxysilane and tetraethylorthosilicate. Despite the different synthetic method, the resulting material was identical to that used for the experimental work presented in Chapter 4. The ^{31}P NMR spectrum contained a single resonance at 33 ppm with respect to H_3PO_4. Conversion to phosphonic acid was achieved via template removal with H_2SO_4 followed by refluxing in concentrated HCl. Upon hydrolysis of the ligand to phosphonic acid, a second resonance at 22 ppm appeared. The authors used double quantum techniques to probe ^{31}P-^{31}P distances in order to rule out the possibility that the second species was due to P-O-P structural motifs that would result from the formation of polyphosphates. They combined density functional theory calculations with ^{29}Si$\{^{31}$P$\}$ REDOR studies that probed ^{29}Si-^{31}P dipolar coupling interactions to show that the second species was due to phosphinic acid moieties hydrogen-bonded to Q^3 surface silanols. Their analysis implies that phosphonic acid is hydrogen-bonded to the surface through its hydrogen-donor hydrogens, O=P(O**H**)$_2$.

A subsequent study by Bibent et al. examines the same material using ^{1}H-^{1}H spin diffusion studies combined with ^{31}P-^{31}P double quantum experiments and a ^{31}P-^{1}H-^{1}H-^{31}P correlation pulse sequence [72]. They use a ^{31}P-^{1}H-^{1}H-^{31}P correlation sequence to argue that the species giving rise to the 22 ppm resonance is from phosphonic acid groups hydrogen bonded to each other, and not to surface silanols.

Solid-state NMR methods probing the dipolar coupling interactions between spin populations provides valuable structural characterization for locally-ordered amorphous silica surfaces. The work summarized above motivated the approach taken in the experimental work described in the next two chapters. This approach combines macroscopic batch sorption studies with spectroscopic NMR methods to investigate the mechanism and limitations of heavy metal sorption on functionalized silica surfaces.

Chapter 4

Interactions between U(VI) and Diethylphosphonate Functionalized Silica

Reproduced in part from reference [166] with permission from the Royal Society of Chemistry.

4.1 Introduction

Diethylphosphatoethyl triethoxysilane (DPTS)-functionalized mesoporous silica has been shown to effectively extract U(VI) from nitric acid solutions above pH 2, with the extent of extraction increasing with increasing pH [62–69]. Previous studies have primarily relied on macroscopic batch and column experiments that probe the solution phase for information about how U(VI) interacts with the phosphonate-modified surface. These studies supply hypotheses regarding U(VI) extraction, but do not directly probe the interaction between U(VI) and the solid surface. Additionally, this work and previous work has shown that the presence of phosphonate ligands inhibits uptake of U(VI) from pH 4 nitric acid compared to non-functionalized silica [65]. Therefore, the precise role of the phosphonate ligand in U(VI) extraction is uncertain. The extraction of U(VI) by non-functionalized silica via ion exchange with silanols is well-established [78, 124, 125, 127, 128, 167, 168]. However, the participation of exposed silanols in extraction of U(VI) has not been addressed for DPTS-modified silica substrates.

The work presented in this chapter combines macroscopic, solution phase experiments with spectroscopic studies on solid phase. Solid-state nuclear magnetic resonance (NMR) spectroscopy was used to evaluate the stability of the material, to characterize the extent and nature of ligand grafting during functionalization, and to gain insight about the mechanism of U(VI) extraction. Solid-state NMR provides a uniquely powerful tool to study the complexation of metal cations to organically-modified silica surfaces [73, 169]. The ^{1}H, ^{13}C,

^{29}Si, and ^{31}P nuclei are all directly observable by NMR allowing us to probe the influence of U(VI) on the silica surface and the phosphonate ligand.

In addition to verifying ligand structure, NMR spectroscopy provides avenues for measuring the dipolar spin coupling interaction between nuclei. For example, NMR spectroscopy has revealed hydrogen bonding between grafted phosphonic acid ligands and with surface silanols [71, 72]. These techniques have not previously been used to investigate the bonding interactions between U(VI) and phosphonate-modified silica surface. Using cross-polarization (CP), the influence of U(VI) on ^{1}H$-^{31}$P dipolar coupling in various samples is investigated. Combined with measurements of macroscopic extraction properties, NMR studies give a more complete analysis of the structure of the functional layer formed during ligand grafting. In solution, free phosphate ligands complex U(VI) in a ligand-to-metal ratio of 2:1 or 3:1, in which the phosphate ligands bind through the electronegative phosphoryl (O=P) group to the $UO_2{}^{2+}$ equatorial positions, the remainder of which are occupied by nitrate ions and water molecules [170, 171]. However, once the ligand is anchored to the surface, the movement of the ligands is restricted, which may limit the extraction of U(VI). Solid-state NMR techniques are used to measure average ^{31}P$-^{31}$P dipolar coupling, which correlates with the phosphorus interatomic distances. As a simple monodentate ligand, DPTS is ideal for testing this approach. This work demonstrates that solid-state NMR is useful for more accurately understanding the functionalization and extraction processes. The majority of the work presented in this chapter examines the extraction of U(VI) by DPTS-SBA. Experiments measuring the sorption of Eu(III) and Pu(VI) were carried out in select conditions. However, for most conditions, significant sorption of only U(VI) occurred.

4.2 Synthesis and Functionalization of SBA-15 Microspheres

SBA-15 microspheres were synthesized using the protocol described by Katiyar et al. [110]. The synthetic method follows the typical hydrothermal synthesis of SBA-15, except that it contains both an aging step at 80 °C followed by hydrothermal treatment at 120 °C. In this chapter, pristine, non-functionalized SBA-15 is referred to as "SBA."

The SBA microspheres were functionalized by adapting the surface polymerization method described by Sander [131]. In this method, silica is first hydrated with stoichiometric amounts of water by adding it directly to a silica-toluene slurry. The ethoxysilane ligand is then added, and the reaction refluxed for 6 hours, followed by distillation to remove excess water and ethanol. A detailed description of the synthetic procedures used is found in Chapter 6. Functionalized silica is referred to as DPTS-SBA.

Table 4.1: Nitrogen adsorption results for SBA and DPTS-SBA

Material	BET Surface Area (m^2 g^{-1})	BJH Pore Volume (cm^3 g^{-1})	Average Pore Diameter (nm)
Non-functionalized SBA	816	1.08	7.38
DPTS-SBA	426	0.49	6.27

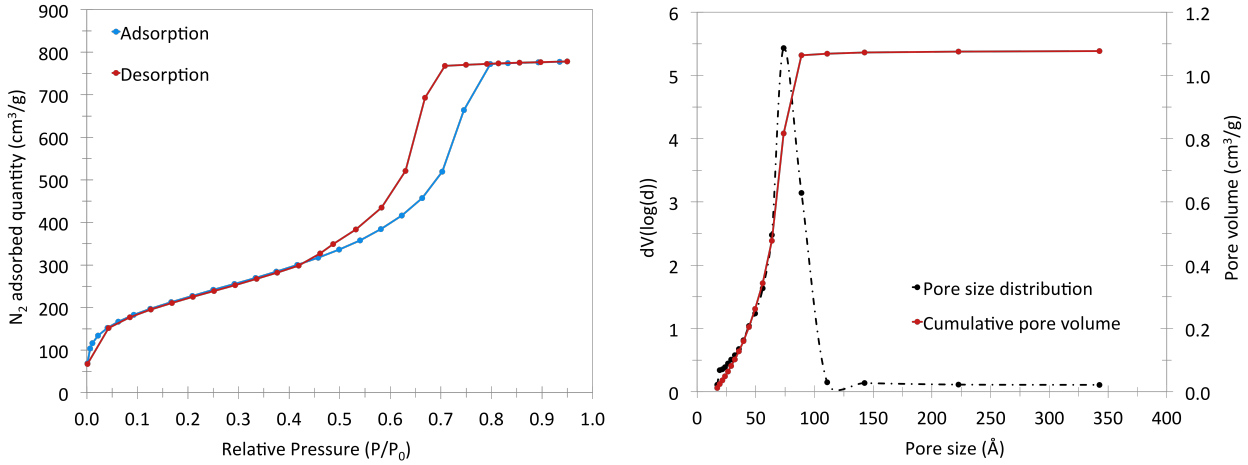

Figure 4.1: (a) N_2 adsorption isotherm for non-functionalized SBA, demonstrating a type IV isotherm with an H_1 hysteresis loop typical for ordered, cylindrical pore structures. (b) Pore size distribution and cumulative pore volume for non-functionalized SBA.

4.3 Material Characterization

N_2 Adsorption Isotherms

The results from the nitrogen adsorption measurements for SBA and DPTS-SBA are summarized in Table 4.1. The nitrogen adsorption isotherm for the unmodified silica demonstrates a Type IV isotherm with an H_1 hysteresis loop typically found for ordered, cylindrical porous structures (Figures 4.1) [92]. This feature is retained for the organically modified silica. Upon grafting of the DPTS, the BET surface area and average pore diameter decrease. This change is consistent with the deposition of not more than one monolayer of the phosphonate ligand onto the silica walls and has been observed in similar materials [172].

^{13}C, ^{29}Si, and ^{31}P NMR

Solid-state NMR measurements were conducted to assess the stability of the DTPS ligand to the acid conditions used for U(VI) extraction. Acid-washed samples were prepared by contacting DPTS-SBA with 3 M $NaNO_3$ adjusted to pH 3 or 4 for approximately 40 hours. These samples are denoted ac-DPTS-SBA in this chapter.

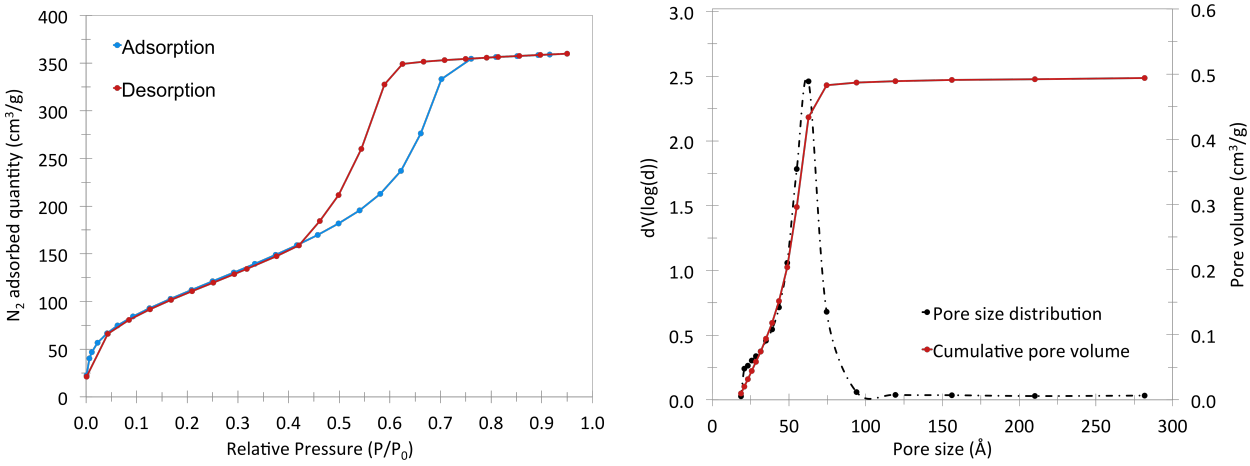

Figure 4.2: (a) N_2 adsorption isotherm for DPTS-functionalized SBA, which also demonstrates a type IV isotherm with an H_1 hysteresis loop. (b) Pore size distribution and cumulative pore volume for DPTS-functionalized SBA.

Figure 4.3 shows the $^{13}C\{^1H\}$ CP/MAS NMR spectra of pristine DPTS-SBA and ac-DPTS-SBA-pH 3.0. Spectral resonances are assigned as follows: δ_C (ppm) = 2.2 (Si–**C**H_2, 12.5 (**C**H_3–CH_2–O–P=O), 15.6 (Si–CH_2–**C**H_2–P=O), and 58.9 (CH_3–**C**H_2–O–P=O).

Any unreacted ethoxysilane groups remaining would give rise to resonances overlapping with those at 12.5 and 58.9 ppm. Individual CP spectra cannot be interpreted quantitatively, but useful qualitative assessments can be made when spectra are collected under identical acquisition conditions. The retention of all expected ^{13}C resonances after 24 hours of contact with pH 3 nitric acid verifies the integrity of the functional layer under the conditions used for this work. Minor changes in the relative peak intensities between the pristine and the acid-contacted samples may be attributed to the adsorption of water onto the surface of the silica. Further comparison of the $^{31}P\{^1H\}$ CP/MAS NMR spectra shows a single resonance at 34.2 ppm for both samples (Figure 4.4).

Previous work on this ligand has shown a -1 ppm shift in the ^{31}P resonance upon hydrolysis of the phosphoryl esters, as well as the disappearance of ^{13}C resonances assigned to these groups. [62, 71, 72] As neither of these effects was observed for the ac-DPTS-SBA-pH 3.0 sample, it is unlikely that a significant number of phosphonate ligands was hydrolyzed to phosphonic acid ligands upon contact with pH 3 nitric acid. $^{29}Si\{^1H\}$ CP/MAS experiments of the DPTS-SBA and ac-DPTS-SBA-pH 3.0 were performed to probe the overall stability of the surface to acid treatment (Figure 4.5). The pristine, non-modified silica contains three resonances between -90 and -110 ppm, depending on the extent of cross-linking between TEOS monomers. Common nomenclature denotes these as Q^n for $SiO_n(OH)_{4-n}$, where n = 2, 3, or 4 [140]. In Figure 4.5, these resonances appear at -109.5 ppm (Q^4), -100.8 ppm (Q^3), and -90.7 ppm (Q^2) for both samples. Upon condensation of alkoxysilanes at the silica surface, a second group of three resonances appear between -50 and -70 ppm. These peaks are denoted T^m for $RSiO_m(OX)_{3-m}$, where $m = 1, 2, or 3$, R is the alkyl chain of the DPTS,

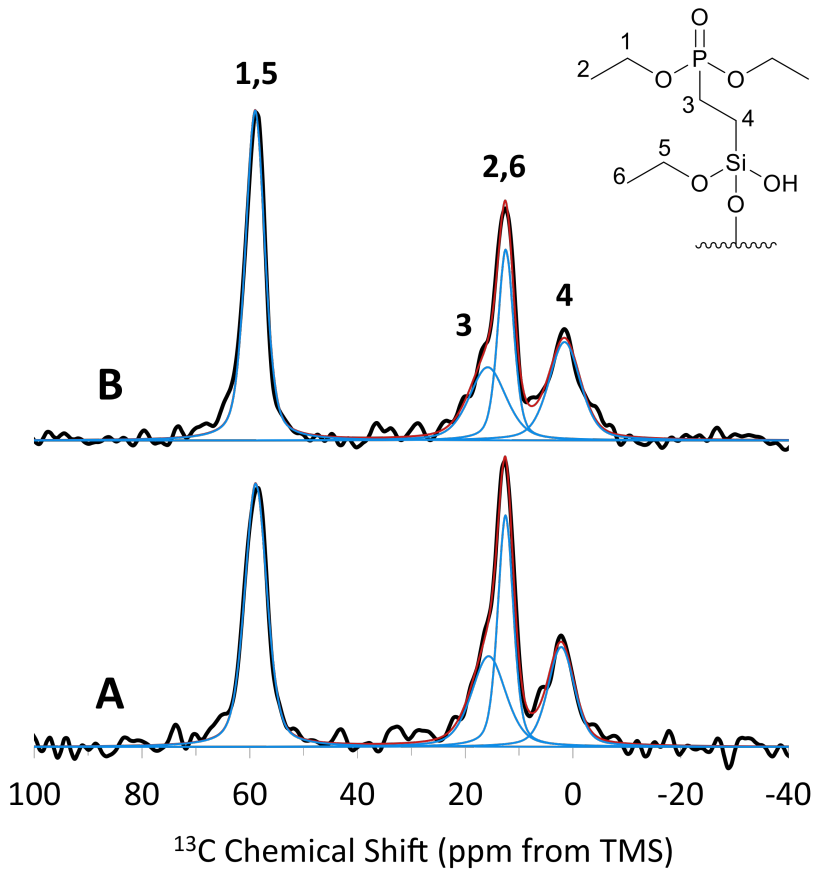

Figure 4.3: $^{13}C\{^{1}H\}$ CP/MAS NMR spectra of pristine DPTS-SBA (bottom) and ac-DPTS-SBA-pH 3.0 (top). Spectra were normalized to the peak at 2.2 ppm. The black line represents the experimental spectrum; the solid red and blue lines represent the spectral fit and the peak deconvolution, respectively.

and $X = H$ or Et. We interpret T^1 peaks as representing ligand monomers, T^2 as ligand dimers or polymer chain terminals, and T^3 as ligands central to a more extended polymer chain. In Figure 4.5, these peaks occur at -67.6 ppm (T^3), -58.7 ppm (T^2), and -51.3 ppm (T^1) for both samples [10]. The presence of the T resonances in both spectra demonstrates that DPTS was successfully grafted onto the silica surface, and that contact with pH 3 nitric acid does not result in total cleavage of ligand from the surface at the Si−C bond.

While there is a decrease in T peak intensity for the acid-contacted sample compared to the pristine sample, peak intensity cannot be used to quantify the absolute amount of each species present, as these spectra were collected using cross polarization. Therefore the decrease in T intensity for ac-DPTS-SBA-pH 3.0 compared to DPTS-SBA may be in part explained by a change in cross-polarization kinetics caused by adsorption of water, as opposed to an overall loss of ligand from the surface [150]. However, the relative ratios of the T peaks can be used to assess changes in population because spectra were collected under identical conditions. Upon contact with pH 3 nitric acid, the $T^3 : T^2$ ratio decreased from

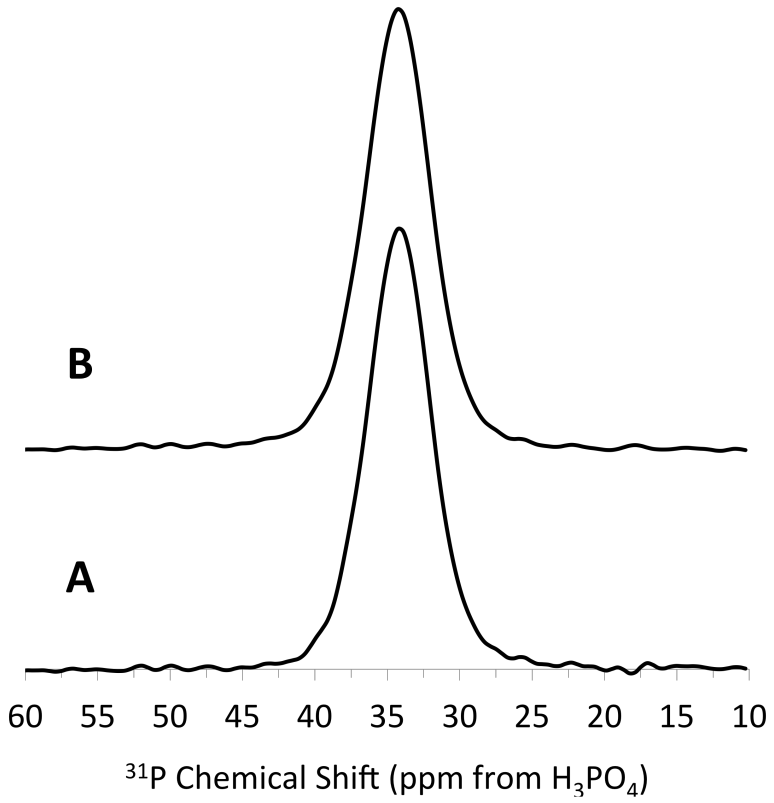

Figure 4.4: $^{31}P\{^{1}H\}$ CP/MAS NMR spectra of DPTS-SBA (A) and ac-DPTS-SBA-pH 3.0 (B). Spectra were normalized to the chemical shift at 34.2 ppm.

0.52 to 0.41, and the T^1 : T^2 ratio decreased from 0.41 to 0.26. This is consistent with previous work showing that T1 species are more readily hydrolyzed from the surface than ligands that are part of a more extended polymer chain [73].

The number of phosphonate ligands per gram of material was quantified using triphenylphosphine (TPP) as an internal standard for single pulse ^{31}P NMR measurements. As the chemical shift of triphenylphosphine (δ_P = -6 ppm, relative to H_3PO_4) is well out of range of that of the phosphonate ligand (δ_P = 34 ppm, relative to H_3PO_4), TPP makes an ideal internal standard for this material. Figure 4.6 shows the single pulse ^{31}P NMR spectrum of pristine-DPTS and ac-DPTS-SBA-pH 3 mixed with a TPP internal standard. Using the mass of triphenylphosphine loaded into the rotor and the relative integrated peak areas above, the number of moles of ligand per gram of material were calculated. A ligand loading of 2.43 $\pm$ 0.02 mmol ligand/g solid was determined for pristine DPTS-SBA and at least 1.78 mmol/g for ac-DPTS-SBA-pH 3.0. The latter number must be regarded as a minimum because there was water adsorbed to the silica surface that added unknown mass to the sample, despite rinsing the sample with acetone and air-drying for several days.

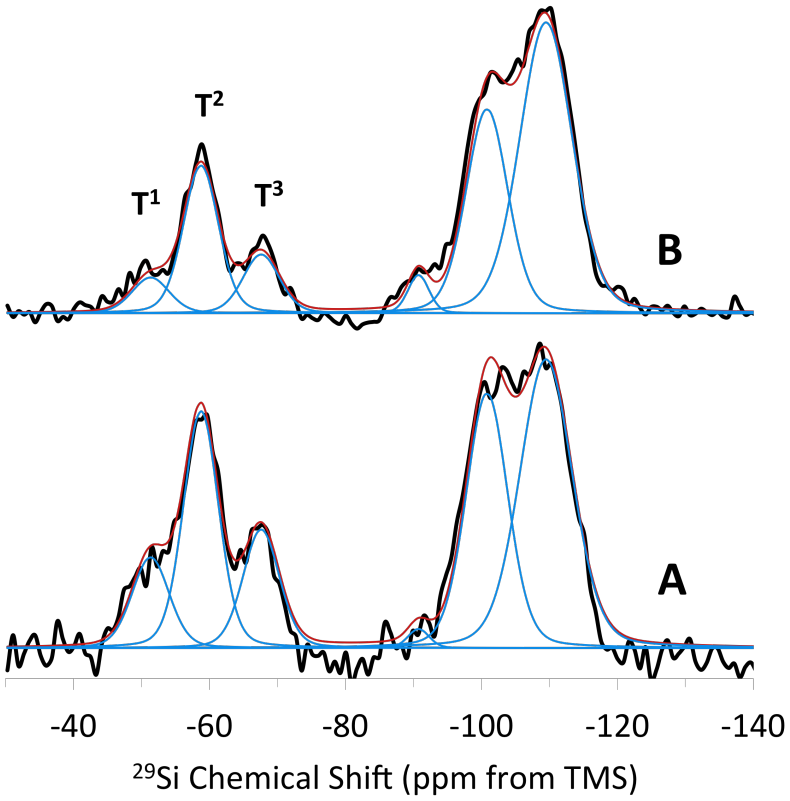

Figure 4.5: ^{29}Si{^{1}H} CP/MAS NMR spectra for pristine DPTS-SBA (A) and ac-DPTS-SBA-pH 3 (B). Spectra were collected with a pulse delay of 2 s, a contact time of 3 ms, and a $\pi/2$ pulse of 8 μs. Upon contact with pH 3 aqueous solution, the $T^3 : T^2$ ratio decreases from 0.52 to 0.41, while the $T^1 : T^2$ ratio decreases from 0.41 to 0.26.

4.4 Batch Contact Results in Nitrate Media

Figure 4.7 shows the pH dependence of sorption of U(VI) from nitric acid solutions by SBA and DPTS-SBA for two different concentrations of $NaNO_3$. Significant sorption of U(VI) by SBA and DPTS-SBA was only observed above pH 2 and increased with increasing pH, consistent with previous studies. [62–69] Increasing the concentration of $NaNO_3$ in solution from 0.1 M to 3 M caused a significant increase in U(VI) uptake in the pH range of 2 to 4. At pH 2, DPTS-SBA sorbed 10 ± 5% U(VI) from 0.1 M $NaNO_3$ and 31 ± 4% U(VI) from 3 M $NaNO_3$. The difference at pH 3 is even more pronounced for DPTS-SBA, which sorbed 28 ± 4% U(VI) from 0.1 M $NaNO_3$ and 70 ± 5% U(VI) from 3 M $NaNO_3$. Non-functionalized SBA also shows a difference in uptake depending on salt concentration. SBA sorbed no measurable U(VI) from 0.1 M $NaNO_3$ solutions and 24 ± 4% U(VI) from 3 M $NaNO_3$ solutions at pH 3. At pH 4, the difference in uptake was similar; SBA sorbed 65 ± 5% and 92 ± 5% U(VI) from 0.1 M and 3 M $NaNO_3$, respectively. At pH 5, both SBA and DPTS-SBA sorbed greater than 95 ± 6% of U(VI) from both concentrations of $NaNO_3$.

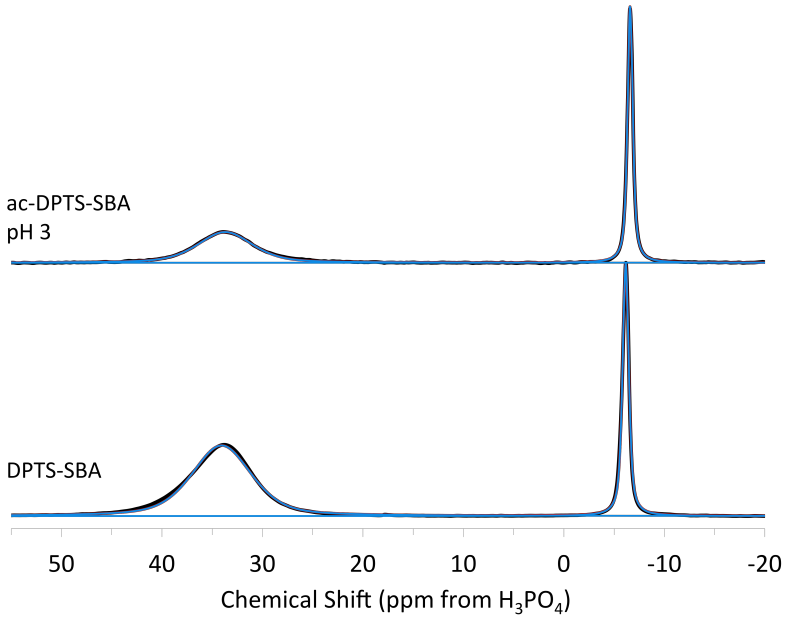

Figure 4.6: Single pulse ^{31}P spectrum of DPTS-SBA (top) and ac-DPTS-SBA-pH 3, both with a triphenylphosphine internal standard. These spectrum was collected with a delay time of 30s.

4.5 Batch Contact Results with U(VI), Pu(VI), and Eu(III)

Batch Contact Experiments with U(VI) and Pu(VI) in Perchlorate Media

Batch contact experiments with U(VI) and Pu(VI) in 3 M $NaClO_4$ media were conducted. An increase in sorption of U(VI) was observed with an increase in the $NaNO_3$ concentration from 0.1 M to 3 M in the pH range 2-4. One possible explanation is increased nitrate complexation of the uranyl ion. At a concentration of 0.1 M $NaNO_3$, uranyl is expected to exist primarily as UO_2^{+2}, whereas at 3 M $NaNO_3$ it is distributed amongst UO_2^{+2}, $UO_2(NO_3)^+$, and $UO_2(NO_3)_2$ species [173]. If phosphonate more readily complexes with neutral species, this could explain increased sorption of U(VI) from 3 M $NaNO_3$ solutions.

This hypothesis was tested by repeating batch contact experiments in 3 M $NaClO_4$ media. The ClO_4^- counterion is non-complexing relative to the NO_3^- counterion. Thus, batch experiments in 3 M $NaClO_4$ allow contact with non-complexed uranyl while controlling for increased ionic strength. Figure 4.8 shows sorption of U(VI) from 3 M $NaClO_4$ adjusted to pH 1-4 by both non-functionalized SBA and DPTS-SBA. DPTS-SBA demonstrates increased sorption of U(VI) at pH 1 and 2 from 3 M $NaClO_4$ compared to U(VI) sorption from 3 M $NaNO_3$. In 3 M $NaClO_4$ media, DPTS-SBA sorbed 29 $\pm$ 4% and 60 $\pm$ 4% from pH 1 and

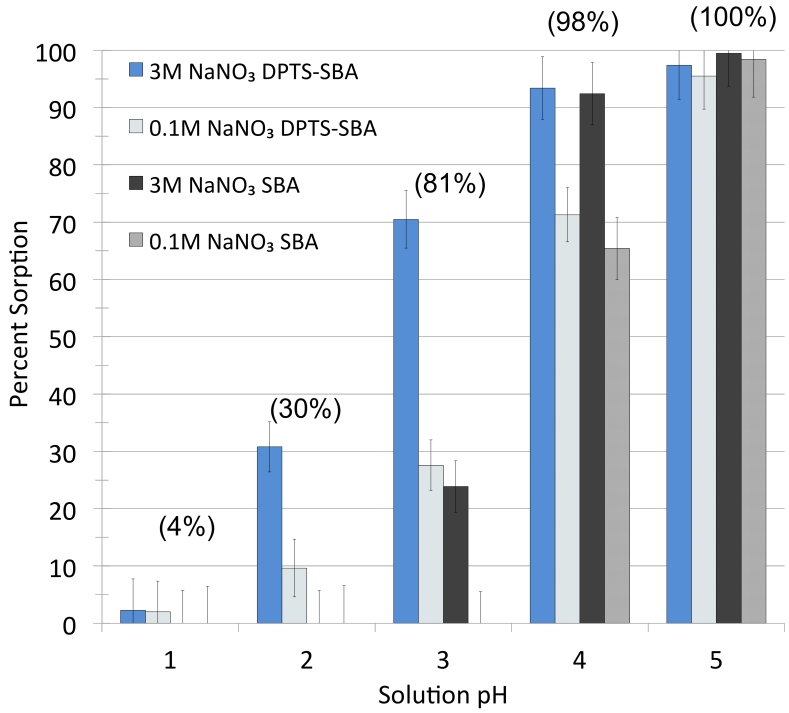

Figure 4.7: Percent sorption of U(VI) from 3 M $NaNO_3$ or 0.1 M $NaNO_3$ as a function of pH for DPTS-SBA (blue) and SBA (dark grey). Data points shown represent the percent sorption after 24 hours of contact. [U(VI)] = 20 μM for all samples. Numbers in parentheses represent an estimate of the percentage of DPTS ligands that are deprotonated, based on a pKa of 2.37 for dimethyl methylphosphonate.

pH 2 solutions, respectively. In contrast, DPTS-SBA sorbed 2 $\pm$ 5% and 31 $\pm$ 4% of U(VI) from 3 M $NaNO_3$ solutions adjusted to pH 1 and 2, respectively.

Therefore, inner-sphere coordination of the nitrate anion does not result in greater complexation of uranyl to the silica surface. Instead, these results suggest that increased ionic strength enhances sorption through a different mechanism, perhaps by "salting out" the cation from solution, as has been observed in solvent extraction. This would be an interesting and novel effect observed for these types of materials. More research should be conducted on the "salting out" effect for solid-phase extraction materials, as it may significantly alter their application as chromatographic resins.

Additionally, more work is needed to evaluate the effect of the $NaClO_4^-$ counterion at a higher pH range. As Figure 4.8 shows, significant loss of U(VI) from solution occurred from 3 M $NaClO_4$ solutions at pH 3, 4, and 5 (not shown) with no SBA or DPTS-SBA present. Loss of U(VI) from the "no solid blank" control samples increased with increasing pH, and was likely due to the formation of insoluble uranyl hydroxide compounds that separated from the bulk of solution upon centrifugation or adhered to the polypropylene tube walls. As the sorption of U(VI) observed at pH 3 and 4 by DPTS-SBA and SBA is likely a combination of sorption to the mesoporous silica and precipitation or adsorption to tube walls, no direct comparison may be made with the batch contact experiments conducted at 3 M $NaNO_3$.

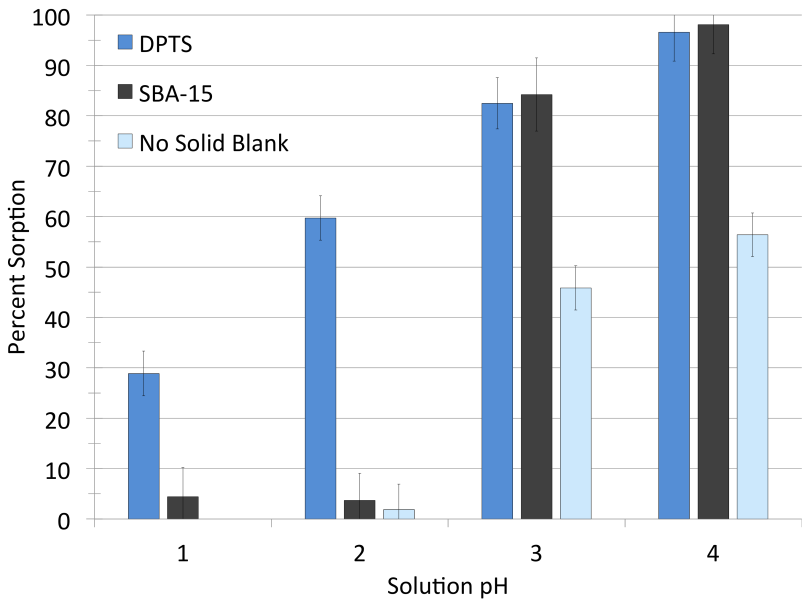

Figure 4.8: Sorption of U(VI) on DPTS-SBA and SBA from 3 M NaClO4 after approximately 24 hours contact time. Initial total uranium concentration was 20 μM with a solid to liquid ratio of 1 mg mL^{-1}.

It should be noted that efforts were made to eliminate or minimize loss of U(VI) from 3 M $NaClO_4$ solutions, but the results were irreproducible. It was observed that use of $NaClO_4$ from two different suppliers resulted in significantly different degrees of loss of U(VI) from the control samples (Figure 4.9. No loss of U(VI) was observed in control samples where no additional $NaClO_4$ had been added, which suggested that trace impurities in the salt may be increasing precipitation of an unknown uranyl compound. To minimize the effect of potential impurities present in the salt, 3 M $NaClO_4$ was made by combining high purity (99.99%) NaOH and $HClO_4$. Duplicate trials using this solution resulted in significantly different percent loss of U(VI) from solution as well (not shown). The cause of loss of U(VI) from solution is unknown and is the subject of further investigation. As no loss of U(VI) was observed in the control samples for the $NaNO_3$ samples, most of the subsequent batch contact work and all of the NMR sample preparation was conducted in nitric acid media.

The sorption of Pu(VI) by non-functionalized SBA and DPTS-SBA from 3 M $NaClO_4$ was measured for pH 1, 3, and 5 (Figure 4.10). No significant quantity of Pu(VI) was sorbed at pH 1 or 3 for either material. At pH 5, DPTS sorbed 31 $\pm$ 4% and SBA sorbed 52 $\pm$ 4% of the initial Pu(VI) present in solution. However, under these conditions, 18 $\pm$ 4% of Pu(VI) was lost from solution in the no solid control sample. Given that DPTS-SBA demonstrated significantly higher sorption of U(VI) from 3 M $NaClO_4$ solutions at pH 1 and 2, and considering that DPTS-SBA sorbed 97 $\pm$ 6% of U(VI) from 3 M $NaNO_3$ solutions at pH 5, uranyl appears to have a significantly higher affinity for both the DPTS-SBA and non-functionalized silica than plutonyl in the pH range 1-5. Development of DPTS-SBA as a chromatographic resin for the separation of U(VI) and Pu(VI) would require further studies

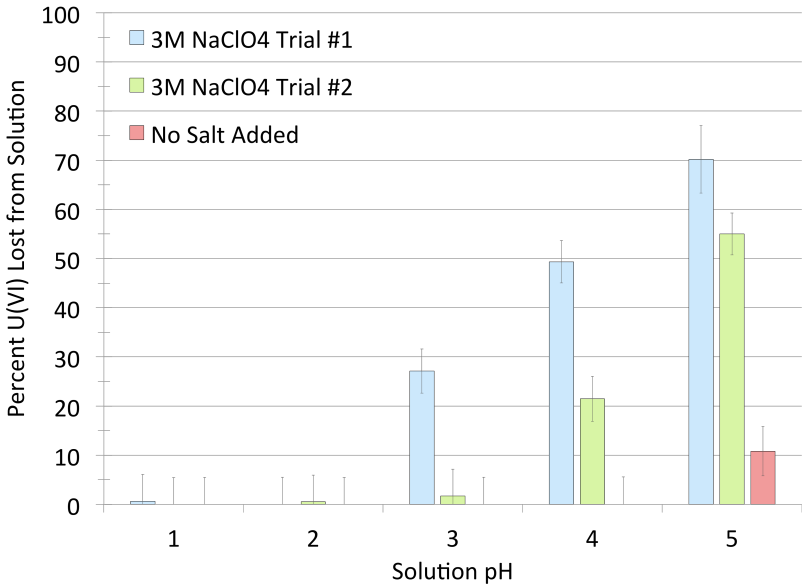

Figure 4.9: Percent U(VI) lost from HClO4 media containing 3 M NaClO4 or no additional salt after 24 hours. Initial total uranium concentration was 20 μM.

assessing how the competition of the actinyl cations affects their sorption under a range of conditions.

Batch Contact Experiments with Eu(III) in Nitrate Media

The sorption of Eu(III) by non-functionalized SBA and DPTS-SBA from 0.1 M $NaNO_3$ was measured for pH 2-6 (Figure 4.11). In general, the sorption of Eu(III) by non-functionalized SBA and DPTS-SBA increases with increasing pH. However, sorption of Eu(III) is lower compared to the sorption of U(VI) under the same solution conditions. No measurable amount of Eu(III) sorbed to non-functionalized SBA until pH 6. In contrast, DPTS sorbed greater than 65% of U(VI) present in solution at pH 4, and greater than 98% at pH 5. DPTS-SBA sorbed 13 $\pm$ 4% and 17 $\pm$ 4% of Eu(III) from 0.1 M $NaNO_3$ adjusted to pH 4 and 5, respectively, but 71 $\pm$ 5% and 95 $\pm$ 6% of U(VI) under similar conditions. Additionally, a larger difference in sorption between the DPTS-functionalized and non-functionalized SBA is observed for U(VI) than for Eu(III). The clear differences in sorption of U(VI) and Eu(III) suggest that DPTS-SBA could be used to selectively extract U(VI) from a mixture of U(VI) and trivalent cations, though more work is needed to quantify the influence of competing cations on the sorption of U(VI) from solution.

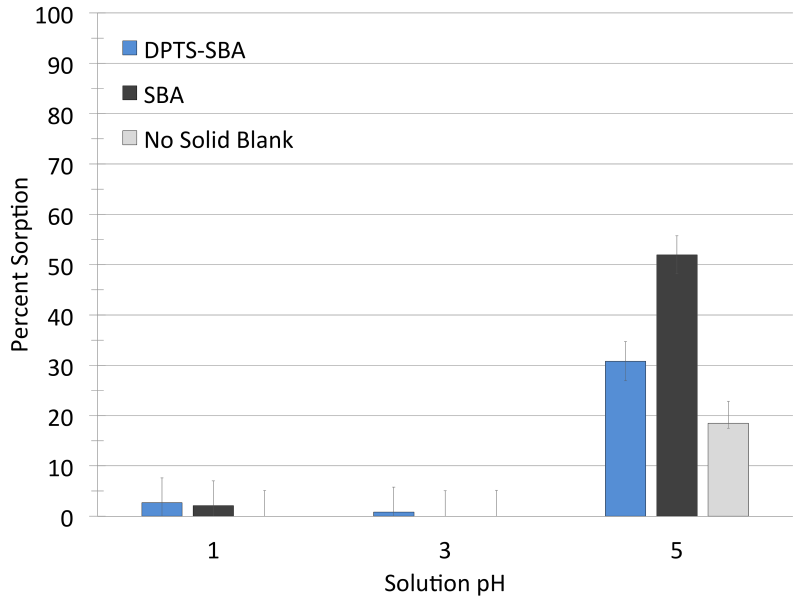

Figure 4.10: Sorption of Pu(VI) on DPTS-SBA and SBA from 3 M NaClO4 at pH 1, 3, and 5 after approximately 24 hours contact time. Initial total plutonium concentration was 20 μM with a solid to liquid ratio of 1 mg mL^{-1}.

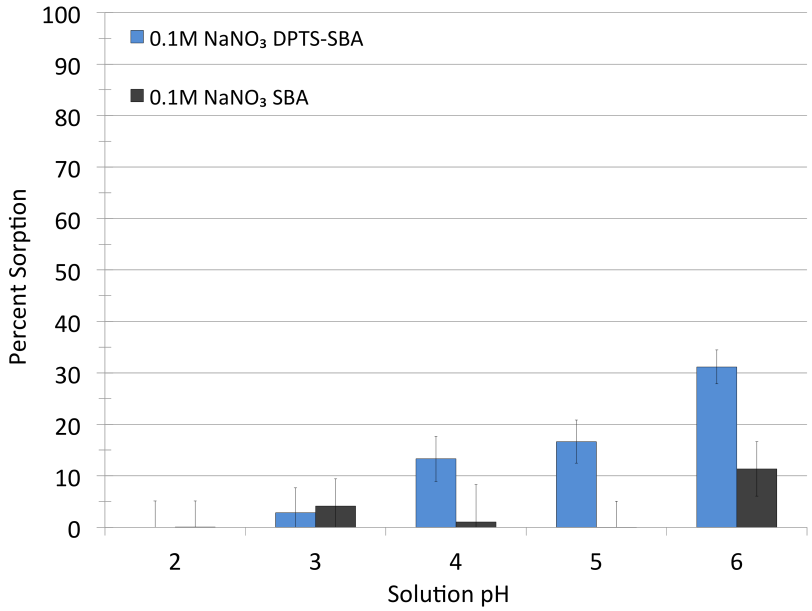

Figure 4.11: Sorption of Eu(III) by DPTS-SBA and SBA from 0.1 M $NaNO_3$ after approximately 30 hours contact time. Initial total europium concentration was 20 μM with a solid to liquid ratio of 1 mg mL^{-1}.

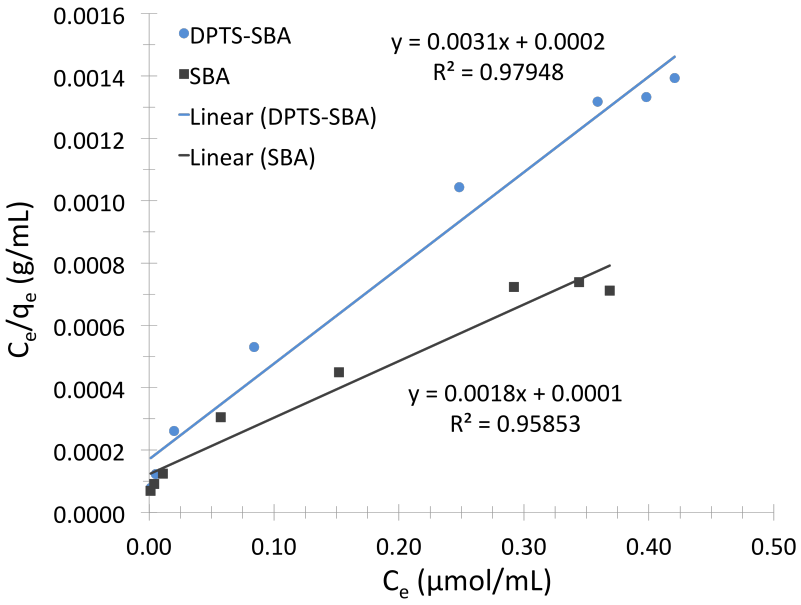

Figure 4.12: Linearized Langmuir U(VI) sorption isotherm fit for DPTS-SBA and SBA. Solution conditions: 3 M $NaNO_3$ adjusted to pH 4.

Table 4.2: U(VI) isotherm fit parameters for SBA and DPTS-SBA

Langmuir Adsorption Model			Freundlich Adsorption Model		
	SBA	DPTS-SBA		SBA	DPTS-SBA
q_m (μmol g^{-1})	551 ± 47	326 ± 19	K_F (μmol$^{(1-1/n)}$ mL$^{1/n}$ g^{-1})	899 ± 74	472 ± 26
K_{eq} (mL μmol^{-1})	15 ± 4	18 ± 5	n	1.80 ± 0.07	2.09 ± 0.07
R^2	0.9585	0.9795	R^2	0.9905	0.9937

U(VI) Sorption Isotherm Results

The Langmuir isotherm sorption capacity of DPTS-SBA under various conditions has been reported [64, 65, 68]. We repeat them here to measure the U(VI) sorption capacity of DPTS-SBA from 3 M $NaNO_3$ solutions adjusted to pH 4. The U(VI) isotherm data were fit to both Langmuir and Freundlich adsorption models. Figures 4.12 and 4.13 show the linearized fit to the isotherm data for pristine DPTS-SBA and non-functionalized SBA. Table 4.2 shows the parameters used for the fits. Consistent with previous studies [65], we found that the presence of the ligands inhibits the uptake of U(VI) at pH 4 compared to SBA. The data yielded a Langmuir maximum U(VI) sorption capacity, q_m, of 551 ± 47 μmol/g for SBA and 326 ± 19 μmol/g for DPTS-SBA. The calculated equilibrium constants, K_{eq}, for SBA and DPTS-SBA were the same within the uncertainty of the Langmuir fit.

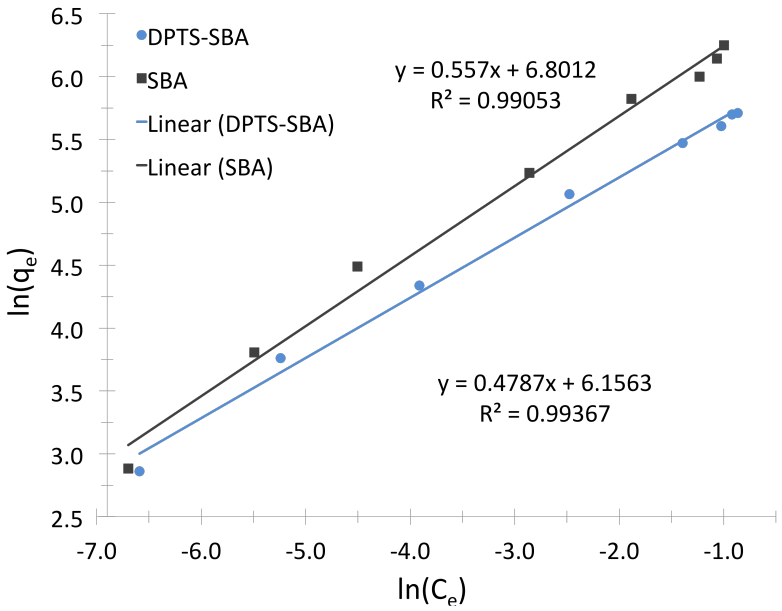

Figure 4.13: Linearized Freundlich U(VI) sorption isotherm fit for DPTS-SBA and SBA. Solution conditions: 3 M $NaNO_3$ adjusted to pH 4.

4.6 ^{31}P NMR Characterization of U(VI) Samples

Single-pulse ^{31}P NMR

U(VI)-DPTS-SBA samples were prepared in a manner similar to the U(VI) sorption isotherm measurements using only depleted ^{238}U. Samples were prepared with 0.5 mmol ^{238}U per gram solid. After 24 hours of contact time, solid samples were recovered and air-dried on filter paper prior to loading in Kel-F rotor inserts.

To gain additional insight about the interaction of the phosphonate ligand and sorbed U(VI) ions, ^{31}P NMR spectra were collected for U(VI)-DPTS-SBA and ac-DPTS-SBA samples prepared at various pH levels in 3 M $NaNO_3$. The single pulse ^{31}P NMR spectra and peak deconvolutions for these samples are shown in Figure 4.14. Table 4.3 gives the fit parameters for each spectrum. The spectrum for ac-DPTS-SBA-pH 4 gives a single resonance at 34.2 ppm (Figure 4.14 A). Upon contact with U(VI) solutions, however, a shoulder resonance appears on the main peak, at 41.5 ppm (Figure 4.14 B-E). The intensity of this resonance increases with increasing pH, which correlates positively with higher U(VI) loading. Therefore, the 41.5 ppm resonance can be assigned to phosphonate functional groups complexed to the uranyl ion. Diethyl ethylphosphonate acts as an electron-donor through the phosphoryl oxygen. Complexation with a metal cation draws electron density away from the phosphoryl group, further de-shielding the ^{31}P nucleus, which results in a chemical shift to a higher frequency. U(VI) complexes with other phosphates, phosphonates, and phosphinic acids have caused a similar downfield shifts in the ^{31}P NMR spectra. [174, 175] The

Table 4.3: Single-pulse ^{31}P NMR resonance fit parameters for U(VI)-DPTS-SBA

Final pH	Peak position (ppm)	Peak FWHM (ppm)	Normalized peak amplitude (a.u.)	Peak Shape[a]
4 (control)	34.2	5.0	1.02	0.8
2.8	34.2	6.8	0.98	0.6
	41.5	4.2	0.07	0.6
3.1	34.2	6.8	0.98	0.6
	41.9	5.4	0.14	0.6
3.5	34.7	6.1	0.98	0.6
	41.5	4.6	0.16	0.6
4.0	34.6	6.4	0.98	0.6
	41.2	4.9	0.29	0.6

[a]Value gives the shape n of the pseudo-Voigt functions, $V_p(x) = nG(x) + (1-n)L(x)$, where $G(x)$ and $L(x)$ are the Gaussian and Lorentzian distribution functions, respectively.

Table 4.4: Correlation between ^{31}P NMR fit data and U(VI) extraction data

Final Sample pH	Percent area (41.5 ppm)	U(VI)-bound ligands[a] (μmol g^{-1})	U(VI) extracted (μmol g^{-1}	Ligand:Metal Ratio
3.1 ± 0.1	10.0 %	243.8	135.5	1.8 ± 0.4
4.0 ± 0.1	18.4 %	450.8	215.1	2.1 ± 0.3

[a]Assuming a ligand loading of 2.43 mmol g^{-1}, as measured by single-pulse ^{31}P NMR with a triphenylphosphine standard.

percent area occupied by the 41.5 ppm peak represents the fraction of phosphonate ligands interacting with U(VI). Table 4.3 shows the percent area of the 41.5 ppm resonance for U(VI)-DPTS-SBA-pH 3.1 and U(VI)-DPTS-SBA-pH 4.0. Based on this fraction, the number of phosphonate groups interacting with U(VI) was calculated for each sample, assuming a ligand loading of 2.43 mmol g^{-1}. Table 4.3 also shows the quantity of U(VI) extracted under each condition, which was measured by batch contact experiments conducted under the same conditions. From these data, an approximate ligand-to-metal ratio of 2:1 was calculated for the pH 3 and 4 samples (Table 4.4). The majority of sorbed U(VI) is thus extracted by two phosphonate ligands, which is consistent with the proposed mechanism in solvent extraction [170, 171].

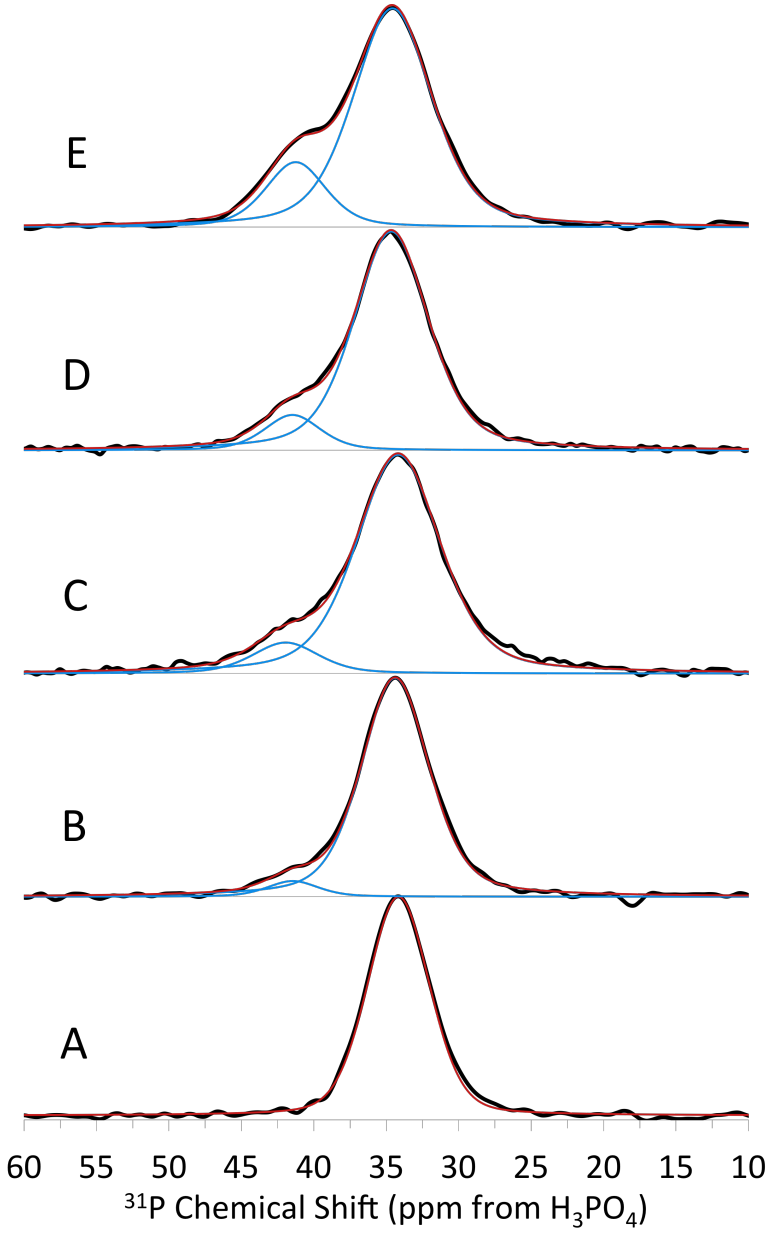

Figure 4.14: Single-pulse ^{31}P MAS spectra of ac-DPTS-SBA-pH 4.0 (A) and U(VI)-DPTS-SBA adjusted to a final pH of 2.8 (B), 3.1 (C), 3.5 (D), and 4.0 (E).

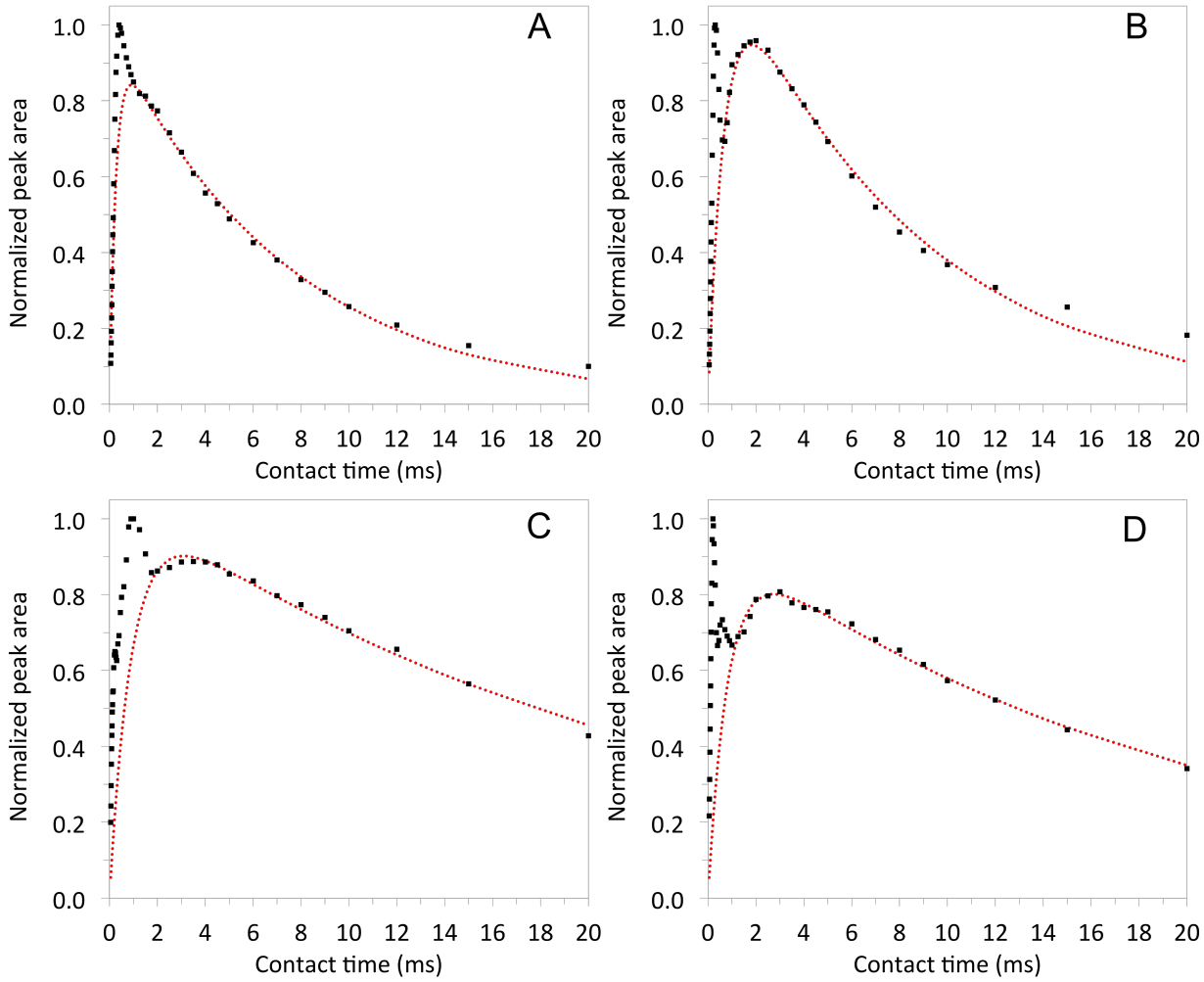

Figure 4.15: $^{31}P\{^{1}H\}$ cross-polarization variable contact time curves for pristine DPTS-SBA (A), ac-DPTS-SBA pH 4.0 (B), U(VI)-DPTS-SBA pH 4.0 (C), and U(VI)-DPTS-SBA pH 3.1 (D). Peak areas at each contact time were normalized to the peak with the maximum intensity. Normalized peak area for C and D represent the sum of the peak areas for the resonances at 34 ppm and 41 ppm.

$^{31}P\{^{1}H\}$ Cross-Polarization Kinetics Measurements

Cross-polarization kinetics were used to probe how changes in the interaction between ^{31}P and ^{1}H spin populations reveal structural information about the binding of U(VI) to DPTS-SBA. In a typical cross-polarization experiment, polarization is transferred from ^{1}H spins to ^{31}P spins during a contact pulse. The magnitude of polarization transfer depends on the length of the contact pulse [148, 149]. In this work, the $^{31}P\{^{1}H\}$ cross-polarization experiment serves as a spectral editing technique to distinguish protonated and deprotonated phosphonate sites based on differences in the ^{31}P polarization kinetics. Instrumental details are given in Section 6.8.

The $^{31}P\{^{1}H\}$ CP/MAS variable contact time curves for pristine DPTS-SBA, ac-DPTS-SBA pH 4, and U(VI)-DPTS-SBA samples adjusted to pH 3 and 4 are compared in Figure 4.15. Each curve shows the normalized ^{31}P peak area as a function of contact time. The normalized sum of the 34.2 and 41.5 ppm resonances was used for the U(VI)-DPTS-SBA samples. It has been shown that polarization transfer occurs through transient harmonic oscillations between spin pairs [150]. If the $^{31}P-^{1}H$ spin pairs are sufficiently isolated from the larger ^{1}H spin population, the rate of ^{1}H spin diffusion between these two groups is reduced, and oscillations are observed in the variable contact time curve. These oscillations are dampened at longer contact times as spin diffusion increases communication between isolated $^{31}P-^{1}H$ spin pairs and the larger ^{1}H spin population. Dampened oscillations at early contact times were observed in the variable contact time curves of each sample (Figure 4.15), which indicate a complex spin environment that contains isolated ^{31}P-^{1}H spin pairs. As the silica surface is amorphous, it contains a distribution of ^{31}P-^{1}H spin pairs that are silated from the bulk ^{1}H spin population to various degrees, and these variations preclude a fully quantitative fit of the curves. Nevertheless, meaningful information can be obtained by conducting a semi-quantitative comparison of the polarization kinetics for different samples.

The goal of this work is to compare the effects of pH and the presence of U(VI) on $^{31}P\{^{1}H\}$ CP kinetics. Rapid polarization at short contact times is dominated by ^{1}H spins closest to the ^{31}P spins, including the protons on the alkyl chains of the ligand itself. These ^{1}H spins account for the sharp spikes in polarization observed in Figure 4.15. At longer contact times, polarization is dominated by protons that are more distant from the ^{31}P spins, such as water and hydronium ions that are hydrogen bonded to the phosphonate functional group or to the silica surface. Classical polarization kinetic theory assumes infinitely rapid proton spin diffusion, and can therefore be applied to longer contact times, where spin diffusion has sufficiently dampened the oscillations from isolated $^{31}P-^{1}H$ spin pairs. Thus, the second half of each curve was fit with the equation describing classical cross-polarization kinetics (Equation 4.1):

$$I(t) = I_0\left(1 - \frac{T_{IS}}{T_{1\rho}^{H}}\right)^{-1}\left[exp\left(\frac{-t}{T_{1\rho}^{H}}\right) - exp\left(\frac{-t}{T_{IS}}\right)\right] \tag{4.1}$$

where I_0 and $I(t)$ are the maximum signal amplitude and the signal amplitude at contact time t, respectively, T_{IS} is the time constant for polarization transfer from ^{1}H spins to ^{31}P, and $T_{1\rho}^{H}$ is the relaxation time constant for proton spins in the magnetic field generated by the contact pulse. The fit parameters for each curve are given in Table 4.5.

Pristine DPTS-SBA has the shortest T_{IS} and $T_{1\rho}^{H}$. Once the surface is hydrated with 3 M $NaNO_3$ at pH 4, both increase slightly. The increase in T_{IS} for ac-DPTS-SBA-pH 4 is indicative of a slightly slower polarization transfer, and a longer $T_{1\rho}^{H}$ demonstrates slower proton relaxation. Addition of U(VI) changes the cross-polarization kinetics significantly. Compared to the pristine and pH 4 control samples, the two U(VI)-DPTS-SBA samples exhibit longer T_{IS} and $T_{1\rho}^{H}$, indicating significantly slower polarization transfer and slower

Table 4.5: $^{31}P\{^{1}H\}$ CP variable contact time curve fit parameters

Sample	Pristine DPTS-SBA	pH 4 control DPTS-SBA	U(VI)-DPTS-SBA pH 4.0	U(VI)-DPTS-SBA pH 3.1
Fit range (points)	26-43	22-43	28-43	25-43
I_0	0.95 ± 0.01	1.18 ± 0.02	1.03 ± 0.01	0.92 ± 0.01
T_{IS} (ms)	0.3 ± 0.1	0.67 ± 0.04	0.92 ± 0.05	0.83 ± 0.04
$T_{1\rho}^{H}$ (ms)	7.4 ± 0.2	8.2 ± 0.3	23.4 ± 0.9	19.8 ± 0.8

proton relaxation. Compared to the curve for U(VI)-DPTS-SBA-pH 3.1, the curve for the pH 4.0 sample exhibits a slightly longer $T_{1\rho}^{H}$, though their T_{IS} values are similar.

We observed that the polarization kinetics of all phosphonate ligands is affected by the presence of U(VI) in the sample. The variable contact time curve shapes and fit parameters were found to be similar for the 34 ppm and 41 ppm resonances (not shown). We believe this occurs because protons are effectively communicating with one another through spin diffusion, most likely mediated by water adsorbed onto the solid surface. Therefore, an average $T_{1\rho}^{H}$ value is observed, which represents both phosphonate ligands that are bound to U(VI) and those that are not.

4.7 $^{31}P-^{31}P$ Dipolar Coupling Measurements

To further investigate whether the spatial distribution of ligands affects U(VI) sorption, we applied a Double-Quantum-based Dipolar recoupling effects Nuclear Alignment Reduction (DQ-DRENAR) method to probe the extent of homonuclear dipolar coupling between ^{31}P atoms in the sample. [164, 165] Based on the commonly-used heteronuclear REDOR technique, [144, 176] this method measures the difference in signal amplitude between a reference and DQ-DRENAR pulse sequence. In the DQ-DRENAR sequence, two pulse sequences are applied in phase to allow homonuclear dipolar recoupling between ^{31}P spins. In the reference sequence, this recoupling is interrupted by the application of two pulse sequences that are out of phase by 90 such that no recoupling occurs. The recoupling of ^{31}P spins produces a signal amplitude decrease for the DQ-DRENAR spectra compared to the reference spectra.

For short signal evolution times, the difference in signal amplitude between the reference and DQ-DRENAR pulse sequence is related to the dipolar coupling constant through Equation 4.2:

$$\frac{S_0 - S'}{S_0} = \frac{0.86\pi^2}{15} \cdot b_{jk}^2 \cdot (NT_r)^2 \tag{4.2}$$

where S_0 and S are the signal amplitudes of the reference and DQ-DRENAR pulse sequences, respectively, N is the number of rotor revolutions, T_r is the rotor period, and bjk is the dipolar coupling constant for two spins j and k. To generalize for multi-spin systems, the term $b_j k^2$

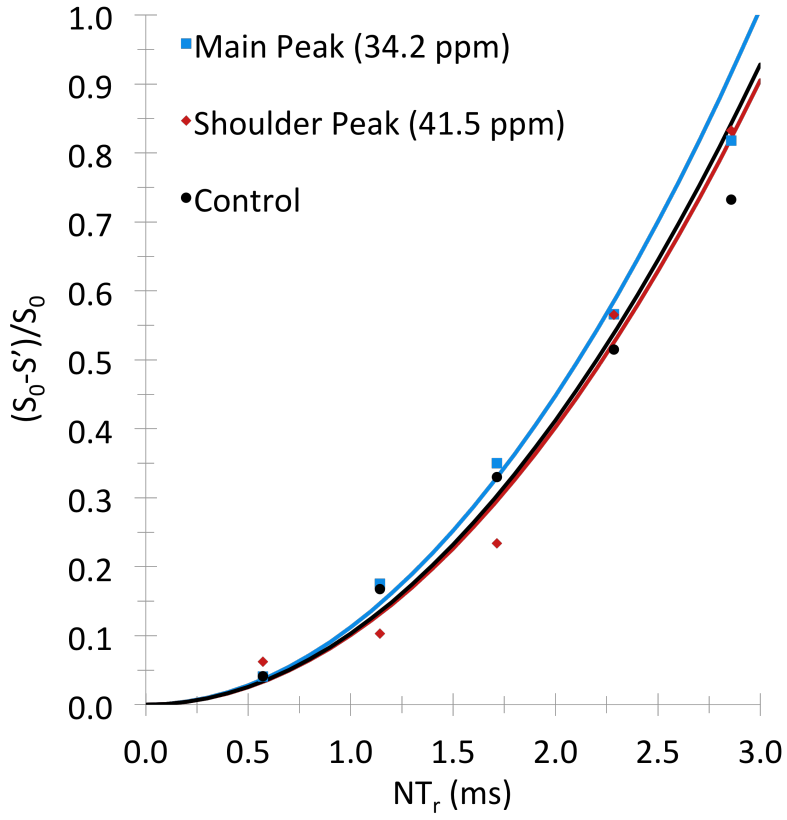

Figure 4.16: The trend in $\Delta S/S_0$ as a function of signal evolution time, NT_r, for the U(VI)-DPTS-SBA-pH 4.0 main peak (blue), shoulder peak (red), and the control sample DPTS-SBA-pH 4.0 (black).

is replaced with $\sum_(j < k) b_j k^2$, the sum of all ^{31}P pairwise dipolar coupling constants. [164] For this work, DQ-DRENAR measurements were made for U(VI)-DPTS-SBA-pH 4.0 and the control sample ac-DPTS-SBA-pH 4.0. Figure 4.16 shows a plot of $\Delta S/S_0$ for $0ms \leq NT_r \leq 3ms$ for both samples, as well as their parabolic fits. Two trends are shown for U(VI)-DPTS-SBA-pH 4.0: one for the main resonance at $\delta_P = 34.6ppm$, and one for the shoulder at $\delta_P = 41.5ppm$ assigned to O=P groups bound to U(VI). As can be seen from Figure 4.16, we observe no significant difference in the signal evolution between the main resonance and the shoulder resonance, or between the U(VI)-contacted sample and the control sample. The $\sum_(j < k) b_j k^2$ obtained from the fits were $1.82 \pm 0.08, 1.98 \pm 0.07, and 1.78 \pm 0.14 (\times 10^5 Hz^2)$, for the ac-DPTS-SBA-pH 4 control sample, the 34.6 ppm resonance of the U(VI)-DPTS-SBA-pH 4.0, and the 41.5 ppm resonance of the U(VI)-DPTS-SBA-pH 4.0, respectively. These values are the same within the uncertainty of the parabolic fit.

The strength of dipolar coupling is related to the distance between coupled spins through Equation 4.3:

$$\sum_{j<k} b_{jk}^2 = h^2\gamma^4\left(\frac{\mu_0}{4\pi}\right)^2 \sum_{j<k} \frac{1}{r_{jk}^6} \tag{4.3}$$

where b_{jk} is in Hz, γ is the gyromagnetic ratio for ^{31}P in Hz/T, and μ_0 is the vacuum permeability constant. Thus, the dipolar coupling constants measured give an indication of the average density of phosphonate ligands on the surface, which appears to be similar for both U(VI)-complexed and non-complexed ligand environments. This observation rules out the possibility that U(VI) is only bound to sites that have a localized high density of phosphonate ligands.

4.8 Discussion

The NMR spectra of pristine DPTS-SBA and ac-DPTS-SBA demonstrate that the DPTS condensed onto the silica surface in a mixture of monomers and polymers, and that the majority of ligands are stable to contact with pH 3 nitric acid in the time regime examined. Contact with acidic solutions may result in hydrolytic cleavage of ligands from the surface, primarily at the monomeric positions. However this loss is estimated to be less than 27 percent. The dependence of U(VI) extraction on pH is clear for both the functionalized and non-functionalized materials. The phosphonate ligand presumably has a pK_a value around 2.37, the value reported for dimethyl methylphosphonate [177]. Assuming a pK_a of 2.37, the percentage of deprotonated ligands can be calculated as a function of pH. These percentages are shown in parentheses in Figure 4.7. The estimated percentage of deprotonated ligands matches the percent sorption of U(VI) from 3M $NaNO_3$ solutions within uncertainty at all pH values, except for pH 3, which shows slightly lower uptake than that predicted by the pK_a. The correlation between the number of deprotonated ligand sites estimated from the pK_a and percent sorption of U(VI) provides compelling evidence that U(VI) complexes to deprotonated phosphoryl sites on the DPTS-SBA surface. The U(VI) sorption capacity of 326 ± 19 μmol/g calculated from the Langmuir model is much lower than the ligand loading of 1.78-2.43 mmol/g. At pH 4, a maximum U(VI) loading of 326 μmol/g would occupy only 27-37% of the ligand sites, assuming a ligand:metal ratio of 2:1. As discussed above, U(VI) extraction is highly pH dependent, but ligand protonation alone cannot explain the discrepancy between expected and measured U(VI) sorption capacity at pH 4, where ninety-eight percent of the ligands are expected to be deprotonated. Furthermore, because the ligand structure and ligand loading is largely unaffected by treatment with nitric acid, the U(VI) sorption capacity of DPTS-SBA is not limited by poor structural integrity of the functional layer in acidic conditions.

The U(VI) isotherm data show that non-functionalized SBA demonstrates increased extraction of U(VI) at pH 4 compared to DPTS-SBA. Non-functionalized SBA-15 type silica has been shown to have two different pK_a values ranging from 2-4.5 and 7.5-8.5 for the Q^3

and Q^2 silanols, respectively [178–180]. At pH 4, U(VI) cations can bind to deprotonated Q^3 silanols through electrostatic interactions. U(VI) isotherm data were fitted to both the Langmuir and Freundlich sorption models (Figures 4.12 and 4.13 and Table 4.2). The U(VI) sorption isotherm data for both SBA and DPTS-SBA are more accurately described by the Freundlich sorption model. The Langmuir model assumes sorption to uniform, independent sites with equal binding energy. A homogeneous monolayer of ligands presenting one type of binding site would be consistent with the Langmuir model. In contrast, the Freundlich model allows for heterogeneous sorption sites with a distribution of binding energies that may be dependent on the surface density of the analyte [181]. This type of isotherm would be more consistent with a functionalized silica surface where U(VI) ions interact with multiple types of binding sites. That the Freundlich model describes the U(VI) isotherm at pH 4 for DPTS-SBA suggests that exposed silanols on the silica surface participate in U(VI) extraction for this material as well. This finding is consistent with the ^{29}Si$\{^1$H$\}$ CP/MAS NMR spectra. Comparison of the ^{29}Si$\{^1$H$\}$ CP/MAS NMR spectra for ac-DPTS-SBA-pH 4.0 and U(VI)-DPTS-SBA-pH 4.0 at a single contact time of 3 ms (Figure 4.17) shows that the presence of U(VI) significantly enhances the signal amplitude of the T and Q^3 resonances. As these two spectra were collected under identical conditions, the signal enhancement for the surface species must be due to a change in ^{29}Si-^{1}H dipolar coupling caused by the U(VI). This provides further evidence that U(VI) interacts not only with the phosphonate ligands, but also with the silanol surface, including silanols in the T positions (Figure 4.18). Unfortunately, full variable contact time curves could not be obtained due to the long acquisition times needed to collect these data.

^{31}P$\{^1$H$\}$ cross-polarization kinetics measurements reveal that complexation of U(VI) changes the rate of polarization transfer between ^{31}P and ^{1}H spin populations at intermediate contact times, as well as the relaxation rate of ^{1}H spins. Spin relaxation is mediated by dipolar spin coupling interactions and is therefore strongly affected by the number and proximity of neighboring spins and molecular motion within the sample. The longer $T_{1\rho}^H$ times observed for the U(VI)-DPTS-SBA samples compared to the control and pristine samples (Figure 4.15) means that relaxation of ^{1}H spins in the vicinity of phosphorus atoms by interaction with nearby ^{1}H spins is slower. This result is consistent with a relative decrease in the number of nearby proton spins, which further supports that U(VI) ions are replacing hydronium ions at phosphonate sites. It has been shown, for example, that deprotonated silanols have a longer $T_{1\rho}^H$ time compared to protonated silanols [158]. Similarly, "proton-rich" and "proton-deficient" spin environments observed in different phosphate domains of human bone have demonstrated vastly different CP kinetics [160]. At a constant pH, complexation of U(VI) to deprotonated ligand sites would cause an overall decrease in the number of protonated ligands as the following equilibrium shifts to the right side of the equation:

$$\mathrm{LH^+} \rightleftharpoons \mathrm{L^+H^+}$$

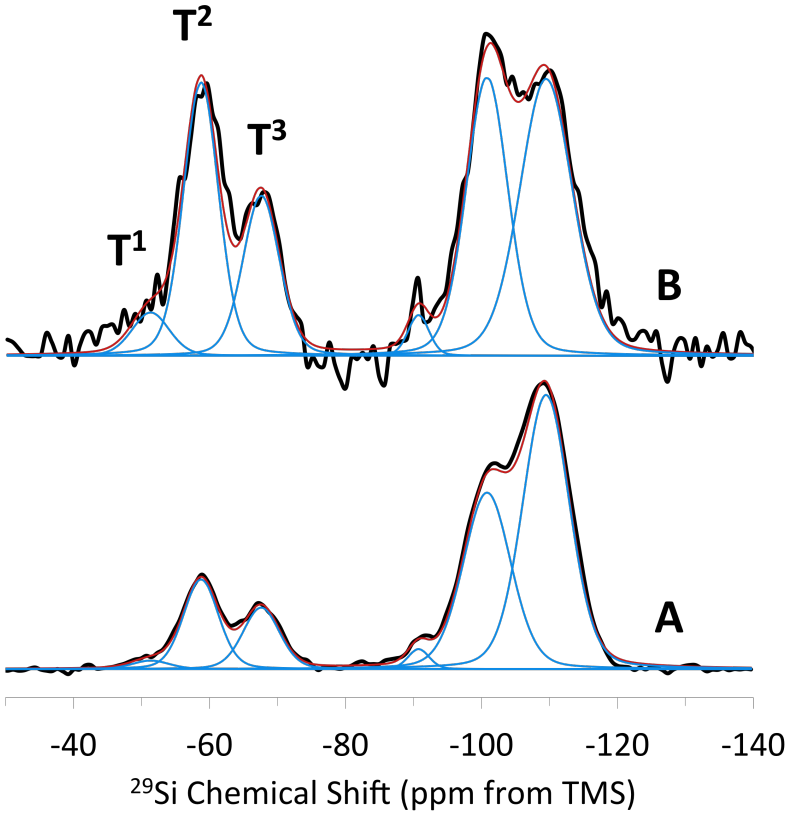

Figure 4.17: $^{29}Si\{^{1}H\}$ CP/MAS NMR spectra for ac-DPTS-SBA-pH 4.0 (A) and U(VI)-DPTS-SBA-pH 4.0 (B). Spectra were normalized to the Q4 peak at -109.5 ppm. Black lines show the experimental spectra. The red lines and blue lines show the spectral fit and the peak deconvolution, respectively.

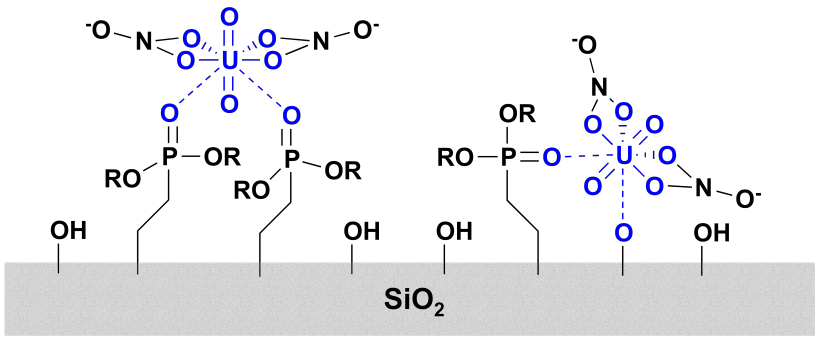

Figure 4.18: Proposed structures for uranyl nitrate complex extracted by DPTS-SBA.

where L is the phosphonate ligand and LH^+ is the protonated ligand. This would explain the relative increase in $T_{1\rho}^H$ for the U(VI)-DPTS-SBA samples compared to the ac-DPTS-SBA-pH 4 sample. The observed $T_{1\rho}^H$ is longer for the U(VI)-DPTS-SBA-pH 4.0 sample compared to that of the U(VI)-DPTS-SBA-pH 3.1 sample simply because the latter has a greater number of protonated ligand sites. This interpretation is consistent with the observed shift in the broad local maximum from 1.75 ms for the ac-DPTS-SBA-pH 4 sample to 3 ms for the two U(VI)-DPTS-SBA samples. A relative decrease in the number of protonated phosphonate sites would result in slower polarization transfer from ^{1}H to ^{31}P spin populations at intermediate contact times, shifting the maximum polarization to longer contact times. These observations support the hypothesis that U(VI) ions are complexed by deprotonated phosphonate moieties.

The relative increase in $T_{1\rho}^H$ time for the U(VI)-DPTS-SBA samples compared to the ac-DPTS-SBA-pH 4.0 control and pristine samples may also be due to increased rigidity of the phosphonate ligands in those samples. In general, molecular motion serves as an effective relaxation agent. As discussed above, ^{31}P solid-state NMR measurements revealed that U(VI) is complexed by two phosphonate ligands on the DPTS-SBA surface, which would lock them into a particular orientation and restrict their motion compared to non-complexed ligands. Overall, the ^{31}P$\{^1$H$\}$ cross-polarization variable contact time curves show that U(VI) complexation alters the polarization transfer rate between ^{1}H and ^{31}P spins. It is likely that the changes observed are due to both a depleted proton environment at the surface and to increased rigidity of the ligands in the U(VI)-DPTS-SBA samples relative to the control and pristine samples.

The variable pH batch and solid-state NMR cross-polarization measurements confirmed that U(VI) binds to deprotonated sites, but that ligand protonation does not account for limited U(VI) extraction at pH 3 and 4. Single-pulse ^{31}P solid-state NMR measurements revealed a ligand:metal binding ratio of approximately 2:1 at pH 3 and 4. We conducted ^{31}P$-^{31}$P DQ-DRENAR experiments to further characterize the density of the functional layer, and to determine if the spatial distribution of ligands limited the number of actual binding sites to a small fraction of the ligands present.

^{31}P$-^{31}$P DQ-DRENAR experiments provide a measure of the average strength of dipolar coupling between phosphorus atoms. An increase in the number or proximity of neighboring ^{31}P spins would result in a relative increase in $\sum_{j,k} b_j k^2$, which would manifest as a sharper rise in the parabolic fit. ^{31}P$-^{31}$P DQ-DRENAR facilitates evaluating the extent of cross-linking between ligands during the grafting procedure. During functionalization, the ethoxy groups on the DPTS ligand hydrolyze upon contact with water adsorbed to the silica surface. Hydrolyzed ligands may condense to each other prior to condensation with surface silanols. A ligand that is central to an extended polymer chain would thus have up to three nearest neighbors, each at a distance of approximately 3.0 Å (Figure 4.19A) [182]. Assuming the ligands are rigid on the timescale of the MAS experiment, this average spacing results in a $\sum_{j,k} b_j k^2$ value of $14.7 \times 10^5 Hz^2$. As the dipolar coupling constants measured for all samples are significantly lower, we conclude that this type of uniform monolayer does not

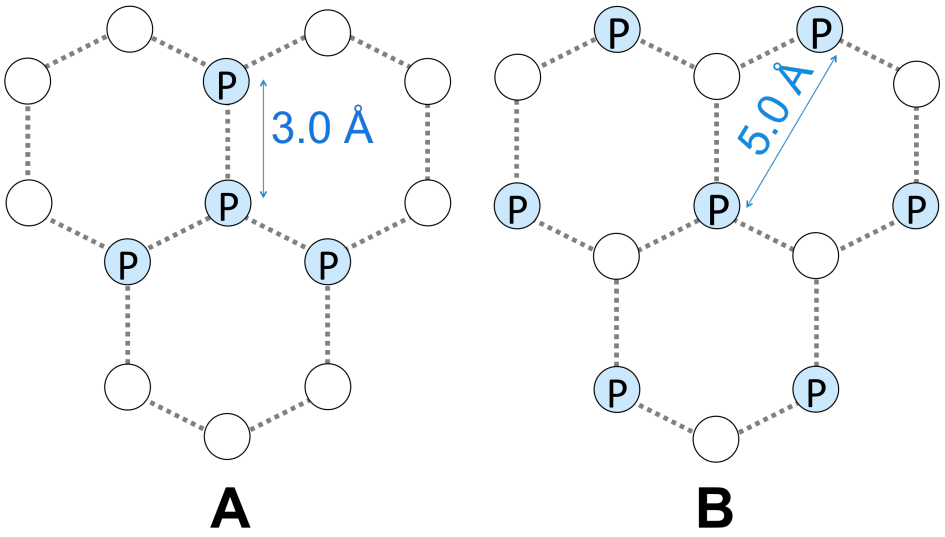

Figure 4.19: Surface modification models based on rigid phosphonate ligands grafted to the 111-surface of β-cristobalite. Cross-linking of ligands during functionalization would result in a polymeric surface (A); condensation of ligands to free silanols without cross-linking would result in a monomeric surface (B).

exist. An isolated dimer yields a $\sum_{j,k} b_j k^2$ value of $4.9 \times 10^5 Hz^2$, which is still significantly higher than those observed. Alternatively, if functionalization involves no cross-linking of the phosphonate ligands and proceeds solely through monomeric condensation to available surface silanols, the ligands will have a larger average spacing. Though amorphous, the silica surface possesses local ordered structure similar to that of β-cristobalite [113]. We approximate the local structure as the (111) plane of β-cristobalite, which contains hexagonal arrays of silanols spaced 5.0 Å apart, assuming a fully hydroxylated surface (Figure 4.19B) [113]. In this case, a given phosphorus atom will have six nearest neighbors, each at a distance of 5.0 Å, resulting in a $\sum_{j,k} b_j k^2$ value of $1.49 \times 10^5 Hz^2$. This value agrees much better with the results obtained, and is likely a better description of the surface functionalization. However, the measured dipolar coupling constants are significantly higher, which could indicate that some cross-linking occurred at a small fraction of sites. This is consistent with the ^{29}Si{^{1}H} CP/MAS characterization of the material discussed earlier. This simple monomeric functionalization resulting in ligands spaced 5.0 Å apart, on average, does not preclude the bonding of two or more ligands to one uranyl. The phosphorus-phosphorus distance in the crystal structure of $UO_2(NO_3)_2$(tert−isobutyl phosphate)$_2$ is approximately 7.7 Å [183]. Thus, the density of phosphonate functional groups on the surface is still high enough to achieve the 2:1 ligand:metal binding ratio observed. The ^{31}P−^{31}P homonuclear DQ-DRENAR experiment has proven to be a powerful tool for comparing internuclear distances between functional groups on the silica surface.

^{31}P−^{31}P DQ-DRENAR experiments revealed no significant difference in the $\sum_{j,k} b_j k^2$ measured for U(VI)-complexed ligand sites and non-complexed sites. Therefore, we conclude that the sorption of U(VI) on DPTS-SBA is not limited by the spatial distribution of

phosphonate ligands. We also conclude that U(VI) does not significantly alter the distance between two ligands upon binding. As U(VI) uptake is controlled neither by ligand protonation nor the spatial distribution of ligands, we conclude that U(VI) binding is limited largely by the stability of the U(VI) surface complex.

4.9 Conclusions and Future Work

The combination of batch studies and advanced solid-state NMR spectroscopy has provided new insight into the U(VI) extraction mechanism and limitations of DPTS-functionalized SBA-15. DPTS is an ideal model ligand for demonstrating the utility of solid-state NMR spectroscopy in understanding the surface distribution of ligands and the extraction mechanism for U(VI). Single-pulse ^{31}P solid-state NMR showed that the number of U(VI)-complexed ligands was limited to a fraction of the total number of ligands present. Using single-pulse ^{31}P solid-state NMR on U(VI)-contacted samples, we find that U(VI) binds to deprotonated phosphonate ligands in a ligand-to-metal ratio of 2:1. There is evidence that deprotonated silanols also interact with U(VI). Furthermore, we find that U(VI) extraction is not limited by non-ideal ligand layer density, but rather by low stability of the complex formed during extraction. These findings aid in optimizing organically-modified surfaces for heavy metal extraction.

Chapter 5

Monolayer Formation and Sorption of U(VI) on Acetamide Diethylphosphonate Functionalized Silica

5.1 Introduction

This chapter presents the synthesis of four acetamide phosphonate (AcPhos)-functionalized SBA-15 materials. The materials were evaluated for resilience of the functional layer to contact with pH 3 nitric acid solutions using solid-state NMR. The ligand density achieved on the surface was compared using ^{31}P-^{31}P dipolar coupling measurements. Finally, the materials were compared for their ability to extract U(VI) from nitric acid media. The AcPhos ligand was adapted from a class of carbamoyl methylphosphine oxide (CMPO) ligands, which are used in solvent extraction for the selective extraction of actinides, primarily trivalent actinides, from the lanthanides (Figure 1.2). Fryxell et al. report the anchoring of CMPO-like ligands to silica supports as an extension of the sol-gel process [1, 11, 12, 14, 184–186]. These materials, along with their hydrolyzed phosphonic acid versions were also found to have a high affinity for uranyl and plutonyl in pH 2-3 nitric acid solutions.

Birnbaum and Fryxell adapted the CMPO functional group specifically for grafting on silica. To reduce the steric bulk, which has been shown to improve ligand loading [187], the large carbon chains were reduced to simple ethoxy groups, and a siloxane anchor was added [11]. Birnbaum [184] synthesized the "AcPhos" ligand via amidation of phosphonoacetic acid with aminopropyl triethoxysiloxane using carbonyl diimidazole (CDI) as an activator (Figure 5.2). According to Birnbaum, the purification of the final product from CDI was difficult, and ultimately not necessary for the successful grafting of the AcPhos ligand to porous silica substrates. Therefore, the entire reaction mixture was used during the functionalization process [184]. Detailed characterization of the structure of the functional layer was difficult

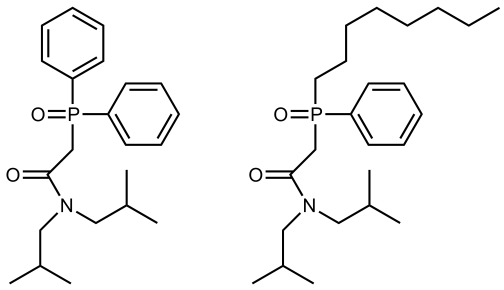

Figure 5.1: Two CMPO-type ligands used for solvent extraction, including diphenyl-N,N-diisobutyl carbamoylmethyl phosphine oxide (left), and octyl(phenyl)-N,N-diisobutyl carbamoylmethyl phosphine oxide (right). The AcPhos ligand was designed to feature these functional groups.

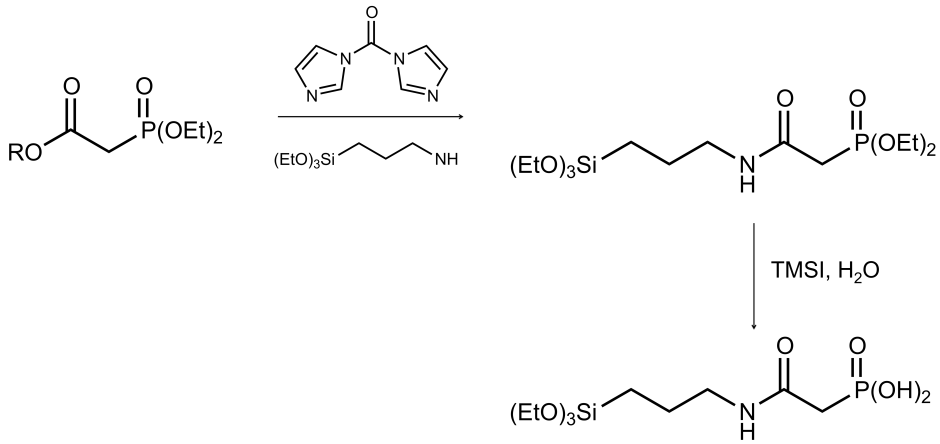

Figure 5.2: Schematic showing the synthesis of the AcPhos ligand described in references [14, 184].

to obtain, since the ^{29}Si spectra collected resulted in "a poorly resolved aggregate signal between approximately -50 and -70 ppm" [11]. No additional work was done to assess the extent of polymerization achieved during synthesis.

Nevertheless, the ester-AcPhos was shown to have high affinity for lanthanides in $NaNO_3$ solutions, with extraction increasing as the pH was increased from 1 to 6.5. Lanthanide extraction was high for the acid-AcPhos materials even from highly acidic solutions [11]. Extraction of U(VI) and Pu(IV) was also measured for both materials [14]. Generally, the kinetics and thermodynamics of sorption were more favorable for the acid-AcPhos materials, though the ester-AcPhos showed high affinity for U(VI) from pH 0.7-4.55 nitric acid solutions, even in the presence of competing ions [14].

The scope of these studies was generally restricted to evaluating materials based on their macroscopic extraction properties using batch contact experiments. In particular, little attention was given to evaluation of the constitution of the functional layer after the grafting procedure, other than routine NMR analysis. Additionally, little is known about the resilience of functional materials to contact with acidic solutions. Previous work by our research group has shown that the synthetic procedure used for these studies is not highly

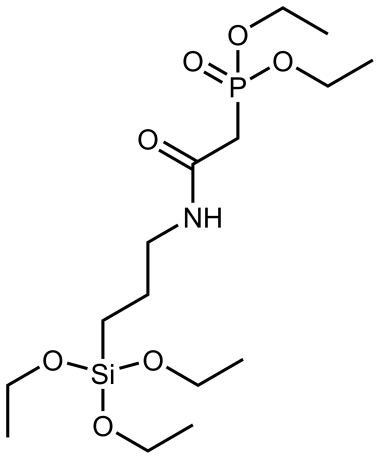

Figure 5.3: The acetamide diethylphosphonate (AcPhos) ligand.

reproducible, perhaps in part due to the impurities in the reaction mixture used for the synthesis of AcPhos. Thus, materials synthesized the same way yielded vastly different Pu(VI) sorption properties [188].

To mitigate some of the factors contributing to poor reproducibility of the functionalization process, the materials described in this chapter were synthesized directly from diethyl (2-oxo-2-((3-(triethoxysilyl)propyl)amino)ethyl)phosphonate (Figure 5.3, which was purchased from Technocomm Ltd. The ligand was synthesized using an alternative synthetic route, which eliminated the need for using the carbonyl diimidazole activator. Thus, it was obtained in its pure form, as indicated by a clean ^{1}H solution NMR spectrum of the final product.

The AcPhos ligand provides an excellent opportunity to study the functionalization process, and the stability of functional layers in contact with acidic solutions. Because AcPhos-functionalized silica possesses ^{1}H, ^{31}P, ^{13}C and ^{29}Si, all of which are spin = 1/2 nuclei observable by NMR, and the first two of which are 100% abundant, it is highly accessible to in-depth study by magnetic resonance techniques. Furthermore, as the optimal extraction conditions for U(VI) have been previously optimized, various functionalization procedures can be compared by their ability to extract U(VI) from nitric acid media.

5.2 Synthesis and Functionalization of AcPhos-SBA

The SBA-15 rod-shaped particles were synthesized using the hydrothermal method described by Sayari, Han, and Yang[117], which is described in detail in Section 6.2. Silica particles were functionalized directly using diethyl (2-oxo-2-((3-(triethoxysilyl)propyl)amino)ethyl) phosphonate (AcPhos) using a method adapted from the surface polymerization method described by Sander [131]. Four materials, AcPhos-SBA (1-4) were synthesized using three different functionalization procedures. All functionalization procedures involved drying of

Table 5.1: Summary of the difference in synthetic procedures for the AcPhos-SBA materials

Material	AcPhos-SBA (1)	AcPhos-SBA (2)	AcPhos-SBA (3)	AcPhos-SBA (4)
Surface hydration (H_2O molecules nm^{-2})	10	10	10	10
Surface hydration time (hours)	2	15	15	15
Catalyst used (molecules nm^{-2})	N/A	N/A	5	5
Silanes added (silanes nm^{-2})	6.25	6.25	6.25	6.25
Reflux time (hours)	6	24	24	24

the silica particles under vacuum overnight followed by the addition of toluene and water (and pyridine, for AcPhos-SBA (3) and (4)) under a nitrogen atmosphere. After surface hydration, the AcPhos ligand was added, and the reaction mixture refluxed for a given reaction time. After a distillation step to remove excess water and ethanol evolved during the reaction, solid materials were collected via vacuum filtration, washed with isopropanol, and stored in an evacuated desiccator. Additional synthetic details are given in Section 6.3. The key differences between synthetic procedures for AcPhos-SBA (1-4) are summarized in Table 5.1. The resulting non-functionalized SBA and AcPhos-SBA materials were characterized for surface area and porosity using nitrogen adsorption isotherms.

Acid-washed samples, AcPhos-SBA (X) AW, where X is 1, 2, 3, or 4 in Table 5.1 were prepared for characterization by NMR spectroscopy. Acid-washing conditions were chosen to match the conditions under which the U(VI) isotherms were measured, that is, 3 M $NaNO_3$ adjusted to pH 3. Samples were contacted with solution for approximately 20 hours before phase separation by centrifugation. After separating the solid from the supernatant, samples were washed several times with isopropanol to remove excess water, and then dried under vacuum before storage in a desiccator with pristine samples to obtain similar levels of hydration.

5.3 Characterization by N_2 Adsorption

Table 5.2 summarizes the nitrogen adsorption isotherm data obtained for non-functionalized SBA-15 and the four AcPhos-SBA materials. The adsorption data and the pore size distribution and cumulative pore volume data for non-functionalized SBA is shown in Figure 5.4. Corresponding data for the AcPhos-SBA materials are shown in Figures 5.5 and 5.6. The non-functionalized material demonstrates the highest specific surface area, specific pore volume, and pore diameter. Its isotherm is consistent with a type IV isotherm with an H_1

Table 5.2: Summary of N_2 adsorption isotherm data for AcPhos-SBA materials

Material	BET Surface Area (m^2 g^{-1})	BJH Pore Volume (cm^3 g^{-1})	BJH Pore Diameter (nm)	Hysteresis Loop Type
SBA-15	831	0.818	7.47	H_1
AcPhos-SBA (1)	442	0.536	7.42	H_1
AcPhos-SBA (2)	383	0.450	6.43	H_1
AcPhos-SBA (3)	125	0.128	4.32	H_1 with desorption hysteresis
AcPhos-SBA (4)	46	0.045	4.32	H_2 or H_4

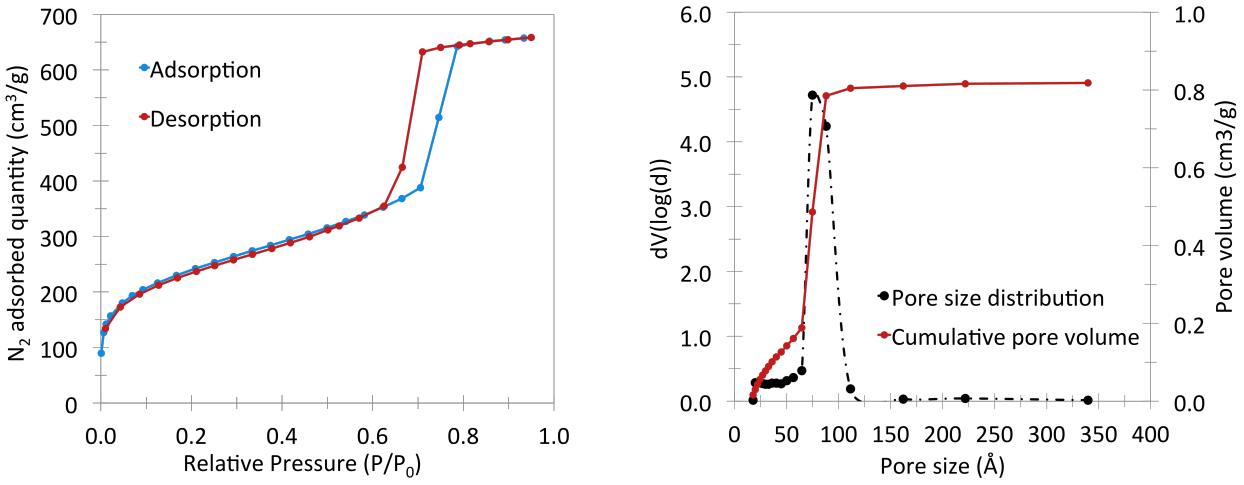

Figure 5.4: Nitrogen adsorption isotherm data for non-functionalized SBA-15 rods used to make the AcPhos-SBA materials. Surface area = 831 m^2 g^{-1}, pore volume = 0.818 cm^3 g^{-1}, pore diameter = 7.47 nm.

hysteresis loop, which is consistent with capillary condensation in a highly ordered, cylindrical mesoporous structure [100].

AcPhos-SBA (1) demonstrates similar isotherm shape and pore diameter, indicating that ligand grafting has not significantly altered the pore structure. The specific surface area and specific pore volume have decreased, which is consistent with an increase in mass that results from functionalization. This was also observed for the other AcPhos-SBA materials, especially AcPhos-SBA (3) and (4), which indicates that these materials have the highest ligand loading of all the materials. AcPhos-SBA (2), (3), and (4) show a more significant decrease in average pore diameter than does AcPhos-SBA (1) compared to the non-functionalized material. Similar 1-3 nm decreases in average pore diameter have been observed in other silica materials after modification with an organic monolayer [166, 169, 189].

While the nitrogen adsorption isotherms of AcPhos-SBA (1) and (2) are both type IV with H_1 hysteresis loops, the shapes of the isotherms for AcPhos-SBA (3) and (4) look different. The isotherm and hysteresis loop for AcPhos-SBA (3) appear to be type IV-H_1. However, there is also hysteresis in the desorption branch at low and high partial pressures (Figure 5.6a). The hysteresis loop in the isotherm of AcPhos-SBA (4) may be a hybrid between

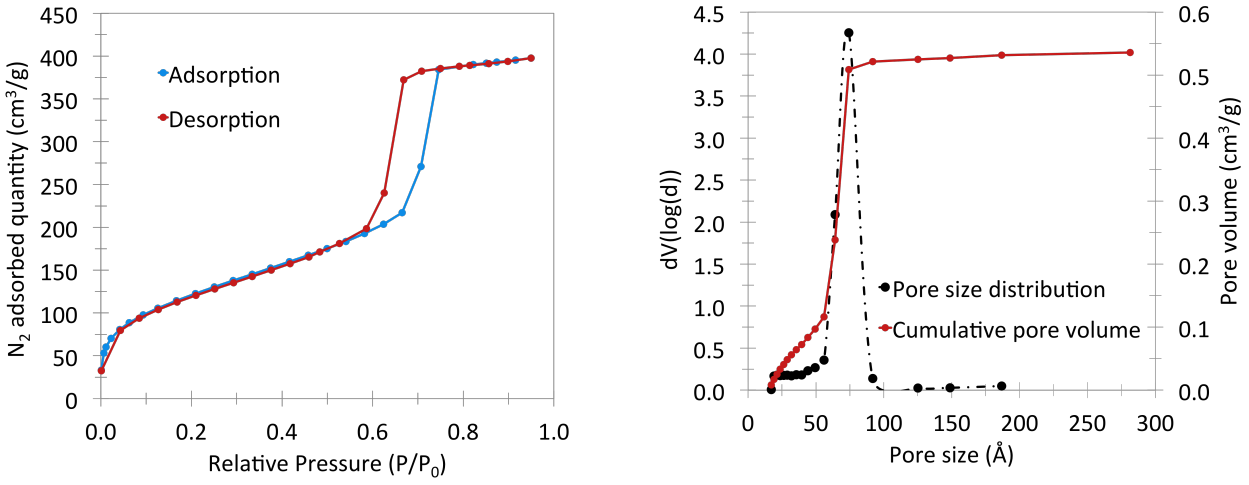

(a) Nitrogen adsorption isotherm data AcPhos-SBA (1). Surface area = 442 m^2 g^{-1}, pore volume = 0.536 cm^3 g^{-1}, pore diameter = 7.42 nm.

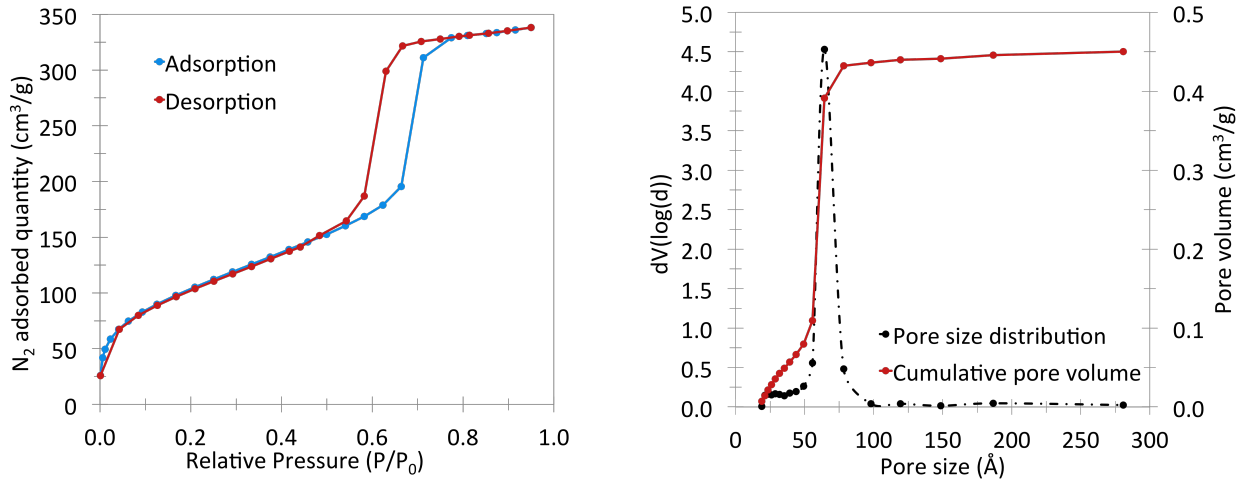

(b) Nitrogen adsorption isotherm data for AcPhos-SBA (1) (top) and AcPhos-SBA (2) (bottom).

(c) Nitrogen adsorption isotherm data AcPhos-SBA (2). Surface area = 383 m^2 g^{-1}, pore volume = 0.450 cm^3 g^{-1}, pore diameter = 6.43 nm.

Figure 5.5

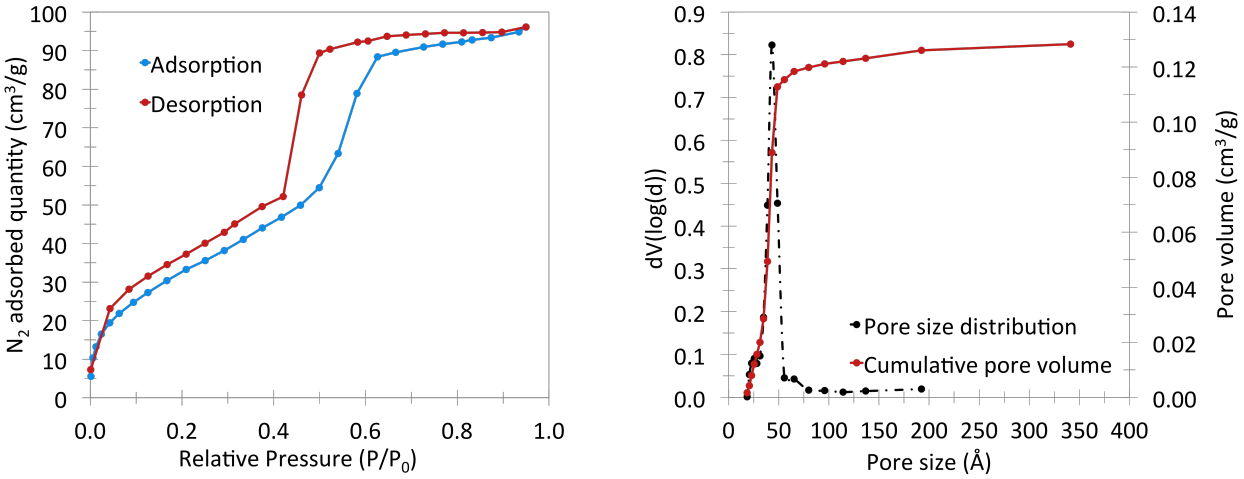

(a) Nitrogen adsorption isotherm data AcPhos-SBA (3). Surface area = 125 m^2 g^{-1}, pore volume = 0.128 cm^3 g^{-1}, pore diameter = 4.32 nm.

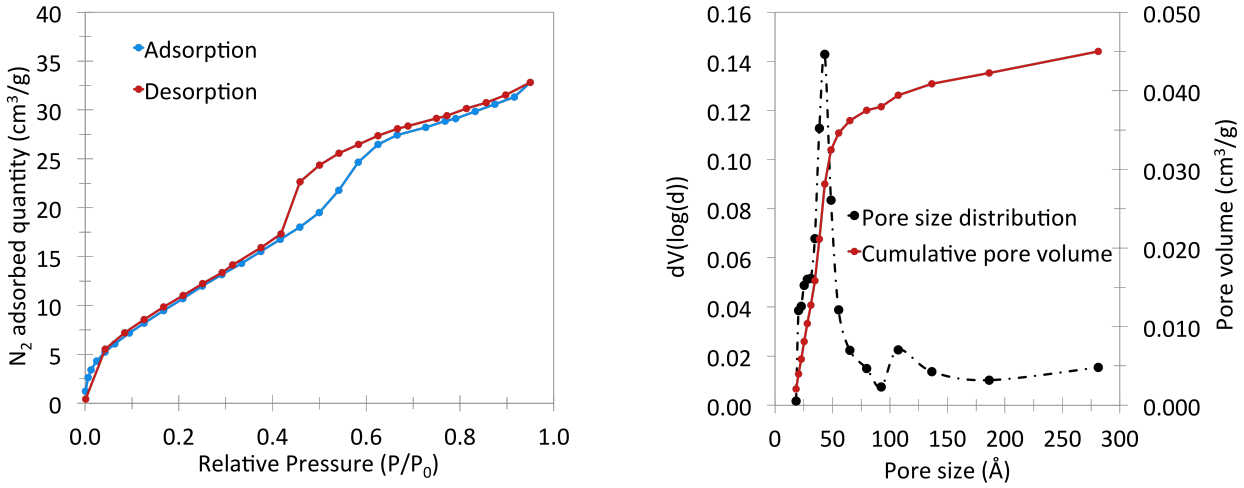

(b) Nitrogen adsorption isotherm data AcPhos-SBA (4). Surface area = 46 m^2 g^{-1}, pore volume = 0.045 cm^3 g^{-1}, pore diameter = 4.32 nm.

Figure 5.6

H_2 and H_4 isotherms, which are most often associated with disordered pore structures with bottle-neck or slit-shaped openings [100]. However, both of these phenomena, desorption hysteresis and similar changes in hysteresis loop shape, have been observed for organically-modified materials when the number of adsorption sites changes with increasing partial pressure of the nitrogen during isotherm measurement [101]. Therefore, the hysteresis loop shapes of AcPhos-SBA (3) and (4) does not necessarily indicate a significant change in pore ordering and structure.

5.4 ^{13}C and ^{29}Si NMR Spectroscopy

$^{13}C\{^1H\}$ CP/MAS spectra were collected for the four AcPhos-SBA materials in their as-synthesized, pristine state, as well as after washing them with pH 3 nitric acid solutions containing 3 M $NaNO_3$. These conditions were chosen to match those used in the measurement of the U(VI) sorption isotherms. Spectra of pristine and acid-washed samples were compared in order to verify ligand structure and to qualitatively assess resiliency of the ligand structure to contact with acid for each material. The AcPhos ligand contains nine distinct carbon sites. As two of these sites have similar chemical shifts, eight resonances are observed in the $^{13}C\{^1H\}$ CP/MAS spectra of all pristine and acid-washed samples. The observed resonances are assigned as follows: δ_C = 8.0 ppm ($-Si-\mathbf{C}H_2-CH_2-$), 14.0 ppm ($0=P-O-CH_2-\mathbf{C}H_3$), 21.7 ppm ($-Si-O-CH_2-\mathbf{C}H_3$), 33.4 ppm ($-Si-CH_2-\mathbf{C}H_2-CH_2-NH-$), 41.8 ppm (mixture of $-CH_2-\mathbf{C}H_2-NH-$ and $-CO-\mathbf{C}H_2-P=0$), 56.6 ppm ($-Si-O-\mathbf{C}H_2-CH_3$), 62.2 ppm ($O=P-O-\mathbf{C}H_2-CH_3$), and 164.7 ppm ($-\mathbf{C}=O$). These chemical shift values are largely consistent with the values reported by Fryxell et al. [11] for MCM-41 materials grafted with the ester AcPhos functional group, with the exception that they assume that all siloxane esters are hydrolyzed during functionalization. In the present work, this assumption is not made, and there is evidence that these groups are still present, as discussed below. Figures 5.7 and 5.8 show the spectra for the pristine and acid-washed samples of AcPhos-SBA (1)-(4). The additional very sharp peak appearing in the spectrum for AcPhos-SBA (1) AW at 28.1 ppm with respect to TMS is believed to be from surface-sorbed isopropanol, which was used in washing the samples.

The ^{13}C NMR spectra were collected using cross-polarization from ^{1}H. Because of the difference in polarization transfer kinetics for the different carbon species, the integrated peak areas are not proportional to the populations of their corresponding carbon atoms. Additionally, differences in the amount of water adsorbed to the pristine versus acid-washed samples may result in different CP dynamics. This difference was minimized by drying the acid-washed samples under vacuum (< 20 μm Hg) for several hours. Therefore, differences in the relative peak amplitude for two spectra may indicate structural changes to the AcPhos ligand.

The $^{13}C\{^1H\}$ CP/MAS spectrum for pristine AcPhos-SBA (2) looks similar to that of AcPhos-SBA (1). Comparison of the spectra for pristine and acid-washed AcPhos-SBA (2) shows significant decrease in peak amplitudes at the C_3 and C_7 positions (black arrows in

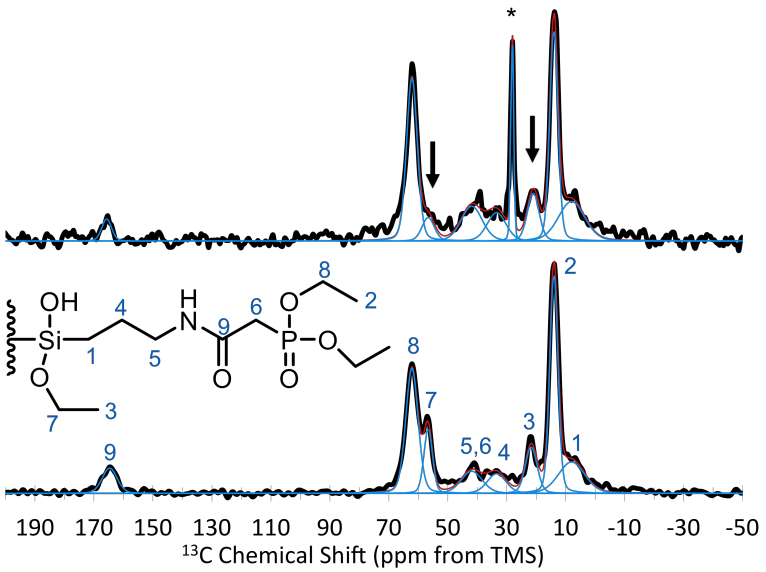

(a) $^{13}C\{^{1}H\}$ CP/MAS spectra for AcPhos-SBA (1) pristine (bottom) and acid-washed (top). Spectra were normalized to the peak at 14 ppm. The black arrows point to the resonances at 21.7 and 56.6 ppm, which correspond to the carbons on the ethoxy groups of the siloxane. Surface-sorbed isopropanol gives rise to a narrow peak at 28.1 ppm, labeled with an asterisk in the figure.

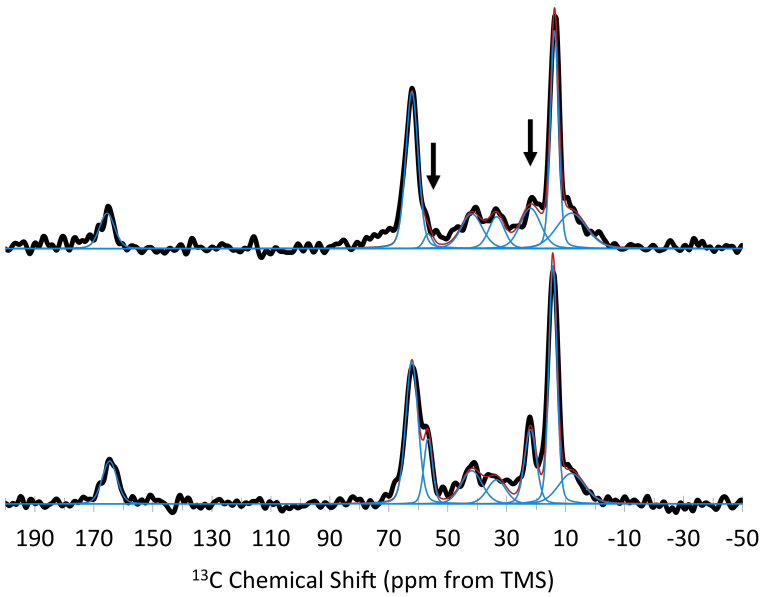

(b) $^{13}C\{^{1}H\}$ CP/MAS spectra for AcPhos-SBA (2) pristine (bottom) and acid-washed (top). Spectra were normalized to the peak at 14 ppm. The black arrows point to the resonances at 21.7 and 56.6 ppm, which correspond to the carbons on the ethoxy groups of the siloxane.

Figure 5.7

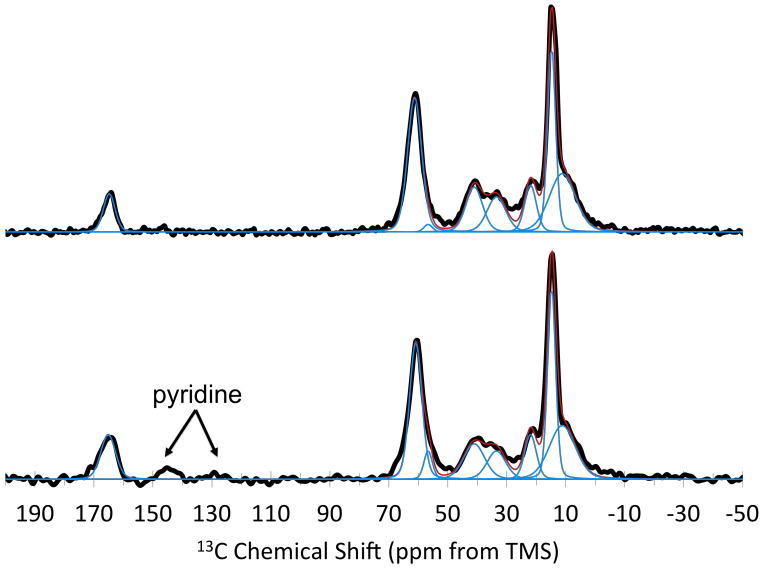

(a) $^{13}C\{^{1}H\}$ CP/MAS spectra for AcPhos-SBA (3) pristine (bottom) and acid-washed (top). Spectra were normalized to the peak at 14 ppm. Experimental data is shown in black. The blue lines show the spectral deconvolution, and the red line is their sum. The resonances at approximately 145 ppm and 128 ppm are from physisorbed pyridine.

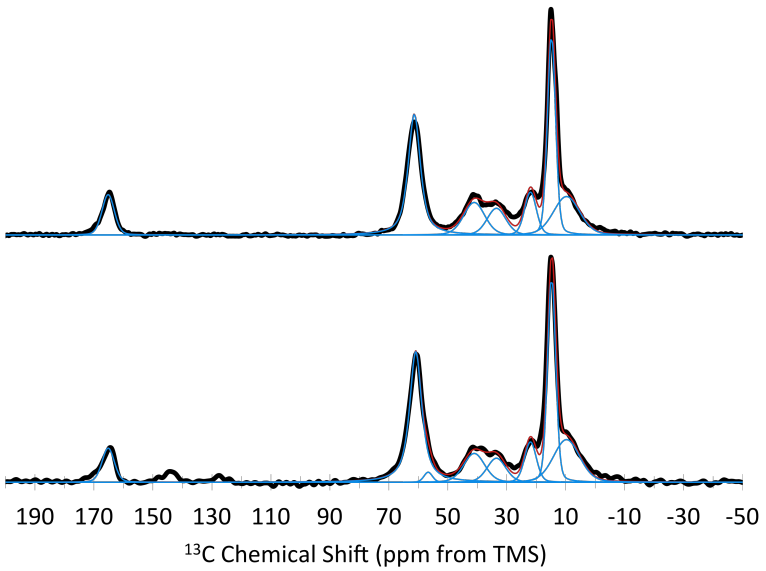

(b) $^{13}C\{^{1}H\}$ CP/MAS spectra for AcPhos-SBA (4) pristine (bottom) and acid-washed (top). Spectra were normalized to the peak at 14 ppm. Experimental data is shown in black. The blue lines show the spectral deconvolution, and the red line is their sum. The resonances at approximately 145 ppm and 128 ppm are from physisorbed pyridine.

Figure 5.8

Table 5.3: Comparison of peak ratios for AcPhos-SBA ^{29}Si{^{1}H} CP/MAS spectra

Material	T^1/T	T^2/T	T^3/T	Q^2/Q	Q^3/Q
AcPhos-SBA (1)	0.82	0.18	0	0.06	0.41
AcPhos-SBA (1) AW	0.24	0.76	0	0.08	0.46
AcPhos-SBA (2)	0.78	0.22	0	0.04	0.37
AcPhos-SBA (2) AW	0.41	0.59	0	0.04	0.43
AcPhos-SBA (3)	0.12	0.71	0.17	0.1	0.44
AcPhos-SBA (3) AW	0.12	0.70	0.17	0	0.43
AcPhos-SBA (4)	0.09	0.74	0.18	0.1	0.44
AcPhos-SBA (4) AW	0.01	0.74	0.25	0	0.43

Figure 5.7b). These changes are consistent with hydrolysis of ethoxy groups from the silane upon contact with acidic media. Similar differences can be observed upon comparing the pristine spectra for AcPhos-SBA (1 and 2) with those of AcPhos-SBA (3 and 4). In contrast to AcPhos-SBA (1) and (2), the acid-washed spectra are nearly identical to the pristine spectra for both AcPhos-SBA (3) and (4).

Figures 5.9 and 5.10 show the ^{29}Si ^{29}C{^{1}H} CP/MAS spectra for AcPhos-SBA (1-4, respectively). The ^{29}Si NMR spectra for silica typically has three spectral resonances. These are named Q^n, for the species $SiO_n(OH)_{4-n}$. The Q^4, Q^3, and Q^2 species are SiO_4, $SiO_3(OH)$, and $SiO_2(OH)_2$, and give rise to peaks at approximately -110.2, -101.9, and -90.8 ppm, with respect to TMS, respectively. These chemical shift values are consistent with previous reports [139, 140]. The amplitude of peaks from surface silicon atoms is enhanced in cross-polarized spectra due to their proximity to ^{1}H. Upon functionalization, some of the surface silanols are replaced by siloxanes, which give rise to a second group of resonances between approximately -49 and -70 ppm. These are the T^m species, corresponding to $RSiO_m(OX)_{3-m}$, where R is the organofunctional group and X is H or an alkoxy group. When water is used during functionalization, the T^1, T^2, and T^3 resonances are usually interpreted as corresponding to isolated ligand monomers, dimers or polymer chain terminals, and more extended polymer networks, respectively. In principle, similar chemical shifts appear for siloxanes which form one, two, or three covalent bonds to surface silanols. In the spectra reported here, the T^1, T^2, and T^3 resonances are observed at -49.7, -57.7, and -66.6 ppm, with respect to TMS, respectively. These chemical shift values are also consistent with previous reports [10, 141].

As these spectra were also collected using cross-polarization, the integrated peak areas cannot be used to quantify the different species. However, since they were collected under identical conditions, the relative peak ratios between samples can be compared to characterize the functional layer qualitatively. Table 5.3 summarizes the percent areas for the T and Q peaks for all four pristine and acid-washed samples.

In comparing the pristine materials, it can be seen that AcPhos-SBA (3) and (4) are very similar to each other. Unlike the spectra for AcPhos-SBA (1) and (2), those of AcPhos-SBA

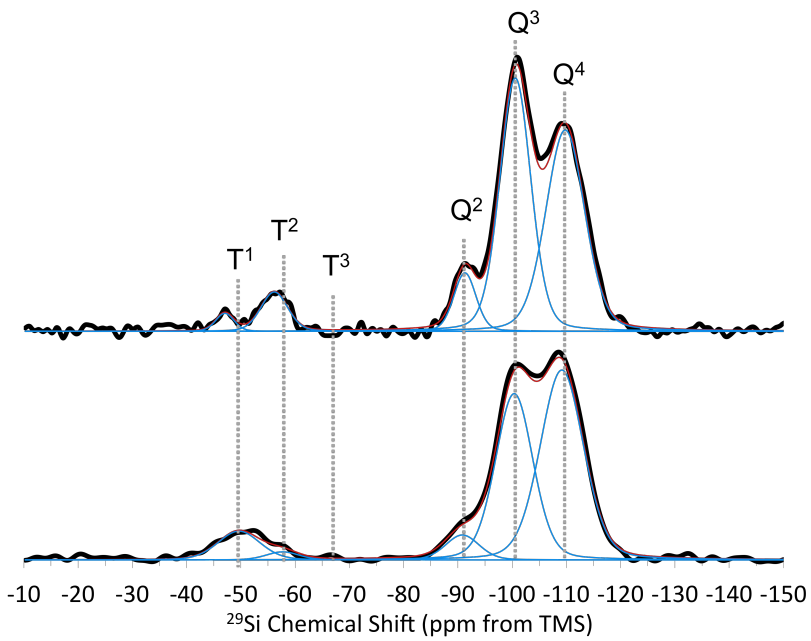

(a) ^{29}Si{^{1}H} CP/MAS spectra for AcPhos-SBA (1) pristine (bottom) and acid-washed (top). Spectra were normalized to the peak at -109 ppm. Experimental data is shown in black. The blue lines show the spectral deconvolution, and the red line is their sum. Gray dashed lines mark the positions of the Q^n and T^m peaks.

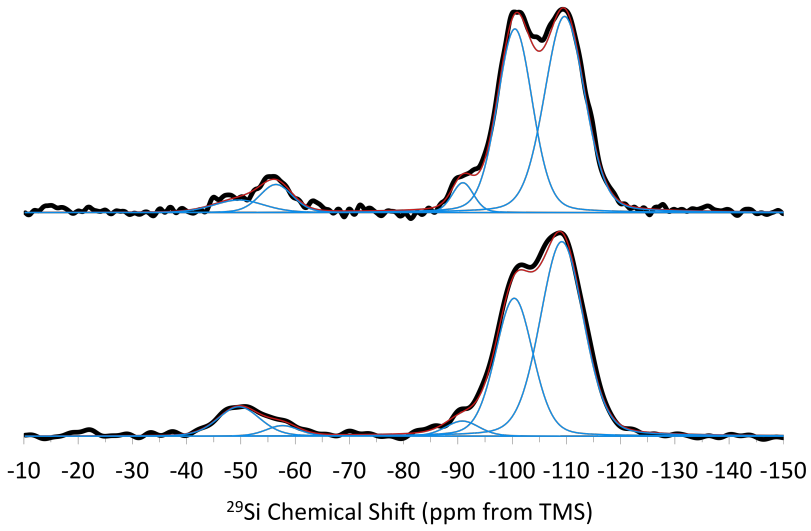

(b) ^{29}Si{^{1}H} CP/MAS spectra for AcPhos-SBA (2) pristine (bottom) and acid-washed (top). Spectra were normalized to the peak at -109 ppm. Experimental data is shown in black. The blue lines show the spectral deconvolution, and the red line is their sum.

Figure 5.9

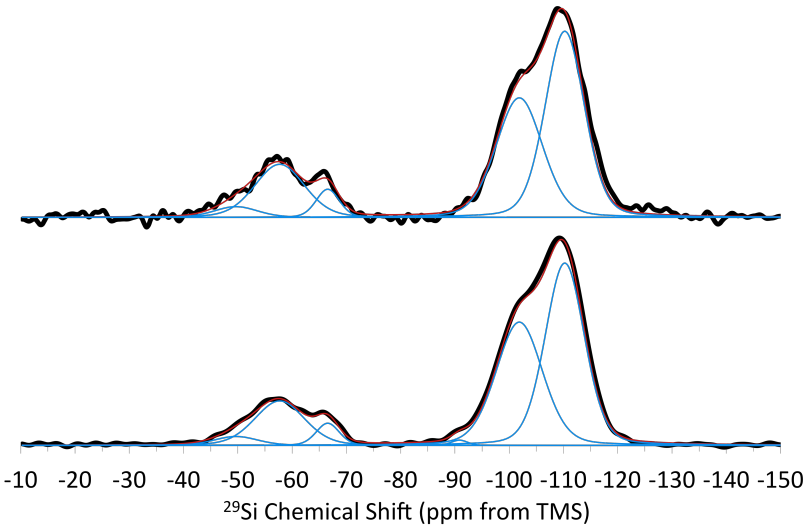

(a) ^{29}Si{^{1}H} CP/MAS spectra for AcPhos-SBA (3) pristine (bottom) and acid-washed (top). Spectra were normalized to the peak at -109 ppm. Experimental data is shown in black. The blue lines show the spectral deconvolution, and the red line is their sum.

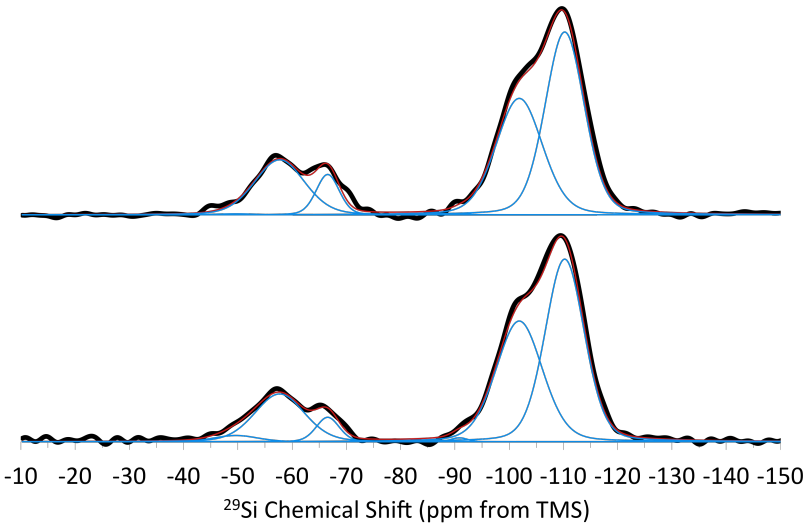

(b) ^{29}Si{^{1}H} CP/MAS spectra for AcPhos-SBA (4) pristine (bottom) and acid-washed (top). Spectra were normalized to the peak at -109 ppm. Experimental data is shown in black. The blue lines show the spectral deconvolution, and the red line is their sum.

Figure 5.10

(3) and (4) have a significant T^3 peak, and the T^2 peaks make a up a much larger percentage of the functionalized silicon atoms. Compared to AcPhos-SBA (3) and (4), AcPhos-SBA (1) and (2) have a larger relative population of Q^2 and Q^3 Si atoms, which is consistent with higher surface silanol content. Pristine AcPhos-SBA (2) has a slightly higher percentage of T^2 and a slightly lower percentage of Q^3 compared to pristine AcPhos-SBA (1). Qualitative comparison of the spectra and the peak ratios in Table 5.3 shows that in general the structure of the functional layer does not change upon contact with acidic solutions for AcPhos-SBA (3) and (4), but it changes significantly for AcPhos-SBA (1) and (2). For both AcPhos-SBA (1) and (2), the T^1 peak amplitude is diminished, and the the Q^3:Q ratio has increased significantly, which again indicates that the silanol content has increased upon contact with acid.

5.5 Single-Pulse ^{31}P NMR Spectroscopy

^{31}P single-pulse (SP) MAS NMR spectra for AcPhos-SBA (1) and (2) show a single resonance around 23 ppm with respect to H_3PO_4. This indicates that there is only one type of chemical environment for the acetamide phosphonates on the surface. The chemical shift and peak shape do not change after contact with acid for these materials. Their spectra are shown in Figure 5.11.

The ^{31}P SP/MAS NMR spectra for AcPhos-SBA (3) and (4) are more complicated, though they are very similar to one another and do not appreciably vary between the pristine and acid-washed samples. As Figure 5.12 shows, each of these spectra show two distinct resonances: one around 23.0 ppm and one at approximately 15 ppm.

Similar observations have been made for silica functionalized with phosphonic acid ligands [71, 72, 190–192]. These studies have attributed the lower chemical shift peak to hydrogen bonding interactions, though there is some disagreement in the literature about the assignment of this peak. A phosphonic acid group involved in hydrogen bonding can act as either a hydrogen bond donor through P−OH or as hydrogen-bond acceptors through O=P. Bibent et al. [72] argue that only the second interaction would involve a significant change int he local electron density of the phosphorus atom, resulting in a chemical shift. However, if O=P acts as a hydrogen bond acceptor, it will serve to de-shield the phosphorus atom, resulting in a chemical shift in the opposite direction (towards higher chemical shift value). Pan et al. [71] make the opposite assignment and argue that the lower chemical shift peak is due to phosphonic acid serving as a hydrogen bond donor. Yang et al. [193] conducted ^{31}P NMR measurements on dimethyl methylphosphonate (DMMP) and its hydrolysis products. They observe a chemical shift of $\delta_P = 36.8$ ppm for DMMP and of $\delta_P = 32.6$ ppm and 29.2 ppm for the first and second hydrolysis products, respectively. Broad peaks observed between 20 and 30 ppm are assigned to hydrolyzed, deprotonated methylphosphonate.

Therefore in the present work, the peak observed at 23 ppm in AcPhos-SBA (3) and (4) are likely a mixture of diethyl phosphonate P−OEt and hydrolyzed phosphonic acid groups P−OH. The resonance appearing at a chemical shift of 15 ppm is assigned to deprotonated

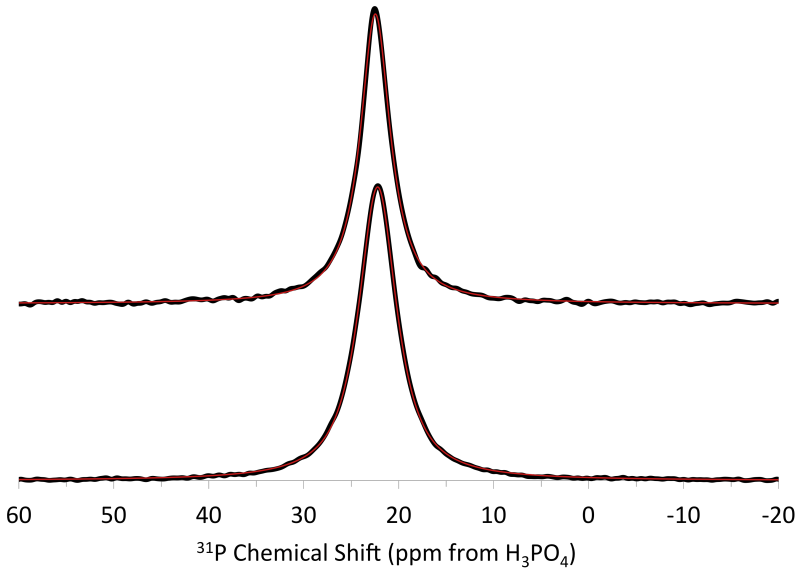

(a) ^{31}P single-pulse MAS spectra for AcPhos-SBA (1) pristine (bottom) and acid-washed (top). Spectra were normalized to the single peak at 22.2 ppm. Experimental data is shown in black, and the red line is the spectral fit. No ^{1}H decoupling was used in the collection of these spectra.

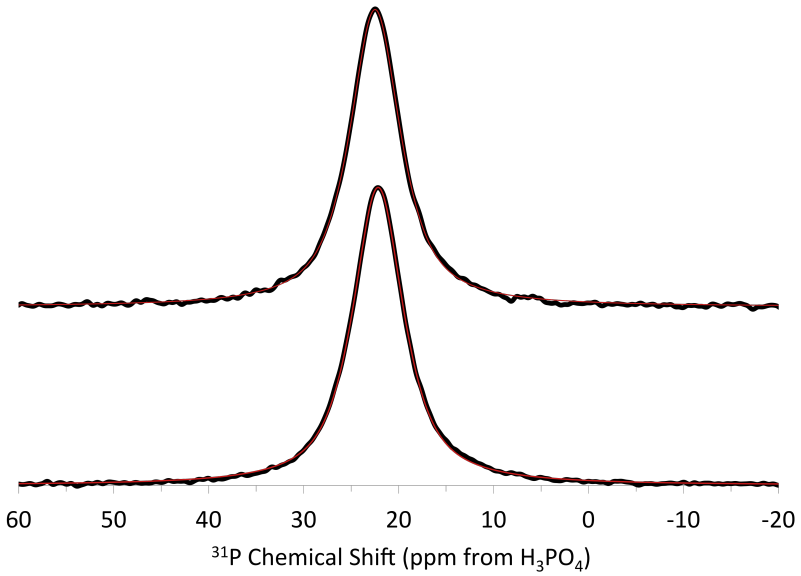

(b) ^{31}P single-pulse MAS spectra for AcPhos-SBA (2) pristine (bottom) and acid-washed (top). Spectra were normalized to the single peak at 22.2 ppm. Experimental data is shown in black, and the red line is the spectral fit. No ^{1}H decoupling was used in the collection of these spectra.

Figure 5.11

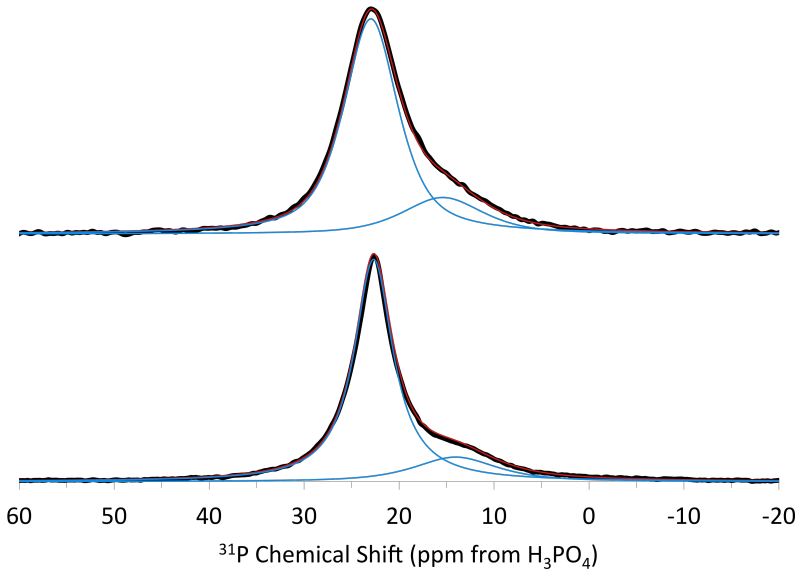

(a) ^{31}P single-pulse MAS spectra for AcPhos-SBA (3) pristine (bottom) and acid-washed (top). Spectra were normalized to the single peak at 22.7 ppm. Experimental data is shown in black. Blue lines show the peak deconvolution, and the red line is their sum. No ^{1}H decoupling was used in the collection of these spectra.

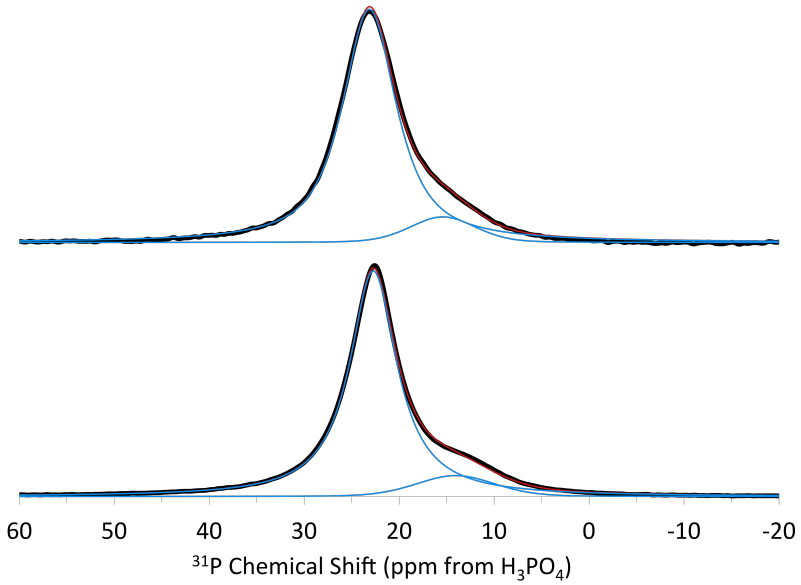

(b) ^{31}P single-pulse MAS spectra for AcPhos-SBA (2) pristine (bottom) and acid-washed (top). Spectra were normalized to the single peak at 22.7 ppm. Experimental data is shown in black, and the red line is the spectral fit. No ^{1}H decoupling was used in the collection of these spectra.

Figure 5.12

Table 5.4: Ligand quantification using tripheylphosphine and ^{31}P NMR

Material	Ligand Content (mmol/g)
AcPhos-SBA (1)	2.9
AcPhos-SBA (2)	1.5
AcPhos-SBA (3)	1.7
AcPhos-SBA (4)	3.5

phosphonic acid groups P−O$^-$, which may then be involved in hydrogen-bonding interactions of the type P−O−H−O−P.

Ligand Quantification using Triphenylphosphine and Single-Pulse ^{31}P NMR

The amount of ligand loaded onto the surface was determined for each material using single-pulse ^{31}PNMR spectroscopy. Each material was thoroughly mixed with triphenylphosphine, which has a chemical shift of δ_P = -7 ppm with respect to H_3PO_4. For single-pulse spectra, the integrated peak area is proportional to the number of phosphorus atoms in each chemical shift environment. Thus, by knowing the mass of triphenylphosphine and the mass of AcPhos-SBA loaded into the rotor, the relative peak areas can be used to calculate the number of ligands per gram of material. Table 5.4 summarizes the results.

The phosphonate ligand content of AcPhos-SBA (3) and (4) presented in Table 5.4 should be considered an estimate. For these two materials, the ^{31}P NMR spectra contained a sharp peak at δ_P = 26.2 ppm, which is consistent with the chemical shift of triphenylphosphine oxide [194, 195]. Therefore, it appears that the triphenylphosphine internal standard is reacting to form triphenylphosphine oxide. The ligand loading for these materials were calculated by adding the sum of the integrated peak areas of the -7 ppm and 26.2 ppm peaks to obtain the relative number of phosphorus atoms from the internal standard, as opposed to just the integrated area for the -7 ppm peak. Before quantitative arguments or conclusions are made based on these ligand loadings, they must be re-measured using an internal standard, such as hydroxylapatite, that is not reactive with the AcPhos-SBA materials.

5.6 Comparison of Ligand Distribution

In previous work ^{31}P-^{31}P homonuclear dipolar coupling measurements via the DQ-DRENAR (Double-Quantum-based Dipolar Recoupling effects Nuclear Alignment Reduction) were used to assess the density of the functional layer for diethylphosphoatoethyl-functionalized SBA-15 [166]. The DQ-DRENAR method consists of two experiments, as described in Chapter 3. In the S' experiment, a series of POST-C7 pulse sequences is applied to achieve

Table 5.5: Dipolar coupling constants measured for AcPhos-SBA using DQ-DRENAR

Material	$\sum_{j<k} b_{jk}^2 (Hz^2 \times 10^5)$
AcPhos-SBA (1)	1.9 ± 0.1
AcPhos-SBA (2)	2.64 ± 0.03
AcPhos-SBA (3) (23 ppm)	2.93 ± 0.07
AcPhos-SBA (4) (23 ppm)	2.45 ± 0.09
AcPhos-SBA (4) (15 ppm)	5.7 ± 0.3

recoupling between ^{31}P nuclei, which results in a decrease in signal amplitude. The control S_0 experiment applies the same POST-C7 pulse sequences, but they are out of phase by 90 °, which prevents recoupling. The difference in signal amplitude, $\Delta S = S_0 - S'$ can be related to the dipolar coupling constant through:

$$\frac{S_0 - S'}{S_0} = \frac{0.86\pi^2}{15} \cdot b_{jk}^2 \cdot (NT_r)^2 \tag{5.1}$$

where b_{jk} is the dipolar coupling constant between two spins j and k. Ren and Eckert [164, 165] show that this method can be extended to multi-spin systems with a distribution of pair-wise dipolar coupling constants, characterized by the sum of all pair-wise dipolar coupling interactions, $\sum_{j<k} b_{jk}^2$.

Figure 5.13 shows the DQ-DRENAR data for the four AcPhos-SBA materials. For AcPhos-SBA (3) and (4), the integrated peak area for the 23 ppm resonance was used to calculate $\Delta S/S_0$. Figure 5.14 compares the $\Delta S/S_0$ versus NT_r curves for the 23 ppm peak and the 15 ppm peak of AcPhos-SBA (4). The data points shown in Figures 5.13 and 5.14 were fit with parabolic functions to extract the $\sum_{j<k} b_{jk}^2$ values for each material, which are summarized in Table 5.5.

AcPhos-SBA (1) demonstrated the lowest dipolar coupling strength, while those of AcPhos-SBA (2), (3), and (4) are higher. A higher ^{31}P-^{31}P dipolar coupling constant indicates a higher average density of phosphonate groups on the surface. Therefore, AcPhos-SBA (1) has the lowest average density, and AcPhos-SBA (2), (3), and (4) have a higher average density of functional groups. For AcPhos-SBA (4), the phosphorus environment corresponding to the peak at 15 ppm demonstrates stronger dipolar coupling than that at 23 ppm. Therefore, the high dipolar coupling constant calculated for the 15 ppm phosphorus environment shows that it has the highest density of phosphonate groups of all materials measured.

5.7 Batch Contact Experiments with U(VI)

Dependence of sorption on pH

The ability of each AcPhos-SBA material to extract U(VI) from various nitric acid media was compared in a series of batch contact experiments. These experiments were conducted both to compare the materials' performance in extraction of uranyl ions from solution, but

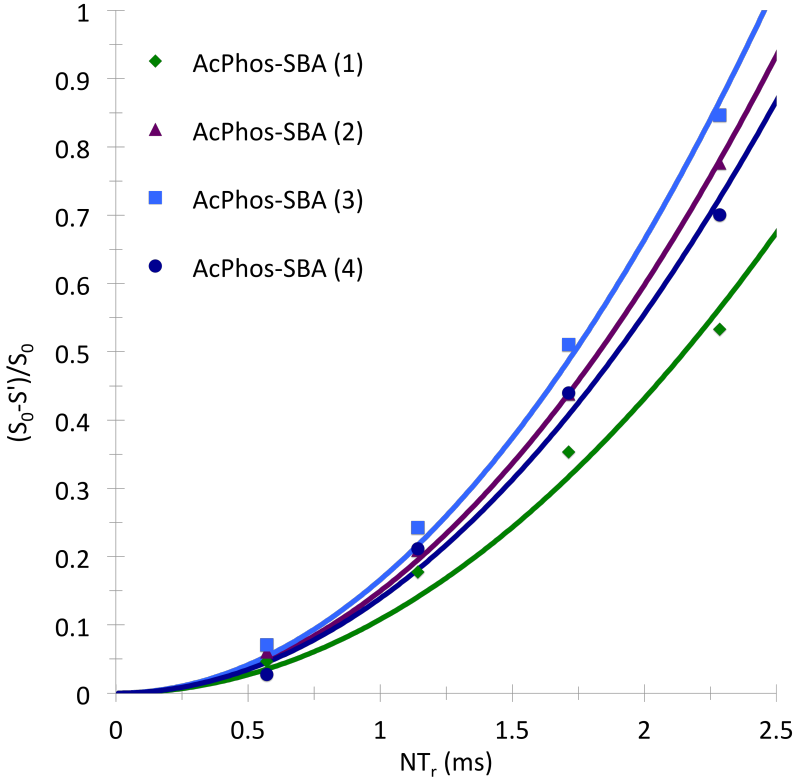

Figure 5.13: DQ-DRENAR data for AcPhos-SBA (1), (2), (3), and (4), acquired at a MAS rate of 7 kHz. For AcPhos-SBA (3) and (4), the integrated peak area for the 23 ppm resonances was used to calculate $\Delta S/S_0$.

also to determine ideal conditions for obtaining the maximum amount of U(VI) loaded onto the samples, which was necessary for preparation of NMR samples. In a typical batch experiment, solid samples are pre-equilibrated with the proper solution for approximately 15 hours before spiking the slurry with ^{233}U and/or ^{238}U to achieve the desired concentration. Samples were rocked continuously, and phase separation was achieved through centrifugation. The concentration of U(VI) in solution was monitored over time using liquid scintillation counting. Experimental details are given in Section 6.7.

Figure 5.15 compares the percent sorption of U(VI) from various concentrations of nitric acid for AcPhos-SBA (1), (2), and (3). The sorption behavior varies widely among the materials. AcPhos-SBA (1) does not extract any significant quantity of U(VI) under any conditions tested. AcPhos-SBA (2) performs slightly better at the lower acid concentrations. It sorbed up to 34% of uranyl present in solution at pH 3. However, at acid concentrations higher than 0.1 M, AcPhos-SBA (2) also did not extract any measurable amount of U(VI) from solution. In contrast, AcPhos-SBA (3) sorbed significant quantities of U(VI) in all conditions tested, including greater than 95% from solutions between pH 1 and 3, and greater than 40% from solutions with nitric acid concentrations between 1 and 3 M.

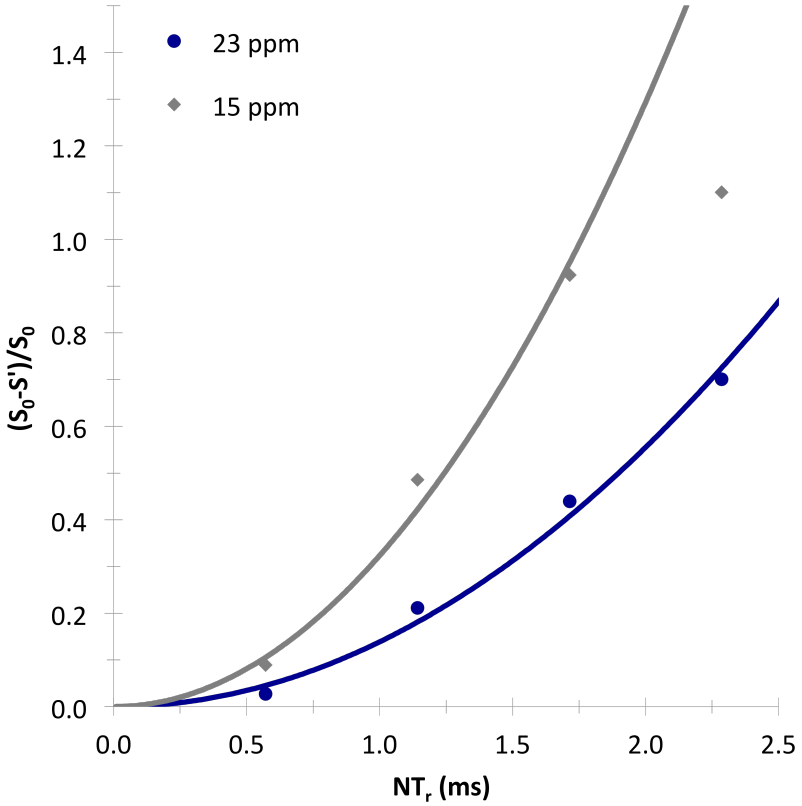

Figure 5.14: DQ-DRENAR data for the 23 ppm (blue circles) and 15 ppm (grey diamonds) resonances of AcPhos-SBA(4).

For the experiments summarized in Figure 5.15, the initial solution concentration of U(VI) was 2×10^{-5} M. A follow-up experiment was conducted to test for sorption at a lower concentration, 1×10^{-6} M (not shown), to ensure that the difference in sorption was not solely due to differences in ligand loading for the AcPhos-SBA materials. The percent sorption for AcPhos-SBA (2) was higher; however, that of AcPhos-SBA (1) was not. In the limits tested, therefore, it does not appear that the inability of AcPhos-SBA(1) to extract U(VI) from solution is simply due to low ligand loading during functionalization.

Dependence of Sorption on Ionic Strength

As discussed in Chapter 4, previous work showed that increasing the ionic strength resulted in an increase in extraction of U(VI) from nitric acid solutions by phosphonate-functionalized SBA-15. Therefore, sorption of U(VI) from pH 2 and pH 3 solutions containing no additional salt and 3 M $NaNO_3$ was compared for AcPhos-SBA (2), (3), and (4). Figure 5.16 summarizes the results. As these experiments were conducted at a higher initial [U(VI)] than those measuring the pH dependence of sorption, the percent sorption is lower for the samples. At pH 2, both AcPhos-SBA (3) and (4) demonstrate slightly higher sorption of U(VI) at high

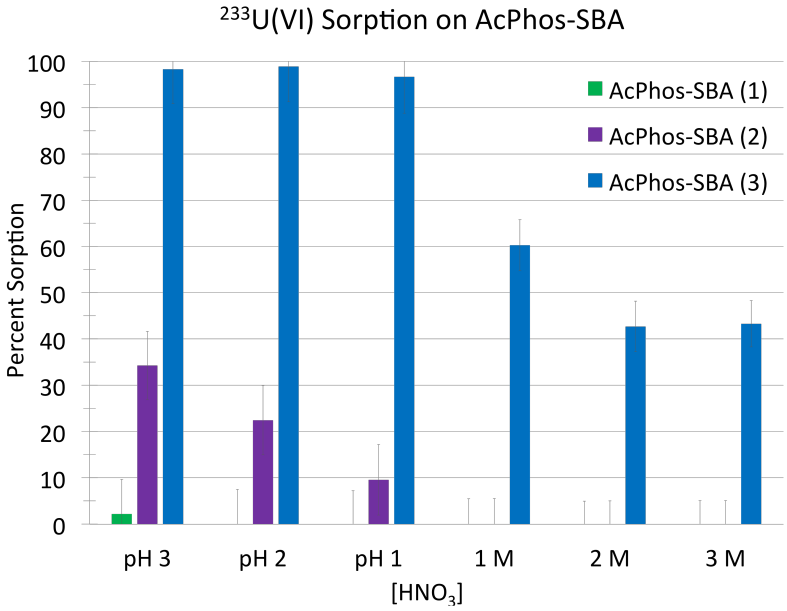

Figure 5.15: Percent sorption of ^{233}U(VI) by AcPhos-SBA materials as a function of nitric acid concentration. The initial concentration of U(VI) in solution was 2×10^{-5} M. No additional salts were added to control for ionic strength. The data points shown represent sorption after 1 hour of mixing time.

ionic strength compared to that at low ionic strength. However, the difference is small, and is within the uncertainly of the measurement for AcPhos-SBA (3). At pH 3, the differences are more significant. The amount of U(VI) extracted from high ionic strength solutions is nearly double the amount at low ionic strength for both AcPhos-SBA (3) and (4). Under these conditions, this difference amounts to an additional 75 μmol sorbed U(VI) g^{-1} silica. For this reason, these conditions were chosen for measurement of the U(VI) sorption isotherms, as well as preparation of U(VI) and acid-washed NMR samples.

U(VI) Sorption Isotherms

The U(VI) sorption isotherms for non-functionalized SBA, AcPhos-SBA (2), (3), and (4) were measured for pH 3 solutions containing 3 M $NaNO_3$. The resulting curves were linearized and fit with both the Langmuir and Freundlich sorption isotherm models. The isotherms of AcPhos-SBA (3) and (4) were better described by the Langmuir model, while that of non-functionalized SBA was better described by the Freundlich model. Both models provided a mediocre fit for the isotherm of AcPhos-SBA (2). These fits are shown in figure 5.17. The parameters extracted from the data are summarized in Table 5.6.

The Langmuir isotherm describes monolayer sorption to uniform binding sites, all with equal binding energy. Its linearized form is:

$$\frac{C_e}{q_e} = \frac{1}{K_{eq} q_m} + \frac{C_e}{q_m} \tag{5.2}$$

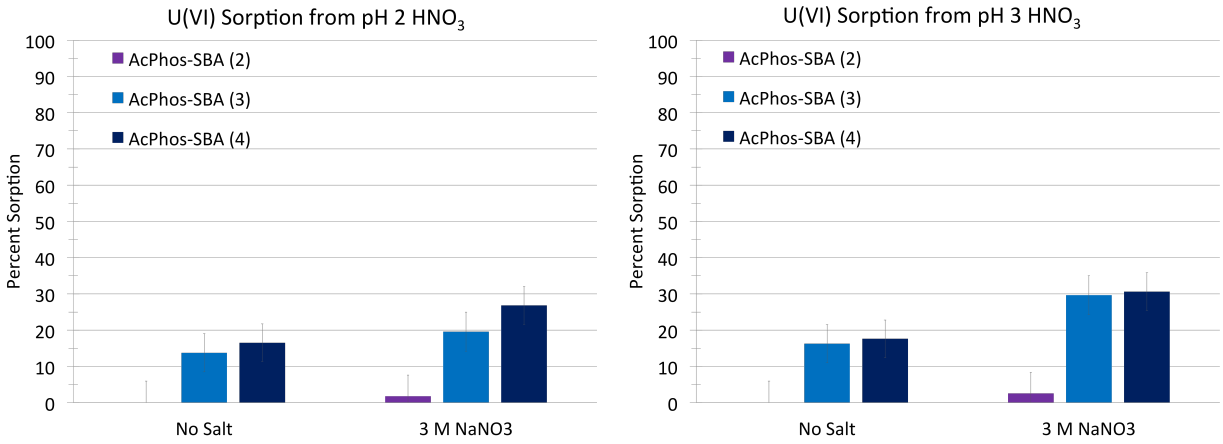

Figure 5.16: Comparison of U(VI) sorption by AcPhos-SBA from solutions with no salt added and 3 M $NaNO_3$ solutions at pH 2 (left) and pH 3 (right). $[U(VI]_{initial} = 5 \times 10^{-4}$ M, including $[^{233}U(VI)] = 2 \times 10^{-5}$ M. Data points shown represent percent sorption after 1 hour of mixing time.

Table 5.6: Langmuir and Freundlich fit parameters for U(VI) isotherms on AcPhos-SBA

Material	Langmuir Isotherm Model		Freundlich Isotherm Model	
	q_m (μmol g^{-1})	K_{eq} (mL μmol^{-1})	K_F (μmol$^{(1-1/n)}$ mL$^{1/n}$ g^{-1})	n
SBA	140 ± 276	1 ± 1	64 ± 16	1.1 ± 0.1
AcPhos-SBA (2)	37 ± 7	11 ± 5	42 ± 12	2.6 ± 0.7
AcPhos-SBA (3)	157 ± 3	119 ± 50	250 ± 58	3.5 ± 0.6
AcPhos-SBA (4)	162 ± 3	114 ± 41	256 ± 81	3.4 ± 0.9

where C_e is the equilibrium concentration of U(VI) (μmol mL^{-1}), q_e is the amount of U(VI) sorbed at equilibrium (μmol g^{-1}), K_{eq} is the Langmuir adsorption constant (equivalent to the equilibrium constant, in mL μmol^{-1}), and q_m is the monolayer sorption capacity (μmol g^{-1}).

In contrast, the Freundlich isotherm describes sorption to heterogeneous biding sites with a distribution of binding energies. Its linearized form is:

$$\ln(q_e) = \ln(K_F) + \frac{1}{n}\ln(C_e) \tag{5.3}$$

where K_F is the Freundlich adsorption constant related to the sorption capacity (μmol$^{(1-1/n)}$ mL$^{1/n}$ g^{-1}), and n is the Freundlich constant related to the energy of adsorption.

AcPhos-SBA (3) and (4) had much higher sorption capacities than AcPhos-SBA (2). The sorption capacities and equilibrium constants calculated for AcPhos-SBA (3) and (4) were the same within the uncertainty of the fit. While the sorption capacity calculated for AcPhos-SBA (2) was similar to that of non-functionalized SBA, the equilibrium constant was much higher, indicating a more stable complex formed with U(VI). The Freundlich model is

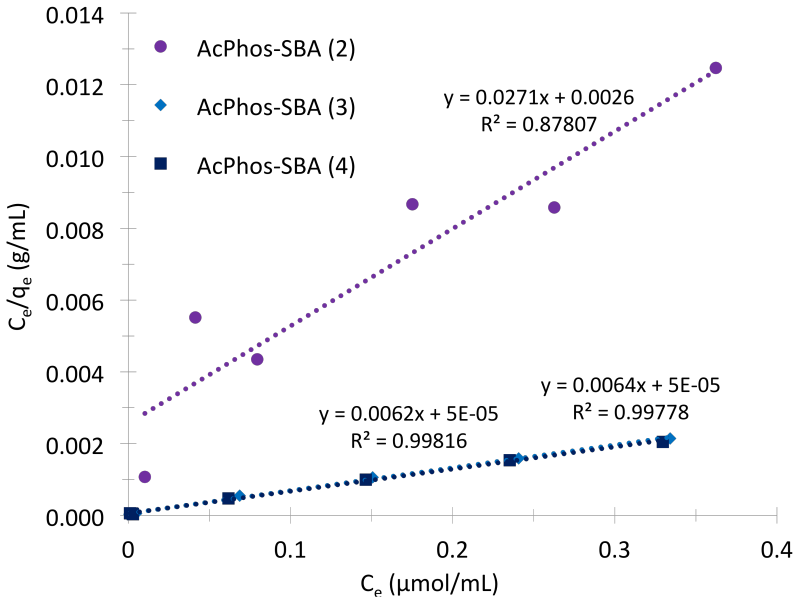

(a) Linearized Langmuir isotherm fit for U(VI) sorption from 3 M $NaNO_3$ solutions at pH 3 by AcPhos-SBA (2), (3), and (4). C_e is the equilibrium concentration of U(VI) in solution in μmol mL^{-1} and q_e is the equilibrium loading of U(VI) on the solid in μmol g^{-1}.

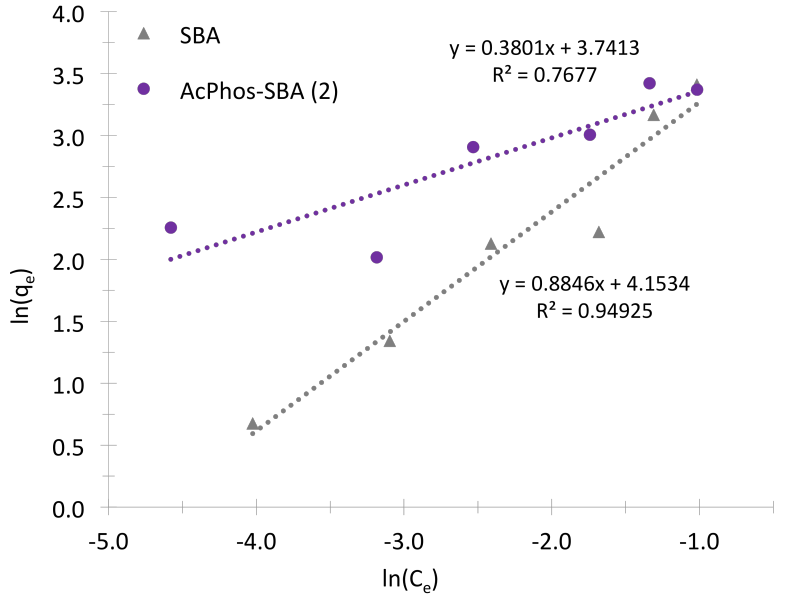

(b) Linearized Freundlich isotherm fit for U(VI) sorption from 3M $NaNO_3$ solutions at pH 3 by AcPhos-SBA (2) and non-functionalized SBA. C_e is the equilibrium concentration of U(VI) in solution in μmol mL^{-1} and q_e is the equilibrium loading of U(VI) on the solid in μmol g^{-1}.

Figure 5.17

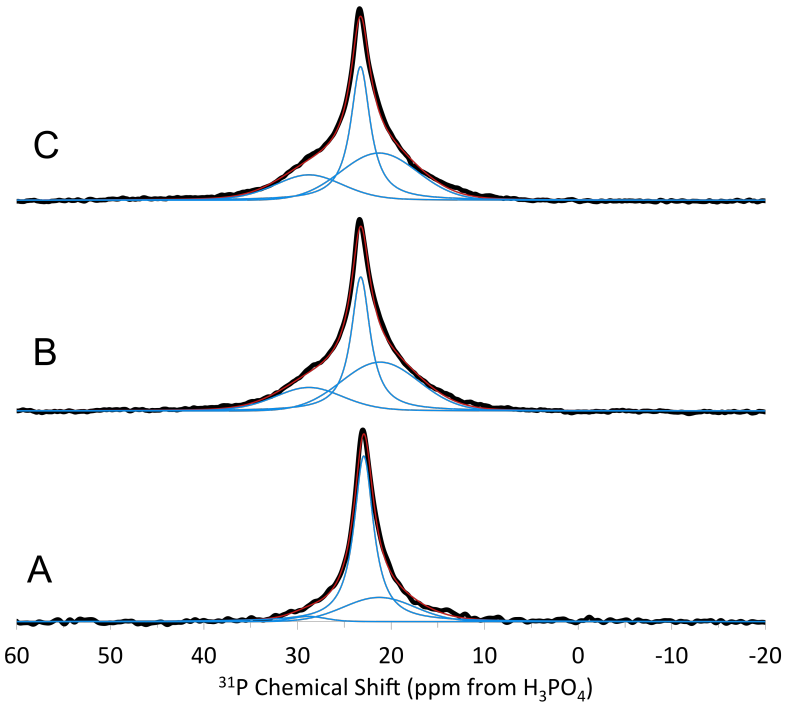

Figure 5.18: Single-pulse ^{31}P NMR spectra for a) U(VI)-AcPhos-SBA (2), b) U(VI)-AcPhos-SBA (3), and c) U(VI)-AcPhos-SBA (4). Spectra were collected with no ^{1}H decoupling.

consistent with sorption to amorphous silica, which has many different types and geometries of binding interactions with a distribution of binding energies.

5.8 ^{31}P NMR Spectroscopy of U(VI)-AcPhos-SBA Samples

The single-pulse ^{31}P NMR spectra for U(VI)-AcPhos-SBA (2), (3), and (4) are presented in Figure 5.18. Sample preparation is described in Section 6.8. It is important to note that samples were air-dried and not rinsed with isopropanol or stored under vacuum, as were the acid-washed samples. Each of the spectra demonstrate three resonances, and the fit parameters for each peak deconvolution are reported in Table 5.7.

The peak shapes and widths of the U(VI)-AcPhos-SBA samples are quite different from their pristine and acid-washed counterparts. For all three sample types (pristine, acid-washed, and U(VI)-contacted), AcPhos-SBA (3) and (4) are very similar. Instead of the two resonances observed in the pristine and acid-washed sample spectra, there are three resonances at approximately 21, 23, and 29 ppm with respect to H_3PO_4. The resonance at 21 ppm is a very broad shoulder to the relatively sharp resonance at 23 ppm. The 23 ppm resonance is narrower than it is in the pristine and acid-washed samples' spectra. Meanwhile,

Table 5.7: Fit parameters used to deconvolute the ^{31}P spectra for the U(VI)-AcPhos-SBA samples

Material	δ_P (ppm)	FWHM (ppm)	Shape[†]	Relative Peak Area (%)
AcPhos-SBA (2)	21.3	8.9	1	26.6
	22.9	2.5	0	70.3
	28.8	4.4	0.8	3.1
AcPhos-SBA (3)	21.3	9.6	1	41.6
	23.2	2.4	0	39.4
	28.8	8.6	0.8	19.0
AcPhos-SBA (4)	21.3	2.5	0	39.5
	23.3	2.5	0	40.1
	28.8	8.6	0.8	20.4

[a]Value gives the shape n of the pseudo-Voigt functions, $V_p(x) = nG(x) + (1 - n)L(x)$, where $G(x)$ and $L(x)$ are the Gaussian and Lorentzian distribution functions, respectively.

the low chemical shift ($\approx$ 15 ppm) is not present at all in the spectra for U(VI)-AcPhos-SBA samples. The changes in peak chemical shift, width, and shape are most likely due to a combination of pH 3 aqueous solution adsorbing to the silica surface, which changes the protonation environment and the hydrogen-bonding interaction observed for the pristine and acid-washed samples, as well as the sorption of U(VI) by the AcPhos ligands, as will be discussed later.

Single-pulse ^{31}P NMR spectra were also collected using continuous wave decoupling on the ^{1}H channel for AcPhos-SBA (4) pristine, acid-washed, and U(VI)-contacted. These spectra are shown in Figure 5.19. Using proton decoupling slightly improved the resolution of the spectra, which aided in fitting both the ^{1}H decoupled and the non-decoupled spectra. However, it did not reveal any additional information about the structural features of the three different samples.

5.9 Discussion

Effect of Ligand Polymerization on Functional Layer Stability

The structure and stability of the functional layer for each AcPhos-SBA can be understood by comparing their pristine and acid-washed ^{13}C{^{1}H} and ^{29}Si{^{1}H} CP/MAS NMR spectra. Contact with acidic solutions resulted in further hydrolysis of the Si−OEt groups for AcPhos-SBA (1), as evidenced by the decrease in signal amplitude in the C_7 and C_3 resonances. This change is even more obvious for the pristine versus acid-washed spectra for AcPhos-SBA (2) (black arrows in Figure 5.7b). Similar differences can be observed upon comparing the

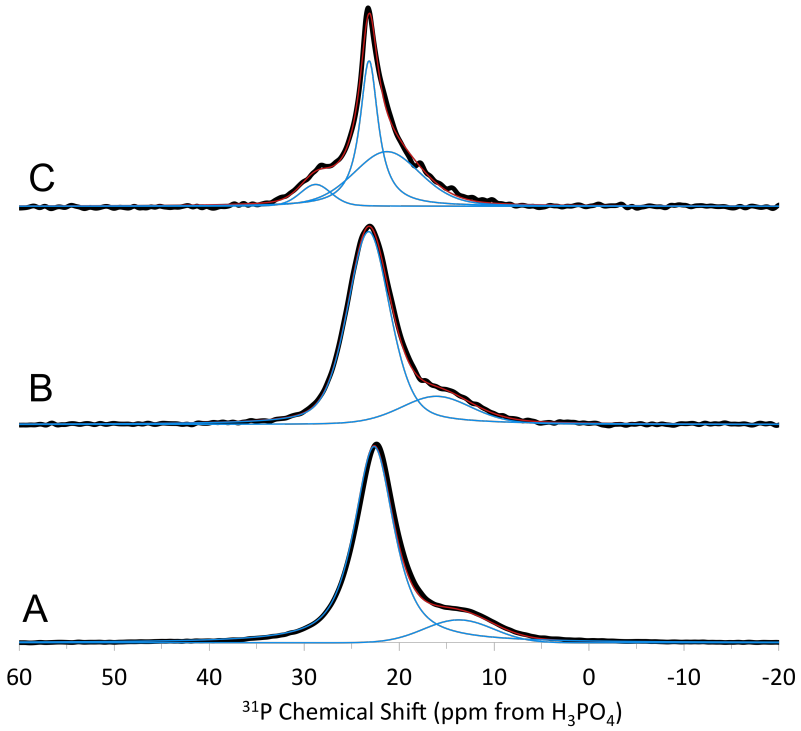

Figure 5.19: ^{1}H decoupled single-pulse ^{31}P NMR spectra for AcPhos-SBA (4) pristine (A), acid-washed (B), and U(VI)-contacted (C).

pristine spectra for AcPhos-SBA (1) and (2) with those of AcPhos-SBA (3) and (4). AcPhos-SBA (3) and (4) were synthesized with pyridine, a basic catalyst, which increases the rate of hydrolysis for the siloxane esters [133, 136]. As a result, the resonances corresponding to the siloxane esters are almost completely absent in their ^{13}C{^{1}H} CP/MAS spectra. This can be interpreted as more complete hydrolysis of the Si−OEt groups during the functionalization procedure. The acid-washed spectra are very similar to the pristine spectra for both AcPhos-SBA (3) and (4), which indicates that no significant structural changes occurred upon contact with nitric acid.

The extent of reaction between the siloxane ligand and the silica surface during functionalization can be evaluated across the four different materials by comparing their ^{29}Si{^{1}H} CP/MAS NMR spectra. Figure 5.20 compares the pristine spectra for each material. The T populations of AcPhos-SBA (1) and (2) are dominated by the monomeric species, T^1, indicating relatively low cross-linking between ligands during functionalization. The slightly higher $T^2 : T$ ratio and slightly lower $Q^2 : Q$ and $Q^3 : Q$ ratios observed for AcPhos-SBA (2) compared to AcPhos-SBA (1) are evidence that a longer surface hydration time and a longer reflux time during functionalization resulted in slightly higher polymerization of ligands and a greater degree of functionalization. For the most part, however, there is little difference between the spectra for AcPhos-SBA (1) and (2). However, the ^{29}Si{^{1}H} CP/MAS spectra

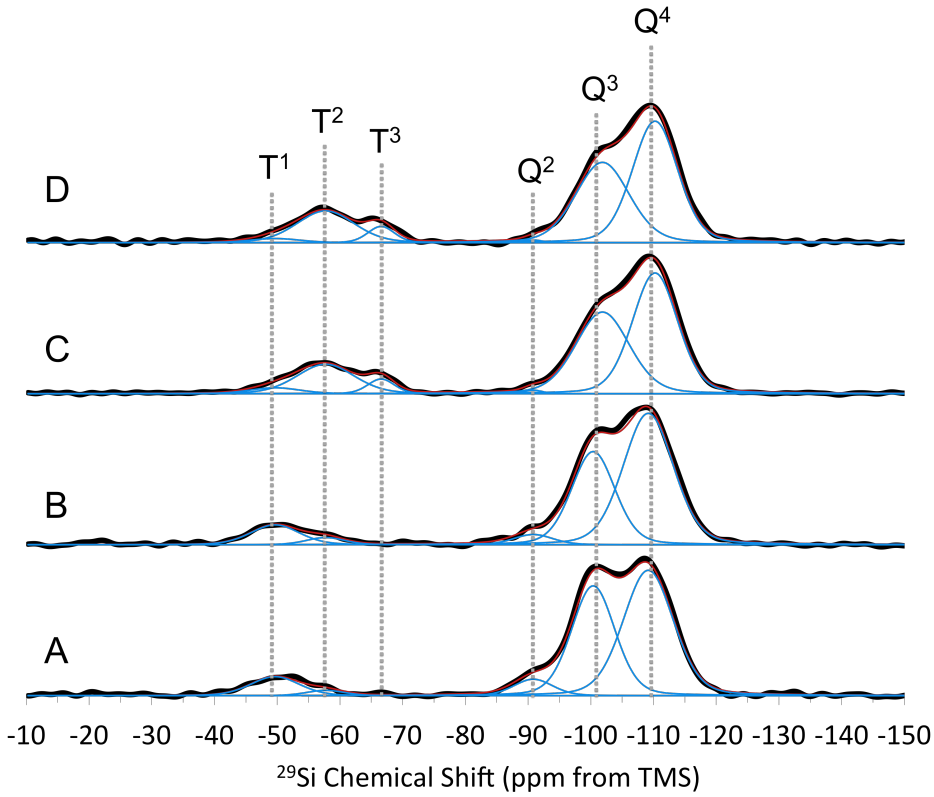

Figure 5.20: Comparison of ^{29}Si{^{1}H} CP/MAS spectra of pristine a) AcPhos-SBA (1), b) AcPhos-SBA (2), c) AcPhos-SBA (3), and d) AcPhos-SBA (4). The gray dashed lines show the positions of the Q^n and T^m peaks.

for the pristine AcPhos-SBA (3) and (4), while consistent with each other, are very different from those of AcPhos-SBA (1) and (2). The T populations of the AcPhos-SBA (3) and (4) spectra are dominated by T^2 and T^3 species. Their ^{13}C{^{1}H} CP/MAS spectra indicated more complete hydrolysis of ethoxy groups. This in turn led to a greater degree of cross-linking between ligands and/or greater reaction with surface silanols, mediated by the basic catalyst, pyridine. Additionally, compared to AcPhos-SBA (1) and (2), AcPhos-SBA (3) and (4) show reduced $Q^2 : Q$ and $Q^3 : Q$ ratios, which is consistent with reduced surface silanol content. This means that the degree of functionalization is higher for AcPhos-SBA (3) and (4) than for (1) and (2).

Comparison of the pristine and acid-washed samples reveals two general categories: the ^{29}Si spectra of AcPhos-SBA (3) and (4) do not change after contact with acid, but those of AcPhos-SBA (1) and (2) do change significantly. For both AcPhos-SBA (1) and (2), the population of T species shifts towards more T^2 and less T^1, and the $Q^3 : Q$ ratio increases, especially for AcPhos-SBA (1). Therefore, contact with acidic solutions changes the functional layer for AcPhos-SBA (1) the most, changes that of AcPhos-SBA (2) to a lesser extent, and does not measurably change those of AcPhos-SBA (3) and (4). The stability of

the functional layer at the silica surface correlates with the stability of the organic layer at the silica-ligand interface. The $^{13}C\{^1H\}$ and $^{29}Si\{^1H\}$ CP/MAS NMR spectra for AcPhos-SBA (1) and (2) both indicated structural changes at the silica surface and for the carbon chains and ethoxy groups. These changes were not observed in either case for AcPhos-SBA (3) and (4), which suggests that stability of the ligand in acid is enhanced when the siloxane is completely reacted, either with neighboring siloxanes or with the silica surface.

Together the $^{13}C\{^1H\}$ and $^{29}Si\{^1H\}$ CP/MAS NMR results for the pristine and acid-washed materials reveal a trend. AcPhos-SBA (1) had the lowest degree of cross-linking between ligands and/or reaction with surface silanols. This material was also the least stable upon contact with nitric acid solutions. These results are consistent with AcPhos-SBA (1) having the lowest sorption of U(VI) from solution. AcPhos-SBA (2) demonstrated slightly higher cross-linking between ligands and/or reaction with surface silanols. As a result, it was slightly more stable to contact with nitric acid solutions and demonstrated slightly higher sorption of U(VI). AcPhos-SBA (3) and (4) had the highest degree of cross-linking and/or reaction with surface silanols and the highest degree of stability in nitric acid solutions. These materials also demonstrated significantly enhanced sorption of U(VI), although this may be due to the formation of phosphonic acid groups, which will be discussed below.

Evidence of Formation of Phosphonic Acid Groups

The single-pulse ^{31}P NMR spectra of pristine AcPhos-SBA (3) and (4) show evidence that hydrolysis of P−OEt groups to phosphonic acid groups, P−OH, occurred during functionalization. In addition to the resonance at 23 ppm, we observed a 15 ppm shoulder. A relatively lower chemical shift environment is consistent with increased shielding resulting from higher local electron density around the phosphorus atoms. This type of shift would only be observed for phosphonate groups acting as hydrogen bond donors through P−OH groups. Phosphonate groups acting as hydrogen-bond acceptors through the P=O group would further de-shield the phosphorus atom, causing a chemical shift in the opposite direction. The 15 ppm peak assigned to hydrolyzed, hydrogen bonding P−OH groups was only observed for AcPhos-SBA (3) and (4), which were synthesized with pyridine. Therefore, hydrolysis of the P−OEt groups is likely the result of a reaction with H_2O hydrolyzed by pyridine. The $^{13}C\{^1H\}$ CP/MAS spectra for these materials still show substantial peaks corresponding to the O=PO$\mathbf{C}H_2\mathbf{C}H_3$ carbons. Therefore, AcPhos-SBA (3) and (4) likely contain a mixture of phosphonic acid and ethyl phosphonate groups. Previous work on ethylphosphonate- and phosphonic acid-functionalized silica has shown that total hydrolysis of O=P$(OEt)_2$ to O=P$(OH)_2$ only results in a ^{31}P chemical shift of approximately -1-3 ppm in the main resonance for those materials [71, 72, 191]. Detecting formation of a mixture of these groups by the chemical shifting of that resonance alone is not likely. However, the presence of the lower-field chemical shift at 15 ppm in the AcPhos-SBA (3) and (4) spectra suggests that hydrolysis has occurred.

Further evidence of the formation of phosphonic acid groups can be found in the single-pulse ^1H NMR spectrum of AcPhos-SBA (4), shown in Figure 5.21. The ^1H spectrum shows

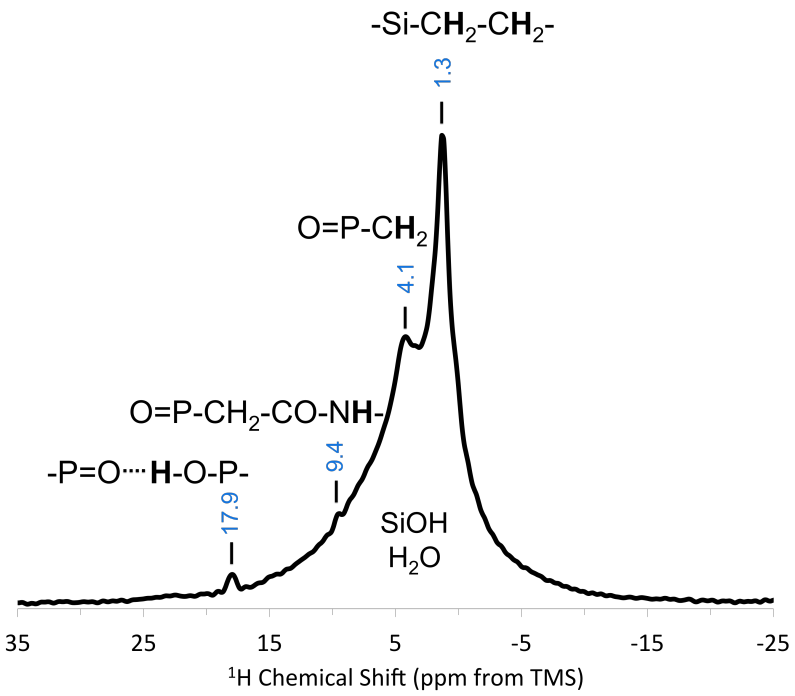

Figure 5.21: Single-pulse ^{1}H NMR spectrum of AcPhos-SBA (4) AW. The resonance at 1.3 ppm is from the hydrogens on the carbon chain; the 4.1 resonance is due to hydrogens on the carbon adjacent to the phosphonate functional group; the relatively unshielded peak at 9.4 is from the amine hydrogen. The peak at 17.9 ppm likely corresponds to hydrogen atoms participating in intra-ligand hydrogen bonding.

peaks corresponding to the aliphatic carbon chain (1.3 ppm), the methylene between the phosphonate and amide groups (4.1 ppm), and the amide hydrogen (9.4). These chemical shifts are consistent with previous reports [72, 196]. There is an additional peak at 17.9 ppm, indicative of a highly acidic proton. There are several reports of hydrogen-bonded phosphonic acid species giving ^{1}H giving chemical shifts in the range 10-17 ppm [197, 198]. The highest chemical shifts are observed for a proton shared between two deprotonated acid groups.

The single-pulse ^{31}P NMR spectra of the U(VI)-AcPhos-SBA samples are consistent with this analysis. Bibent's study compared dried and hydrated samples of phosphonate- and phosphonic acid-functionalized SBA-15 [72]. This study also observed the disappearance of the low chemical shift peak, a narrowing of the main ^{31}P peak, and the presence of shoulder peaks at close chemical shift to the central peak which broadened its base significantly. Bibent ascribed these changes to a disruption of the hydrogen-bonding network upon the adsorption of water. Water sorbed to the ligand sites will prevent or reduce hydrogen-bonding interactions between ligands, so the low chemical-shift peak at 15 ppm disappears. As a consequence, the ligands themselves become less rigid, and their increased mobility results in narrower peak shape. Bibent assigns the the different resonances observed to ligand environments with different degrees of hydration, leading to measurably different peak

widths. The same argument can be used to rationalize the spectra of U(VI)-AcPhos-SBA (2), (3), and (4).

An additional peak is observed at 29 ppm for AcPhos-SBA (2), (3), and (4). This peak is shifted approximately +6 ppm from the central peak at 23 ppm and has significant amplitude in the spectra for U(VI)-AcPhos-SBA (3) and (4). As discussed in Chapter 4, a similar chemical shift has been observed for phosphonate species bound to uranyl cations. Therefore, we attribute the chemical shift at 29 ppm to AcPhos-ligands interacting with uranyl cations. These AcPhos-ligands could contain two P – OEt groups, two P – OH groups, or one of each. Further justification for this assignments is the observation that the amplitude of the 29 ppm resonance is higher for the U(VI)AcPhos-SBA (3) and (4) spectra than it is for the U(VI)-AcPhos-SBA (2) spectrum (Figure 5.18), and it is known from the batch contact experiments that AcPhos-SBA (3) and (4) sorb significantly more U(VI) under these conditions than AcPhos-SBA (2).

Influence of Functionalization Procedure on U(VI) Sorption

The three different functionalization methods tested (AcPhos-SBA (3) and (4) were synthesized using the same method) yielded significantly different U(VI) sorption properties. AcPhos-SBA (3) and (4) demonstrated significantly different U(VI) sorption isotherms than AcPhos-SBA (2). The data for AcPhos-SBA (3) and (4) was well-described by the Langmuir adsorption isotherm. For these materials, the average sorption capacity measured was 160 $\pm$ 2 μmol g^{-1} silica, and the average K_{eq} was 117 $\pm$ 32 mL μmol^{-1}. In contrast, the data for AcPhos-SBA (2) was described equally well by the Langmuir and Freundlich isotherm models, but not very well by either of them. The Langmuir fit for AcPhos-SBA (2) U(VI) isotherm data yielded a sorption capacity of 37 $\pm$ 7 μmol g^{-1} and a K_{eq} of 11 $\pm$ 5 μmol^{-1}. The different isotherm behavior is consistent with different chemical processes occurring in the extraction of U(VI) by each type of material. This difference may be the result of an ion-exchange extraction mechanism occurring on hydrolyzed AcPhos ligands in AcPhos-SBA (3) and (4) versus an interaction between a neutral ligand and U(VI) for the non-hydrolyzed ligands on AcPhos-SBA (2). The interaction between a negatively charged phosphonic acid species and cationic uranyl would result in a higher stability constant than the interaction between uranyl and a neutral ligand, as is observed here.

The Langmuir sorption isotherm model assumes a single type of binding site characterized by one binding energy, which is uniform across the surface and independent of the concentration of the analyte sorbed to the surface. In contrast, the Freundlich sorption isotherm model accounts for a more complex interaction, with more than one type of binding site and a distribution of binding energies. We observe that the U(VI) sorption isotherm for non-functionalized SBA-15 is described well by the Freundlich model. This model is consistent with the amorphous silica surface, which presents a distribution of densities and geometries of surface silanols, the primary binding sites for uranyl cations. In contrast, the Langmuir model describes the shape of the U(VI) sorption isotherm for AcPhos-SBA (3) and (4). A strong, electrostatic interaction between phosphonate anions and a uranyl cations would

manifest as a single type of binding interaction dominating the sorption isotherm, resulting in a Langmuir fit to the data.

The U(VI) sorption isotherm for AcPhos-SBA (2) was not described particularly well by either the Langmuir or Freundlich models, which is evidence that a more complex sorption environment exists between uranyl cations and AcPhos-SBA (2). In our previous work [166], we observed that the sorption of U(VI) on diethylphosphonate (DPTS)-functionalized SBA-15 from pH 4 nitric acid solutions was described slightly better by the Freundlich model than the Langmuir model. Combined with evidence from NMR spectroscopy, observation of the Freundlich sorption isotherm led us to believe that the uranyl ions were complexed to both ligands and surface silanols. It is likely that sorption of U(VI) to AcPhos-SBA (2) contains a similar extraction mechanism involving both phosphonate ligands and surface silanols. This mechamism is consistent with the lack of hydrolyzed phosphonate groups for AcPhos-SBA (2), as evidenced by a single resonance in the ^{31}P NMR spectrum, and also by the higher surface silanol content, as evidenced by higher $Q^2 : Q$ and $Q^3 : Q$ ratios compared to AcPhos-SBA (3) and (4). For AcPhos-SBA (3) and (4) the surface silanol content is decreased, and the presence of P$-$OH groups makes stronger, electrostatic binding interactions accessible, resulting in a more uniform, Langmuir-type interaction between U(VI) and the surface.

Higher U(VI) sorption is also correlated with higher stability of the functional layer. Formation of phosphonic acid groups during functionalization accounts for the different uptake observed for AcPhos-SBA (3) and (4) compared to (1) and (2). However, the presence of phosphonic acid groups cannot account for the difference in sorption observed for AcPhos-SBA (2) compared to (1), since no hydrolysis of ethylphosphonate was observed for these samples. Despite its low U(VI) sorption capacity, AcPhos-SBA (2) did sorb measurable amounts of uranyl from nitric acid solutions above pH 3, but AcPhos-SBA (1) did not. The lack of any measurable sorption of U(VI) on AcPhos-SBA (1) may be due to the degradation of its functional layer, as evidenced by changes in its ^{29}Si NMR spectra. Ultimately increased stability resulted in greater uptake of U(VI) from solution.

Comparison of Ligand Density and Distribution for AcPhos-SBA Materials

^{31}P-^{31}P homonuclear dipolar coupling measurements were made to compare the average density of AcPhos ligands on the silica surface as well as their degree of polymerization for each material. The strength of dipolar coupling depends on the number and proximity of nearby spins. The sum of all pairwise spin dipolar coupling constants, $\sum_{j<k} b_{jk}^2$, is related to the distance between each spin, r_{jk} through:

$$\sum_{j,k} b_{jk}^2 = h^2\gamma^2\left(\frac{\mu_0}{4\pi}\right)\cdot\sum_{j,k}\frac{1}{r_{jk}^6} \tag{5.4}$$

where b_{jk} is in Hz, γ is the gyromagnetic ratio for ^{31}P in Hz T^{-1}, and μ_0 is the vacuum permeability constant. Therefore, a "denser" ligand layer will demonstrate stronger ^{31}P-^{31}P

coupling. This manifests as a greater difference in signal amplitude, ΔS, and a steeper rise in the plot of $\Delta S/S_0$ versus NT_r. AcPhos-SBA (1) had the lowest $\sum_{j<k} b_{jk}^2 = (1.9 \pm 0.1) \times 10^5 Hz^2$ of all four materials. This is consistent with its lower T^2 and T^3 peak intensities compared with the other materials. A longer surface hydration and refluxing time resulted in slightly higher cross-linking between ligands for AcPhos-SBA (2). This material also had a higher $\sum_{j<k} b_{jk}^2 = (2.64 \pm 0.03) \times 10^5 Hz^2$. AcPhos-SBA (3) and (4), which had a much higher degree of cross-linking based on their ^{29}Si{^{1}H} CP/MAS spectra, demonstrated similarly high dipolar coupling interactions, with $\sum_{j<k} b_{jk}^2$ values of $(2.93 \pm 0.07) \times 10^5$ and $(2.45 \pm 0.09) \times 10^5$, respectively. That the difference in dipolar coupling strength between the AcPhos-SBA (2) and (4) samples is not significant is surprising, given the vast differences in the T^2 and T^3 Si populations. However, this may constitute evidence that the T^2 and T^3 chemical shifts are due not only to a higher degree of ligand polymerization, but also due to a higher degree of reaction with the surface, that is, formation of R–Si–(OX), where X is Si from the silica substrate rather than from a neighboring siloxane. The addition of pyridine catalyzes hydrolysis of siloxane groups, but would also tend to deprotonate surface silanols. Therefore, the rate of polymerization and the rate of condensation to the surface are both affected by the addition of pyridine.

The two difference chemical shift environments present in AcPhos-SBA (4) demonstrate significantly different ^{31}P-^{31}P dipolar coupling strength. The parabolic rise of the 15 ppm resonance is steeper than that of the 23 ppm resonance. This results in a higher $\sum_{j,k} b_{jk}^2$ value of $(5.7 \pm 0.3) \times 10^5 Hz^2$ compared to $(2.45 \pm 0.09) \times 10^5 Hz^2$ for the 23 ppm peak, which corresponds to a higher overall ligand density for this phosphorus environment.

Chapter 4 establishes a model of the modified silica surface based on the crystal structure of β-cristobalite [113, 166]. Assuming ligands are rigid on the timescale of the NMR experiment, two phosphorus atoms that are part of a pair of cross-linked ligands (i. e. R–Si–O–Si–R, where R is the AcPhos ligand) would be spaced approximately 3.0 Å apart [182]. If no cross-linking between ligands occurred, and only exposed silanols were functionalized, phosphorus atoms would be spaced approximately 5.0 Å apart, with a maximum of six nearest neighbors (see Figure 4.19). Using Equation 5.4, the expected $\sum_{j,k} b_{jk}^2$ values can be calculated for a given number of spins at a fixed distance apart. For example, "monomeric" functionalization, resulting in six nearest neighbors at a distance of 5 Å would yield $\sum_{j,k} b_{jk}^2 = 1.49 \times 10^5 Hz^2$. This value is similar to the $\sum_{j,k} b_{jk}^2$ calculated for the DPTS-SBA material in the previous chapter and the AcPhos-SBA materials in this chapter. The slightly higher values observed in each case may be due to a small percentage of cross-linking that occurs for some ligands, but not for all. A dimerized ligand pair, where there is one nearest neighbor at a distance of 3.0 Å yields $\sum_{j,k} b_{jk}^2 = 5.31 \times 10^5 Hz^2$, which is very similar to the value observed for the 15 ppm peak in the AcPhos-SBA (4) sample. The slightly higher $\sum_{j,k} b_{jk}^2$ value observed for the 15 ppm peak of AcPhos-SBA (4) can be explained by the presence of 1 or 2 other phosphonate groups at a distance of 5.0 Å, which would yield $\sum_{j,k} b_{jk}^2$ values between $5.56 \times 10^5 Hz^2$ and $5.81 \times 10^5 Hz^2$. These values match that observed for the 15 ppm peak, $\sum_{j,k} b_{jk}^2 = (5.7 \pm 03) \times 10^5 Hz^2$ within the uncertainty of

the fit. Combined with single pulse ^{31}P and ^{1}H NMR, the DQ-DRENAR data shows that the phosphorus chemical environment corresponding to the 15 ppm peak corresponds to ligand pairs that dimerized at their alkoxysilane anchors during functionalization, were hydrolyzed to contain one or more P−OH groups upon contact with pyridine, and are involved in hydrogen-bonding interactions between P−OH groups.

5.10 Conclusions and Future Work

Three different functionalization methods were used to modify SBA-15 rods with an acetamide phosphonate ligand, and the materials were evaluated for their ability to uptake U(VI) from nitric acid solutions and for the resilience of the functional layer to contact with nitric acid during these experiments. Increasing the hydration time and refluxing time during functionalization resulted in marginal increases in the cross-linking of ligands, which improved its stability in pH 3 nitric acid. The addition of pyridine as a basic catalyst during functionalization was found to increase hydrolysis of ethoxysilane groups, which provided for greater reactivity between ligands and between the ligands and the silanol surface. ^{13}C{^{1}H} and ^{29}Si{^{1}H} showed that materials synthesized with pyridine were more stable to contact with 3 M $NaNO_3$ adjusted to pH 3 than those synthesized without it. Additionally, they showed increased sorption under all conditions tested. Measurement of U(VI) isotherms revealed significantly different sorption behavior, including a stronger interaction between U(VI) and the AcPhos ligand for materials synthesized with pyridine.

Additionally, single-pulse ^{31}P and ^{1}H NMR showed evidence that pyridine had partially hydrolyzed ethyl phosphonate to phosphonic acid groups. Consistent with previous reports, a lower chemical shift peak was observed at 15 ppm in the ^{31}P NMR spectra only for materials synthesized with pyridine, and this peak was assigned to hydrolyzed phosphonates involved in hydrogen bonding interactions. The DQ-DRENAR method was used to compare the strength of ^{31}P-^{31}P dipolar coupling for each of the materials synthesized. These measurements revealed that chemical environments corresponding to hydrolyzed, deprotonated phosphonic acid ligands engaged in hydrogen bonding interactions demonstrate higher dipolar coupling interactions and are therefore characterized by a higher average ligand density than the free AcPhos ligands.

Single-pulse ^{31}P NMR spectra collected for U(VI)-AcPhos-SBA samples revealed that the combination of sorption of uranyl cation to the AcPhos ligand and of water to the functional layer resulted in disruption of the hydrogen bonding interaction between ligands. Additionally, a +6 ppm shift from the main peak at 23 ppm was observed for AcPhos ligands bound to U(VI). An obvious next step would be to test AcPhos materials where the extent of hydrolysis of the ethyl phosphonate groups is controlled. Increasing the number of phosphonic acid groups may increase the sorption capacity of these materials to a level that would make the effects of uranyl more observable by NMR.

Dipolar coupling measurement by NMR spectroscopy is very useful for studying self-assembled monolayers on silica substrates, especially for ligands containing ^{31}P. The process

of functionalization is complex and differs based on the precise conditions used and the chemistry of the functional group involved. The DQ-DRENAR method provides an elegant and fast way to measure the distribution of ligands on a surface. Variations in the functionalization procedure, including the use of different catalysts, as well as the use of substrates with different surface features (e.g. pore curvature) could be rapidly evaluated using this method.

The policy implications of developing more efficient, robust, solid-phase extraction materials for the sequestration and separation of rare earths and actinides are far-reaching. In addition to their potential for simplifying and improving the efficiency of routine, laboratory- and commercial-scale separation procedures, these materials could be optimized for the sensing and sequestration of low concentrations of actinides in the environment. Therefore, they could aid in the timely detection of undeclared nuclear activities or in large scale environmental clean-up efforts after a nuclear accident. Additionally, the production of highly selective solid-phase materials for use in high pressure liquid chromatography would facilitate rapid actinide separations, which is necessary for the timely processing and analysis of post-detonation nuclear forensics debris. Silica substrates provide the advantage that they can be vitrified after use, which simplifies their long-term storage after use to extract heavy metals from solution. High surface area organically functionalized mesoporous silica materials have vast potential for improving aqueous extraction and separation procedures in all aspects of environmental and analytical actinide chemistry.

Chapter 6

Experimental Methods

6.1 Synthesis of SBA-15 Microspheres

Pluronic P-123 (polyethylene glycol-polypropylene glycol-polyethylene glycol), 1,3,5-trimethyl benzene (TMB), tetraethyl orthosilicate (TEOS), and hexadecyl trimethylammonium bromide (CTAB) were purchased from Sigma Aldrich. Anhydrous toluene (99.8%) was purchased from Alpha Aesar. The ligand diethylphosphatoethyl triethoxysilane (DPTS) (95%) was purchased from Gelest.

Mesoporous silica microspheres were synthesized by adapting the protocol for spherical particle synthesis developed by Katiyar et al.[110] In a typical synthesis, 2.25 g of P-123 was combined with 45 mL 1.5 M HCl. In a separate vial were combined 0.45 g CTAB, 18.75 mL water, and 0.780 mL TMB. Solutions were mixed for several hours to ensure homogeneity, then combined together with 15 mL ethanol (added dropwise) into a polytetrafluoroethylene (PTFE) bottle at 35 °C and stirred for 3 hours. To this mixture, 7.5 mL TEOS was added dropwise. The PTFE bottle was then sealed and left stirring at 35 °C for an additional 45 minutes, followed by aging in a thermostatic bath at 80 °C for 5 hours. Finally, the sealed PTFE bottle was transferred to an oven at 120 °C for approximately 15 hours. The silica particles were collected via vacuum filtration and rinsed thoroughly with water. Calcination was carried out in a Thermolyne muffle furnace under ambient conditions by heating to 550 °C at a rate of 1 °C min^{-1}, holding for 6 hours at 550 °C, and cooling back to room temperature at a rate of 5 °C min^{-1}. Calcined particles (SBA) were stored in an evacuated desiccator.

6.2 Synthesis of SBA-15 Rods

SBA-15 rods were synthesized by a standard hydrothermal synthetic method following the procedure established by Sayari, Han, and Yang.[117] In a typical synthesis, 2 g P123 were combined with 60 g 2 M HCl and 15 g H_2O. The mixture was gently rocked for approximately 2 hours, until homogeneous. The mixture was then transfered to a PTFE reaction vessel in

a water bath heated to 35 °C, where it was stirred at 350 rpm for approximately 20 hours. Following this equilibration, 4.25 g tetraethyl orthosilicate (TEOS) was added dropwise under 500 rpm stirring. The reaction mixture was stirred at 500 rpm for five minutes, followed by 20 hours under static conditions in the same 35 °C water bath. For this stage, the stir bar was removed and the vessel sealed tightly for the remainder of the synthesis. The PTFE reaction vessel was then transferred to an oven at 100 °C and left under static conditions for 24 hours. The reaction vessel was allowed to cool completely before opening. Particles were collected by vacuum filtration, rinsed thoroughly with water, and dried under atmospheric conditions in an oven at 100 °C. Template removal was achieved via calcination in air using the following procedure: particles were transferred to an alumina crucible and heated in a muffle furnace. The temperature was ramped to 550 °C at a rate of 1 °C min^{-1}, held at 550 °C for 6 hours, and then cooled at a rate of 5 °C min^{-1}. Particles were stored in an evacuated desiccator to minimize adsorption of water to the surface.

6.3 Functionalization Procedures

Functionalization with Diethylphosphonate (DPTS)

The mesoporous silica spheres were functionalized with DPTS via toluene reflux using a solution polymerization method.[131] Particles were first dried under vacuum at 100 °C overnight before addition of toluene. Water was added stoichiometrically in a ratio of 10 water molecules per square nanometer, and the resulting mixture was stirred under nitrogen at room temperature for 2 hours. Diethylphosphatoethyl triethoxysilane (Gelest, 95%) was added in a ratio of 6.25 molecules per square nanometer, and the mixture was refluxed for six hours. This was followed by distillation to 110 °C to eliminate any water and ethanol formed during functionalization, and to further condense the siloxane ligand onto the silica surface. Functionalized particles (DPTS-SBA) were vacuum filtered, rinsed thoroughly with toluene followed by isopropanol, and stored in an evacuated desiccator.

Functionalization with Acetamide Diethylphosphonate (AcPhos)

The compound dietyl (2-oxo-2-((3-(triethoxysilyl)propyl)amino)ethyl)phosphonate, "AcPhos" (Figure 5.3), was purchased from Technocomm, Ltd. The compound was stored under nitrogen gas in an evacuated desiccator to minimize reaction with moisture in the air. Nonetheless, after several months, ^{29}Si NMR revealed that partial hydrolysis and polymerization had occured to form dimeric species, which accounted for approximately 15 percent of the total compound. It is unlikely that these dimers negatively impacted the functionalization procedure.Formation of trimers or more extended polymers was not observed.

Four different functionalization procedures were used to synthesize the materials AcPhos-SBA (1-4). These procedures were adapted from a surface polymerization method [131] designed to encourage cross-linking of the AcPhos only at the silica surface simultaneously

with condensation reactions grafting the ligands to the surface at the siloxane anchor. For the synthesis of AcPhos-SBA (1), 0.5 g silica particles were first dried under Schlenk line vacuum at 110 ° for 15 hours to remove adsorbed water. Nitrogen gas was introduced to the reaction flask slowly prior to the addition of 35 mL of toluene and water added stoichiometrically to achieve a surface coverage of 10 H_2O molecules nm^{-2} (approximately 0.126 mL for this material). Upon addition of water, the silica-toluene-water slurry formed aggregates. It was stirred under nitrogen at room temperature for two hours to allow water to diffuse through the pores, until a homogeneous slurry was obtained. Any remaining aggregates were dispersed by sonicating the entire reaction flask for 5-10 minutes. The AcPhos siloxane was added under stirring in a ratio of 6.25 siloxane molecules nm^{-2}. The reaction mixture was then refluxed under nitrogen for 6 hours. A distillation step was added to remove excess water and ethanol from the surface, which has been shown to increase cross-linking between siloxanes. After cooling, the particles were recovered by vacuum filtration and washed with 20 mL toluene and 40 mL isopropanol. Final particles were stored in an evacuated desicator. Synthesis of AcPhos-SBA (2) followed the procedure above with the following exceptions: the mixing time of the silica-toluene-water slurry was increased to 15 hours, and the reflux time was increased to 24 hours. Synthesis of AcPhos-SBA (3) was the same as that of AcPhos-SBA (2), except that 5 molecules pyridine nm^{-2} silica was added with the water. Synthesis of AcPhos-SBA (4) was a duplicate of the procedure used for AcPhos-SBA (3).

Pore Characterization via Nitrogen Adsorption Isotherms

Nitrogen adsorption measurements were performed on a Micromeritics Accelerated Surface Area and Porosity (ASAP) 2420 System instrument. In a typical measurement, approximately 30 mg of solid sample was transferred to a pre-weighed glass sample tube under an atmosphere of nitrogen and capped with a Transeal. The sample was then transferred to a Micromeritics ASAP 2420 gas adsorption analyzer and heated at a rate of 0.5 K min^{-1} from room temperature to a final temperature of 343 K under dynamic vacuum. The sample was considered activated when the outgas rate at 343 K was less than 2 μbar min^{-1} (approximately 24 hours). The evacuated tube containing degassed sample was then transferred to a balance and weighed to determine the mass of sample. The tube was transferred to the analysis port of the instrument where the outgas rate was again determined to be less than 2 μbar min^{-1} at 343 K. For all isotherms, free space correction measurements were performed using ultra-high purity He gas (UHP grade 5.0, 99.999% purity). Nitrogen isotherms at 77 K were measured in liquid nitrogen baths using UHP-grade gas sources. Oil-free vacuum pumps and oil-free pressure regulators were used for all measurements to prevent contamination of the samples during the evacuation process or of the feed gases during the isotherm measurements. The average surface area per gram of material was determined using the Brunauer-Emmett-Teller (BET) method,[98] and average pore volume and pore diameter were obtained using the Barrett-Joyner-Halenda (BJH) method.[99]

6.4 Measurement and Detection of Radioisotopes

Alpha Spectroscopy

Alpha spectra were measured under vacuum using surface barrier semiconductor detectors. Energy calibration was done using a mixed $^{241}Am/^{239}Pu$ source. Alpha plates were made by electrodeposition onto stainless steel plates. Since alpha spectroscopy was used mainly to determine stock radiopurity, and not to quantify radioisotopes, the efficiency was not calibrated.

Electrodeposition was carried out in a cell fitted with a teflon cap, a platinum wire, which acts as the anode, and a base connected to a voltage source and the stainless steel plate, which acts as the cathode. The cell is shown in Figure 6.1. The following procedure was used. The cell was assembled by placing a clean stainless steel plate onto the base of the cell and screwing in the cell container to secure the plate. The cell was then leak checked with water prior to loading any ^{233}U solutions. A constant current voltage source was used. The voltage source was attached to the electrodeposition cell such that the positive lead was attached to the platinum wire anode and the negative lead to the screw of the white cell base, which is in contact with the stainless steel plate when the cell is fully assembled. The voltage source was set to maintain a constant current of 1.00 A.

An aliquot of the ^{233}U stock was combined with 2 mL $NaHSO_4$ (5 % w/w), 1 mL $^{H}2\,O$, and 4 mL $NaSO_4$ (15 % w/w), which buffers the solution to pH 2. The amount of ^{233}U stock used was chosen so as not to exceed 20 μg total, which ensured a thin, uniform deposition. This mixture was added to the cell and the voltage turned on. The plate was electrodeposited for approximately thirty minutes. During deposition, the voltage decreased from approximately 11 V to 7 V. The cell typically became very warm, even to the point of boiling. Additional water was added if the volume of the cell dropped by more than 25 %Ḟollowing deposition, the power supply was disconnected and 2 mL 4 M KOH was added to prevent the uranyl hydroxide deposit from redissolving. The power supply was then reconnected, and deposition continued for two more minutes, typically at a lower voltage (constant current of 1 A). The power supply was disconnected and a the solution in the cell discarded. The cell was rinsed thoroughly with NH_4OH (5 % w/w). The cell was then disassembled to recover the stainless steel plate, which was rinsed with a few drops of ethanol and acetone. Finally, the plate was dried on a hote plate for five minutes prior to counting.

The advantage of preparing alpha plates by electrodeposition is that a very thin, uniform, and robust layer is formed. Thin films increase the resolution of alpha spectra. Additionally, since the deposited layer contains little or no salt, it does not flake off of the steel plate, which means that it lasts longer. The alpha plate can therefore be saved and measured periodically to assess working stock purity.

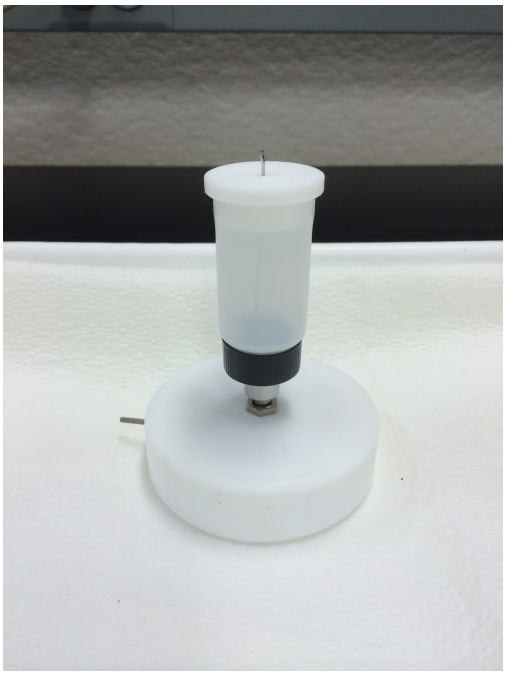

Figure 6.1: Electrodeposition cell for preparing alpha plates.

Liquid Scintillation Counting

For batch contact experiments, the concentration of alpha emitters, including ^{233}U and ^{239}Pu was quantified using a Wallac 1414 liquid scintillation counter with α/β descrimination. The pulse shape analysis level was set to 150 for all samples measured. This level was optimized empirically to obtain accurate pulse shape discrimination for a range of assay volumes and electrolyte concentrations. All assays were measured using Eppendorf pipettors. Stock assays were typically 5 μL in volume, while sample assays were typically 10 muL in volume. Assays were added to 5 mL of Ecolume liquid scintillation cocktail. Typically statistical counting uncertainty was limited to 1-2% either by increasng the volume of the assay or by extending the counting time. The counting efficiency was assumed to be 100%.

Gamma Spectroscopy

The concentration of europium in solution was determined by gamma spectroscopy on a ^{152}Eu radiotracer using high-purity germanium (HPGe) detectors. The energy and efficiency of these detectors were calibrated using a mixed radioisotope source purchased from Eckert and Ziegler. Uncertainty in geometric efficiency was minimized by placing each sample in a holder designed to fit snugly against the detector in the same orientation each time. Stock and sample assays were measured using Eppendorf pipettors. Assays were approximately 50 μL in volume, which was kept constant for each experiment because the detector efficiency is influenced by assay volume.

6.5 Radioisotope Stock Preparation

U(VI) Stock Preparation

A 0.4 M ^{238}U(VI) stock solution was prepared by dissolution of $UO_2(NO_3)_2 \cdot 6\,H_2O$ in 1 M HNO_3, and was used for measurement of the U(VI) sorption capacity and for preparation of solid-state NMR samples. This stock was made of depleted uranium. All batch contact experiments were conducted using ^{233}U as a ratiotracer, because it has much higher specific alpha activity than depleted ^{238}U. A ^{233}U(VI) stock solution was purified using Dowex analytical grade cation exchange resin (AG 50W-X8, 100-200 mesh, hydrogen form). Prior to loading onto a Dowex cation exchange column, the ^{233}U(VI) was first precipitated from solution via dropwise addition of 10 M NaOH. The precipitate was collected by centrifugation, and redissolved in 0.5 mL 0.1 M HCl, then loaded onto the cation exchange column. ^{233}U(VI) was eluted with 3 M HCl. Final ^{233}U(VI) stock radipurity was determined to be greater than 99.9 % using alpha spectroscopy following electrodeposition of aliquots of the final stock onto stainless steel plates. For batch experiments, a 1 mM ^{233}U(VI) working stock was prepared in 1 M HNO_3 by evaporation and redissolution in 1M HNO_3, repeated at least three times. Final working stock uranium concentrations were assayed via liquid scintillation counting of the ^{233}U alpha activity.

Eu(III) Stock Preparation

Eu(III) stocks were prepared by dissolution of solid $Eu(NO_3)_3 \cdot 6\,H_2O$ or $EuCl_3$ in nitric acid. ^{152}Eu was purchased from Eckert and Ziegler and came in a 10 μg mL^{-1} of $EuCl_3$ carrier (500 μCi, 100μCi/mL, $EuCl_3$ in 0.5 M HCl, greater than 95% radiopure, with a 3.42% impurity of ^{153}Gd). ^{152}Eu was used as a radiotracer to determine the total concentration of Eu after contact with solid samples. To insure purity of the anion present, combined carrier-tracer stocks were typically evaporated to dryness under a heat lamp and redissolved in nitric acid at least three times prior to use in contact experiments.

Pu(VI) Stock Preparation

All plutonium stock preparation and batch contact experiments were carried out under air in a negative pressure glove box. The ^{239}Pu stock was made by dissolving PuO_2 powder in boiling, concenrated HNO_3 and 0.09 M HF. To ensure that all plutonium was in the +4 oxidation state, excess $NaNO_2$ was added, and the oxidation state verified by UV-Vis, as discussed below. For this work, the ^{239}Pu used was weapons-grade, indicating at least 93% isotopic purity. However, beta decay of a ^{241}Pu ($t_{1/2}$ = 14.35 years) impurity introduces a significant amount of ^{241}Am. To purify the plutonium stock of americium, an anion exchange column was used. The procedure was performed by Tashi Parsons-Moss and is described in detail in reference [188]. To summarize, the dissolved Pu^{4+} was loaded onto a Bio-Rad AG 1x8 100-200 mesh resin conditioned with 8 M HNO_3 and subsequently washed with 10 M

HCl. The Pu is eluted by reducing it to Pu(III) using a 9:1 mixture of concentrated HCl and freshly distilled HI. Americium is eluted immediately after loading because it does not form anionic complexes in 8 M HNO_3. Any U(VI) or Np (V) impurities present are not reduced by HI and can be removed from the column after the plutonium has been eluted by thoroughly washing the column with 1 M HCl.

A stock free of I^- was prepared by refluxing in HNO_3, which also destroys any organic material existing in the flask. This step is necessary prior to contact with $HClO_4$, which can react violently with organic materials. Stocks of Pu(VI) were prepared by boiling the stock solution in concentrated $HClO_4$ under argon for several hours. A custom boiling flask apparatus was made to bubble $HClO_4$ vapors through three flasks containing H_2O, 7 M NaOH, and H_2O. Extreme caution should be taken when handling $HClO_4$. Dried perchlorate salts are shock-sensitive and can explode when dried at high tempratures. Perchloric acid is a very strong oxidizer when hot, so trace organic matter must first be destroyed by boiling in nitric acid. Aqueous plutonium chemistry is complicated by the stability of multiple oxidation states in solution. These oxidation states can be distinguished by their color for solutions of sufficient concentration and purity. The concentration of different oxidation states can be estimated using UV-Vis absorption spectroscopy. Characteristic absorption spectra of Pu^{3+}, Pu^{4+}, $PuO_2{}^+$, and $PuO_2{}^{2+}$ in $HClO_4$ are documented by Cohen [199]. The extinction coefficients for various oxidation states are given by Cohen [200] and by Nitsche and Silva [201]. Aqueous solutions of $PuO_2{}^{2+}$ are known to auto-reduce to a mixture of lower oxidation states over time. Thus, prior to conducting any batch experiments, fresh stocks of Pu(VI) were prepared by boiling in concentrated $HClO_4$. The oxidation state of the stock was verified just prior to contact with solid samples using UV-Vis.

6.6 Batch Contact Procedures: Diethylphosphonate-functionalized silica

All reagents, including nitric acid, perchloric acid, sodium nitrate, sodium hydroxide, and depleted uranium nitrate hexahydrate (ACS reagent), were purchased from Sigma Aldrich. The ^{233}U stock was prepared in-house and purified as described above. The initial ^{233}U stock was obtained from a larger stock stored at Lawrence Berkeley National Laboratory, and had previously been purified by Robert Silva in 2002.

All samples were pre-equilibrated with 0.1 M or 3 M $NaNO_3$ solutions adjusted to the desired pH for approximately 15 hours before contact with U(VI) to ensure thorough wetting of the samples. Samples were prepared with a solid-to-solution ratio of 1 mg mL^{-1}. All samples prepared for batch contact experiments were spiked with ^{233}U(VI) stock to achieve an initial sample concentration of $[^{233}U(VI)] = 20\ \mu M$. For measurement of the U(VI) isotherms, samples were spiked with a mixed $^{233}U(VI)/^{238}U(VI)$ stock to achieve an initial sample concentration of $[^{233}U(VI)] = 20\ \mu M$ and $[^{238}U(VI)] = 30$, 80, 230, or 480 μM. After spiking samples with U(VI), the pH was readjusted to the appropriate level by addition of NaOH,

and samples were rocked continuously. The solid and solution were separated by centrifugation at 7000 rpm (8765 g) for five minutes. Aliquots of the solution were taken at various mixing times. Final concentration was determined by liquid scintillation counting for samples containing ^{233}U and ^{239}Pu, and by gamma spectroscopy for samples containing ^{152}Eu.

Dependence on pH

The sorption of U(VI) on DPTS-SBA and SBA from 0.1 M and 3 M $NaNO_3$ solutions was compared in the pH range 1-5. Samples were spiked with ^{233}U, $^{151/152}$Eu, or ^{239}Pu stock such that the initial metal concentration was 20 μM. Samples were assayed after approximately 1, 3, and 24 hours mixing time. Solution pH was measured and adjusted after each aliquot was taken. Controls containing no solid, but equivalent metal concentrations for each condition tested, were conducted to quantify precipitation or metal hydroxide species or adsorption onto the polypropylene vials. Unless noted otherwise, no loss of U(VI), Eu(III), or Pu(VI) occurred for the conditions tested.

U(VI) sorption isotherms

The uranium sorption capacities of DPTS-SBA and SBA were compared by measuring uranium sorption isotherms in 3 M $NaNO_3$ solutions adjusted to pH 4 using NaOH. Following the procedure above, samples were pre-equilibrated with solution, spiked with mixed $^{233/238}$U stocks to various initial [U(VI)] concentrations and then adjusted to pH 4. Sample assays were taken approximately 72 hours after contact with U(VI).

6.7 Batch Contact Procedures: Acetamide diethylphosphonate-functionalized silica

Dependence on [HNO_3] and [$NaNO_3$]

In a typical batch experiment, the solid sample is pre-equilibrated in solution for approximately 15 hours in a ratio of 3 mg solid mL^{-1} solution. Samples are then spiked with U(VI) stocks to achieve the desired concentration, and the pH readjusted using NaOH. Centrifugation at 7000 rpm (8765 g) achieved phase separation, and 10 μL aliquots were taken for liquid scintillation counting. Samples were typically assayed after 1, 4, and 24 hours, though in every case, additional sorption was not observed after 1 hour mixing time. In between assays, samples were gently rocked on a rotoshake. For samples at pH 2 and 3, the pH was measured and adjusted after each asasy. To measure the dependence of U(VI) sorption on [HNO_3], samples were prepared with an initial concentration of [^{233}U(VI)] = 2×10^{-5}, in solutions containing 3 M, 2 M, 1 M, pH 1, pH 2, and pH 3 nitric acid. Additionally, sorption of U(VI) was compared at pH 2 and pH 3 for samples containing no additional $NaNO_3$ and

3 M $NaNO_3$. These samples contained an initial [U(VI)] = 500 μM, comprised of [^{233}U(VI)] = 20 μM as a tracer and [^{238}U(VI)] =480 μM.

U(VI) Sorption Isotherms

U(VI) isotherms were measured for non-functionalized SBA, AcPhos-SBA (2), AcPhos-SBA (3), and AcPhos-SBA (4) from 3 M $NaNO_3$ solutions adjusted to pH 3. Solid samples were pre-equilibrated with solution in a ratio of 3 mg solid mL^{-1} solution for approximately 15 hours. Samples were then spiked with U(VI) stocks to obtain initial concentrations of $[U(VI)_{total}]$ = 20, 50, 100, 200, 300, 400, and 500 μM. For each sample, the [^{233}U] = 20 μM. Samples were rocked continuously. After 1, 4, and 24 hours of mixing time, samples were centrifuged at 7000 rpm, and 10 μL assays were taken for liquid scintillation counting of the ^{233}U alpha activity. No additional sorption was observed after 1 hour of mixing time. A control sample containing no solid and $[U(VI)]_{total}$ = 500 μM was assayed with the samples to verify that no uranyl species precipitated or adsorbed to the polypropylene tube walls.

6.8 NMR Spectroscopy and Instrumentation

Preparation of NMR Samples

U(VI)-DPTS-SBA samples were prepared by pre-equilibrating approximately 10 mg of solid with 3 M $NaNO_3$ solutions at pH 3 or 4 for approximately 15 hours. They were then spiked with depleted ^{238}U stocks to achieve a concentration of 0.5 mmol depleted ^{238}U(VI) per gram of solid. Samples were mixed for 24 hours on a rocker. Solids were rinsed with fresh $NaNO_3$ solution adjusted to the proper pH and air dried for several days prior to measurement. Control samples (ac-DPTS-SBA) were treated with similar solutions without U(VI).

U(VI)-AcPhos-SBA (2, 3, and 4) samples were prepared using conditions similar to those tested in the U(VI) isotherm measurements, in 3 M $NaNO_3$ adjusted to pH 3. After pre-equilibration, samples were spiked with only ^{238}U stock to achieve an initial concentration of 5×10^{-4} M. After 24 hours mixing, samples were centrifuged at 7000 rpm, and the supernatant withdrawn. Samples were washed with approximately 100 μL fresh 3 M $NaNO_3$ adjusted to pH 3 and then air dried in a fume hood prior to packing into Kel-F rotor inserts.

Acid-washed AcPhos-SBA samples, denoted AcPhos-SBA (X) AW, where X is 1, 2, 3, and 4 were prepared by contacting each material with 3 M $NaNO_3$ adjusted to pH 3 for approximately 20 hours. Approximately 50 mg of solid sample was washed with 10 mL of solution. As usual, the phases were separated by centrifugation. The supernatant was withdrawn, and each sample was washed with 2-3 mL isopropanol to rinse excess water away from the surface. This was repeated twice. Finally, the samples were air-dried, collected in glass vials, and placed in a desicator evacuated to less than 20 mtorr Hg for 7 hours. Finally, samples were stored in the same evacuated desiccator as pristine samples to achieve similar levels of hydration.

Instrumentation Details

Solid-state NMR spectra were collected on a 300 MHz (7.5 T) Tecmag Apollo fitted with a Bruker HX CP/MAS probe configured for 4 mm (o.d.) rotors. Operating frequencies were 59.82, 75.73, 301.13, and 121.90 MHz for ^{29}Si, ^{13}C, ^{1}H, and ^{31}P, respectively. Unless otherwise noted, all spectra were collected at a magic angle spinning rate of 10 kHz. The DQ-DRENAR data were collected at a MAS rate of 7 kHz. The single-pulse ^{1}H NMR spectra collected on AcPhos-SBA materials were collected with a MAS rate of 13 kHz. Spectral resonances were fitted with pseudo-Voigt functions, as detailed below. All ^{29}Si spectra were referenced with respect to tetramethylsilane (TMS), using kaolinite as a secondary reference set to δ_{Si} = -91.5 ppm.[202] The ^{13}C spectra were referenced to TMS, using glycine as a secondary reference set to δ_C = 42.8 and 173.6 ppm.[203] The ^{31}P spectra were referenced to 85% H_3PO_4 using hydroxylapatite as a secondary reference set to δ_P = 2.65 ppm.[204] Finally, all ^{1}H spectra were referenced to TMS using hydroxyapatite as a secondary reference set to δ_H = 0.2 ppm.[205]

The ^{29}Si{^{1}H} cross-polarization magic angle spinning (CP/MAS) NMR spectra were collected using 3 ms continuous wave (CW) polarization transfer and a 2 s pulse delay. The ^{13}C{^{1}H} CP/MAS NMR spectra were collected using 1 ms ramped amplitude polarization transfer on the ^{13}C channel, CW decoupling on the ^{1}H channel during acquisition, and a 2 s pulse delay. The ^{31}P single-pulse magic angle spinning (SP/MAS) spectra were collected using a pulse delay of 60 s, a pulse width ranging from 3.6 to 4.7 μs, and where noted CW decoupling on the ^{1}H channel during acquisition. The single pulse ^{1}H spectra were collected using a $\pi/2$ pulse width of 7.3 μs, a π pulse width of 14.6 μs, and a pulse delay of 2 s. The sequence used to collect single-pulse ^{1}H spectra was modified using π pulses in order to decrease the background from protons outside the sample.

The ^{31}P{^{1}H} CP/MAS variable contact time experiments conducted for U(VI)-DPTS-SBA samples used a pulse delay of 2 s, a pulse width of 5.6 μs, and CW polarization transfer on the ^{31}P channel ranging from 0.05 to 20 μs. For both DPTS-SBA and AcPhos-SBA, homonuclear ^{31}P – ^{31}P Double-Quantum-based Dipolar recoupling effects Nuclear Alignment Reduction (DQ-DRENAR) measurements were made.[164, 165] Spectra were collected at a MAS rate of 7 kHz (0.143 ms rotor period) using a $\pi/2$ pulse width of 5.1 μs, a 2π pulse width of 20.4 μs, and a $3\pi/2$ pulse width of 15.3 μs. The POST-C7 pulse sequence applied in this method is rotor-synchronized. The amplitude of the pulses was adjusted such that the desired pulse sequence could be completed in two rotor cycles. Spectra were acquired after the application of two POST-C7 pulse sequences n times, where n is an integer number between 1 and 10. Therefore, signal was acquired after ten different "signal evolution times" ranging from NT_r = 0.57 to 5.7 ms where N is an integer number of rotor periods (always a multiple of four) and T_r is the rotor period. For the control experiment, the second POST-C7 pulse sequence is out of phase by $\pi/2$, which prevents dipolar recoupling.

Fitting NMR Spectra with Pseudo-Voigt Distributions

As discussed in Chapter 3, it is standard practice to fit solid-state NMR spectra with pseudo-Voigt functions. The lineshapes of solid-state spectra are mathematically equivalent to a Gaussian distribution of Lorentizian distributions, which can be accurately approximated by a pseudo-Voigt of the form:

$$V_p(x) = \eta \cdot G(x) + (1 - \eta) \cdot L(x) \tag{6.1}$$

$$G(x) = exp\left[- ln(2) \cdot \left(\frac{x - x_0}{\omega} \right)^2 \right] \tag{6.2}$$

$$L(x) = \frac{1}{1 + \left(\frac{x - x_0}{\omega} \right)^2} \tag{6.3}$$

where x_0 is the peak centroid and $2\omega = FWHM$. The term η can take any value between zero and 1, and describes the *shape* of the peak. A value of $\eta = 1$ gives a Gaussian distribution, and a value of $\eta = 0$ gives a Lorentzian distribution.

All spectra were fit using the open source software Peak-O-Mat. The user has the option to select a background correction line shape as well as any number of a variety of distributions with which to fit the peaks. Typically spectra are first corrected with a quadratic background, and the background-corrected spectrum re-loaded into Peak-O-Mat for peak fitting.

Peak-O-Mat does not automatically fit peaks. For the most part, selection of the number, location, width, and shape of the peaks was done in concert with consultation of the literature, which aided in the assignment of the peaks to physical structures in the samples. Often solid-state spectra have multiple overlapping peaks, and these were more difficult to interpret. Peak-O-Mat uses initial guesses for each peak location, width, and shape (i.e. percent Gaussian versus Lorentzian) to fit the spectrum holistically. It attempts to minimize the difference between the calculated and experimental spectrum for each point. Unless specified by the user, these parameters (centroid, width, and shape) are not constrained to those with physical meaning. For example, the fit can return negative peak amplitudes or shapes that correspond to over 100% Gaussian or Lorentzian in shape. In such cases, the parameters were constrained to physically meaningful values (e.g. amplitude = 0 or n = 0.8, which is typical for solid-state spectra) and the spectrum was re-fit by the program.

After obtaining the fit parameters for each peak, they were used to calculate the total spectral fit by adding them together in a plotting program such as Microsoft Excel or QtiPlot. Peak deconvolutions can then be shown by plotting the individual pseudo-Voigt profiles along with their sum. The advantage of using Peak-O-Mat is that it is able to use the same fit for multiple spectra. This allowed rapid fitting of the many spectra collected for cross-polarization variable contact time curves and for the DQ-DRENAR data.

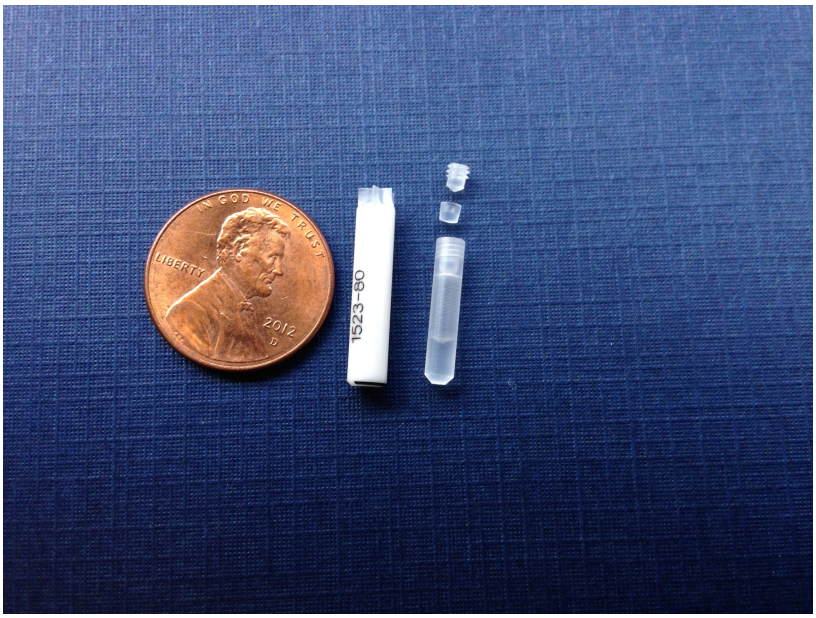

Figure 6.2: NMR rotor and rotor inserts used for samples containing depleted ^{238}U.

Solid-State NMR Rotors and Rotor packing

NMR samples containing no radioactive materials were packed into 4 mm (o.d.) zirconia rotors sealed with Kel-F rotor caps using standard rotor packing tools. To maximize the amount of material in each rotor for the purpose of improving the signal-to-noise ratio of spectra, these samples were packed down tightly using a plastic or wooden rod. Samples containing depleted ^{238}U were first packed into a Kel-F rotor insert fitted with both a taper and a screw cap, purchased from Bruker (Figure 6.2). To minimize contamination, these samples were not packed tightly, which resulted in only 10 mg loaded into each rotor insert. To minimize the impact of contamination in the event of a rotor crash during magic-angle spinning, the total activity inside a single rotor insert was kept below 1 nCi.

6.9 Fitting of Other Data

The fitting of cross-polarization variable contact time curves and DQ-DRENAR data was done using the data analysis software program IgorPro. Fitting of the U(VI) sorption isotherms was done using Microsoft Excel.

Bibliography

(1) Yantasee, W.; Lin, Y.; Fryxell, G. E.; Busche, B. J.; Birnbaum, J. C. Removal of Heavy Metals from Aqueous Solution Using Novel Nanoengineered Sorbents: Self-Assembled Carbamoylphosphonic Acids on Mesoporous Silica. *Separation Science and Technology* **2003**, *38*, 3809–3825.

(2) Margolese, D; Melero, J. A.; Christiansen, S. C.; Chmelka, B. F.; Stucky, G. D. Direct Syntheses of Ordered SBA-15 Mesoporous Silica Containing Sulfonic Acid Groups. *Chemistry of Materials* **2000**, *12*, 2448–2459.

(3) Martínez, A.; López, C.; Márquez, F.; Díaz, I. Fischer-Tropsch Synthesis of Hydrocarbons over Mesoporous Co/SBA-15 Catalysts: the Influence of Metal Loading, Cobalt Precursor, and Promoters. *Journal of Catalysis* **2003**, *220*, 486–499.

(4) Wang, S. Ordered Mesoporous Materials for Drug Delivery. *Microporous and Mesoporous Materials* **2009**, *117*, 1–9.

(5) Vavsari, V. F.; Ziarani, G. M.; Badiei, A. The Role of SBA-15 in Drug Delivery. *RSC Advances* **2015**, *5*, 91686–91707.

(6) Song, S. W.; Hidajat, K.; Kawi, S. Functionalized SBA-15 Materials as Carriers for Controlled Drug Delivery: Influence of Surface Properties on Matrix Drug Interactions. *Langmuir* **2005**, *21*, 9568–9575.

(7) Liu, X.; Li, L.; Du, Y.; Guo, Z.; Ong, T. T.; Chen, Y.; Ng, S. C.; Yang, Y. Synthesis of Large Pore-Diameter SBA-15 Mesostructured Spherical Silica and its Application in Ultra-High-Performance Liquid Chromatography. *Journal of Chromatography A* **2009**, *1216*, 7767–7773.

(8) Ma, Y.; Qi, L.; Ma, J.; Wu, Y.; Liu, O.; Cheng, H. Large-Pore Mesoporous Silica Spheres: Synthesis and Application in HPLC. *Colloids and Surfaces A: Physicochemical and Engineering Aspects* **2003**, *229*, 1–8.

(9) Giaquinto, A. P. Synthesis, Modification, and Chracterization of Spherical SBA-15 Ordered Mesoporous Silica and Evaluation in High Performance Liquid Chromatography., Ph.D. Thesis, Seton Hall University, 2012.

(10) Feng, X.; Fryxell, G. E.; Wang, L.-Q.; Kim, A. Y.; Liu, J.; Kemner, K. M. Functionalized Monolayers on Ordered Mesoporous Supports. *Science* **1997**, *276*, 923–926.

(11) Fryxell, G. E.; Wu, H.; Lin, Y.; Shaw, W. J.; Birnbaum, J. C.; Linehan, J. C.; Nie, Z.; Kemner, K.; Kelly, S. Lanthanide Selective Sorbents: Self-Assembled Monolayers on Mesoporous Supports (SAMMS). *Journal of Materials Chemistry* **2004**, *14*, 3356.

(12) Fryxell, G. E.; Mattigod, S. V.; Lin, Y.; Wu, H.; Fiskum, S.; Parker, K.; Zheng, F.; Yantasee, W.; Zemanian, T. S.; Addleman, R. S.; Liu, J.; Kemner, K.; Kelly, S.; Feng, X. Design and Synthesis of Self-Assembled Monolayers on Mesoporous Supports (SAMMS): The Importance of Ligand Posture in Functional Nanomaterials. *Journal of Materials Chemistry* **2007**, *17*, 2863.

(13) Davidson, J. D.; Wiacek, R. J.; Burton, S.; Li, X. S.; Fryxell, G. E.; Addleman, R. S.; Yantasee, W.; Sangvanich, T.; Pattamakomsan, K. Improved Deposition and Deprotection of Silane Tethered 3,4 Hydroxypyridinone (HOPO) Ligands on Functionalized Nanoporous Silica. *Inorganic Chemistry Communications* **2012**, *18*, 92–96.

(14) Fryxell, G. E.; Lin, Y.; Fiskum, S.; Birnbaum, J. C.; Wu, H.; Kemner, K.; Kelly, S. Actinide Sequestration Using Self-Assembled Monolayers on Mesoporous Supports. *Environmental Science & Technology* **2005**, *39*, 1324–1331.

(15) Li, X. S.; Courtney, A. R.; Yantasee, W.; Mattigod, S. V.; Fryxell, G. E. Templated Synthesis of Mesoporous Titanium Phosphates for the Sequestration of Radionuclides. *Inorganic Chemistry Communications* **2006**, *9*, 293–295.

(16) Addleman, R. S.; Egorov, O. B.; O'Hara, M. J.; Busche, B.; Zemanian, T. S.; Fryxell, G. Preconcentration and Assay of Radionuclides with Self Assembled Monolayers on Mesoporous Supports. *Journal of Radioanalytical and Nuclear Chemistry* **2005**, *263*, 59–64.

(17) Makowski, P.; Deschanels, X.; Grandjean, A.; Meyer, D.; Toquer, G.; Goettmann, F. Mesoporous Materials in the Field of Nuclear Industry: Applications and Perspectives. *New Journal of Chemistry* **2012**, *36*, 531.

(18) Kim, J.; Tsouris, C.; Mayes, R. T.; Oyola, Y.; Saito, T.; Janke, C. J.; Dai, S.; Schneider, E.; Sachde, D. Recovery of Uranium from Seawater: A Review of Current Status and Future Research Needs. *Separation Science and Technology* **2013**, *48*, 367–387.

(19) Zhao, D. Triblock Copolymer Syntheses of Mesoporous Silica with Periodic 50 to 300 Angstrom Pores. *Science* **1998**, *279*, 548–552.

(20) Zhao, D.; Sun, J.; Li, Q.; Stucky, G. D. Morphological Control of Highly Ordered Mesoporous Silica SBA-15. *Chem. Mater.* **2000**, *12*, 275–279.

(21) Lee, H. I.; Kim, J. H.; Stucky, G. D.; Shi, Y.; Pak, C.; Kim, J. M. Morphology-Selective Synthesis of Mesoporous SBA-15 Particles over Micrometer, Submicrometer and Nanometer Scales. *Journal of Materials Chemistry* **2010**, *20*, 8483–8487.

(22) Zhao, D.; Huo, Q.; Feng, J.; Chmelka, B. F.; Stucky, G. D. Nonionic Triblock and Star Diblock Copolymer and Oligomeric Surfactant Syntheses of Highly Ordered, Hydrothermally Stable, Mesoporous Silica Structures. *Journal of the American Chemical Society* **1998**, *120*, 6024–6036.

(23) Bunn, M.; Fetter, S.; Holdren, J. P.; van der Zwann, B. *The Economics of Reprocessing vs. Direct Disposal of Spent Nuclear Fuel*; tech. rep.; Belfer Center for Science and International Affairs, 2003, p 127.

(24) Ramana, M. V.; Suchitra, J. Y. Costing Plutonium: Economics of Reprocessing in India. *International Journal of Global Energy Issues* **2007**, *27*, 454–471.

(25) Glaser, A.; Mian, Z.; Suzuki, T. *Plutonium Separation in Nuclear Power Programs: Status, Problems, and Prospects of Civilian Reprocessing Around the World*; tech. rep.; International Panel on Fissile Materials, 2015.

(26) Glaser, A.; Mian, Z. *2015 Fissile Materials Report: Nuclear Weapon and Fissile Material Stockpiles and Production*; tech. rep.; International Panel on Fissile Material, 2015.

(27) Joint Statement on U. S. - Japan Cooperation., Washington, D.C., 2016.

(28) Podvig, P. United States and Japan to Remove Plutonium and HEU from Fast Critical Assembly., 2014.

(29) NNSA Announces Arrival of Plutonium and Uranium from Japan's Fast Critical Assembly at Savannah River Site and Y-12 National Security Complex., 2016.

(30) Salvatores, M.; Palmiotti, G. Radioactive Waste Partitioning and Transmutation within Advanced Fuel Cycles: Achievements and Challenges. *Progress in Particle and Nuclear Physics* **2011**, *66*, 144–166.

(31) Lewis, F.; Hudson, M.; Harwood, L. Development of Highly Selective Ligands for Separations of Actinides from Lanthanides in the Nuclear Fuel Cycle. *Synlett* **2011**, *18*, 2609–2632.

(32) Taylor, R. J.; Gregson, C. R.; Carrott, M. J.; Mason, C.; Sarsfield, M. J. Progress towards the Full Recovery of Neptunium in an Advanced PUREX Process. *Solvent Extraction and Ion Exchange* **2013**, *31*, 442–462.

(33) Nash, K. L.; Choppin, G. R. Separations Chemistry for Actinide Elements: Recent Developments and Historical Perspective. *Separation Science and Technology* **1997**, *32*, 255–274.

(34) Horwitz, E. P.; Kalina, D. G. The Extraction of Am(III) from Nitric Acid by Octyl (phenyl)-N,N-Diisobutylcarbamoylmethylphosphine Oxide-tri-n-butyl Phosphate Mixtures. *Solvent Extraction and Ion Exchange* **1984**, *2*, 179–200.

(35) Horwitz, E. P.; Kalina, D. C.; Diamond, H.; Vandegrift, G. F.; Schulz, W The TRUEX Process - A Process for the Extraction of Transuranic Elements from Nitric Acid in Wastes Utilizing Modified PUREX Solvent. *Solvent Extraction and Ion Exchange* **1985**, *3*, 75–109.

(36) Schulz, W. W.; Horwitz, E. P. The TRUEX Process and the Management of Liquid TRU Waste. *Separation Science and Technology* **1988**, *23*, 1191–1210.

(37) Lambert, T. N.; Jarvinen, G. D. Syntheses of Some New Polyaminocarboxylate and CMPO Calix[4]arene Chelators for the Selective Extraction of Actinide Ions. **1999**, *40*, 1613–1616.

(38) Delmau, L. H.; Simon, N.; Schwing-Weill, M.-J.; Arnaud-Neu, F.; Dozol, J.-F.; Eymard, S.; Tournois, B.; Grüttner, C.; Musigmann, C.; Tunayar, A.; Böhmer, V. Extraction of Trivalent Lanthanides and Actinides By CMPO-Like Calixarenes. *Separation Science and Technology* **1999**, *34*, 863–876.

(39) Casnati, A.; Pochini, A.; Ungaro, R.; Ugozzoli, F.; Arnaud, F.; Fanni, S.; Schwing-Weill, M.-J.; Egberink, R. J. M.; de Jong, F.; Reinhoudt, D. N. Synthesis, Complexation, and Membrane Transport Studies of 1, 3-Alternate Calix[4]arene-crown-6 Conformers: A New Class of Cesium Selective Ionophores. *Journal of the American Chemical Society* **1995**, *117*, 2767–2777.

(40) Peters, M. W.; Werner, E. J.; Scott, M. J. Enhanced Selectivity for Actinides over Lanthanides with CMPO Ligands Secured to a C3-Symmetric Triphenoxymethane Platform. *Inorganic Chemistry* **2002**, *41*, 1707–1716.

(41) Ansari, S. A.; Pathak, P.; Mohapatra, P. K.; Manchanda, V. K. Chemistry of Diglycolamides: Promising Extractants for Actinide Partitioning. *Chemical Reviews* **2012**, *112*, 1751–72.

(42) Visser, A. E.; Rogers, R. D. Room-Temperature Ionic Liquids: New Solvents for f-element Separations and Associated Solution Chemistry. *Journal of Solid State Chemistry* **2003**, *171*, 109–113.

(43) Visser, A. E.; Jensen, M. P.; Laszak, I.; Nash, K. L.; Choppin, G. R.; Rogers, R. D. Uranyl Coordination Environment in Hydrophobic Ionic Liquids: An In Situ Investigation. *Inorganic Chemistry* **2003**, *42*, 2197–2199.

(44) Modolo, G.; Odoj, R. The Separation of Trivalent Actinides from Lanthanides by Dithiophosphinic Acids from HNO_3 Acid Medium. *Journal of Alloys and Compounds* **1998**, *271-273*, 248–251.

(45) Geist, A.; Weigl, M.; Gompper, K. Minor Actinide Partitioning By Liquid-Liquid Extraction: Using a Synergistic Mixture of Bis(Chlorophenyl)-Dithiophosphinic Acid and TOPO in a Hollow Fiber Module for Americium(II)Lanthanides(III) Separation. *Separation Science and Technology* **2002**, *37*, 3369–3390.

(46) Wang, X.; Zhu, Y.; Jiao, R. Separation of Am from Macro Amount of Lanthanides by a Countercurrent Multistage Extraction with Purified Cyanex 301 and TBP. *Solvent Extraction and Ion Exchange* **2001**, *6299*, 37–41.

(47) Coupez, B.; Boehme, C.; Wipff, G. Importance of Interfacial Phenomena and Synergistic Effects in Lanthanide Cation Extraction by Dithiophosphinic Ligands: A Molecular Dynamics Study. *Journal of Physical Chemistry B* **2003**, *107*, 9484–9490.

(48) Aneheim, E.; Ekberg, C.; Fermvik, A.; Foreman, M. R. S. J.; Retegan, T.; Skarnemark, G. A TBP/BTBP-based GANEX Separation Process. Part 1: Feasibility. *Solvent Extraction and Ion Exchange* **2010**, *28*, 437–458.

(49) Horwitz, P.; Chiarizia, R.; Dietz, M. L.; Diamond, H.; Nelson, D. M. Separation and Preconcentration of Actinides from Acidic Media by Extraction Chromatography. **1993**, *281*, 361–372.

(50) Yamaura, M.; Matsuda, H. T. Sequential Separation of Actinides and Lanthanides by Extraction Chromatography using a CMPO-TBP/XAD7 Column. *Journal of Radioanalytical and Nuclear Chemistry* **1999**, *241*, 277–280.

(51) Svoboda, K.; Kyrš, M.; Vaňura, P. Synergism in the Sorption of Europium on Chromatographic Supports Impregnated with Dicarbollide Acid and Bidentate Phosphororganic Extractant. *Journal of Radioanalytical and Nuclear Chemistry* **1997**, *220*, 47–54.

(52) Yantasee, W.; Lin, Y.; Fryxell, G.; Wang, Z. Carbon Paste Electrode Modified with Carbamoylphosphonic Acid Functionalized Mesoporous Silica: A New Mercury-Free Sensor for Uranium Detection. *Electroanalysis* **2004**, *16*, 870–873.

(53) Bhattacharyya, A.; Mohapatra, P. K.; Manchanda, V. K. Separation of Am^{3+} and Eu^{3+} using an Extraction Chromatographic Resin Containing Bis(2,4,4-trimethyl pentyl) dithiophosphinic Acid as the Stationary Phase. *Journal of Chromatography A* **2006**, *1123*, 26–30.

(54) Wei, Y; Kumagai, M; Takashima, Y; Modolo, G; Odoj, R Studies on the separation of minor actinides from high-level wastes by extraction chromatography using novel silica-based extraction resins. *Nuclear Technology* **2000**, *132*, 413–423.

(55) Bhattacharyya, A; Mohapatra, P. K.; Manchanda, V. K. Solvent extraction and extraction chromatographic separation of Am3+ and Eu3+ from nitrate medium using Cyanex® 301. *Solvent Extraction and Ion Exchange* **2007**, *25*, 27–39.

(56) Horwitz, E. P.; Dietz, M. L.; Nelson, D. M.; LaRosa, J. J.; Fairman, W. D. Concentration and Separation of Actinides from Urine using a Supported Bifunctional Organophosphorus Extractant. *Analytica Chimica Acta* **1990**, *238*, 263–271.

(57) Horwitz, E. P.; Dietz, M. L.; Chiarizia, R.; Diamond, H. Separation and Preconcentration of Uranium from Acidic Media by Extraction Chromatography. *Analytica Chimica Acta* **1992**, *266*, 25–37.

(58) Yang, Q.; Yang, L.; Liu, J.; Li, Y.; Li, C. Synthesis and Characterization of Phosphonic Acid Functionalized Organosilicas with Bimodal Nanostructure. *Chemistry of Materials* **2005**, *17*, 3019–3024.

(59) Mauder, D.; Akcakayiran, D.; Lesnichin, S. B.; Findenegg, G. H.; Shenderovich, I. G. Acidity of Sulfonic and Phosphonic Acid-Functionalized SBA-15 Under Almost Water-Free Conditions. *Journal of Physical Chemistry C* **2009**, *113*, 19185–19192.

(60) Wang, P.; Zhao, L.; Wu, R.; Zhong, H.; Zou, H.; Yang, J.; Yang, Q. Phosphonic Acid Functionalized Periodic Mesoporous Organosilicas and Their Potential Applications in Selective Enrichment of Phosphopeptides. *The Journal of Physical Chemistry C* **2009**, *113*, 1359–1366.

(61) Nesterenko, P. N.; Zhukova, O. S.; Shpigun, O. A.; Jones, P Synthesis and Ion-Exchange Properties of Silica Chemically Modified with Aminophosphonic Acid. *Journal of Chromatography A* **1998**, *813*, 47–53.

(62) Corriu, R. J. P.; Datas, L.; Guari, Y.; Mehdi, A.; Reyé, C.; Thieuleux, C. Ordered SBA-15 Mesoporous Silica Containing Phosphonic Acid Groups Prepared by a Direct Synthetic Approach. *Chemical Communications* **2001**, 763–764.

(63) Lebed, P. J.; de Souza, K.; Bilodeau, F.; Larivière, D.; Kleitz, F. Phosphonate-Functionalized Large Pore 3-D Cubic Mesoporous (KIT-6) Hybrid as Highly Efficient Actinide Extracting Agent. *Chemical Communications* **2011**, *47*, 11525–7.

(64) Lebed, P. J.; Savoie, J.-d.; Florek, J.; Bilodeau, F.; Larivière, D.; Kleitz, F. Large Pore Mesostructured Organosilica-Phosphonate Hybrids as Highly Efficient and Regenerable Sorbents for Uranium Sequestration. *Chemistry of Materials* **2012**, *24*, 4166–4176.

(65) Wang, Y.-L.; Zhu, L.; Guo, B.-L.; Chen, S.-W.; Wu, W.-S. Mesoporous Silica SBA-15 Functionalized with Phosphonate Derivatives for Uranium Uptake. *New Journal of Chemistry* **2014**, *38*, 3853.

(66) Vivero-Escoto, J. L.; Carboni, M.; Abney, C. W.; DeKrafft, K. E.; Lin, W. Organo-Functionalized Mesoporous Silicas for Efficient Uranium Extraction. *Microporous and Mesoporous Materials* **2013**, *180*, 22–31.

(67) Zhang, W.; Ye, G.; Chen, J. Novel Mesoporous Silicas Bearing Phosphine Oxide Ligands with Different Alkyl Chains for the Binding of Uranium in Strong HNO_3 Media. *Journal of Materials Chemistry A* **2013**, 3–6.

(68) Yuan, L.-Y.; Liu, Y.-L.; Shi, W.-Q.; Lv, Y.-L.; Lan, J.-H.; Zhao, Y.-L.; Chai, Z.-F. High Performance of Phosphonate-Functionalized Mesoporous Silica for U(VI) Sorption from Aqueous Solution. *Dalton Transactions* **2011**, *40*, 7446–53.

(69) Wang, X.; Yuan, L.; Wang, Y.; Li, Z.; Lan, J.; Liu, Y.; Feng, Y.; Zhao, Y.; Chai, Z.; Shi, W. Mesoporous Silica SBA-15 Functionalized with Phosphonate and Amino Groups for Uranium Uptake. *Science China Chemistry* **2012**, *55*, 1705–1711.

(70) Dudarko, O. A.; Gunathilake, C.; Wickramaratne, N. P.; Sliesarenko, V. V.; Zub, Y. L.; Górka, J.; Dai, S.; Jaroniec, M. Synthesis of Mesoporous Silica-Tethered Phosphonic Acid Sorbents for Uranium Species from Aqueous Solutions. *Colloids and Surfaces A: Physicochemical and Engineering Aspects* **2015**, *482*, 1–8.

(71) Pan, Y.-c.; Tsai, H.-h. G.; Jiang, J.-c.; Kao, C.-c.; Sung, T.-l.; Chiu, P.-j.; Saikia, D.; Chang, J.-h.; Kao, H.-m. Probing the Nature and Local Structure of Phosphonic Acid Groups Functionalized in Mesoporous Silica SBA-15. *Journal of Physical Chemistry C* **2012**, *116*, 1658–1669.

(72) Bibent, N.; Charpentier, T.; Devautour-Vinot, S.; Mehdi, A.; Gaveau, P.; Henn, F.; Silly, G. Solid-state NMR Spectroscopic Studies of Propylphosphonic Acid Functionalized SBA-15 Mesoporous Silica: Characterization of Hydrogen-Bonding Interactions. *European Journal of Inorganic Chemistry* **2013**, 2350–2361.

(73) Shusterman, J.; Mason, H.; Bruchet, A.; Zavarin, M.; Kersting, A. B.; Nitsche, H. Analysis of Trivalent Cation Complexation to Functionalized Mesoporous Silica using Solid-State NMR Spectroscopy. *Dalton Transactions* **2014**, *43*, 16649–16658.

(74) Cotton, S., *Lanthanide and Actinide Chemistry*; John Wiley & Sons, Ltd.: West Sussex, England, 2006.

(75) Moseley, H. XCIII. The High-Frequency Spectra of the Elements. *Philosophical Magazine Series 6* **1913**, *26*, 1024–1034.

(76) Moseley, H. LXXX. The High-Frequency Spectra of the Elements. Part II. *Philosophical Magazine Series 6* **1914**, *27*, 703–713.

(77) Seaborg, G. T., *Modern Alchemy*, 1994.

(78) Reich, T; Moll, H; Arnold, T; Denecke, M.; Hennig, C; Geipel, G; Bernhard, G; Nitsche, H; Allen, P.; Bucher, J.; Edelstein, N.; Shuh, D. An EXAFS Study of Uranium(VI) Sorption onto Silica Gel and Ferrihydrite. *Journal of Electron Spectroscopy and Related Phenomena* **1998**, *96*, 237–243.

(79) *The Chemistry of the Actinide and Transactinide Elements*, 3rd; Morss, L. R., Edelstein, N. M., Fuger, J., Katz, J. J., Eds.; Springer: Dordrecht, The Netherlands, 2006.

(80) Vallet, V.; Privalov, T.; Wahlgren, U.; Grenthe, I. The Mechanism for Water Exchange in $[Am_{O2}(H_2O)_5]^{2+}$ and in the Isoelectronic $[UO_2(H_2O)_5]^{2+}$ and $[NpO_2(H_2O)_5]^{2+}$ Complexes as Studied by Quantum Chemical Methods. *Journal of the American Chemical Society* **2004**, *126*, 7766–7767.

(81) Wahlgren, U; Moll, H; Grenthe, I; Schimmelpfennig, B; Maron, L; Vallet, V; Gropen, O Structure of Uranium(VI) in Strong Alkaline Solutions. A Combined Theoretical and Experimental Investigation. *Journal of Physical Chemistry A* **1999**, *103*, 8257–8264.

(82) Neuefeind, J; Soderholm, L; Skanthakumar, S Experimental Coordination Environment of Uranyl (VI) in Aqueous Solution. *The Journal of Physical Chemistry A* **2004**, *108*, 2733–2739.

(83) Vallet, V.; Wahlgren, U.; Schimmelpfennig, B.; Szabó, Z.; Grenthe, I. The Mechanism for Water Exchange in $[UO_2(H_2O)_5]^{2+}$ and $[UO_2(oxalate)_2(H_2O)]^{2-}$, as Studied by Quantum Chemical Methods. *Journal of the American Chemical Society* **2001**, *123*, 11999–12008.

(84) Zalkin, A.; Templeton, L. K.; Templeton, D. H. Structure of Rubidium Uranyl(VI) Trinitrate. *Acta Cryst. C* **1989**, *45*, 810–11.

(85) Anderson, A.; Chieh, C.; Irish, D. E.; Tong, J. P. K. An X-ray Crystallographic, Raman, and Infrared Spectral Study of Crystalline Potassium Uranyl Carbonate, $K_4UO_2(CO_3)_3$. *Canadian Journal of Chemistry* **1980**, *58*, 1651–1658.

(86) Gorman-Lewis, D.; Burns, P. C.; Fein, J. B. Review of Uranyl Mineral Solubility Measurements. *Journal of Chemical Thermodynamics* **2008**, *40*, 335–352.

(87) Grenthe, I.; Fuger, J.; Konings, R. J. M.; Lemire, R. J.; Muller, A. B.; Nguyen-Trung, C.; Wanner, H., *Chemical Thermodynamics of Uranium*; Wanner, H., Forest, I., Eds.; Nuclear Energy Agency OECD: Amsterdam, The Netherlands, 1992.

(88) Silva, R. J.; Yee, A. W. *Uranium Retardation Mechanisms*; tech. rep.; Berkeley, California: Earth Science Division, Lawrence Berkeley National Laboratory (LBL-13600), 1981.

(89) Endrizzi, F.; Leggett, C. J.; Rao, L. Scientific Basis for Efficient Extraction of Uranium from Seawater. I: Understanding the Chemical Speciation of Uranium under Seawater Conditions. *Industrial & Engineering Chemistry Research* **2016**, *55*, 4249–4256.

(90) Bernhard, G.; Geipel, G.; Reich, T.; Brendler, V.; Amayri, S.; Nitsche, H. Uranyl (VI) Carbonate Complex Formation: Validation of the $Ca_2UO_2(CO_3)_3$ Species. *Radiochimica Acta* **2001**, *89*, 511–518.

(91) Moll, H.; Geipel, G.; Matz, W.; Bernhard, G.; Nitsche, H. Solubility and Speciation of $(UO_2)_2SiO_4 \cdot H_2O$ in Aqeuous Systems. *Radiochimica Acta* **1996**, *74*, 3–7.

(92) ALOthman, Z. A Review: Fundamental Aspects of Silicate Mesoporous Materials. *Materials* **2012**, *5*, 2874–2902.

(93) Unger, K.; Kumar, D. In *Adsorption on Silica Surfaces*, Papirer, E., Ed.; Mercel Dekker, Inc.: 2000; Chapter 1, pp 1–7.

(94) Wan, Y.; Zhao, D. On the Controllable Soft-Templating Approach to Mesoporous Silicates. *Chemical Reviews* **2007**, *107*, 2821–2860.

(95) Everett, D. H. Manual of Symbols and Terminology for Physicohemical Quantities and Units. *Pure and Applied Chemistry* **1971**, *31*, 577–638.

(96) Naumov, S. Hysteresis Phenomena in Mesoporous Materials., Ph.D. Thesis, Universität Leipzig, 2009.

(97) Vansant, E. F.; Van Der Voort, P.; Vrancken, K. C., *Characterization and Chemical Modification of the Silica Surface*; Elsevier Science B. V.: 1995.

(98) Brunauer, S.; Emmett, P. H.; Teller, E. Adsorption of Gases in Multimolecular Layers. *Journal of the American Chemical Society* **1938**, *60*, 309–319.

(99) Barrett, E. P.; Joyner, L. G.; Halenda, P. P. The Determination of Pore Volume and Area Distributions in Porous Substances. I. Computations from Nitrogen Isotherms. *Journal of the American Chemical Society* **1951**, *73*, 373–380.

(100) Sing, K. S. W.; Everett, D. H.; Haul, R. A. W.; Moscou, L.; Pierotti, R. A.; Rouquérol, J.; Siemieniewska, T. Reporting Physisorption Data for Gas-Solid Systems with Special Reference to the Determination of Surface Area and Porosity. *Pure and Applied Chemistry* **1985**, *57*, 603–619.

(101) Boutin, A.; Coasne, B.; Fuchs, A. H.; Galarneau, A.; Di Renzo, F. Experiment and Theory of Low-Pressure Nitrogen Adsorption in Organic Layers Supported or Grafted on Inorganic Adsorbents: Toward a Tool to Characterize Surfaces of Hybrid Organic/Inorganic Systems. *Langmuir* **2012**, *28*, 9526–9534.

(102) Hench, L. L.; West, J. K. The Sol-Gel Process. *Chem. Rev.* **1990**, *90*, 33–72.

(103) Zhao, D.; Wan, Y.; Zhou, W., *Ordered Mesoporous Materials*; Wiley-VCH: Weinheim, Germany, 2013.

(104) Huo, Q.; Margolese, D. I.; Ciesla, U.; Demuth, D. G.; Feng, P.; Gier, T. E.; Sieger, P.; Firouzi, A.; Chmelka, B. F.; Schuth, F.; Stucky, G. D. Organization of Organic Molecules with Inorganic Molecular Species into Nanocomposite Biphase Arrays. *Chemistry of Materials* **1994**, *6*, 1176–1191.

(105) Huo, Q.; Margolese, D. I.; Ciesla, U.; Feng, P.; Gier, T. E.; Sieger, P.; Leon, R.; Petroff, P. M.; Schüth, F.; Stucky, G. D. Generalized Synthesis of Periodic Surfactant/Inorganic Composite Materials. *Nature* **1994**, *368*, 317–321.

(106) Zholobenko, V. L.; Khodakov, A. Y.; Impéror-Clerc, M.; Durand, D.; Grillo, I. Initial Stages of SBA-15 Synthesis: an Overview. *Advances in Colloid and Interface Science* **2008**, *142*, 67–74.

(107) Lukens, W. W.; Schmidt-Winkel, P.; Zhao, D.; Feng, J.; Stucky, G. D. Evaluating Pore Sizes in Mesoporous Materials: a Simplified Standard Adsorption Method and a Simplified Broekhoff-de Boer Method. *Langmuir* **1999**, *15*, 5403–5409.

(108) Chan, H. B. S.; Budd, P. M.; deV. Naylor, T. Control of Mesostructured Silica Particle Morphology. *Journal of Materials Chemistry* **2001**, *11*, 951–957.

(109) Yasmin, T.; Müller, K. Synthesis and Characterization of Surface Modified SBA-15 Silica Materials and their Application in Chromatography. *Journal of Chromatography A* **2011**, *1218*, 6464–6475.

(110) Katiyar, A.; Yadav, S.; Smirniotis, P. G.; Pinto, N. G. Synthesis of Ordered Large Pore SBA-15 Spherical Particles for Adsorption of Biomolecules. *Journal of Chromatography A* **2006**, *1122*, 13–20.

(111) Li, C.; Di, B.; Hao, W.; Yan, F.; Su, M. Aminopropyl-Functionalized Ethane-Bridged Periodic Mesoporous Organosilica Spheres: Preparation and Application in Liquid Chromatography. *Journal of Chromatography A* **2011**, *1218*, 408–415.

(112) Huo, Q.; Margolese, D. I.; Stucky, G. D. Surfactant Control of Phases in the Synthesis of Mesoporous Silica-Based Materials. *Chemistry of Materials* **1996**, *8*, 1147–1160.

(113) Chuang, I.-s.; Maciel, G. A Detailed Model of Local Structure and Silanol Hydrogen Bonding of Silica Gel Surfaces. *The Journal of Physical Chemistry B* **1997**, *101*, 3052–3064.

(114) Zhuravlev, L. The Surface Chemistry of Amorphous Silica. Zhuravlev Model. *Colloids and Surfaces A: Physicochemical and Engineering Aspects* **2000**, *173*, 1–38.

(115) Ide, M.; El-Roz, M.; De Canck, E.; Vicente, A.; Planckaert, T.; Bogaerts, T.; Van Driessche, I.; Lynen, F.; Van Speybroeck, V.; Thybault-Starzyk, F.; Van Der Voort, P. Quantification of Silanol Sites for the Most Common Mesoporous Ordered Silicas and Organosilicas: Total versus Accessible Silanols. *Physical Chemistry Chemical Physics* **2013**, *15*, 642–50.

(116) Tucker, M. G.; Dove, M. T.; Keen, D. A. Direct Measurement of the Thermal Expansion of the Si-O Bond by Neutron Total Scattering. *Journal of Physics: Condensed Matter* **2000**, *12*, L425–L430.

(117) Sayari, A.; Han, B. H.; Yang, Y. Simple Synthesis Route to Monodispersed SBA-15 Silica Rods. *Journal of the American Chemical Society* **2004**, *126*, 14348–14349.

(118) Jiao, L.; Regalbuto, J. R. The Synthesis of Highly Dispersed Noble and Base Metals on Silica via Strong Electrostatic Adsorption: II. Mesoporous Silica SBA-15. *Journal of Catalysis* **2008**, *260*, 342–350.

(119) Kokunešoski, M.; Gulicovski, J.; Matović, B.; Logar, M.; Milonjić, S. K.; Babić, B. Synthesis and Surface Characterization of Ordered Mesoporous Silica SBA-15. *Materials Chemistry and Physics* **2010**, *124*, 1248–1252.

(120) Kosmulski, M. In *Adsorption on Silica Surfaces*, Papirer, E., Ed.; Marcel Dekker, Inc.: 2000; Chapter 13, pp 399–440.

(121) Milonjic, S.; Cokesa, R.; Stevanovic, R. V Dynamic Adsorption of Uranium(VI) and Zirconium(IV) on Silica Gel. *Journal of Radioanalytical and Nuclear Chemistry* **1992**, *158*, 79–90.

(122) Ahrland, S.; Grenthe, I.; Noren, B. The Ion Exchange Properties of Silica Gel I. The Sorption of Na^{+}, Ca^{2+}, Ba^{2+}, $UO_2{}^{2+}$, Gd^{3+}, Zr(IV), Nb, U(IV) and Pu(IV). *Acta Chemica Scandinavica* **1960**, *14*, 1059–1076.

(123) Ahrland, S.; Grenthe, I.; Norén, B. The Ion Exchange Properties of Silica Gel II. Separation of Plutonium and Fission Products from Irradiated Uranium. *Acta Chemica Scandinavica* **1960**, *14*, 1077–1090.

(124) Pathak, P. N.; Choppin, G. R. Kinetic and Thermodynamic Studies of Uranium(VI) Sorption on Hydrous Silica. *Journal of Radioanalytical and Nuclear Chemistry* **2007**, *95*, 507–512.

(125) Wang, X.; Zhu, G.; Guo, F. Removal of Uranium(VI) Ion from Aqueous Solution by SBA-15. *Annals of Nuclear Energy* **2013**, *56*, 151–157.

(126) Dent, A. J.; Ramsay, J. D. F.; Swanton, S. W. An EXAFS Study of Uranyl Ion in Solution and Sorbed onto Silica and Montmorillonite Clay Colloids. *Journal of Colloid And Interface Science* **1992**, *150*, 45–60.

(127) Reich, T.; Moll, H.; Denecke, M. A.; Geipel, G.; Bernhard, G.; Nitsche, H.; Allen, P. G.; Bucher, J. J.; Kaltsoyannis, N.; Edelstein, N. M.; Shuh, D. K. Characterization of Hydrous Uranyl Silicate by EXAFS : Radiochimca Acta. *Radiochimica Acta* **1996**, *74*, 219–223.

(128) Sylwester, E.; Hudson, E.; Allen, P. The Structure of Uranium(VI) Sorption Complexes on Silica, Alumina, and Montmorillonite. *Geochimica et Cosmochimica Acta* **2000**, *64*, 2431–2438.

(129) Massey, M. S.; Lezama-Pacheco, J. S.; Nelson, J. M.; Fendorf, S.; Maher, K. Uranium Incorporation into Amorphous Silica. *Environmental Science & Technology* **2014**, *48*, 8636–44.

(130) Gabriel, U.; Charlet, L.; Schläpfer, C. W. In Situ Speciation of Uranium (VI) at the Silica-Water Interface: A Combined TRLIFS and Surface Complexation Study. *Water-Rock Interactions, Ore Deposits, and Environmental Geochemistry: A Tribute to David A. Crerar* **2002**, *7*, 423–440.

(131) Sander, L. C.; Wise, S. A. Influence of Stationary Phase Chemistry on Shape Recognition in Liquid Chromatography. *Anal. Chem.* **1995**, *67*, 3284–3292.

(132) Hoffmann, F.; Cornelius, M.; Morell, J.; Fröba, M. Silica-Based Mesoporous Organic-Inorganic Hybrid Materials. *Angewandte Chemie (International Ed.)* **2006**, *45*, 3216–3251.

(133) Arkles, B.; Steinmetz, J.; Zazyczny, J.; Mehta, P. Factors Contributing to the Stability of Alkoxysilanes in Aqueous Solution. *Journal of Adhesion Science and Technology* **1992**, *6*, 193–206.

(134) Onclin, S.; Ravoo, B. J.; Reinhoudt, D. N. Engineering Silicon Oxide Surfaces using Self-Assembled Monolayers. *Angewandte Chemie (International Ed.)* **2005**, *44*, 6282–304.

(135) Ulman, A. Formation and Structure of Self-Assembled Monolayers. *Chemical Reviews* **1996**, *96*, 1533–1554.

(136) Martin, T.; Galarneau, A.; Renzo, F. D.; Brunel, D.; Fajula, F; Heinisch, S; Cretier, G; Rocca, J.-L. Great Improvement of Chromatographic Performance Using MCM-41 Spheres as Stationary Phase in HPLC. *Chemistry of Materials* **2004**, *16*, 1725–1731.

(137) Wirth, M. J.; Fatunmbi, H. Horizontal Polymerization of Mixed Trifunctional Silanes on Silica: A Potential Chromatographic Stationary Phase. *Anal. Chem.* **1992**, *64*, 2783–2786.

(138) Wirth, M. J.; Fatunmbi, H. O. Horizontal Polymerization of Mixed Trifunctional Silanes on Silica. 2. Application to Chromatographic Silica Gel. *Anal. Chem.* **1993**, *65*, 822–826.

(139) Sindorf, D. W.; Maciel, G. E. Silicon-29 Nuclear Magnetic Resonance Study of the Surface of Silica Gel by Cross Polarization and Magic-Angle Spinning. *Journal of the American Chemical Society* **1980**, *102*, 7607.

(140) Liu, C. C.; Maciel, G. E. The Fumed Silica Surface: A Study by NMR. *Journal of the American Chemical Society* **1996**, *118*, 5103–5119.

(141) Sindorf, D. W.; Maciel, G. E. Silicon-29 CP/MAS NMR Studies of Methylchlorosilane Reactions on Silica Gel. *Journal of the American Chemical Society* **1981**, *103*, 4263–4265.

(142) Fatunmbi, H.; Bruch, M. D.; Wirth, M. J. ^{29}Si and ^{13}C NMR Characterization of Mixed Horizontally Polymerized Monolayers on Silica Gel. **1993**, 2048–2054.

(143) Levitt, M. H., *Spin Dynamics: Basics of Nuclear Magnetic Resonance*; John Wiley & Sons, Ltd.: Sussex, England, 2001.

(144) Duer, M. J., *Introduction to Solid-State NMR Spectroscopy*; Blackwell Publishing Ltd.: 2004.

(145) Mackenzie, K. J. D.; Smith, M. E., *Multinuclear Solid-State NMR of Inorganic Materials*; Elsevier Science Ltd.: Oxford, 2002.

(146) Gorenstein, D. G. Non-Biological Aspects of Phosphorus-31 NMR Spectroscopy. *Progress in Nuclear Magnetic Resonance Spectroscopy* **1984**, *16*, 1–98.

(147) Bronnimann, C.; Zeigler, R.; Maciel, G. Proton NMR Study of Dehydration of the Silica Gel Surface. *Journal of the American Chemical Society* **1988**, *110*, 2023–2026.

(148) Hartmann, S. R.; Hahn, E. L. Nuclear Double Resonance in the Rotating Frame. *Physical Review* **1962**, *128*, 2042–2053.

(149) Pines, A.; Gibby, M. G.; Waugh, J. S. Proton-Enhanced NMR of Dilute Spins in Solids. *The Journal of Chemical Physics* **1973**, *59*, 569.

(150) Kolodziejski, W.; Klinowski, J. Kinetics of Cross-Polarization in Solid-State NMR: A Guide for Chemists. *Chemical Reviews* **2002**, *102*, 613–628.

(151) Müller, L.; Kumar, A.; Baumann, T.; Ernst, R. R. Transient Oscillations in NMR Cross-Polarization Experiments in Solids. *Physical Review Letters* **1974**, *32*, 1402–1406.

(152) Naito, A.; McDowell, C. A. Anisotropic Behavior of the ^{13}C Nuclear Spin Dynamics in a Single Crystal of l-Alanine. *The Journal of Chemical Physics* **1986**, *84*, 4181.

(153) Sindorf, D. W.; Maciel, G. E. Solid-state NMR Studies of the Reactions of Silica Surfaces with Polyfunctional Chloromethylsilanes and Ethoxymethylsilanes. *Journal of the American Chemical Society* **1983**, *105*, 3767–3776.

(154) Sindorf, D.; Maciel, G. Cross-polarization magic-angle-spinning silicon-29 nuclear magnetic resonance study of silica gel using trimethylsilane bonding as a probe of surface geometry and. *The Journal of Physical Chemistry* **1982**, *86*, 5208–5219.

(155) Sindorf, D. W.; Maciel, G. E. Silicon-29 Nuclear Magnetic Resonance Study of Hydroxyl Sites on Dehydrated Silica Gel Surfaces, using Silylation as a Probe. *The Journal of Physical Chemistry* **1983**, *87*, 5516–5521.

(156) Sindorf, D. W.; Maciel, G. E. 29Si NMR Study of Dehydrated/Rehydrated Silica Gel Using Cross Polarization and Magic-Angle Spinning. *Journal of the American Chemical Society* **1983**, 1487–1493.

(157) Maciel, G. E.; Sindorf, D. W.; Bartuska, V. J. Characterization of Silica-Attached Systems by ^{29}Si and ^{13}C Cross-Polarization and Magic-Angle Spinning Nuclear Magnetic Resonance. *Journal of Chromatography* **1981**, *205*, 438–443.

(158) Mason, H. E.; Harley, S. J.; Maxwell, R. S.; Carroll, S. a. Probing the Surface Structure of Divalent Transition Metals using Surface Specific Solid-State NMR Spectroscopy. *Environmental Science & Technology* **2012**, *46*, 2806–12.

(159) Mason, H.; Begg, J. D.; Maxwell, R. S.; Kersting, A. B.; Zavarin, M. A Novel Solid-State NMR Method for the Investigation of Trivalent Lanthanide Sorption on Amorphous Silica at Low Surface Loadings. *Environmental Science: Processes & Impacts* **2016**, *18*, 802–809.

(160) Kaflak, A.; Chmielewski, D.; Górecki, A.; Kolodziejski, W. Kinetics of ^{1}H $\longrightarrow$ ^{31}P Cross-Polarization in Human Trabecular Bone. *Solid State Nuclear Magnetic Resonance* **1998**, *10*, 191–195.

(161) Klimavicius, V.; Kareiva, A.; Balevicius, V. Solid-State NMR Study of Hydroxyapatite Containing Amorphous Phosphate Phase and Nanostructured Hydroxyapatite: Cut-Off Averaging of CP-MAS Kinetics and Size Profiles of Spin Clusters. *Journal of Physical Chemistry C* **2014**, *118*, 28914–28921.

(162) Mason, H. E. Solid-State NMR Spectroscopic Investigation of Structural and Chemical Defects in Minerals., Ph.D. Thesis, Stony Brook University, 2009.

(163) Levitt, M. H.; Suter, D; Ernst, R. R. Spin Dynamics and Thermodynamics in Solid-State NMR Cross Polarization. *The Journal of Chemical Physics* **1986**, *84*, 4243–4255.

(164) Ren, J.; Eckert, H. A Homonuclear Rotational Echo Double-Resonance Method for Measuring Site-Resolved Distance Distributions in I=1/2 Spin Pairs, Clusters, and Multispin Systems. *Angewandte Chemie (International Ed.)* **2012**, *51*, 12888–12891.

(165) Ren, J.; Eckert, H. DQ-DRENAR: A New NMR Technique to Measure Site-Resolved Magnetic Dipole-Dipole Interactions in Multispin-1/2 Systems: Theory and Validation on Crystalline Phosphates. *Journal of Chemical Physics* **2013**, *138*, 1–16.

(166) Uribe, E. C.; Mason, H. E.; Shusterman, J. A.; Bruchet, A.; Nitsche, H. Probing the Interaction of U(VI) with Phosphonate-Functionalized Mesoporous Silica using Solid-State NMR Spectroscopy. *Dalton Trans.* **2016**, 10447–10458.

(167) Stanton, J.; Maatman, R. W. The Reaction Between Aqueous Uranyl Ion and the Surface of Silica Gel. *Journal of Colloid Science* **1963**, *18*, 132–146.

(168) Michard, P.; Guibal, E.; Vincent, T.; Le Cloirec, P. Sorption and Desorption of Uranyl Ions by Silica Gel: pH, Particle Size and Porosity Effects. *Microporous Materials* **1996**, *5*, 309–324.

(169) Shusterman, J. A.; Mason, H. E.; Bowers, J.; Bruchet, A.; Uribe, E. C.; Kersting, A. B.; Nitsche, H. Development and Testing of Diglycolamide Functionalized Mesoporous Silica for Sorption of Trivalent Actinides and Lanthanides. *Applied Materials & Interfaces Interfaces* **2015**, *7*, 20591–20599.

(170) Hlushak, S.; Simonin, J.; Caniffi, B.; Moisy, P.; Sorel, C.; Bernard, O. Description of Partition Equilibria for Uranyl Nitrate, Nitric Acid and Water Extracted by Tributyl Phosphate in Dodecane. *Hydrometallurgy* **2011**, *109*, 97–105.

(171) Benedict, M.; Pigford, T. H.; Levi, H. W., *Nuclear Chemical Engineering*, 2nd; McGraw-Hill: 1981.

(172) Jaroniec, C.; Kruk, M Tailoring Surface and Structural Properties of MCM-41 Silicas by Bonding Organosilanes. *The Journal of Physical Chemistry B* **1998**, *102*, 5503–5510.

(173) Couston, L.; Pouyat, D.; Moulin, C.; Decambox, P. Speciation of Uranyl Species in Nitric Acid Medium by Time-Resolved Laser-Induced Fluorescence. *Applied Spectroscopy* **1995**, *49*, 349–353.

(174) Muntean, J. V.; Nash, K. L.; Rickert, P. G.; Sullivan, J. C. Dynamic NMR Study of Ligand Exchange Reactions in U(VI)-Phosphonic Acid Systems. *Journal of Physical Chemistry A* **1999**, *103*, 3383–3387.

(175) Bowen, S. M.; Duesler, E. N.; Paine, R. T. Synthesis and Crystal and Molecular Structure of Bis(nitrato)[diisopropyl (N,N-diethylcarbamyl)methylenephosphonate] dioxouranium(VI). *Inorganic Chemistry* **1983**, 286–290.

(176) Gullion, T.; Schaefer, J. Rotational-Echo Double-Resonance NMR. *Journal of Magnetic Resonance* **1989**, *81*, 196–200.

(177) *The Merck Index - An Encyclopedia of Chemicals, Drugs, and Biologicals*; O'Neil, M. J., Ed.; Merck and Co., Inc.: 2006, p 573.

(178) Rosenholm, J. M.; Czuryszkiewicz, T.; Kleitz, F.; Rosenholm, J. B.; Lindén, M. On the Nature of the Brønsted Acidic Groups on Native and Functionalized Mesoporous Siliceous SBA-15 as Studied by Benzylamine Adsorption from Solution. *Langmuir* **2007**, *23*, 4315–4323.

(179) Shaw, A. M.; Hannon, T. E.; Li, F.; Zare, R. N. Adsorption of Crystal Violet to the Silica-Water Interface Monitored by Evanescent Wave Cavity Ring-Down Spectroscopy. *Journal of Physical Chemistry B* **2003**, *107*, 7070–7075.

(180) Zhao, X.; Ong, S.; Eisenthal, K. B. Polarization of Water Molecules at a Charged Interface. Second Harmonic Studies of Charged Monolayers at the Air/Water Interface. *Chemical Physics Letters* **1993**, *202*, 513–520.

(181) Reed, B. E.; Matsumoto, M. R. Modeling Cadmium Adsorption by Activated Carbon Using the Langmuir and Freundlich Isotherm Expressions. *Separation Science and Technology* **1993**, *28*, 2179–2195.

(182) Pluth, J. J.; Smith, J. V.; Faber, J. Crystal Structure of Low Cristobalite at 10, 293, and 473 K: Variation of Framework Geometry with Temperature. *Journal of Applied Physics* **1985**, *57*, 1045–1049.

(183) Burns, J. H.; Brown, G. M. Structure of Dinitratodioxobis (triisobutyl phosphate) uranium(Vl) at 139 K. *Acta Crystallographica Section C Crystal Structure Communications* **1985**, *C41*, 1446–1448.

(184) Birnbaum, J. C.; Busche, B.; Lin, Y.; Shaw, W. J.; Fryxell, G. E. Synthesis of Carbamoylphosphonate Silanes for the Selective Sequestration of Actinides. *Chemical Communications* **2002**, 1374–1375.

(185) Yantasee, W.; Fryxell, G. E.; Addleman, R. S.; Wiacek, R. J.; Koonsiripaiboon, V.; Pattamakomsan, K.; Sukwarotwat, V.; Xu, J.; Raymond, K. N. Selective Removal of Lanthanides from Natural Waters, Acidic Streams and Dialysate. *Journal of Hazardous Materials* **2009**, *168*, 1233–8.

(186) Fryxell, G. E. *Actinide-Specific Interfacial Chemistry of Monolayer Coated Mesoporous Ceramics*; tech. rep.; 2001.

(187) Linehan, J. C.; Stiff, C. M.; Fryxell, G. E. A Simple Determination of Alkylsilane Monolayer Population Density. *Inorganic Chemistry Communications* **2006**, *9*, 239–241.

(188) Parsons-Moss, T. Interactions of Plutonium and Lanthanides with Ordered Mesoporous Materials. *UC Berkeley Ph.D. Dissertation* **2014**.

(189) Antochshuk, V.; Jaroniec, M. Functionalized Mesoporous Materials Obtained via Interfacial Reactions in Self-Assembled Silica-Surfactant Systems. *Chemistry of Materials* **2000**, *12*, 2496–2501.

(190) Aliev, A.; Ou, D. L.; Ormsby, B.; Sullivan, A. C. Porous Silica and Polysilsesquioxane with Covalently Linked Phosphonates and Phosphonic Acids. *Journal of Materials Chemistry* **2000**, *10*, 2758–2764.

(191) Melnyk, I. V.; Fatnassi, M.; Cacciaguerra, T.; Zub, Y. L.; Alonso, B. Spray-Dried Porous Silica Microspheres Functionalised by Phosphonic Acid Groups. *Microporous and Mesoporous Materials* **2012**, *152*, 172–177.

(192) Lee, Y. J.; Bingo, B.; Murakhtina, T.; Sebastiani, D.; Meyer, W. H.; Wegner, G.; Spiess, H. W. High-Resolution Solid-State NMR Studies of Poly(vinyl phosphonic acid) Proton-Conducting Polymer: Molecular Structure and Proton Dynamics. *Journal of Physical Chemistry B* **2007**, *111*, 9711–9721.

(193) Yang, S. W.; Doetschman, D. C.; Schulte, J. T.; Sambur, J. B.; Kanyi, C. W.; Fox, J. D.; Kowenje, C. O.; Jones, B. R.; Sherma, N. D. Sodium X-type Faujasite Zeolite Decomposition of Dimethyl Methylphosphonate (DMMP) to Methylphosphonate: Nucleophilic Zeolite Reactions I. *Microporous and Mesoporous Materials* **2006**, *92*, 56–60.

(194) Zeldin, M.; Mehta, P.; Vernon, W. D. Phosphorus-31 NMR of Triphenylphosphine Oxide Complexes with Compounds of Silicon, Germanium, and Tin. *Inorganic Chemistry* **1979**, *18*, 463–466.

(195) Amatore, C.; Jutand, A.; M'Barki, M. A. Evidence of the Formation of Zerovalent Palladium from $Pd(OAc)_2$ and Triphenylphosphine. *Organometallics* **1992**, *11*, 3009–3013.

(196) Byrne, L. T.; Ferro, V.; Stevenson, S.; Stick, R. V. Analysis of the ^{1}H NMR Spectra of Some Diethyl Phosphonates. **1994**, *32*, 749–752.

(197) Blanchard, J. W.; Groy, T. L.; Yarger, J. L.; Holland, G. P. Investigating Hydrogen-Bonded Phosphonic Acids with Proton Ultrafast MAS NMR and DFT Calculations. *Journal of Physical Chemistry C* **2012**, *116*, 18824–18830.

(198) Harris, R. K.; Jackson, P.; Merwin, L. H.; Say, B. J.; Hgele, G. Perspectives in High-Resolution Solid-State Nuclear Magnetic Resonance, with Emphasis on Combined Rotation and Multiple-Pulse Spectroscopy. *Journal of the Chemical Society, Faraday Transactions 1* **1988**, *84*, 3649.

(199) Cohen, D. The Absorption Spectra of Plutonium Ions in Perchloric Acid Solutions. *J. Inorg. Nucl. Chem.* **1961**, *18*, 211–218.

(200) Cohen, D. Electrochemical Studies of Plutonium Ions in Perchloric Acid Solution. *J. Inorg. Nucl. Chem.* **1961**, *18*, 207–210.

(201) Silva, R. J.; Nitsche, H. In *Advances in Plutonium Chemistry 1967-2000*, Hoffman, D. C., Ed.; American Nuclear Society: La Grange Park, IL, 2002, pp 89–111.

(202) Magi, M.; Lippmaa, E.; Samoson, a.; Engelhardt, G.; Grimmer, a. R. Solid-State High-Resolution Silicon-29 Chemical Shifts in Silicates. *The Journal of Physical Chemistry* **1984**, *88*, 1518–1522.

(203) Rabenstein, D. L.; Sayer, T. L. Carbon-13 Chemical Shift Parameters for Amines, Carboxylic Acids, and Amino Acids. *Journal of Magnetic Resonance* **1976**, *24*, 27–39.

(204) Li, W.; Xu, W.; Parise, J. B.; Phillips, B. L. Formation of Hydroxylapatite from Co-sorption of Phosphate and Calcium by Boehmite. *Geochimica et Cosmochimica Acta* **2012**, *85*, 289–301.

(205) Yesinowski, J. P.; Eckert, H. Hydrogen Environments in Calcium Phosphates: Proton MAS NMR at High Spinning Speeds. *Journal of the American Chemical Society* **1987**, *109*, 6274–6282.